University of Southampton

Parametric feedback cooling and squeezing of optically levitated particles

by

Jamie Vovrosh

A thesis submitted in fulfillment for the
degree of Doctor of Philosophy

in the

Faculty of Physical Sciences and Engineering
Department of Physics and Astronomy

June 2018

University of Southampton

Abstract

Faculty of Physical Sciences and Engineering
Department of Physics and Astronomy

Doctor of Philosophy

by Jamie Vovrosh

Free space gradient force traps are hugely versatile experimental systems. Their realisation opens up new avenues for the exploration of various areas of fundamental physics, including both quantum physics and thermodynamics. Their high levels of sensitivity also have attractive implications for force sensing. In this thesis a novel experimental setup will be presented, along with experimental protocols, as a framework upon which such studies can be built.

Using a paraboloidal mirror to create a diffraction limited, gradient force optical trap, the motion of nanoparticles ranging from 18 nm to 312 nm in diameter was detected via a single photodiode. Several properties of the levitated particles were measured, including: the mass, radius, oscillation amplitude (via the use of a volts to metre conversion factor) and the damping experienced at various pressures. This was done via two methods. The first, widely established, method required fitting a power spectral density, derived using the kinetic theory of gases, to the motion of the particle. The second, novel method, involved scanning the wavelength of the trapping laser. Using this method, it was possible to determine the mass of a levitated particle without assuming the kinetic model and material density. From the wavelength scan, the sensitivity of the experimental system was measured to be 200 fm/$\sqrt{\text{Hz}}$. Within this optical setup, the ability to control the trap frequencies of all three motional degrees of freedom, through varying the power of the trapping laser, was demonstrated. The ability to independently control and separate the transverse trapping frequencies from one another, as well as from the z axis, was also shown to be possible, using elliptically polarized light. The effect of changing the pressure inside the chamber in which a levitated nanoparticle is trapped is also explored. Trapping of nanoparticles at pressures as low as 10^{-5} mbar, without any active feedback, was achieved.

A method for measuring the internal temperature of levitated particles was then demonstrated. This was done through measuring and fitting the Planck equation to the emitted thermal spectrum of a levitated silica nanoparticle. It was then shown that the temperature of levitated particles can be controlled via the intensity of the laser light as well as the pressure within the chamber. Over a pressure range of 1000 mbar to 0.04 mbar, an increase of temperature from 388 K to 480 K was measured. In the range of trapping laser intensities between 0.21 TW/m^2 and 0.4 TW/m^2, the resulting change of a particle's temperature, from 367 K to 463 K, was observed.

To control the centre of mass motion of levitated particles within the optical trap, parametric feedback cooling was implemented via modulation of the trap depth. Using this technique, the effect different feedback parameters have on particle motion was explored. The combination of optimizing the feedback parameters, alongside reducing the pressure, resulted in temperatures of $T_z = 14\pm1$ mK, $T_x = 5\pm1$ mK and $T_y = 7\pm1 =$ mK. The observed Q factors on the order of 10^7 with predicted Q factors on the order of 10^{12} hold great promise for the realisation of ultrasensitive force detection. The system presented here has a force sensitivity on the order of 10^{-20} N/$\sqrt{\text{Hz}}$. Theoretical

considerations show that, with some improvements to the experimental system, it would be possible to achieve centre of mass temperatures, and thus low phonon numbers, close to the quantum ground state.

The second method to control the centre of mass motion of a levitated nanoparticle used squeezing pulses to classically squeeze its mechanical motion. This quadrature squeezing was achieved via non-adiabatic shifts of the nanoparticle's trap frequency and was carried out on a number of particles. The squeezing pulses implemented consisted of a rapid reduction in the trap frequency, followed by a brief period in time where the system was allowed to evolve, before the trapping frequency was rapidly returned to its original value. The effect of using single and multiple pulses to control this was explored and the optimal duration for a squeezing pulse characterized. For a single pulse, the maximum amount of squeezing was found to be $\lambda = 3.2 \pm 0.2$ dB.

To further increase the amount of squeezing applied to the levitated nanoparticle, a multiple pulse scheme was implemented. The effect of varying the time between pulses was investigated and the optimal time was found. The maximum amount of squeezing achieved in the system, occurred after 5 pulses, giving a squeezing factor of $\lambda = 9.4 \pm 0.1$ dB. The multiple pulse scheme was then applied to parametrically feedback cooled nanoparticles. The effect on the phase space, including its decay to a thermal state, after the application of squeezing pulses was characterized. The squeezing on parametricaly cooled particles. after the application of 5 pulses, was measured and the squeezing factor found to be $\lambda = 8.4 \pm 0.1$ dB.

Contents

List of Figures

Declaration of Authorship

I, Jamie Vovrosh, declare that this thesis titled, Parametric feedback cooling and squeezing of optically levitated particles and the work presented in it are my own. I confirm that:

- This work was done wholly or mainly while in candidature for a research degree at this University.
- Where any part of this thesis has previously been submitted for a degree or any other qualification at this University or any other institution, this has been clearly stated.
- Where I have consulted the published work of others, this is always clearly attributed.
- Where I have quoted from the work of others, the source is always given. With the exception of such quotations, this thesis is entirely my own work.
- I have acknowledged all main sources of help.
- Where the thesis is based on work done by myself jointly with others, I have made clear exactly what was done by others and what I have contributed myself.

Signed: _____

Date: _____

Acknowledgements

Very few individuals' achievements in life can be described as truly ones own, but instead more accurately as the sum of their own effort and all the help they have had along the way. This thesis is no exception to this rule. Firstly I would like to acknowledge The Templeton Foundation for funding my PhD and allowing me to undertake the body of research presented here.

I would like to thank my supervisor (Hendrik Ulbricht) for providing me the opportunity to do a PhD. Under his supervision I have had the opportunity to learn and develop as a scientist. His drive to turn ideas into reality is epitomised in his catch phrase "Just do it". My secondary source of supervision for the first half of my PhD came from James Bateman. His knowledge of and passion for physics was truly inspirational. His contributions towards the development of the experimental system and my work have been pivotal, he suggested and designed the paraboloidal mirror and wrote a large percentage of the code used for data collection in the lab.

I would also like to mention the contributions from Mudassar Rashid and David Hempston, over the course of my PhD. This thesis is deeply interwoven with both their contributions both in terms of ideas and experimental contributions. I worked closely with both Muddassar and David during the development of the optical trap and implementation of the parametric feedback system. Muddassar's blue sky thinking and willingness to explore any idea while keeping a critical mind has truly been a lesson in how a scientist should think. Davids analytical mind along with his skill and advice in regards to programing has been invaluable when analysing data. I could not give David and Mauddassar high enough praise when it comes to their impact on my time as a PhD student both in terms of working with them professionally and as friends.

Despite joining late towards the end of my PhD Ash Setter quickly became my partner in crime in regards to the squeezing experiments preformed here. Ash developed a large amount of the code used when preforming these experiments often anticipating my next request and having it ready sometimes before I asked. Without his contributions these experiments could not have been finished before the end of my PhD.

In addition to the people mentioned previously, during my time in the Quantum nanophysics and matterwave interferometry group there have been several people who have been members of the group who more than deserve a mention. Notably Nathen Cooper, Chris Dawson, Paul Clark, Chris Timberlake,George Winstone and Markus Rademacher whom have provided thought provoking discussions and an extremely enjoyable working environment.

I would like to thank the everyone in the Physics and Astronomy Department, specifically the Quantum light and matter research group for providing a supportive and friendly atmosphere in which to undertake my PhD. In addition the contributions of the Mechanical and Electronics Workshops should be noted. They have helped with vacuum chamber modifications and the majority of the electronics in the lab.

Externally from the University of Southampton the contributions from the following collaborators should be acknowledged for their contributions to various parts of this thesis including Mauro Paternostro, Tommaso Tufarelli and Myungshik Kim.

The remaining individuals mentioned in this thesis while not having directly contributed to the experimental work undertaken in this thesis, have made significant contributions by other means.

The biggest contribution to my success in life is naturally my parents (Ian and Sue Vovrosh) whom without I would never have had the opportunity to hand in this thesis. My parents have supported me throughout my education in many ways with love, encouragement and a helping hand when needed. This thesis would have not been possible without them. A few sentences here, cannot convey their contribution.

My Nan (Pam Knowles) has always been a friend and a role model to me from a young age. She has supported me in every stage of my education, often reminding me to work hard and play hard. My three siblings have no idea how much they have helped me through the course of my PhD. My sister Katie has always made life look so easy, her strength and caring nature has always been an inspiration to me. My brother Ben whose ability to put a smile on anyones face has been of particular comfort during times of experimental strife. My brother Joseph who in addition to providing an interested ear for discussions about physics, briefly worked in my research group during my PhD, making several experimental contributions to the work carried out.

There is no way I could have completed this work without the love and encouragement from my wonderful partner Amber Watts, to her a great deal of thanks is owed.

In addition to those mentioned previously many friends have supported me in many ways from encouraging me and providing welcome distractions, making the duration of my studies an enjoyable experience. A few notable mentions include Allan Skellett, Ben Chichester and Rory Penman.

I would like to dedicate this thesis to my parents, for believing and supporting me in all aspects of my life.

Chapter 1

Introduction

An optomechanical system can be defined as one in which light and a mechanical system interact. These types of systems exist in many forms and sizes, with variations including optical cavities [4–6], macroscopic mirrors [7–9], micromechanical cantilevers [10] and optical tweezers [11–13]. This wide range of devices, as well as their high sensitivity, has allowed for optomechanical systems to be used in a variety of fields such as magnetic resonance force microscopy [14], measurement of the Casimir force [15–17], biology [18–20], spectroscopy [21] and thermodynamics [22–24]. These far-ranging applications illustrate that optomechanics is an area of research with great potential, capable of pushing the boundaries of both science and metrology [25]. The most famous example of this is the detection of gravity waves by the LIGO project [9].

One of the most promising of these optomechanical systems is optical trapping, which has been proven to be achievable in both liquid and vacuum environments. An optical trap is formed by tightly focusing a laser beam with a high numerical objective. A dielectric particle near the focus will experience forces arising from the particle's interaction with the light, which can be used to confine the particle within the focus of the laser beam [26]. Optically levitated particles in vacuum environments are particularly attractive systems to work with for many reasons, with one of the most significant benefits being the particle's decoupled nature from the environment, resulting in expected quality factors approaching 10^{12} [13], alongside the high degree of control over the levitated particles motion within the trap [3, 27].

The work presented in this thesis concerns itself with constructing a system capable of optically trapping nanoparticles within a vacuum environment in order to develop experimental techniques and methods which could be used to test fundamental physics.

A description of the questions posed within the field of physics that motivate the construction of such a system will follow, after which a summary of the contents of this thesis will be provided.

1.1 Thesis motivation

This section will briefly outline some of the physical principles which an optically levitated nanoparticle could be used to test.

1.1.1 Quantum to classical transition

The predictions given by quantum mechanics have been verified by all tests to date [28], but still seem to be in conflict with our common sense. As quantum theory knows no boundaries, in theory everything within existence should fall under the scope of the superposition principle. In practise however, quantum effects have only been observed on the small scales of molecular [29], atomic [30] and subatomic [31] particles, leading us to question why macroscopic objects are only ever found in classical states. This division illustrates that there is a point at which matter ceases to behave according to the laws of quantum physics, instead undergoing a quantum to classical transition. This is invariably linked to the quantum measurement problem. The Quantum Measurement Problem can be defined as our inability to determine the mechanisms behind an object moving from a state of quantum superposition, to a classical state. Studies of this problem seek to gain a deeper understanding of the mechanism behind wave function collapse, and to determine whether wave function collapse even occurs at all. An example of such a theory that circumvents the need for wavefunction collapse is the many-worlds interpretation [32]. These topics are major areas of discussion and debate within the scientific community [33–37].

A full discussion is beyond the scope of this thesis, however it is worth highlighting that decoherence theory, which describes how a system will effectively lose its quantum features when coupled to a quantum environment of sufficient size [37, 38] is often given as a justification for the lack of macroscopic quantum super positions. Alternatively, it is possible that quantum mechanics breaks down beyond a certain mass or complexity scale. In order to investigate these theories further, quantum superpositions of truly massive, complex objects are required.

Many argue that if the environment is the mechanism which causes the quantum to classical transition to occur, a system would behave quantum mechanically if the environment was removed, regardless of particle mass or size. Others argue that in the

absence of environmental factors, such as in a highly isolated, massive system, other possible sources of decoherence would become apparent. Various theoretical ideas of what these sources could be have been proposed [39, 40], and are referred to as collapse models. Therefore if a macroscopic quantum system can be realized the possibility to study various quantum to classical transition mechanisms could be studied.

To date, the largest mass for which the quantum superposition principle has been observed is on the order of 10^4 atomic mass units (amu) [41], however this has not been sufficient to rule out the various collapse theories which have been proposed. In order to test these theories further, it is therefore necessary to realise the quantum superposition of more massive objects. Optically levitated particles are extremely promising systems for enabling such tests to be achieved due to their high level of isolation from mechanical and environmental influences, in addition to their high sensitivity to small forces [42]. Several proposals currently exist as to how best to test stochastic collapse models through the use of levitated nanoparticles. One such proposal suggests mechanically isolating a nanosphere within a vaccum and, once this has been achieved, reducing the temperature and pressure to a low enough level such that the particle becomes susceptible to decoherence processes other than the environment [43]. Alternative proposals include nanoparticle matterwave interferometry, such as that presented in reference [44]. The findings herein illustrate that a levitated nanosphere as small as 20 nm diameter, cooled down to 20 mK in its centre of mass motion, could be used as a point source for nanoparticle interferometry on Earth.

1.1.2 Single particle thermodynamics

Macroscopic thermodynamics operates within a regime in which thermal fluctuations are irrelevant. However, during the last couple of decades, significant progress in the fabrication and control of nanoscale mechanical devices has been achieved [45]. For the regime in which these devices operate, thermal fluctuations are relevant [46–51], making research into stochastic thermodynamics possible. Research into stochastic thermodynamics has very successfully extended the laws of macroscopic thermodynamics to the level of single trajectories [52, 53]. Furthermore, the discovery of fluctuation theorems has also allowed for systematic investigations into out of equilibrium processes [50, 54].

Optical tweezers are an example of one of the aforementioned systems which operate on the scale where thermal fluctuations are detectable. Optical tweezers possess several desirable traits which make them particularly valuable in the study of stochastic thermodynamics, including the ability to quickly control the potential landscape experienced by a particle and also to record the particle's trajectories with a high level of precision

[55]. Several studies involving particles optically trapped within a liquid solution have been carried out to date [48], including demonstrations not only of individual thermodynamic processes [23] but also of a classical, micromechanical Stirling engine [22]. This heat engine was created by varying the temperature of the liquid heat bath (controlled with laser absorption). Despite the success of carrying out this experiment within a liquid solution, the liquid solution itself places limitations on the accessible parameter regime for the temperature and optimization of the heat engine. These limitations can, however, be overcome by performing similar experiments within a vacuum environment.

Conducting a heat engine within a vacuum environment enables access to a much larger temperature regime, potentially as low as the quantum ground state [27]. It also presents the opportunity to perform a thermodynamic cycle in both the over damped and under damped regime. Several experiments have already been carried out in vacuum to explore stochastic thermodynamics, including the use of fluctuation theorems to investigate a system relaxing from a non-equilibrium state, towards equilibrium [24]. Further to this, there now exist proposals to create heat engines using optically levitated nanoparticles within a vacuum environment [56].

Creating such thermodynamic cycles in vacuum holds the potential to realise quantum heat engines, due to the isolated nature of this type of environment. To date, the only heat engine which has been demonstrated within a vacuum was classical in nature and was created using an ion, held within a modified linear Paul trap [57]. Despite the fact that there has been no experimental realization of a quantum heat engine thus far, there exists a body of theory [58] regarding how one could be created, as well as well as several proposed experimental schemes [59]. If a heat engine operating in the quantum regime could be realized, it could potentially be used to investigate the quantum limits of classical thermodynamical concepts. This includes the Carnot efficiency limit which could, as a result, be overcome [60].

1.1.3 Force sensing

The use of nanotube resonators within a cryogenic system has successfully demonstrated sensitivities on the order of 10^{-21} $N/\sqrt{Hz}$ [61] [1]. Ultimately however, the limiting factor restricting the sensitivity of the nanotube resonators and other clamped systems is thermal noise. The minimum detectable force in the presence of thermal noise is

[1] The noise-equivalent power (NEP) is a measure used to quantify the sensitivity of a detection system and can be used to compare it with other detection systems. The NEP is the power that results in an SNR of 1. The NEP represents the threshold above which a signal can be detected. The minimum detectable power P_{min} is equal to $P_{min} = NEP \times \sqrt{\text{measurement bandwidth}}$. At higher input powers, a low NEP is beneficial since it will lead to lower noise characteristics in the output signal. A low NEP value corresponds to a lower noise floor and therefore a more sensitive detector.

inversely proportional to the square root of the mechanical quality factor (Q factor) of the oscillator. The Q factor in clamped systems is limited by surface imperfections, material loss and clamping loss. Taking this into consideration, it becomes obvious that both high mechanical quality, as well as decoupling from the physical environment, are exceedingly desirable traits in force sensors. Both of these are properties found in levitated nanoparticle systems.

Optically levitated nanoparticle systems have reported Q factors on the order of 10^7, with predicted Q factors on the order of 10^{12} for the particles centre of mass motion [13]. Optically levitated particles have been shown to have force sensitivities on the order of 10^{-21} $N/\sqrt{Hz}$ [62, 63] for the levitated particles centre of mass motion and predicted sensitivities as high as 10^{-29} $N/\sqrt{Hz}$ for the torsional degree of freedom [64]. The coupling of levitated particles to electric [65] and magnetic fields [66–68] opens up possibilities for alternative sensing techniques. Several proposals exist for the utililsation of levitated nanoparticle systems, including the detection of gravitational forces such as high frequency gravitational waves [69], sensing van der Waals and Casimir forces [70], sensing non-Newtonian gravity [71], conducting nuclear spins [72] and detecting dark matter [73].

1.2 Aim of this thesis

To achieve the aforementioned motivations, the ability to optically trap a particle and control its motion is required. The research outlined within this thesis has therefore been carried out with the aim of creating an experimental system capable of both trapping a nanoparticle and manipulating its centre of mass motion. Specifically the goals of the research undertaken, as outlined in this thesis, were as follows:

- To build an experimental system to optically levitate nanoparticles.
- To develop tools to characterise the particle within the optical trap.
- To demonstrate cooling of a levitated particle's centre of mass motion below 20 mK via parametric feedback.
- To perform squeezing of the nanoparticle motion.
- To perform squeezing of cooled nanoparticle motion.

1.3 Thesis outline

In this thesis, the development of a levitated nanoparticle system is described. Using a high numerical aperture (NA) parabolic mirror in order to tightly focus a laser beam, a high electric field gradient is created. In the presence of an electric field, a nanoparticle behaves as a dipole. When the particle is in the focus of a laser beam, the focused electric field generates a gradient force on the dipole, which pushes it towards the center of the laser focus. This restorative force causes the motion of the particle to oscillate within the trap. The vast majority of the research presented in this thesis concerns itself with controlling and manipulating the centre of mass motion of the levitated particle by modulating the intensity of the laser. A brief outline of the contents of this thesis is provided here:

- **Chapter 1 - Introduction.** This thesis begins with an outline of the various motivations for carrying out the research presented within.
- **Chapter 2 - Gradient force optical traps.** The second chapter provides an overview of the fundamental theory used to understand optical trapping. This theory underpins the work presented in this thesis. Several important quantities used throughout this study are also defined.
- **Chapter 3 - Experimental methods and setup for optical trapping of nanoparticles.** This chapter details the experimental setup used throughout the study, to optically trap nanoparticles. Details are given on the methods used to deliver particles into the trapping region, the design of the parabolic mirror trapping objective and the detection system used to detect the trapped particles.
- **Chapter 4 - Optomechanics of levitated particles.** Underpinning all the work detailed in this thesis is the ability to control and measure the motion of a particle within an optical trap. The methods used to extract various parameters about trapped particles are discussed.
- **Chapter 5 - Nanoscale temperature measurements using blackbody like radiation from a levitated nanoparticle.** This chapter outlines the experimental method used to detect blackbody like radiation from an optically trapped particle. Using the measured blackbody radiation the internal temperature of the particle is calculated.
- **Chapter 6 - Parametric feedback cooling of levitated particles' centre of mass motion.** This chapter details the method by which parametric feedback cooling was implemented on optically trapped nanoparticles. Studies into the

optimisation of parametric feedback cooling are presented and after optomisation cooling on the order of 5-14 mK is achieved. This section ends with a discussion of the limitations of the parametric feedback cooling applied in the system.

- **Chapter 7 - Classical squeezing of the motion of levitated nanoparticles.** In this chapter classical squeezing of an optically levitated particle via a pulsed laser intensity scheme is demonstrated. The application of multiple pulses to an uncooled and cooled nanoparticle is reported.

- **Chapter 8 - Conclusion** The experimental results are summarised and a summery is given of the future work needed to advance the experimental techniques detailed.

1.4 Supporting Publications

From the work outlined above the following papers have been produced.

Parametric feedback cooling of levitated optomechanics in a parabolic mirror trap. *Jamie Vovrosh, Muddassar Rashid, David Hempston, James Bateman, Mauro Paternostro, Hendrik Ulbricht* JOSA B. 2017 Jul 7;34(7):1421-8.

Experimental realization of a thermal squeezed state of levitated optomechanics. *Muddassar Rashid, Tommaso Tufarelli, James Bateman, Jamie Vovrosh, David Hempston, M.S. Kim, Hendrik Ulbricht* Physical Review Letters. 2016 Dec 30;117(27):273601.

Force sensing with an optically levitated charged nanoparticle. *David Hempston, Jamie Vovrosh, Marko Toros, Muddassar Rashid, Hendrik Ulbricht* Applied Physics Letters 2017 Sep ;111(13):133111

Chapter 2

Gradient force optical traps

To form a stable optical trap one must generate optical forces that act against gravity and other forces to keep an object localised. The most straightforward way to do this is to tightly focus a Gaussian laser beam using a high-power lens. In such an arrangement, two forces act upon the particle; the gradient force $\mathbf{F}_{grad}$ and the scattering force $\mathbf{F}_{scat}$. The total force on the particle can thus be written as

$$\mathbf{F}_{Total} = \mathbf{F}_{scat} + \mathbf{F}_{grad}. \tag{2.1}$$

The gradient force points towards the region of highest laser intensity. In contrast, the scattering force points in the direction of the beam propagation and thus pushes the particle away from the laser focus. Therefore, there are two methods which can be used to create a stable optical trap, the first of which is to eliminate the scattering force. There are several methods which can be used to achieve this. The scattering force can be compensated for by another force such as gravity [74], the scattering force can be cancelled by two counter-propagating beams [75], providing the two beams are of the same power, shape and are well aligned, or alternatively the back reflection from a mirror could be used to form a standing wave [76, 77]. However, inaccuracies in alignment can result in these trap schematics being unstable. The second method by which a stable optical trap can be created is to make the gradient force dominate over the scattering force, such that the particle is held at the laser focus. To achieve such a feat a tightly focused beam is required. This is referred to as an optical tweezer [78] (see figure 2.1). This is the sort of trap we use and discuss in this thesis.

This section will begin, with a brief overview of different types of optical traps to provide context. Then the physics required to understand the realization of a gradient force optical trap, created with a Gaussian laser beam will be given. To begin with, the

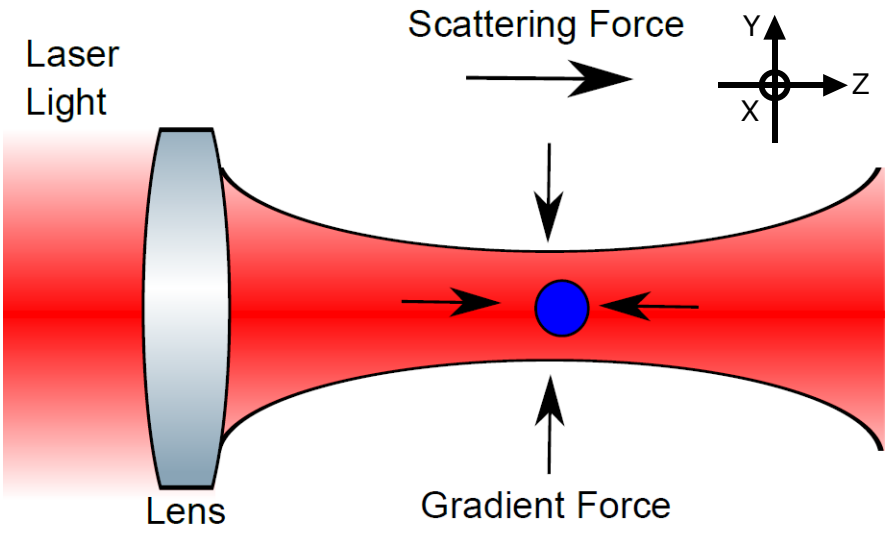

FIGURE 2.1: **Forces present in a gradient force optical trap.** To create the gradient force trap a laser beam is focused by a lens. A nanoparticle is shown in blue and the optical forces which arise due to the particle's presence in the trap are shown. The gradient force acts as a restorative force pushing the particle towards the centre of the trap and the scattering force pushes the particle in the direction of laser beam propagation.

shape and intensity of a Gaussian laser beam will be discussed. Then the gradient and scattering forces will be derived, followed by a discussion about balancing these forces to create a stable trap. After this, several key parameters which are useful when describing the optical trap and motion of the particle within the trap will be defined.

2.1 Methods for optically trapping nanoparticles

This section will give a brief history of optical trapping, along with a description of a few of the various experimental methods used to optically trap nanoparticles.

2.1.1 Origins of optical trapping

Kepler in 1619 stipulated that light can impart momentum to matter, as an explanation for why comet's tails face away from the sun [79]. Later Maxwell's electromagnetic theory was able to show that light does, in fact, impart momentum to matter. It took many years and the invention of new technologies, namely the laser, before optical traps could be realized; that is to say, instruments which use highly focused laser beams to impart forces to hold or move macroscopic objects.

Ashkin was the first to experimentally demonstrate that light could indeed impart momentum to matter [80]. Ashkin achieved this by focusing an argon ion laser through a fluid vessel containing a solution of liquid and micron scale particles. He observed that these particles were pushed in the direction of laser propagation, due to radiation pressure from the light. This force is referred to as the scattering force $\mathbf{F}_{scat}$. He also observed that particles, with refractive indexes higher than the medium were attracted into the centre of the lasers focus. The force responsible for this is referred to as the gradient force $\mathbf{F}_{grad}$. Using these realizations, Ashkin and Dziedzic were able to demonstrate levitation of a 20 μm diameter silica microsphere in free space, using gravity to balance the upwards force from an upwards directed laser beam [81, 82]. This method was later demonstrated in a vacuum of roughly 1 mbar [11].

In 1986, Ashkin extended this work to trapping a particle in all three spatial degrees of freedom in liquid [78]. This was the first demonstration of a gradient force optical trap. In this gradient force trap, the focus was tight enough that the restorative force on the particle, due to the high laser intensity gradient at the focus, was greater than the force due to radiation pressure. In 1997, a single beam gradient force trap was realised for 5 μm diameter dielectric microspheres in air, using a single laser beam pointed downwards [83].

In the years that have followed, a huge variety of experimental configurations have been used to form optical traps, in different environments. All of these optical traps utilize either the scattering or gradient force. This section describes the three main experimental approaches to optical trapping (see figure 2.2). Depending on the set up optical traps have been shown to be useful tools in a variety of fields, including biophysical studies [18, 84–87], tests of the fundamental natures of gravity [88], quantum mechanics [88, 89], as well as rotational and torsional dynamics, both in fluids [90, 91] and free-space [92, 93].

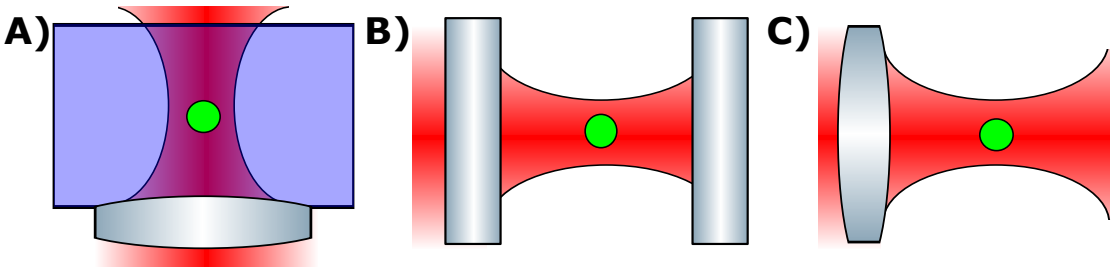

FIGURE 2.2: **Common optical trap types. A)** Optical tweezing of particles in solutions often takes advantage of high numerical aperture oil or water immersion microscope objectives to generate high laser intensity gradients. **B)** Nanoparticle levitation in optical cavities, where the particle is levitated in the standing wave of a resonant mode in an optical cavity. **C)** Free space gradient force traps are created using high numerical aperture optics such as parabolic mirrors.

2.1.2 Optical tweezers in liquid solutions

Optical tweezers in liquid solutions have become an invaluable tool in many research areas, including biochemistry and biophysics [18, 84–87], where their uses, for example, include single molecule force spectroscopy [86]. Complete optical tweezer setups are so widely used they can be purchased commercially from large optics suppliers (e.g Thorlabs), as well as small specialist companies. Optical tweezer setups utilize focused optical beams to trap microspheres and other particles in liquid environments such as aqueous solutions. Optical tweezers resemble inverted optical microscopes. The position of the trapped particle can be monitored in real time, via camera or a quadrant photodetector [94].

The liquid surrounding an optically tweezed particle has several purposes. Firstly, the liquid solution provides a buoyancy force, which partially offsets the force of gravity. This reduces the required strength of the trapping force in the vertical direction [78], which is often chosen to be the propagation direction. A liquid solution also allows for high numerical aperture (NA) immersion microscope objectives to be used, providing the possibility for a greater gradient force achievable for a given laser power. Biological samples can be studied in vivo and in an appropriate solution [19]. The liquid solution also provides a damping force to the particles of interest, reducing its speed, thus allowing a particle to be tracked, targeted and trapped easily. In addition, collisions provide a mechanism for heat dissipation caused by particles absorbing light. However, the Brownian dynamics of a liquid solution drown out the ability to detect the effects of the optical potential affecting the particle. This results in solution-based traps being unable to conduct studies of classical or quantum optomechanics. For more information on optical trapping in liquid solution, the following reviews are recommended [95, 96]. The remainder of this thesis will discuss and present data taken by optical trapping in gaseous environments, with pressures ranging from atmospheric to ultra-high vacuum.

2.1.3 Cavity levitation of nanoparticles

Optical trapping in a cavity follows the same principle as using counter-propagating beams to levitate particles, using a standing wave of a resonant mode in an optical cavity. The symmetry of a cavity field ensures that the time average of the scattering force is zero, enabling particles to become trapped via the scattering and gradient forces [97]. The standing wave within the cavity is a stationary wave, resulting in particles becoming trapped by the gradient force at stationary antinodes [98]. This means that cavity traps have very strong axial confinement, but poor radial confinement, because of the relatively large cavity waists (corresponding to low NA). Unlike single beam

traps, cavities are able to contain stable trapping points at each field antinode. This enables trapping of a number of particles in close proximity to one another. Cavity trapping allows for passive cooling and control of axial motion of the particle [99–102]. There is also the potential to implement previously developed techniques from cavity optomechanics.

2.1.4 Free space gradient force traps

Unlike optical trapping in liquid solution, particles in free space optical traps are able to move ballistically under drastically reduced drag, due to the elimination of the viscous force arising from the liquid environment. Initially, this presented some experimental challenges, when free space gradient force traps were first realized, in terms of loading particles into the trap [81]. Since then a multitude of methods have been developed (see section 3.3.2). One advantage of free space traps is that the reduced damping on a trapped particle has allowed for studies of classical and potentially quantum optomechanics. The rest of this chapter will cover the theory necessary to understand a gradient force trap. Firstly a discussion of the properties of the laser used to create the trap will be given, before providing the theory required to understand a gradient force trap.

2.2 Gaussian beam optics

The nature of an optical trap depends on the properties of the laser used to created the optical trap. Therefore, it is necessary to have an understanding an understanding of the properties of the laser beam that will be used to create the trap. The profile of the light beam generated by the laser used in the experiments in this thesis can be best approximated by a Gaussian function. That is to say, a beam whose transverse magnetic and electric field amplitude profiles are given by the Gaussian function; thus implying a Gaussian intensity profile. The amplitude of the beam can be expressed as a solution to the time independent paraxial Helmholtz equation as [103]:

$$E(r_{rad}, z) = E_0 \frac{W_0}{W(z)} \exp\left(\frac{-r_{rad}^2}{W(z)^2}\right) \exp\left(-i\left(kz + k\frac{r_{rad}^2}{2R(z)} - \psi(z)\right)\right), \tag{2.2}$$

where r_{rad} is the radial distance from the centre of the beam, z is the axial distance from the beams focus, $k = 2\pi/\lambda$ is the wavenumber for a laser wavelength λ, $E_0 = E(0,0)$ is the electric field amplitude at the origin. $W(z)$ is the radius of the field amplitude given by equation 2.4. $W_0 = W(0)$ is the beam waste at the origin given by equation 2.4. R(z) is the radius of the curvature of the beams wavefronts at z and $\psi(z)$ is the Gouy phase.

The Gouy phase is the phase shift a Gaussian beam acquires as it passes through a focal point, with respect to that of a plane wave with the same optical frequency [104]. The Gouy phase is given by,

$$\psi(z) = \arctan\left(\frac{z}{z_R}\right). \tag{2.3}$$

Overall, the Gouy phase shift introduced in a Gaussian beam passing through a focus (from the far field to the far field on the other side of the focus) is equal to π.

Equation 2.2 is the static model of a Gaussian laser beam derived using the paraxiamal approximation. For the purposes of this thesis, this equation provides a rough figure to evaluate the experimental setup. As some of the experiments discussed in this thesis will use a highly divergent beam, the paraxial approximation will not be a completely accurate description of the experimental setup. This can be seen when examining the relative error introduced by approximating $sin(\Theta) \approx \Theta$, where increasing the angle Θ from 0 to $\pi/2$ results an error of up to 57%. Therefore, the values quoted in this chapter should be treated as ball park figures when dealing with highly diverging beams, in our case resulting from high NA optical elements. To perform a more in-depth analysis would require the use of a full vectoral treatment of the Gaussian laser beam [105].

2.2.1 Gaussian beam profile

In an optical trap, the particle is trapped at the focus of the laser beam used to create it. The properties of the particle motion in the laser focus will therefore depend on the properties of a Gaussian beam at its focus. The shape of a focused Gaussian beam at a given wavelength is given by [103],

$$W(z) = W_0\sqrt{1 + \left(\frac{z}{z_R}\right)^2}. \tag{2.4}$$

where z_R is the Rayleigh range given by

$$z_R = \frac{\pi W_0^2}{\lambda}. \tag{2.5}$$

The Rayleigh range is used to define the depth of the focus of the beam shown in figure 2.3. The radius of curvature of the beam waist is given by [76],

$$R(z) = z\left[1 + \left(\frac{z}{z_R}\right)^2\right]. \tag{2.6}$$

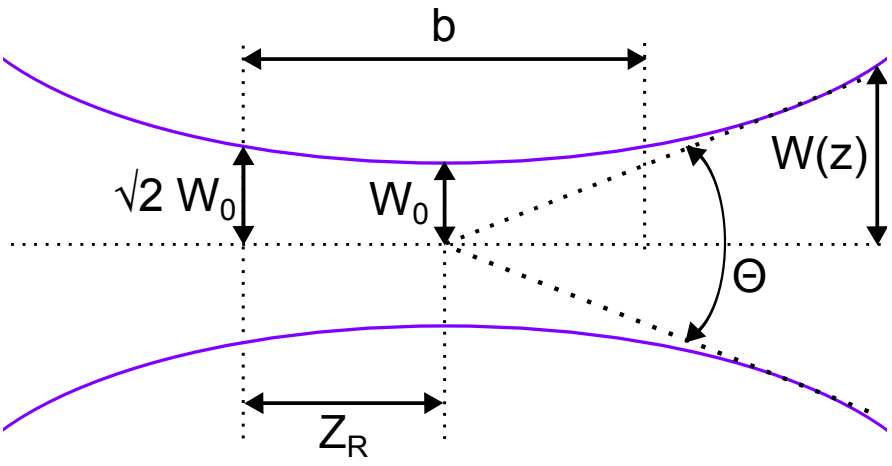

FIGURE 2.3: **Gaussian beam waist.** The purple lines describes the beam width $W(z)$ of a focused Gaussian beam as a function of the distance z along the beam. Here W_0 is the beam waist, b is the depth of focus, z_R is the Rayleigh range and Θ is the total angular spread.

2.2.2 Laser intensity and power

The intensity of the laser beam used to create an optical trap affects several important properties of the trap, such as the shape and depth of the trapping potential. The shape and intensity of the Gaussian beam can be seen in figure 2.4. The intensity distribution of a Gaussian beam can be found by evaluating the time averaged Poynting vector and using equation 2.2 to get:

$$\begin{aligned} I(r_{rad}, z) &= \frac{|(\mathbf{E} \times \mathbf{H}^*)|}{2} \\ &= \frac{|\mathbf{E}(r_{rad}, z)|^2}{2\eta} \\ &= I_0 \left(\frac{W_0}{W(z)}\right) \exp\left(\frac{-2r_{rad}^2}{W(z)^2}\right) \end{aligned} \tag{2.7}$$

where $\mathbf{H}$ is the magnetic field polarized in the y direction and given by $\mathbf{H}(r, z) = \hat{y}E_x(r, z)/\eta$, * denotes the complex conjugate, η is the the characteristic impedance of the medium in which the beam is propagating. The characteristic impedance of free space is an expression of the relationship between the electric-field and magnetic-field

intensities in an electromagnetic field propagating through a vacuum. In free space $\eta \approx 337\ \Omega$. The beam intensity profile at the laser focus can be seen in figure 2.5.

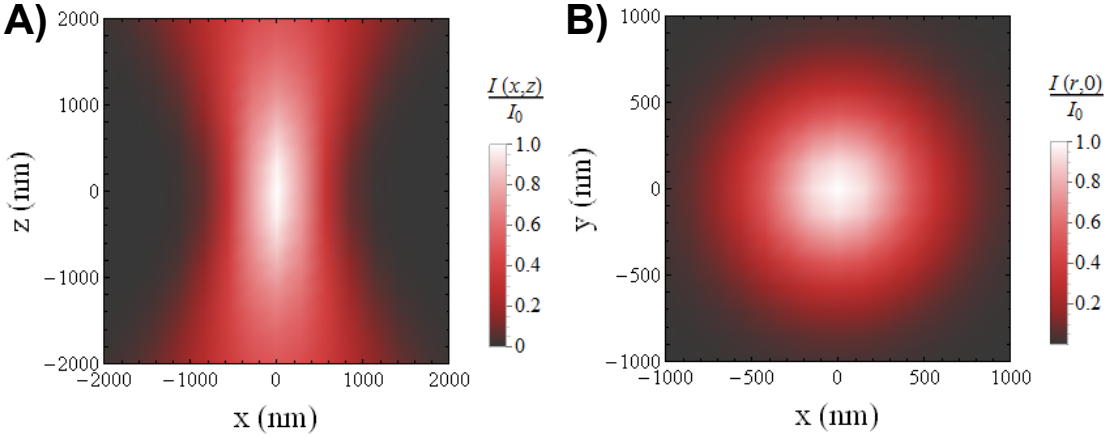

FIGURE 2.4: **Intensity at a Gaussian beam waist** for a laser beam $\lambda = 1550$ nm, focused through an objective with an $NA = 1$. **A)** The beam waist is elongated in the direction of laser propagation, in this case z. **B)** The beam waist is symmetric in the axial directions x and y. Where $r_{rad} = \sqrt{x^2 + y^2}$.

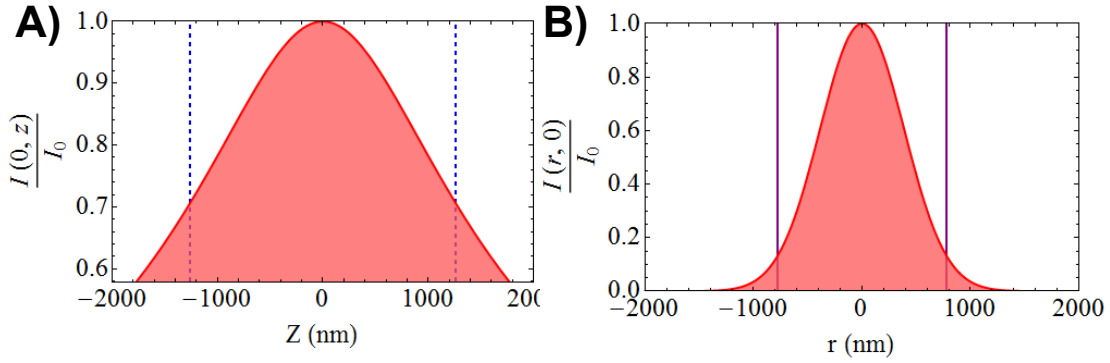

FIGURE 2.5: **Gaussian beam intensity profiles**, for a Gaussian beam with $\lambda = 1550$ nm focused by a focusing objective with NA=1. **A)** The intensity profile in the direction of beam propagation, where the dashed line shows the Rayleigh range. **B)** The intensity profile in the axial direction, where the purple solid line shows the beam waist.

2.2.2.1 Beam power through an aperture

When designing the optical system it is important to select optical components such that the maximum amount of light passes through each of the optical elements. The laser power that passes through an aperture of radius r_{app} in the transverse plane at position in z is given by,

$$P(r_{app}, z) = P_0 \left[1 - e^{\frac{-2r_{app}^2}{W(z)^2}} \right], \tag{2.8}$$

where P_0 is the total power transmitted by the beam given by,

$$P_0 = \frac{1}{2}\pi I_0 W_0^2. \tag{2.9}$$

The fraction of power transmitted through an aperture of radius $r = W(z)$ is $0.865P_0$. To achieve $0.99P_0$ we require an aperture of $r = 1.52W(z)$.

2.3 Gradient force traps

2.3.1 Derivation of the gradient force

The way light interacts with matter, specifically a spherical object, depends on the size of the particle. In cases where the dimensions of the particle are much greater than the wavelength $r >> \lambda$, a simple ray optics treatment is sufficient. However, in our case the wavelength of the trapping laser (1550 nm) far exceeds the particle dimensions (between 18 and 312 nm) $r << \lambda$. Thus, the particles can be treated as point dipole charges in an electric field and the conditions for Rayleigh scattering are satisfied. We treat the particle as a dipole in an inhomogeneous electromagnetic field. The force applied on a single charge in an electromagnetic field is known as the Lorentz force,

$$\mathbf{F} = \sum_i \mathbf{F}_i = \sum_i q_i \left(\mathbf{E}_i + \frac{d\mathbf{x}_i}{dt} \times \mathbf{B} \right), \tag{2.10}$$

where $\mathbf{F}$ is the Lorentz force, q is the charge of the particle, the index i is the number of charges, $\mathbf{E}$ is the electric field, dx_i/dt is the particle velocity and $\mathbf{B}$ is the magnetic field. We can calculate the force on the dipole by substituting in terms for the electric field in equation (2.10). For a dipole, the distance $x_1 - x_2$ is the distance between the two charges. Taking into account two charges have opposite signs and expanding $\mathbf{E}_2$:

$$\begin{aligned}
\mathbf{F} &= q \left(\mathbf{E}_1 - \mathbf{E}_2 + \frac{d(\mathbf{x}_1 - \mathbf{x}_2)}{dt} \times \mathbf{B} \right) \\
&= q \left(\mathbf{E}_1 + ((\mathbf{x}_1 - \mathbf{x}_2) \cdot \nabla)\mathbf{E} - \mathbf{E}_1 + \frac{d(\mathbf{x}_1 - \mathbf{x}_2)}{dt} \times \mathbf{B} \right) \\
&= q \left(((\mathbf{x}_1 - \mathbf{x}_2) \cdot \nabla)\mathbf{E} + \frac{d(\mathbf{x}_1 - \mathbf{x}_2)}{dt} \times \mathbf{B} \right).
\end{aligned} \tag{2.11}$$

We assume that the dielectric particle is a linear dielectric. In this situation the dipole moment is given by $\mathbf{P} = q\mathbf{d} = \alpha\mathbf{E}$, where $\boldsymbol{d}$ is the distance between the two charges and

α is the polarizability of the particle in question. We can write this equation in terms of the electric field, the magnetic field and polarizability:

$$\begin{aligned}\mathbf{F} &= (\mathbf{P}\cdot\nabla)\mathbf{E} + \frac{d\mathbf{P}}{dt}\times\mathbf{B} \\ &= \alpha\left((\mathbf{E}\cdot\nabla)\mathbf{E} + \frac{d\mathbf{E}}{dt}\times\mathbf{B}\right).\end{aligned} \tag{2.12}$$

By using the Maxwell-Faraday equation (2.13), along with the vector identity equation (2.14), we can rearrange equation (2.12) to give us equation (2.15).

$$\nabla\times\mathbf{E} = -\frac{d\mathbf{B}}{dt}, \tag{2.13}$$

$$(\mathbf{E}\cdot\nabla)\mathbf{E} = \nabla\left(\frac{\mathbf{E}^2}{2}\right) - \mathbf{E}\times(\nabla\times\mathbf{E}). \tag{2.14}$$

Thus,

$$\begin{aligned}\mathbf{F} &= \alpha\left(\nabla\frac{\mathbf{E}^2}{2} - \mathbf{E}\times(\nabla\times\mathbf{E}) + \frac{d\mathbf{E}}{dt}\times\mathbf{B}\right) \\ &= \alpha\left(\nabla\frac{\mathbf{E}^2}{2} - \mathbf{E}\times(-\frac{d\mathbf{B}}{dt}) + \frac{d\mathbf{E}}{dt}\times\mathbf{B}\right) \\ &= \alpha\left(\nabla\frac{\mathbf{E}^2}{2} + \frac{d}{dt}(\mathbf{E}\times\mathbf{B})\right).\end{aligned} \tag{2.15}$$

It can easily be seen that the second term in equation (2.15) is the time derivative of the Poynting vector, which describes the power per unit area passing through a surface. When sampling over frequencies much shorter than the frequency of the laser's light (which is $\sim$ 194 THz for 1550 nm laser light), the power of the laser is constant and therefore the second term averages to zero. Thus, we are able to obtain the following equation, where we have renamed the force as the gradient force $\mathbf{F}_{grad}$ [106]:

$$\mathbf{F}_{grad} = \frac{\alpha}{2}\nabla\mathbf{E}^2, \tag{2.16}$$

where α is the polarizability of the particle given by,

$$\alpha = 4\pi n^2\varepsilon_0 r^3\frac{m^2-1}{m^2+2}, \tag{2.17}$$

where n is the refractive index of the particle, r is the radius of the particle, ε_0 is the vacuum permittivity, $m = n/n_m$ is the relative refractive index between the particle and the surrounding medium n_m. Substituting equation 2.17 into 2.16 and using the relation

$$I = cn\varepsilon_0 \frac{|\mathbf{E}|^2}{2}, \tag{2.18}$$

we find,

$$\mathbf{F}_{grad} = \frac{4\pi n r^3}{c}\left(\frac{m^2-1}{m^2+2}\right)\nabla I(\mathbf{z}, \mathbf{r_{ad}}). \tag{2.19}$$

This equation shows that the force on the dielectric particle is proportional to the gradient of the intensity of the beam. The gradient force changes sign as the particle passes through the focus, such that the force always acts towards the focus (as shown in figure 2.6). This means that when the particle moves away from the focus it will feel a force pulling back towards the focus. In other words, the gradient force described here tends to attract the particle to the region of highest intensity, thus acting as a restorative force. This causes the particle to oscillate back and forth through the focus with a predictable trapping frequency and potential (see equations 2.31 and 2.27 respectively).

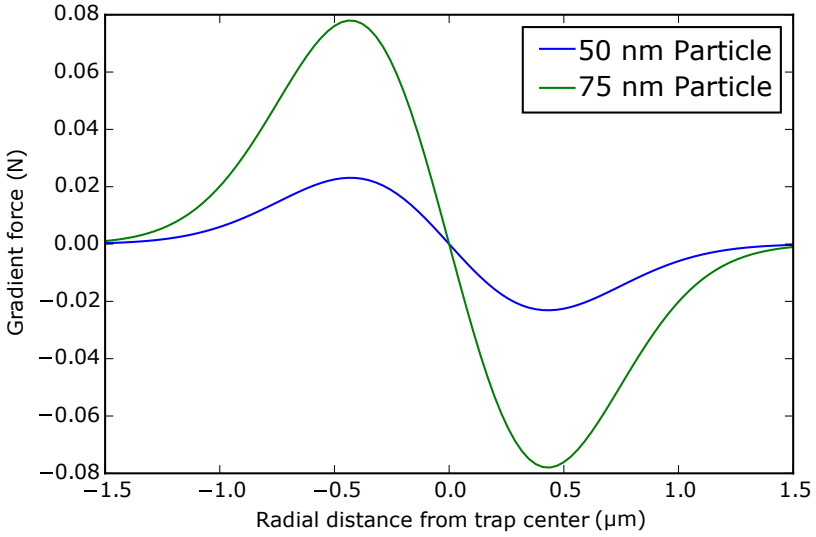

FIGURE 2.6: **The gradient force on a silica nano-particle as a function of radial distance from the trap centre,** with a laser power of 55 mW and a focusing NA of 0.9. It should be noted that forces are much weaker in the axial direction due to lower intensity gradient.

2.3.2 Balancing optical forces

In reality, we find that our particle is not positioned exactly at the focus of the trapping laser. This occurs due to photon pressure, which results in the force referred to as the scattering force $\mathbf{F}_{scat}$. The scattering force arises due to photons from the trapping laser scattering off the trapped nanoparticle. As scattering is an anisotropic process, with light being scattered in all directions, with intensity proportional to $\cos^2(\Psi)$, where Ψ is the scattering angle. This results in a net momentum transfer is in the axial direction of the trap, and the scattering force exerted from the laser light works against the gradient force in the axial direction $\widehat{z}$ of the trap.

On the quantum level, this can be understood by considering the gradient force as forward Rayleigh scattering, in which identical photons are created and annihilated concurrently. In contrast, for the scattering force the incident photons all travel in the direction of the trapping beam and scatter in all directions. By conservation of momentum, therefore, the particle will accumulate each photons' original momentum, resulting in a forward force in the direction of the beam [107].

In a scenario where the scattering force is stronger than the gradient force, the particle will be forced out of of the optical trap. However, if the gradient force is greater than the scattering force, the resulting trapping position is displaced slightly downstream of the intensity maximum. The sum of optical forces effecting an optically trapped nanoparticle can be written as,

$$\mathbf{F}_{Total} = \mathbf{F}_{grad} + \mathbf{F}_{scat}. \tag{2.20}$$

The scattering force, on a particle can be calculated by considering the photon flux impinging on and leaving a particle under the conservation of momentum. This allows us to write,

$$\mathbf{F}_{scat} = \frac{n\sigma_s}{c}\langle \mathbf{S} \rangle, \tag{2.21}$$

where σ_s is the Rayleigh scattering cross section and $\langle \mathbf{S} \rangle$ is the time-averaged Poynting vector. The Rayleigh scattering cross section is given by,

$$\sigma_s = \frac{128\pi^5}{3}\frac{r^6}{\lambda^4}\left(\frac{m^2-1}{m^2+2}\right). \tag{2.22}$$

While the time averaged Poynting vector can be written as,

$$\langle \mathbf{S} \rangle = \frac{|\mathbf{E}|^2}{2\epsilon_0 c}. \tag{2.23}$$

Substituting equations 2.18, 2.22 and 2.23 into equation 2.21, we can write an expression for the scattering force[1]:

$$\mathbf{F}_{scat} = \frac{128\pi^5 n}{3c} \frac{r^6}{\lambda^4} \left(\frac{m^2 - 1}{m^2 + 2} \right)^2 I(\mathbf{r_{ad}}) \widehat{z}. \tag{2.24}$$

From this equation it can be seen that the scattering force scales with the particle size as r^6 and from equation 2.19 the gradient force scales as r^3. Therefore, for particles with a radius larger than the following condition, the scattering force will dominate (See appendix A for derivation).

$$r > \sqrt[3]{\frac{3\lambda^4}{16\pi^4} \frac{\nabla I}{I} \left(\frac{m^2 + 2}{m^2 - 1} \right)}. \tag{2.25}$$

In the case where the scattering force is dominant, the particle will experience a net force in the propagation direction of the laser beam and will be pushed out of the trapping region created by the gradient potential. For the optical trapping setup outlined in section 3, we find that $\mathbf{F}_{scat} = \mathbf{F}_{grad}$ for a particle with a diameter of 580 nm, suggesting this is the largest particle which can be trapped in the system (see figure 2.7).

The strength of the scattering and gradient force in the axial direction of the trap for a 150 nm diameter particle can be seen in figure 2.8. In the case where the gradient force dominates, the particle is pulled towards the center of the focus and its motion can be described as harmonic, within a potential well created by the gradient force.

2.3.3 Trapping Potential

The depth of the potential well U created by our beam can be found by considering the energy of a dipole $U = -\mathbf{p}.\mathbf{E}$, where $\mathbf{p}$ is the dipole moment. Substituting in $\mathbf{p} = \alpha\mathbf{E}$ we arrive at,

[1] It should be noted that the scattering force equation and derivation shown here is true for the case in which the small-size approximation is true. The small size approximation is true, provided that the circumference of the trapped nanoparticle particle is smaller than the wavelength of scattered laser light. In this situation the scattering of the photons is in phase with the incoming photons. This approximation breaks down as the size of the particle becomes comparable to $\lambda/2$ and interference effects begin to be introduced due to phase variations introduced by the surface of the particle. Since the particles used in the experiments are very small compared to the wavelength ($\lambda = 1550$ nm) this approximation holds for the work presented in this thesis.

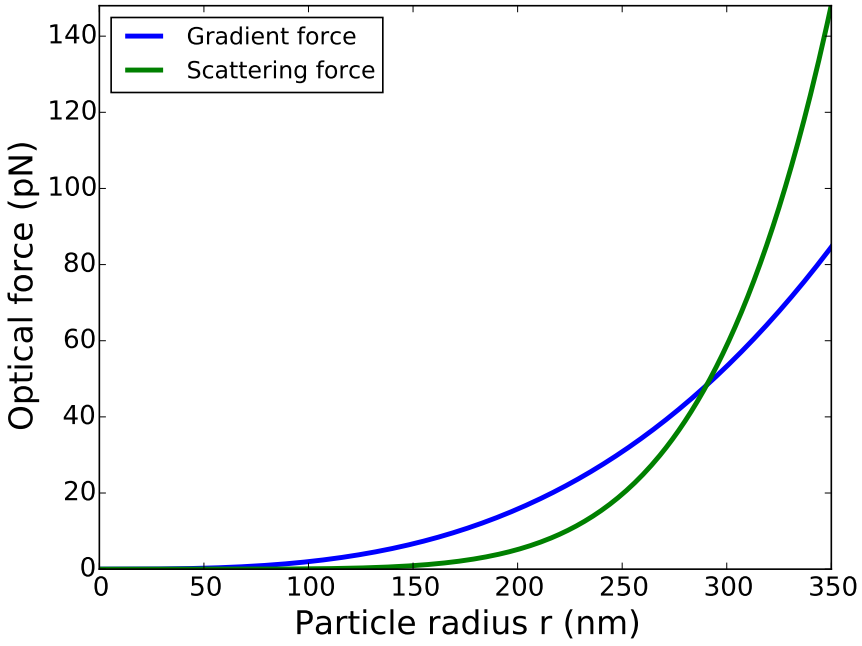

FIGURE 2.7: **Comparison of the gradient and scattering force as a function of particle radius.** It can be seen that particles with a radius less than $r_{max} \sim 290\ nm$ will experience a net force in favour of the gradient force and remain trapped. However, in contrast particles with a radius greater than $r_{max} \sim 290\ nm$ will experience a greater effect from the scattering force and be expelled from the trap.

$$U = \alpha |\mathbf{E}|^2, \tag{2.26}$$

using equation 2.17 and 2.18 we arrive at

$$U = \frac{8\pi I(z,r) r^3}{c} \left(\frac{n^2 - 1}{n^2 + 2} \right). \tag{2.27}$$

It should be noted that an assumption has been made that the focus is unaffected by the presence of a particle. For particles with a small radius compared to the waist of the focus, this assumption holds true, but if $r \approx W_0$ a more complete model for the 3 dimensional intensity should be used [108, 109].

The size of the focus of our trapping laser has a great effect on our ability to trap a particle. The shape of the trapping potential for a range of particle sizes can be seen in figure 2.9. The tighter the focus, the deeper the potential well that our particle finds

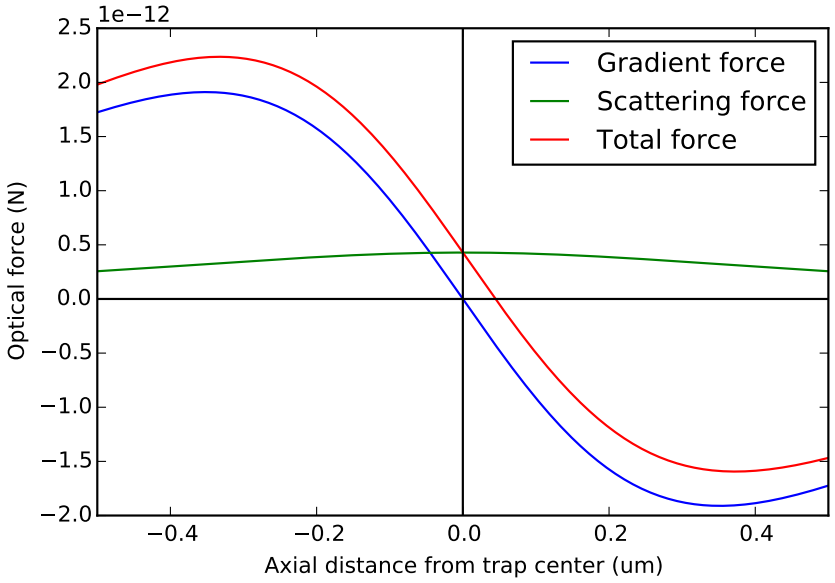

FIGURE 2.8: **Optical forces affecting an optically trapped silicon particle,** with a 150 nm diameter, 55 mW trapping power and a NA of 0.9. In the case shown here the gradient force dominates. The equilibrium point around which the particle oscillates occurs when the total force experienced by the particle is zero.

itself within. The depth of the potential well plays a large role in keeping a trapped nanoparticle within the optical trap. If the thermal energy of the particle is roughly equal to, or greater than the depth of the potential, then the particle can escape from the trap. In thermal equilibrium, to keep a particle optically trapped, the depth of the trapping potential must be at least $\simeq 10k_bT$ [78] to make particle escape via thermal excitation improbable. Figure 2.10 shows, for a given set of parameters, the size range of particles where their size becomes too small to trap easily.

2.3.4 Trap stiffness

An important concept in applications of laser tweezers is the trap stiffness, k_0. For small displacements x, y, z from equilibrium, the trapping potential can be approximated by a harmonic function and the restoring gradient force becomes linearly dependent upon x, y, z. In this situation the relationship between the gradient force, trap stiffness and particle position can be written as,

$$\begin{aligned} F_{grad}^{(x,y)} &= -k_{(x,y)} r_{rad}, \\ F_{grad}^{(z)} &= -k_z z. \end{aligned} \tag{2.28}$$

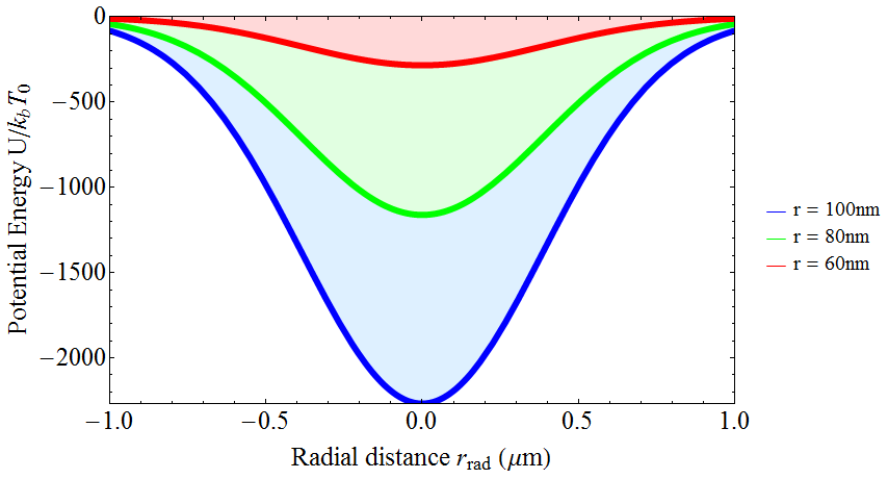

FIGURE 2.9: **Trapping Potential depth as a function of radial distance r_{rad} from the trap for silica nanoparticles of varying radius.** Calculated under the following experimental parameters; NA= 0.995, power = 700 mW and λ = 1550 nm. It can be seen that the trap depth increases with larger particles. This contributes to the difficulty in trapping smaller nanopartilces.

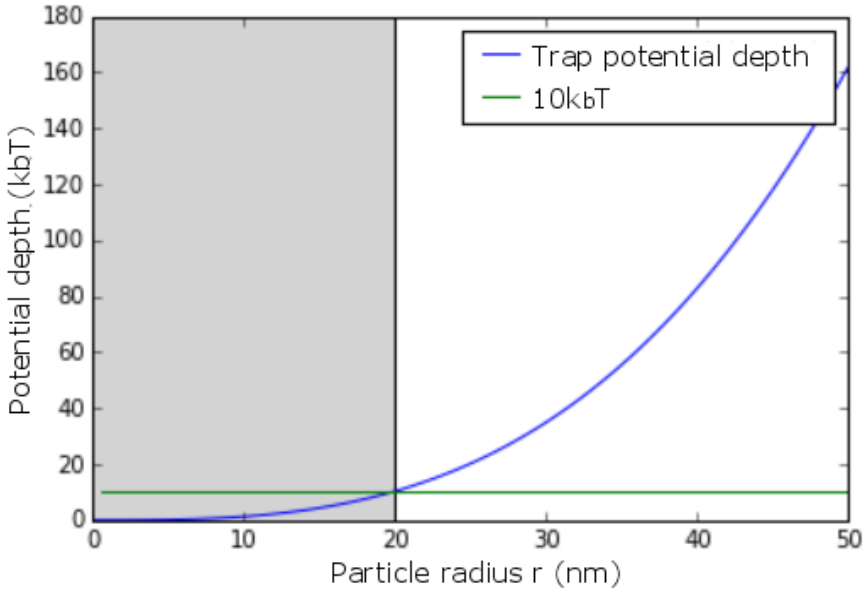

FIGURE 2.10: **Trapping Potential depth as a function of silica nano-particle radius.** Calculated under the following experimental parameters; NA= 0.9, power = 55 mW and a λ = 1550 nm. The grey region marks the area where particle sizes are small enough that, with the given NA and power, trapping will be difficult; in this case, particles with a radius of less than roughly 20nm.

The trap stiffness depends on the direction of displacement. For a single beam gradient trap, it is often sufficient to distinguish between transverse and longitudinal stiffness. The trap stiffness can be found in the transverse[2] x and y dimensions and longitudinal

[2]This is because the intensity gradient in the x and y dimensions is equal to each other and much higher than that of the z dimension. See figures 2.4 and 2.5.

stiffness z by taking the derivatives of equations 2.28, assuming the paraxial approximation and expanding the trap stiffness to the first order to find [13],

$$k_{(x,y)} = \frac{4\alpha(\mathrm{NA})^4\pi^3}{c\varepsilon_0\lambda^4}P_0, \tag{2.29}$$

and,

$$k_z = \frac{2\alpha(\mathrm{NA})^6\pi^3}{c\varepsilon_0\lambda^4}P_0. \tag{2.30}$$

Using the trap stiffness we can define our trap frequency f_0 to be:

$$\omega_0 = 2\pi f_0 = \sqrt{\frac{k_0}{m}}. \tag{2.31}$$

The subscript 0 has been used to denote the equation is the same for any degree of freedom. The trap stiffness and trap frequency play an important part when trying to cool the trapped particle to lower temperature, as will be explained in section 6.1.

2.3.5 Ratio of Trap Frequencies

The ratio between the trap frequencies can be used as a tool for analyzing the shape of the potential well of a three dimensional trap and will be used as such in section 4. To derive this ratio we consider the potential energy U_i of a harmonic oscillator, for each spatial degree of freedom ($i = x, y, z$) given by,

$$U_i = \frac{1}{2}m\omega_i^2 q_i^2, \tag{2.32}$$

where ω_i is the trap frequency and q_i is the particle position in the transverse or z directions. Substituting equation 2.9 into equation 2.27 and performing a Taylor expansion to second order in z and r_{rad} for $r_{rad} = 0$ and $z = 0$ respectively we obtain,

$$U_{r_{rad}}|_{z=0} = -\frac{2\alpha}{\pi W_0^2 c\epsilon_0} P_0 + \frac{4\alpha}{\pi W_0^4 c\epsilon_0} P_0 r_{rad}^2 + \mathcal{O}(r)^3 \tag{2.33}$$

$$U_z|_{r_{rad}=0} = \frac{2\alpha}{\pi W_0^2 c\epsilon_0} P_0 + \frac{2\alpha\lambda^2}{\pi^3 W_0^6 c\epsilon_0} P_0 z^2 + \mathcal{O}(z)^3 \tag{2.34}$$

Equating the second order coefficients with U_i from equation (2.32).

$$\omega_{r_{rad}}^2 = \frac{4\alpha}{m\pi W_0^4 c\epsilon_0} P_0 \tag{2.35}$$

$$\omega_z^2 = \frac{2\alpha\lambda^2}{m\pi^3 W_0^6 c\epsilon_0} P_0 \tag{2.36}$$

The ratio between the transverse and axial direction of the trap can thus be calculated to be,

$$\frac{\omega_{0r_{rad}}}{\omega_{0z}} = \frac{\pi W_0}{\lambda}\sqrt{2} \tag{2.37}$$

Providing the electric field can be described by equation 2.2, the wavelength of laser light used is $\lambda = 1550$ nm and a $W_0 \approx 750$ nm, we find a ratio of 2.22. Throughout the previous discussions we have assumed that the trap is perfectly symmetric in the x and y direction, however this may not be the case experimentally. For example the intensity profile of the Gaussian laser beam, or the alignment of the optical trap may may result in the x and y directions not being perfectly symmetric. If this was the case, then we would be able to observe it via a deviation of the ratio of the trap frequencies from the expected value of 2.22.

2.3.6 Linear spring approximation

In the model presented so far in this chapter, we have assumed that the spring constant is linear. However, this is not strictly true for large amplitude oscillations [62]. As can be seen in figure 2.11, at the center of the trap the gradient force behaves linearly. However at a distance of roughly 300 nm the gradient force begins to no longer behave in a linear fashion. For the majority of investigations in this thesis, the particle explores the linear region of the trap. In the case where the particle explores the nonlinear region of the

trap and therefore nonlinear dynamics become apparent, further detail will be given in the appropriate chapters (see sections 4.6 and 7.6.4).

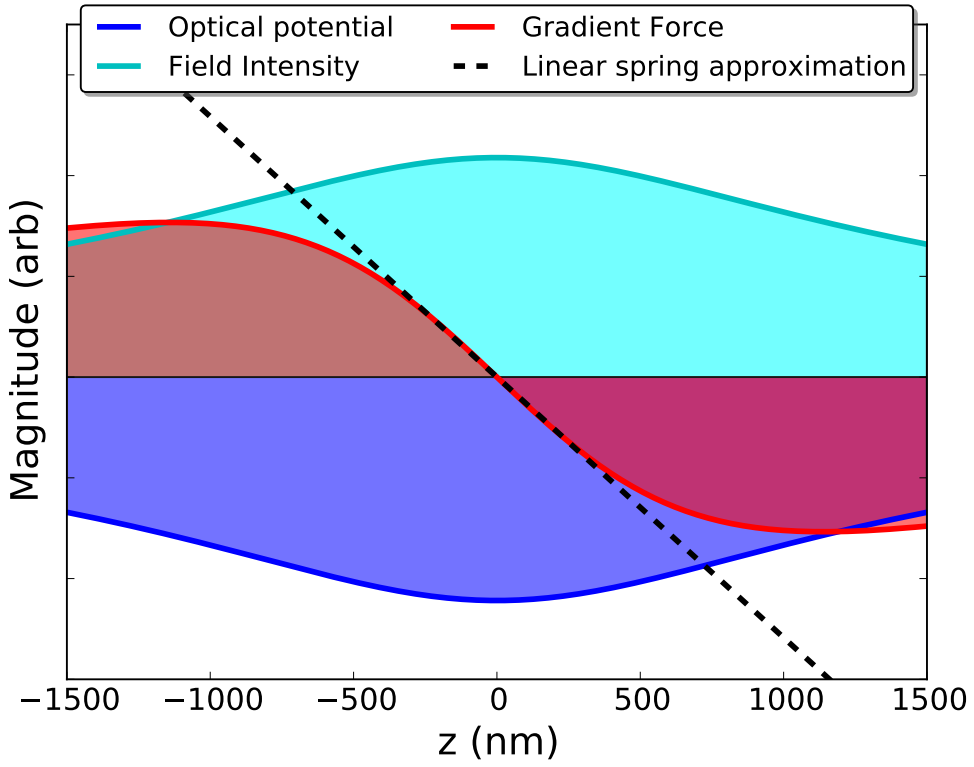

FIGURE 2.11: **Domain of the linear spring approximation.** In the model presented here, the electric field intensity has a Gaussian profile as a function of distance from the centre of the trap (cyan curve) (see equation 6.7). This results in a Gaussian shaped optical potential well (blue curve) (see equation 2.27). The resulting optical gradient force is given by differentiation of the laser intensity (red curve) (see equation 2.19) and the gradient force near the centre of the trap is approximately linear (black dashed line), with slopes given in equation's 2.29 and 2.30 depending on the direction of interest.

Chapter 3

Experimental methods and setup for optical trapping of nanoparticles

Since Arthur Ashkin first demonstrated optical trapping of micrometer sized particles using lasers [75], many experimental schemes have been realised to trap and manipulate particles; With trapping schemes ranging from simple lens based traps [20], to complex setups integrating multiple optical technologies [110]. A variety of novel techniques have been developed for use in optical traps, including trap stiffness manipulation [62], and devices to apply forces [71]. In addition, the use of optical tweezers in combination with other technologies, such as fluorescence spectroscopy [111], has turned them into extremely useful and versatile tools. Despite the large variety of experimental schemes which have been realised to control and manipulate optically trapped particles, each part of the experiment can be broken down into the same components based on function, namely: the laser system, the nanoparticle source, the optical tweezer, the detection scheme, and the manipulation apparatus. Below, each of these components will be elaborated upon.

The laser system: The laser system consists primarily of the laser which will be focused by the trapping objective, but also of the various components used to generate the ideal beam properties, such as beam shape, light polarisation, beam intensity modulation etc.

The nanoparticle source: The nanoparticle source is responsible for selecting and delivering the particle into the optical trap itself, ideally at any pressure for any particle reproducibly. This in itself is a much harder task than it initially seems and is at the time of writing, currently a major hurdle in the field. Practically, several different

methods are used for a variety of different particles at different pressures. A few examples of particle delivery method include: laser-induced thermomechanical stress (LITHMOS) [112], launching particles coated to a ultrasonic transducer [113], dispersion via vaporised solution into the chamber [1, 114]. The later of which is the method used here.

The optical tweezer: The optical tweezer itself is the region in which a nanoparticle's motion will become bound within a potential well. Several experimental methods are utilised to form such a trap, multiple laser beams [115–117], single objective lens [13, 118], optical cavities [119], hybrid magnetic Paul traps [120] and finally the method used in this body of work, a parabolic mirror objective [3, 114].

In addition to the method used to create the optical trapping site, the properties of the trap are also governed by the surrounding environment, specifically the density and constituency of the particles in the trapping chamber. This is determined by the vacuum chamber in which the optical tweezer operates.

The detection system: The detection system is responsible for providing information on the particle's motion within the optical trap. Several schemes have been developed, most of which are based on interference between light which has been scattered by the trapped nanoparticle, with either unscattered trap light or a local oscillator [12, 13, 119]. Once the information is detected, it is then saved for analysis and often utilised in feedback loops to control the particle motion [13].

The manipulation apparatus: The manipulation apparatus is used to impart some kind of change to the nanoparticle motion within the trap. Examples include needles used to displace trapped particles via electric fields [121] and reduction in the oscillation amplitude, by modulating the the trapping laser light [3] to name just a couple of examples. The manipulations that will be demonstrated in this thesis include parametric feedback cooling, capable of reducing the center of mass motion of the optically trapped particle and pulsed squeezing scheme, able to squeeze the phase space of the parametric oscillator.

In this chapter a discussion of the development of the optical tweezer system will be provided, along with details of the experimental scheme used in the following studies to optically trap nanoparticles. The methods of particle manipulation once optically trapped will be discussed in later chapters, along with the results of the experimental manipulation.

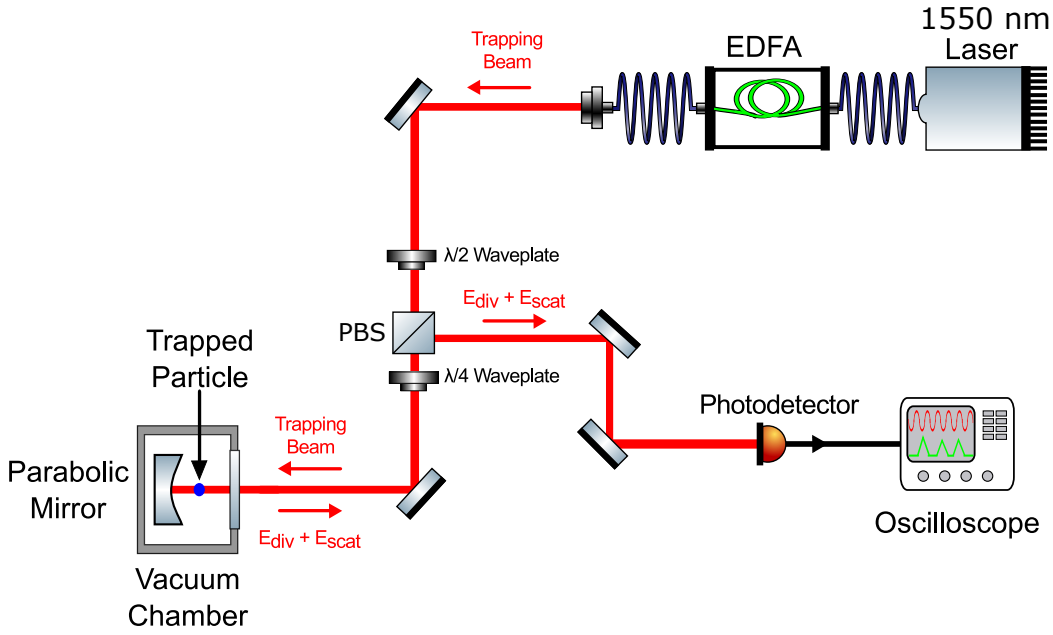

FIGURE 3.1: **Optical setup for trapping nanoparticles.** The $\lambda/2$ wave plate controls the power of the trapping laser beam, as well as allowing a small amount of the trapping laser light to be picked off and monitored when desired. The beam splitter shown in this figure is a polarising beam splitter (PBS). This optical setup forms the basis for all the experiments carried out in subsequent chapters.

3.1 Experimental setup overview

The basic optical setup used to create an optical trap is generated with light from a stabilised fibre laser ($\lambda = 1550$ nm, *NKT Koheras Basik CI5*, 40 mW). The light then seeds an erbium doped fibre amplifier (*EDFA, NuPhoton*) to a maximum power of 1W. The light is focused by a high numerical aperture (NA=0.995) parabolic aluminium mirror, which is mounted in a vacuum chamber. The optical setup can be seen in figure 3.1. In this setup, a variety of particles have been trapped, with silica (SiO_2) nanoparticles trapped in vacuum as low as $1{\times}10^{-6}$ mbar. The $\lambda/4$ wave plate controls the polarization of the light entering the optical trap, as well as the direction of the scattered and diverging light thought the polarizing beam splitter. This light is then collected by a single photodiode (*Thorlabs PDB450C*). The signal measured on the photodiode is then recorded on an oscilloscope (*Teledyne LeCroy HDO6104*).

The vacuum chamber was connected to a roughing pump (*Oerlikon lybold vacuum pump 140125T*), capable of reducing the chamber to roughly 10^{-2} mbar and a turbo pump (Pfeiffer PM Z01300) capable of reducing the pressure further to 10^{-6} mbar. The pressure is read from a (*Oerlikon Leybold Vacuum, D-50968 Koln, Type: ITR 90 No: 12094, F-No:1669/2012*) pressure sensor.

3.2 The laser system

Earlier experiments were carried out using an IPG fibre laser (λ = 1550 nm, 10 W). However, due to laser stability issues, the laser was later replaced with a *NKT Koheras Basik CI5* fibre laser. This laser is used for all the experiments outlined in this thesis[1]. The stabilised fibre laser (λ = 1550nm, *NKT Koheras Basik CI5*, 40mW) then seeds an erbium doped fibre amplifier (*EDFA, NuPhoton*). The beam diameter is entirely dependant upon the fibre collimator used for output from the EDFA fibre output. The collimator chosen was a Thorlabs 3.0 mm diameter FC/PC fibre collimator, which produces a beam waist marginally larger than parabolic mirror dimensions. This allows for a large amount of the laser light to be collected (see section 2.2.2.1) and the alignment method used in these experiments (see section 3.4 for details). The *NKT Koheras Basik CI5* fibre laser emits 40 mW of laser power which is amplified up to a maximum power of 1 W. Loss in the optical setup through processes such as absorption results in about 700 mW reaching the optical trap.

3.3 Nanoparticle Source

The nanoparticle source for an optical trap consists of two parts, the particles themselves and the equipment used to deliver the particles to the trapping region. The ideal source would be able to reliably deliver particles to the trapping region at any pressure, without affecting the pressure in the chamber itself, or introducing any contaminant. Finally, the delivery system should be controllable and repeatable. Such an ideal system has yet to be developed and is an area of active research within the community.

There are several methods to deliver a particle into an optical trap which operate at vacuum. Some methods used rely on coating/growing nanoparticles on a surface and then firing the particles off the surface. These methods include Laser-induced thermomechanical stress (LITHMOS) [112], launching particles coated to a ultrasonic transducer [113] and laser ablation. These methods have the drawback of relying on producing a large number of particles being flung in the direction of the optical trap. A more precise delivery method can be created by using a standing wave trap inside a hollow-core photonic crystal fibre. A particle trapped at one end of the fibre can be moved through the fibre by means of the standing wave trap, to create an optical conveyor belt. By placing the fibre between two different vacuum chambers, one at atmospheric pressure and one at the desired vacuum, it's possible to transfer a single particle into an optical trap in a vacuum, in a controllable way [122].

[1] With the exception of figure 3.3.

The method implemented in this work is dispersion via vaporised solution into the chamber [114]. This method is experimentally much simpler than the aforementioned methods, however has the drawback of only working at atmospheric pressure and emitting large amounts of water vapor into the vacuum chamber.

3.3.1 Nanoparticle selection

There are several parameters to consider when selecting a nanoparticle to optically trap. Firstly the nanoparticle requires a high polarisability, allowing it to couple strongly with the optical gradient field. Secondly, it must have low absorption at the wavelength of light used to form the optical trap, in our case 1550 nm. This is to prevent the particle heating within the optical trap, to an extent where it deforms, melts or emits a large amount of blackbody radiation. Low emission of blackbody radiation is a desirable characteristic for proposed nanoparticle interferometry experiments, such as [44].

These criteria are met by silica and silicon particles, however due to the ease of availability of silica nanospheres, they are the material of choice for the experiments carried out in this thesis unless otherwise specified. In addition to trapping silica particles, trapping of polystyrene, nanodiamonds[2], silicon and carbon nanotubes has also been achieved. The silica spheres that have been used range between 18 nm and 312 nm in diameter.

3.3.2 Particle delivery method

Nanoparticles are loaded into the optical trap via the use of an Omron micro-Air nebuliser, shown in figure 3.2. The nebuliser uses a 3 μm mesh to generate aerosol droplets of the liquid solution. To trap a particle in the system the vacuum chamber is opened at atmospheric pressure, then the nebuliser is used to disperse droplets of liquid containing nanoparticles into the chamber near the trapping region. Once a particle is trapped, the chamber is closed and evacuated.

To prepare a solution of nanoparticles for use in optical trapping, we purchase a premade solution of nanoparticles and dilute to the required concentration. The suspension is then sonicated for 15 minutes (37 kHz, 300 K), before being loaded into the nebuliser (for more details on the method used to prepare the particles see appendix B). To reduce the chance of aggregation, or particle clusters becoming trapped in the optical setup, we dilute the system to a concentration of roughly 1 nanoparticle per droplet. The mass of a nanoparticle is given by,

[2] As a point of interest several studies using optically trapped nanodimonds have been demonstrated in multiple optical trapping systems [68, 116, 123].

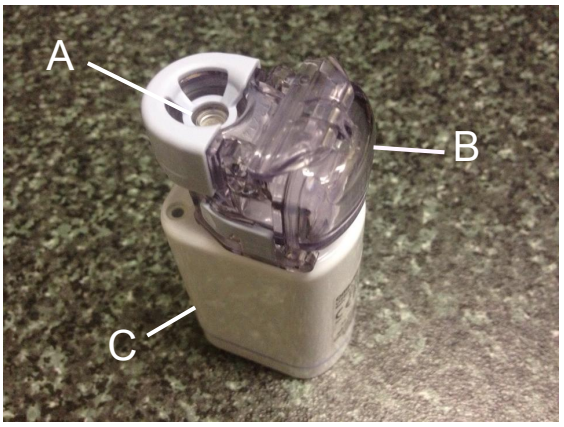

FIGURE 3.2: **The nebuliser** consists of three parts **A)** A mesh on top of a piezoelectric crystal element. Liquid in the space between the piezoelectric crystal and the mesh is pushed through the mesh by the motion of the piezoelectric crystal. The mesh breaks the liquid into micrometer sized droplets of water. Under standard humidity conditions, the droplets quickly evaporate and only the solid nanoparticles are left behind [1]. **B)** The nanoparticle solution loading area. **C)** The power supply.

$$m = \rho V_p = \frac{4}{3}\pi\rho r^3. \tag{3.1}$$

where ρ is the density of the nanoparticles in question, V_p is volume of a nanoparticle. From this, and using the concentration of the purchased nanaoparticle solution C_{Sol} we can calculate the number of particles in the solution:

$$N_{\text{particles}} = C_{\text{sol}} \frac{V_{\text{droplet}}}{\rho V_p} = \frac{C_{\text{sol}}}{\rho} \frac{r^3_{\text{aerosol}}}{r^3}. \tag{3.2}$$

where V_{droplet} is the volume of the aerosol droplet and r_{aerosol} is the radius of the aersol droplet. Therefore, we can write the dilution factor required to dilute a commercial nanoparticle solution to provide a single particle per droplet as $DF = 1/N_{\text{particles}}$. The concentration of a typical off the shelf nanoparticle solution is 25 kg/m^3. Therefore, for example we can calculate a dilution factor for nanoparticles with radius of 65 nm to be equal to 0.001.

3.4 The Optical trap

Several iterations and refinements were made over the course of the PhD, to create a stronger and more stable trap. Initially we started with lens based traps, before moving

onto a parabolic mirror to create the an optical trap.

3.4.0.1 Problems with Refractive Optics

Initially, optical trapping was performed using an aspheric lens from *Thorlabs (AL1210-C)* with an NA of 0.6 and a focal length of 10 mm. However, this was found to be more problematic than initially anticipated. The issues turned out to be a consequence of the way the Thorlabs lens was designed. The aspherical lens used was cut for a wavelength of 780 nm and then coated with an antireflection coating for 1550 nm[3]. At the design wavelength (780 nm), the focus waist is 0.6 μm and has a clean focus with minimal aberrations. However, as the design wavelength of the lens is significantly lower than the wavelength of our trapping laser (1550 nm), we find the focus waist to be 66 μm, with significant aberrations. To quantify the increase of aberrations in the focus when using 1550 nm laser light we use the Strehl ratio. The Strehl ratio is a measure of the image quality ranging between 0 and 1 [124]. For the design wavelength of the lens (780 nm) the Strehl ratio of the *Thorlabs (AL1210-C)* lens is 0.82. However, with the 1550 nm trapping laser light, the Strehl ratio equals 0.2, a much lower value. The larger focal beam waist, resulting from chromatic aberrations when using 1550 nm light resulted in the need for higher laser powers to trap nanoparticles, than the parabolic mirror used throughout this thesis. Additionally, the aberrations resulted in multiple trapping sites forming at the focus (shown in figure 3.3). The use of several lenses to correct for these aberrations provided some improvement, without solving these problems completely. The problems resulting from chromatic aberrations motivated the switch from refractive to reflective optics.

3.4.0.2 The Mirror Trap

A solution to the problems raised by lens-based traps was found in the form of parabolic mirrors, one of which can be seen in figure 3.4. The mirrors were designed and then commissioned from Symons Mirror Technology, who machined the mirrors with a diamond lathe from an aluminium block, with a surface roughness of less than 4 nm. There is no optical or protective coating attached to the aluminium surface.

The parabolic mirror as a reflective high NA optic offers several advantages and acts as a cheap alternative to comparable lens optics. The mirror is easy to implement and to use at ultra-high vacuum, which is more difficult for high NA objective lenses. Another

[3]It should be noted that since switching to a parabolic mirror trap low cost aspheric lens have become commercially available, with the design wavelength of 1550 nm such as Thorlabs C660TME-C. Trapping with the *Thorlabs C660 TME-C* was tested and found possible, without the creation of multiple trapping sites.

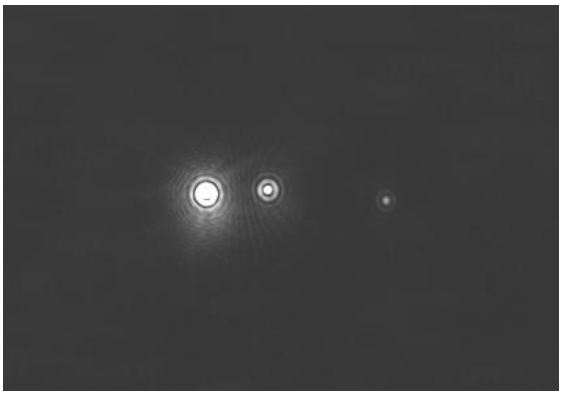

FIGURE 3.3: **Optical trapping with an aspherical lens from Thorlabs (*AL1210-C*)** multiple particles can be levitated at the focus. This image was taken perpendicular to the direction of beam propagation. The laser used to trap these particles was a IPG Laser (10 W,1550 nm) outputting a power of 4 W. This is the only time this laser was used to collect data presented in this thesis.

advantage, is that the mirror does not have chromatic effects, which make the position of the focal point independent of the wavelength used. The latter might be interesting for multi-wavelength spectroscopy and manipulation techniques.

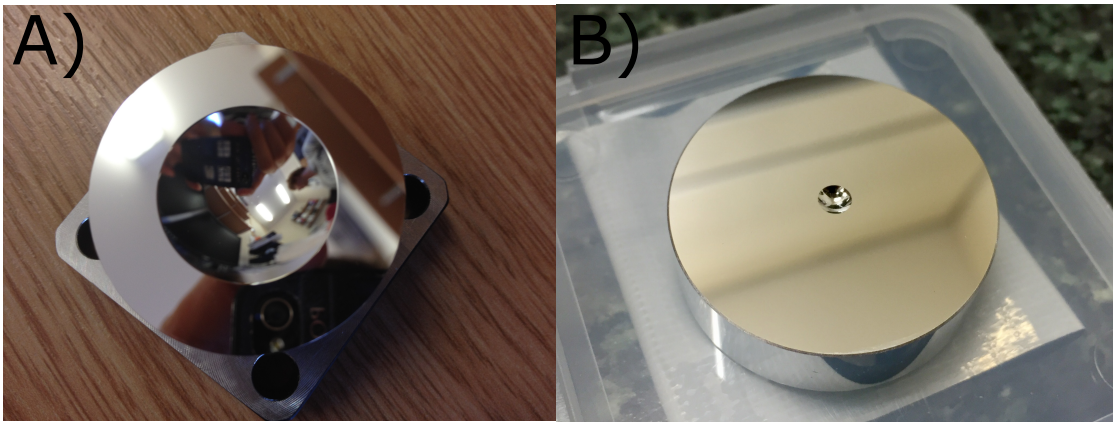

FIGURE 3.4: **The parabolic mirror used for trapping**. A) The first iteration of the parabolic mirror had a diameter of 20 mm, a depth of 4.5 mm, a surface roughness of less than 10 nm and a max NA of 0.9. This mirror has not been used to collect any of the experimental data shown in this thesis. B) This mirror is one of the two mirrors used throughout the work presented here with an $NA = 0.9951$. The mirrors were made to be smaller than the beam width such that the alignment method outlined in 3.5.1 could be used.

3.4.1 Evaluation of the numerical aperture

Figure 3.5 A shows a parabola. Parabolas made from a reflective material have the property that light which travels parallel to the parabolas axis of symmetry and strikes its concave side will be reflected to its focus, independent of where the reflection occurs on the parabola. Conversely, for a point source located at the focus, all the light emitted

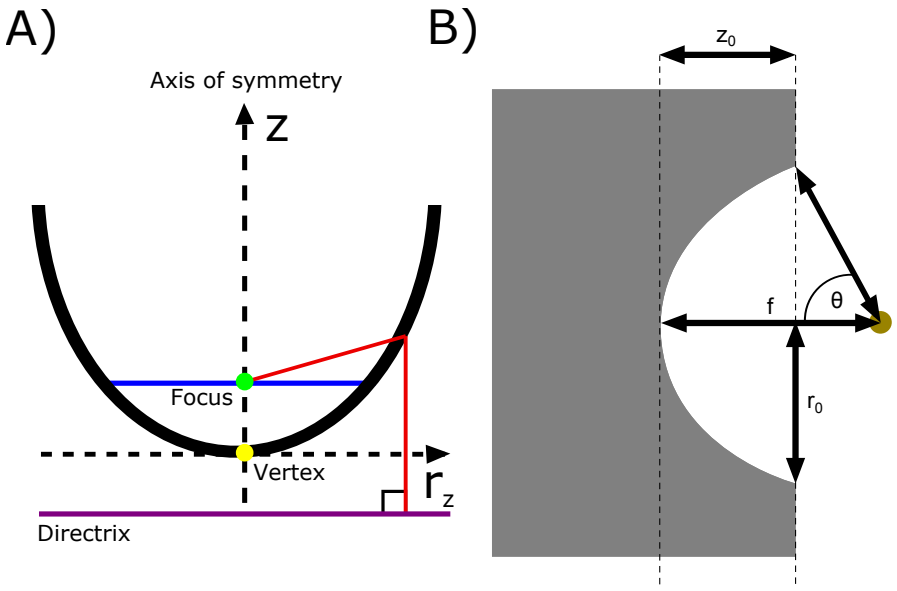

FIGURE 3.5: **A) Geometry of a parabola** A parabola is a plane curve (solid black line), which can be defined using the focus (green dot) and the directrix (solid purple line). The focus by definition does not lie on the directrix. The parabola is a line, in which all constituent points are equidistant from both the focus and the directrix (shown by the red lines, which are of equal length). The line perpendicular to the directrix, and which passes through the focus is called the axis of symmetry. The point on the parabola that intersects the axis of symmetry is called the vertex (yellow dot). The distance between the vertex and the focus, measured along the axis of symmetry, is the focal length f. **B) Geometry of the parabolic mirror.** The polarisable particle is trapped in the diffraction limited focal point of the parabolic mirror. We have used a number of different mirror designs thoughout the experiment, which differ in the working distance, the focal point with respect to the plane surface of the mirror and the NA. The more of the paraboloid used for the mirror, the higher the NA. The NA can also be varied/reduced for a given mirror by modification of the waist of the laser light incident on the mirror: If the light spot is smaller than the machined paraboloid, the NA is reduced.

would be reflected into a collimated beam, leaving the parabola parallel to the axis of symmetry.

The geometry of the mirror trap is illustrated in figure 3.5 B. The numerical aperture (NA) is defined as the light acceptance cone of the parabolic mirror. As the scattered light from a trapped particle diverges from the focus, we consider the solid angle at the distance z_0 as a fraction of the maximum angle of acceptance 2π. Thus allowing us to write [125]:

$$\mathrm{NA} = \int_0^{\theta} \sin\theta' \mathrm{d}\theta' = 1 - \cos\theta. \tag{3.3}$$

The general paraboloid function is $z = r_z^2/(4f)$, where z is the height above the bottom of the mirror, r_z is the radius of the paraboloid at z, and f is the focal length (see figure 3.5 A). For the paraboloid as shown in Fig.(3.5) at the maximum radius r_0 and at the

corresponding height z_0, with $z_0 \leq f$, the angle θ between the optical axis and the edge of the paraboloid is given by

$$\tan(\theta) = \frac{r_0}{(f - z_0)} = \frac{r_0}{f - r_0^2/(4f)}. \tag{3.4}$$

We can thus define the NA of the parabolic mirror to be

$$\mathrm{NA} = 1 - \cos\left(\arctan\left[\frac{\mathrm{r_0}}{\mathrm{f} - \mathrm{r_0^2/(4f)}}\right]\right). \tag{3.5}$$

There are two mirrors used in the experiments presented here. The first mirror used has a focal length of f=3.1 mm and r_0=1.27 mm, which gives a NA of 0.995. The second had the same focal length of f=3.1 mm but larger radius of r_0=6.9 mm, resulting in a lower NA equal to 0.9.

3.5 Continuous Detection System

3.5.1 Alignment of the Detection System

The trapping laser used has a beam diameter slightly larger than the width of the parabolic mirror, the reflection from the flat surfaces of the mirror (seen in figure 3.4) results in wave interference, to create a bright spot in the center of the detection beam, overlapping the E_{scat} and E_{div} fields. The bright spot is a result of near field diffraction by the flat mirror edges around the parabolic mirror. The spot can be used to align the beam reflected from the parabolic mirror to the photodiode used for detection. However, due to the high power of the Poisson spot, it increases the signal-to-noise ratio (SNR), reducing the position resolution we are able to detect. To remove the Possion spot when trapping nanoparticles in the setup, an iris is placed in front of the parabolic mirror. When the iris is open, the Possion spot can be seen by placing a CCD in the setup. While the iris is open, the Posssion spot can be observed; reducing the size of the iris aperture reduces the size of the Possion spot and it finally disappears when the iris aperture is equal to the size of the parabolic mirror (This process is shown in figure 3.6). Any reduction in the iris aperture's diameter below that of the parabolic mirror width results in a decrease in the trap frequency of any optically trapped nanoparticle, as the power entering the trap is reduced. An image of a trapped particle taken while the iris is closed can be seen in figure 3.7.

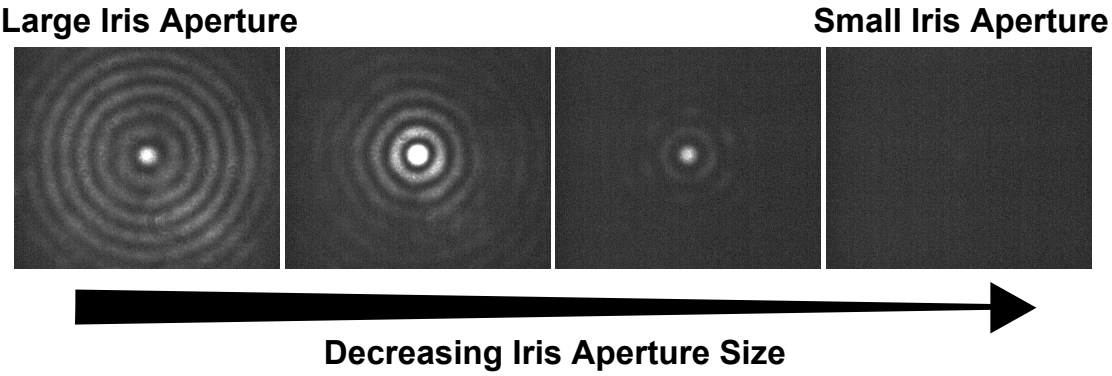

FIGURE 3.6: **Removal of Poisson spot.** As the iris aperture is closed, the size of the Poisson spot starts to decrease in size, until the iris aperture size matches that of the parabolic mirror, at which point it vanishes completely.

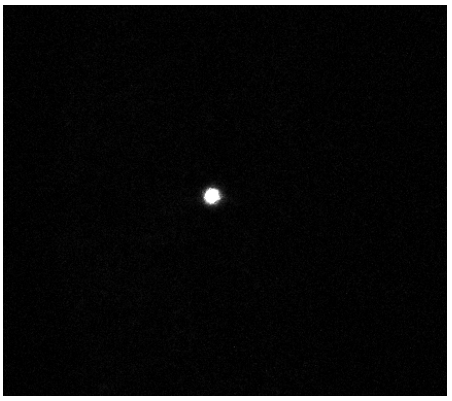

FIGURE 3.7: **Image of a trapped 100 nm silica particle** The image was captured with a CCD (*Point Gray Research CMLN-12S2M-CS*) placed in the beam path just in front of the photodiode.

3.5.2 Homodyne detection

In the absence of a trapped particle, the light focused by the mirror will be highly divergent and very little of it will reach the detection system. However, if a particle is trapped, then a portion of the scattered light from our nanoparticle is scattered back toward the parabolic mirror and as the light is coming from the focus of our parabolic mirror, it will become collimated before being sent to the detector. Interference between this back scattered field E_{scat} and the highly divergent field which passes without interacting with the particle through the focus E_{div} (the reference field), provides interferometric position resolution. These fields can be seen in figure 3.8.

The resulting interferometric signal E_{total} is given by

$$|E_{\text{total}}|^2 \approx |E_{scat} + E_{div}|^2, \tag{3.6}$$

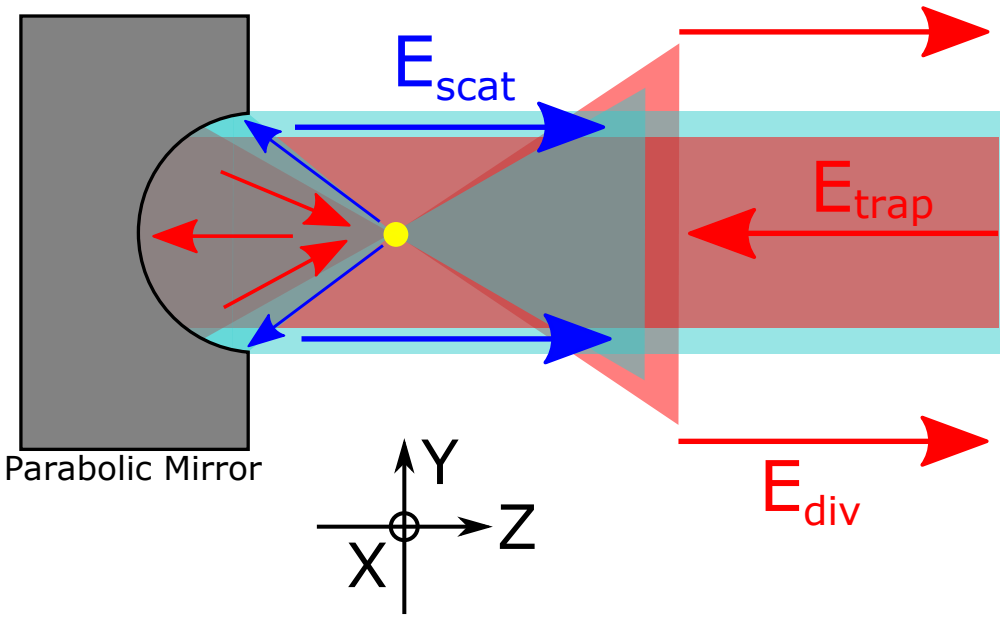

FIGURE 3.8: **The wave fronts present with a particle in the optical trap.** The amount of scattered field E_{scat} collected and thus collimated by the parabolic mirror depends on the NA of the parabolic mirror, with larger NA's collecting a larger percentage of the scattered field.

and is proportional to the phase difference between the E_{div} and E_{scat} field. A phasor diagram of the signal components is shown in figure 3.9. The length of E_{scat} remains constant, as the particle is sub-wavelength and confined towards the center of the laser focus, however the phase does change due to the change in path length of the scattered light. This change in path length is caused by the particle oscillation within the trap. This causes a change in the length of E_{total}. It is this modulation that we detect to monitor the particle position. More detail on the detection scheme used can be found in section 4.5.

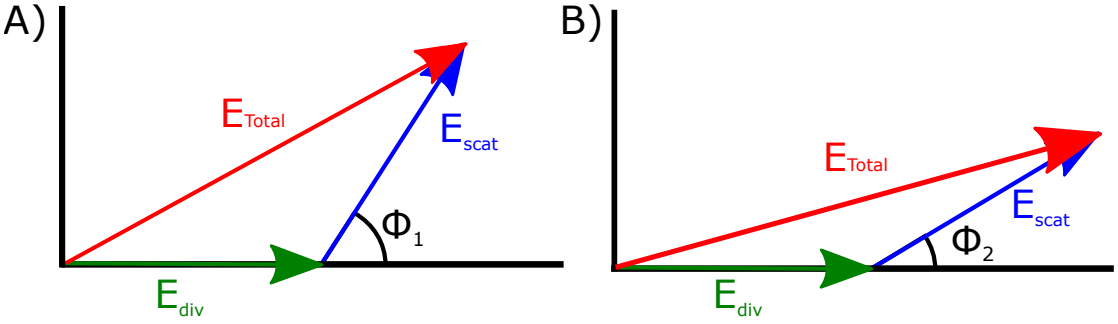

FIGURE 3.9: **Phasor diagram of detected signal components.** The length of E_{scat} is constant as the particle is sub-wavelength and is confined close to the center of the focus, however the phase does change due to the change in path length. This changes the angle ϕ causing a change in the length of E_{total}. **A)** The phasor diagram for a particle with phase ϕ_1. **B)** The phasor diagram for a particle with phase ϕ_2. It can be seen that E_{total} has increased compared to ϕ_1.

In the detection arm of the experimental set up, the reference field is allowed to diverge. By making the reference field amplitude comparable with that scattered by the particle, a large modulation visibility is observed at the detector. This results in a high particle position resolution. For optimal detection efficiency, the detector must be sufficiently far away so that the divergent beam wavefronts are approximately flat over the detector area. For a detector of radius a at a distance d from a point-like source, the distance from point source to edge of detector is $\sqrt{d^2 + a^2}$. The difference between this and the on-axis distance d must be less than $\approx \lambda/4$.

$$\begin{aligned} \sqrt{d^2 + a^2} - d < \lambda/4 &\implies \sqrt{1 + (a/d)^2} - 1 < \lambda/(4d) \\ &\implies (a/d)^2/2 < \lambda/(4d) \\ &\implies d > 2a^2/\lambda. \end{aligned} \tag{3.7}$$

For example in the case of a 1 mm diameter detector ($a = 500\ \mu m$) with 1550 nm light, the detector must be at least 30 cm away.

Chapter 4

Optomechanics of levitated particles

The first demonstration of optical trapping was carried out by Ashkin in 1970, [75] who demonstrated for the first time, optical trapping of micrometer sized particles. Subsequently through several studies by Ashkin and others [126], methods of manipulating and trapping with light were extended to molecules and atoms. This resulted in the branching of the field into two distinct fields: one concerned with the optical trapping of atoms and molecules and the other microscopic objects.

The latter field, concerned with the trapping and manipulation of microscopic objects is referred to as "optical tweezers". Optical tweezers, as discussed previously, can take many forms, with each system offering different levels of control over the particle size and motion within the trap and therefore are suitable for differing studies of particle motion. Such studies include measurement of a particle's velocity [12], the relaxation of the particle motion from a non-equilibrium steady state [24] and the rotation of birefringent particles [127].

As mentioned before, the type of trap used in these experiments is a gradient force trap. The first demonstration of a gradient force trap was carried out in 1997 by Omori et al. [83] who trapped a micro-particle in air. Later in 2011 Giesler et al. [13] used parametric feedback cooling to optically cool and trap a particle at vacuum, advancing the versatility of gradient force traps. The work presented in this chapter will demonstrate optical control over a particle's motion within a gradient force trap created using a parabolic mirror objective.

In this chapter, we will discuss the motion of the particle within the aforementioned optical gradient force trap (described in section 3). In addition to this, control over

the frequency of the motional degrees of freedom will be presented and a description of two different methods to extract key experimental parameters of an optically trapped particle will be demonstrated.

4.1 Harmonic particle motion

For a particle in a harmonic potential with a trap stiffness of $k_0 = m\omega_0^2$, experiencing a damping force (with damping rate Γ_0), the equation of motion can be written as,

$$m\ddot{x}(t) + m\Gamma_0\dot{x}(t) + k_0 x(t) = F_{\mathrm{th}}(t) \tag{4.1}$$

where $F_{th}(t)$ is an external noise experienced due to thermal stochastic noise. The equation written here is for the x motion, but similar equations apply in the y and z degrees of particle motion, all of which have there own distinctive frequency of oscillations (ω_z, ω_x and ω_y). The solution to this equation can be written as,

$$x(t) = x_0 \sin(\omega_0 t + \phi) \tag{4.2}$$

where x_0 is the amplitude of motion and ϕ is an arbitrary phase. The power spectral density (PSD) is a useful tool for analysing the dynamics of a trapped nanoparticle and can be derived from equation 4.1. The PSD for the particle motion can be calculated using the Fourier relationship and details how much each frequency component contributes to the variance of the particle position signal.

$$\frac{d^n f(t)}{dt^n} = (i\omega)^n \tilde{f}(\omega) \tag{4.3}$$

applying this Fourier relationship to equation 4.1,

$$m(i\omega)^2\tilde{x}(\omega) + m\Gamma_0(i\omega)\tilde{x}(\omega) + k_0\tilde{x}(\omega) = \tilde{F}_{\mathrm{th}}(\omega) \tag{4.4}$$

where $\sim$ denotes the term in question is now in terms of frequency. rearranging $\tilde{x}(\omega)$ to be the subject

$$\tilde{x}(\omega) = \frac{1}{m}\left(\frac{\tilde{F}_{\mathrm{th}}(\omega)}{(\omega_0^2 - \omega^2) + (i\omega\Gamma_0)}\right). \tag{4.5}$$

Taking the squared magnitude will yield the power spectral density $S_{xx}(\omega) = \langle|\tilde{x}(\omega)|^2\rangle$,

$$S_{xx}(\omega) = \frac{1}{m^2}\frac{\langle|\tilde{F}_{\mathrm{th}}(\omega)|\rangle^2}{(\omega_0^2-\omega^2)^2+(\omega\Gamma_0)^2}. \tag{4.6}$$

This equation shows how the energy is distributed across frequency space. This equation can be expressed in more intuitive quantities by integrating equation 4.6 to find the positional variance of the particles oscillation $\langle x^2\rangle$.

$$\begin{aligned}\langle x^2\rangle &= \int_0^\infty S_{xx}(\omega)d\omega \\ &= \frac{1}{2}\int_{-\infty}^{\infty} S_{xx}(\omega)d\omega \\ &= \frac{\langle|\tilde{F}_{th}|\rangle^2}{2m^2}\int_{-\infty}^{\infty}\frac{1}{(\omega_0^2-\omega^2)^2+(\omega\Gamma_0)^2}d\omega \\ &= \frac{\langle|\tilde{F}_{th}|\rangle^2}{2m^2}\frac{\pi}{\omega_0^2\Gamma_0}\end{aligned} \tag{4.7}$$

Using equipartition theorem $\frac{1}{2}k_bT_{cm} = \frac{1}{2}m\omega_0^2\langle x^2\rangle$, where T_{cm} is the centre of mass temperature of the particle motion. Thus we find

$$\langle|\tilde{F}_{th}|\rangle^2 = \frac{m}{\pi}2k_bT_{cm}\Gamma_0^2. \tag{4.8}$$

Thus we can write equation 4.6 as,

$$S_{xx}(\omega) = \frac{k_bT_0}{\pi m}\frac{\Gamma_0}{(\omega_0^2-\omega^2)^2+\omega^2\Gamma_0}, \tag{4.9}$$

This equation is the power spectral density of the particle motion and forms a useful tool for analysing the motion of optically levitated particles. The motion of an optically trapped particle and corresponding PSD can be seen in figure 4.1.

4.1.1 Damping

The viscous damping rate Γ_0 is a result of the collisions with air molecules in the surrounding environment. From kinetic theory Γ_0, can be written as [128],

$$\Gamma_0 = \frac{6\pi\eta_{air}r}{m}\frac{0.619}{0.619+Kn}(1+c_K) \tag{4.10}$$

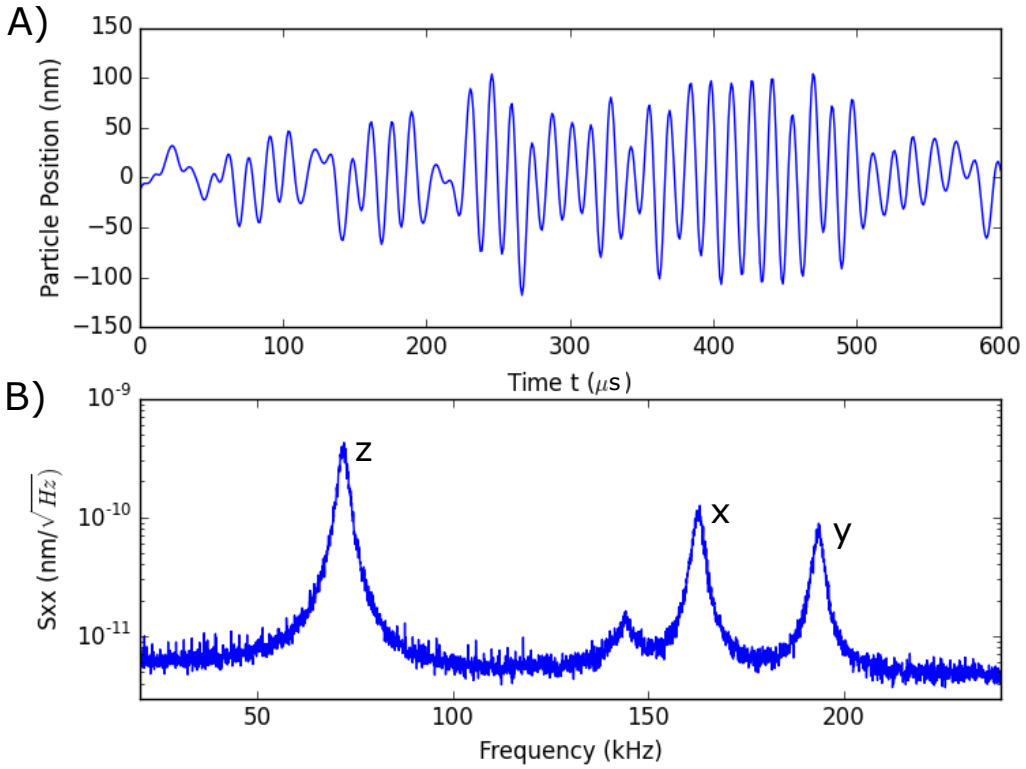

FIGURE 4.1: **A) Time domain data** of a 50 nm diameter particle at 1 mbar. The particle position relative to the centre of the trap is shown over time. The data has been passed through a 50 kHz low pass filter to remove noise in the system. The method used to extract the positional information is described in section 4.2. **B) Corresponding PSD** showing the frequency peaks arising from the motion of the particle in all three spatial degrees of freedom. The x and y peaks have different frequencies, due to deliberate breaking of the symmetry between the x and y spatial degrees of freedom and is discussed further in section 4.4. The additional peak that can be seen between the z and x peak is due to nonlinear effects discussed in more detail in section 4.3.

where η_{air} is the viscosity of air ($\eta_{air} = 18.2$ μPa s [129]), r is the radius of the nanoparticle, $c_K = (0.31Kn)/(0.785 + 1.152Kn + Kn^2)$ which is a function of Kn the Knudsen number. The Knudsen number is a dimensionless number which indicates whether the description of the system via fluid dynamics should take into account statistical mechanics (in the case where $Kn \geq 1$), or continuum mechanics ($Kn << 1$). The Knudsen number is defined to be $Kn = \bar{l}/r$, where l is the mean free path of air molecules.

The form of the equation to express the mean free path, used to describe the system, depends on whether the particles in question are considered to be "soft" spheres, following a Lenard-Jones potential, or hard spheres colliding. In the case of our experiment we find that the assumption of hard spheres corresponds with experimental results and therefore we can write the mean free path as,

$$\bar{l} = \frac{k_b T_0}{\sqrt{2}\pi d_{gas}^2 P_{gas}}. \tag{4.11}$$

where d_{gas} is the diameter of the gas particles ($d_{gas} = 0.375$ nm [130]), T_0 is the temperature of the environment and P_{gas} is the pressure of the gas. It is possible to relate Γ_0 linearly to the measured pressure by expanding equation 4.10 in Kn^{-1} to get,

$$\Gamma_0 = 0.619 \frac{9\pi}{\sqrt{2}} \frac{\eta_{air} d^2}{\rho k_b T_0} \frac{P_{gas}}{r} \tag{4.12}$$

Therefore at low pressures where the mean free path is relatively large, for example at P=10^{-3} mbar, $\bar{l} = 6.6$ cm and it can be seen that Γ_0 is linearly proportional to P_{gas}.

4.2 Extraction of parameters from fit to PSD

This section details a method to extract parameters of an optically trapped particle such as mass m and radius r, and parameters about the motion of the nanoparticle in the trap, such as damping of the particle motion Γ_0, from fitting to the measured power spectral density. Experimental data is directly recorded from the photodiode signal, which means the particle position is recorded in volts as function of time. Directly plotting the PSD from a recorded time trace will have units of V^2/Hz, therefore the experimental PSD can be written as,

$$S_{xx}(\omega) = \gamma^2 \frac{k_b T_0}{\pi m} \frac{\Gamma_0}{(\omega_0^2 - \omega^2)^2 + \omega^2 \Gamma_0^2}, \tag{4.13}$$

where γ is a conversion factor from volts to meters in units of V/m[1]. To fit this equation to the experimental data we simplify equation (5.13) as

$$S_{xx}^{exp} = \frac{A}{(B^2 - \omega^2)^2 + \omega^2 C^2}. \tag{4.14}$$

Where $A := \frac{\gamma^2 k_b T_0 \Gamma_0}{\pi m}$, $B := \omega_0$ and $C := \Gamma_0$ are free fit parameters. The conversion factor γ is a result of the detector's measurement is in Volts. To convert our power spectral density to $\frac{m^2}{Hz}$, we require a conversion factor with units of $\frac{m}{V}$. The conversion factor can be calculated using

[1]Due to the nature of the detection scheme described in section 3.5.2, the relationship between particle position and voltage measured on the detector is not completely linear, however it can be treated as linear to a good approximation.

$$\gamma = \sqrt{\frac{A}{C}\frac{\pi m}{k_b T_0}}. \tag{4.15}$$

where the particle is assumed to be in thermal equilibrium at T_0 =300 K. Extracting the fit parameter C from equation 4.15 and using equation 4.12 it is possible to calculate the mass of the trapped particle.

4.2.1 Measuring particle radius and mass

To calculate the particle's radius from equation 4.12, we use the fit parameter $C = \Gamma_0$ extracted from the Lorentzian fit, pressure P measured from a pressure sensor and known constants. This allows us to write,

$$r = 0.619\frac{9\pi}{\sqrt{2}}\frac{\eta_{air} d^2}{\rho k_b T_0}\frac{P_{gas}}{C}. \tag{4.16}$$

Using the calculated radius from equation 4.16 it is possible to calculate the mass M using $M = 4\pi\rho r^3/3$. An example of fit and extracted parameters is shown in figure 4.2. The methods used to calculate the errors in the values of r and m can be found in appendix C.

4.2.2 Calculating position sensitivity

Once the mass of the particle has been calculated, the conversion factor can be obtained using equation 4.15. The noise equivalent power (NEP) of a detector characterises the resolution of a detector. For the balanced photodiode detectors used the $\mathrm{NEP_{det}} = 70$ $\mathrm{nV}/\sqrt{\mathrm{Hz}}$. Equivalently, we can work out the position resolution of our setup,

$$S_{xx,min} = \frac{\mathrm{NEP_{det}}}{\gamma}. \tag{4.17}$$

A typical value for $S_{xx,min}$ is 17 $\mathrm{fm}/\sqrt{\mathrm{Hz}}$ in our system. The current experimental position resolution, $S_{xx,exp} = 0.53\ pm/\sqrt{\mathrm{Hz}}$, is limited by the noise floor, which currently is at $\mathrm{NEP_{exp}} = 2\ \mu\mathrm{V}/\sqrt{\mathrm{Hz}}$ as analysed from experimental data.

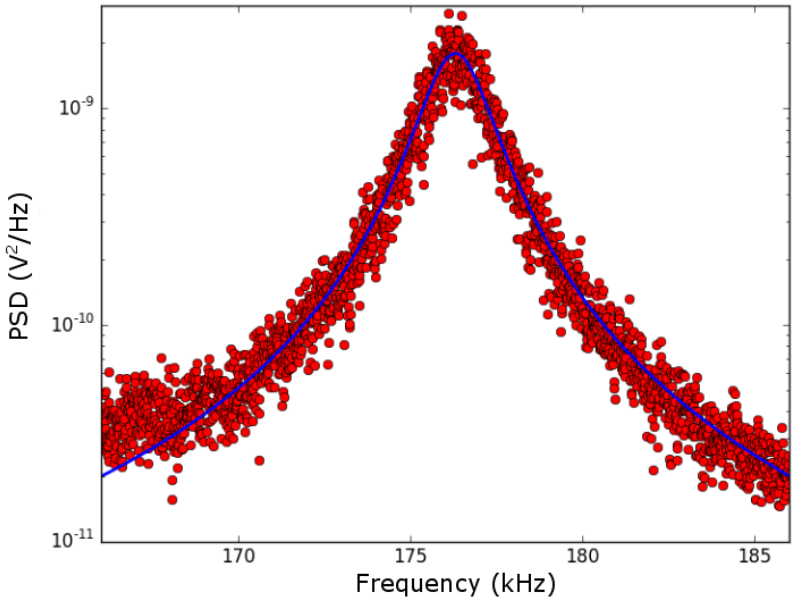

FIGURE 4.2: **Fit to PSD of particle motion.** Equation 4.15 is fitted to the x frequency peak for a particle trapped at 1 mbar with 700 mW laser power trapped with a parabolic mirror with an NA of 0.995. From this fit it is possible to evaluate the following parameters for the particle; $m = 1.4 \times 10^{-18}$ kg, radius $r = 50 \pm 1$ nm and $\Gamma_0/2\pi = 270 \pm 10$ Hz.

4.3 Reducing pressure - Emergence of particle motion

At atmospheric pressure, the particle motion within the trap is heavily damped such that any coherent oscillatory behaviour is suppressed by 1/f noise, due to a frequent collisions with gas particles. As the pressure is reduced in the vacuum chamber, the rate of collisions with particles is decreased and thus so is the damping (see equation 4.12). This results in the particle motion becoming less perturbed by gas collisions and the sinusoidal motion of the particle becomes more prominent. This can be seen by examining the PSD's for a particle at different pressures. In figure 4.3 a 75 ± 3nm diameter particle's motion in the z axis is shown. As the pressure is reduced the particle motion resembles the oscillatory motion expected from a damped harmonic oscillator and can be seen in figure 4.1.

Looking at a wider frequency range, we begin to see the emergence of cross terms between the transverse and axial degree of freedom (see figure 4.4), in addition to the expected frequency peaks from the motion in the z, x and y spatial degrees of freedom. These cross terms arise due to the nature of the experimental detection scheme described in section 3.5.2.

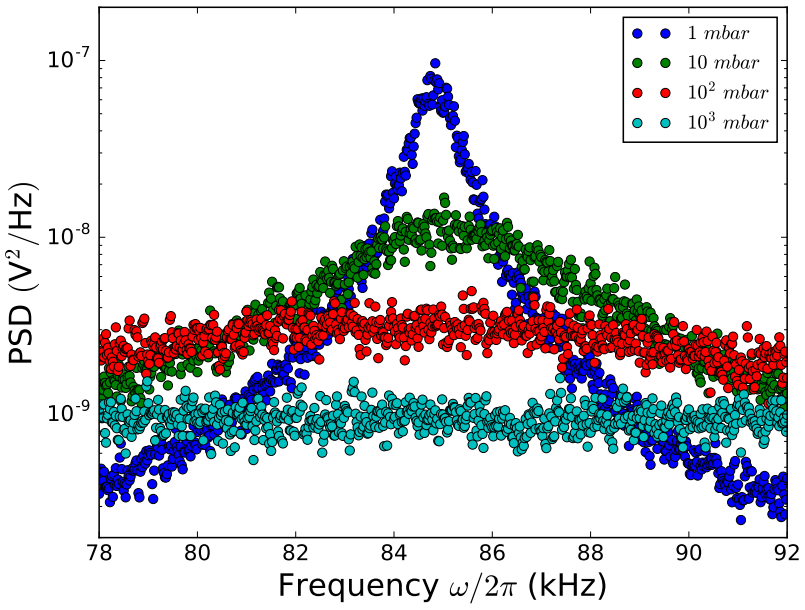

FIGURE 4.3: **The viscous damping experienced by a trapped particle at different pressures.** The data shown is for a 75 ± 3 nm particle trapped with 0.7 W, in a parabolic mirror trap with NA=0.995.

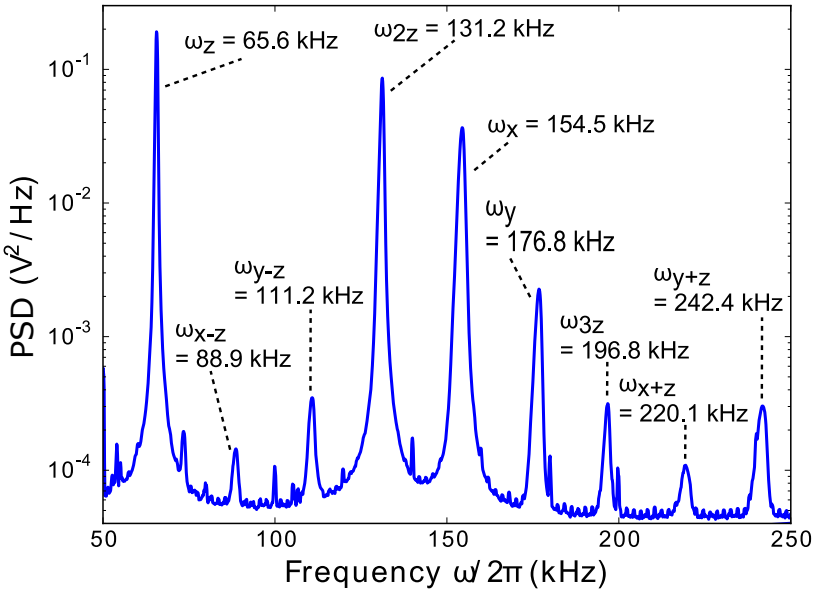

FIGURE 4.4: **Observed experimental frequency peaks as the pressure is reduced bellow 1 mbar.** This results in sum/difference cross terms emerging in the measured signal. The data shown here is for a 72 ± 4 nm diameter particle trapped in a parabolic mirror with NA = 0.9, with 700 W laser power and at 1×10^{-1} mbar.

4.4 Controlling the particle's trap frequency

As highlighted in section 4.3, as we reduce the pressure, several peaks emerge corresponding to a modulation of the laser light by particle motion. These peaks can be identified and controlled, based on their dependency on the proprieties of the laser focus in which the particle is trapped. For the motional degrees of freedom, the frequency peaks corresponding to particle motion are constant with pressure and vary proportionally to $\sqrt{P}$, as shown in figure 4.5 and in equations 2.29, 2.30 and 2.31. Therefore, the trap frequency can be controlled by varying the laser power and hence the optical spring constant, to achieve a ω_0 in the range 10 kHz to 300 kHz.

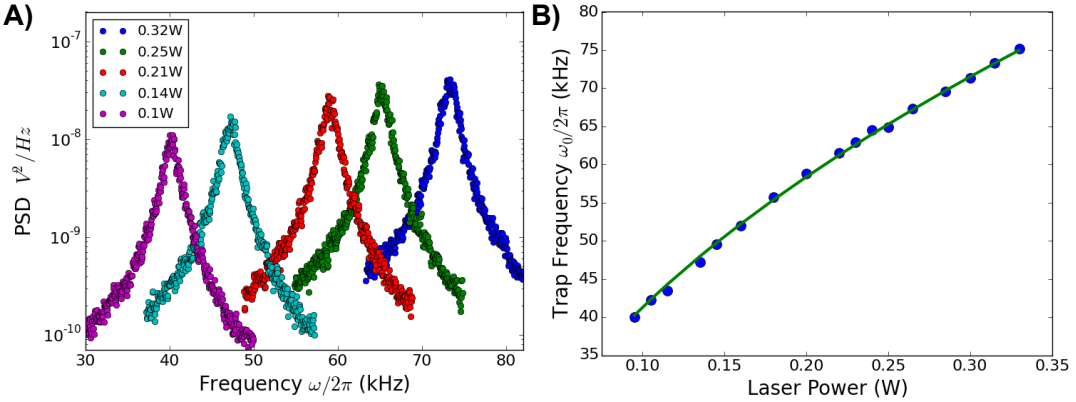

FIGURE 4.5: **Controlling the trap frequency by use of laser power. A) Z frequency peak at different laser powers.** As the intensity is decreased in the trapping region, the trapping potential becomes shallower, resulting in a reduction in the trap frequency. **B) The z trap frequency with different trapping laser powers.** These measurements where taken with a 100 ± 1 nm particle at 1 mbar, while the laser output power was varied.

The optical focus is elongated in the direction of the propagating beam, in comparison to the transverse axis. This results in the z frequency peak having a lower trap frequency than the x and y dimension. In addition to this, the system is more sensitive to the z motional dimension, resulting in a greater amplitude of the peak comparatively to the x and y frequency peaks[2]. The final identifying feature of the z motional peak is that as the polarization of the trapping light is changed, via a quarter wave plate between elliptical and circular the z peak remains constant in frequency. In contrast changing the quarter wave plate alters the trapping potential in the transverse axis, allowing for control of the transverse frequency peaks. As the wave plate angle is changed, the x and y frequency peaks can be brought together, or separated as shown in figure 4.6. From the discussion in section 2.3.5, we would expect the ratio of the axial and transverse frequency peaks

[2]The greater sensitivity is a result of the particle oscillating with a larger amplitude than in the x and y degrees of freedom. This larger oscillation amplitude is due to the lower trap stiffness in this dimension.

to be 2.22. However, this is not what we observe (when the axial frequency are of the same frequency), instead we observe a ratio of 2.5. This suggests that the minimum beam waist is actually $W_0 = 872$ nm.

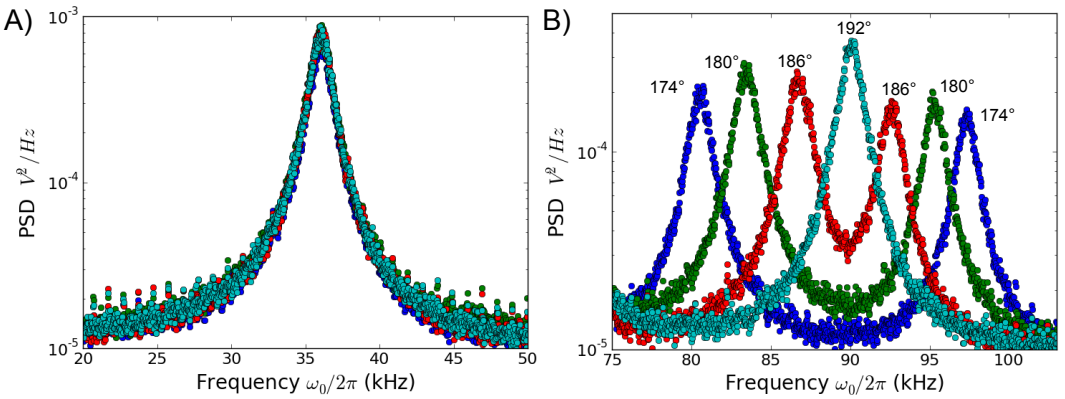

FIGURE 4.6: **Separating the x and y frequency peaks** of a 100 ± 2 nm particle at 1 mbar. Changing the quarter wave plate results in a change in the polarisation of the laser light used to form the optical trap in question. **A) Z frequency peak for different quarter wave plate orientations.** It can be seen that the z peak is unaffected and remains at the same trap frequency. **B) The X and Y peaks for different quarter wave plate angles.** By changing the quarter wave plate the x and y peak can be separated. The numbers on top of each peak represent the associated angle of the wave plate.

Finally, it should be noted that the frequency of oscillation for the spatial degrees of freedom of the nanoparticle motion are constant in pressure. Recently it has been shown that the rotational and torsional peaks of non-spherical nanoparticles can be observed in optical traps [90, 93, 127]. Frequency peaks arising from rotational motion[3] [93, 131] depend on the pressure, allowing them to be separated from the motional degrees of freedom. Torsional peaks[4] are constant in pressure, but depend on the polarisation of the light in the optical trap, allowing them to be identified [90].

4.5 Extraction of parameters from wavelength scan

As described in section 3.5.2 the optically trapped nanoparticle modulates the trapping laser field, as the back-scattered laser light from the particle accrues a position-dependent phase shift. For simplicity, to model the particle movement, we will omit the stochastically driven nature of the particle and therefore model the particle motion in the trap as $z(t) = z_0 \sin(\omega t)$, where z_0 is the amplitude of the motion of the particle in the z direction.

[3] Rotational peaks arise when a trapped particle is rotating in the optical trap.
[4] Torsional peaks would arise due to a twisting of a trapped particle due to an applied torque.

The oscillating trapped particle Rayleigh scatters the trapping light in all directions, according to a dipole emission pattern. Roughly half of which is then collected and collimated by the paraboloidal mirror, in the opposite direction to the trapping laser. The interference of both the scattering field and the reference field forms a homodyne detection scheme. Where the intensity modulation of the detected light at the fundamental frequency of the particle's motion can be written as [3] [5],

$$I_1(t) \approx 2E_{div}E_{scat}J_1(\beta)\sin(\theta)\sin(\omega_0 t). \tag{4.18}$$

where $\mathrm{J_n}(\beta)$ is a Bessel function, with n=(0,1,2...) and $\theta = 2fk + \pi$, where $k = 2\pi/\lambda$ and is the wavenumber. The intensity modulation of the detected light at the second harmonic frequency of the particle's motion can be written as,

$$I_2(t) \approx 2E_{div}E_{scat}J_2(\beta)\cos(\theta)\sin(2\omega_0 t) \tag{4.19}$$

It can be seen that $J_1(\beta)$ and $J_2(\beta)$ are proportional to the amplitude of first and second trap frequencies of the particle in question. The ratio of these two amplitudes allows for z_0 to be extracted. Expanding the Bessel functions to first order we have

$$\begin{aligned}\frac{J_2(\beta)}{J_1(\beta)} &= \frac{\beta^2/8}{\beta/2}, \\ &= \frac{1}{4}\beta.\end{aligned} \tag{4.20}$$

from reference [3] we know

$$\beta = kz_0 - \frac{z_0}{z_R}. \tag{4.21}$$

Substituting this into 4.22 and rearranging for z_0 we find

[5] The theory for extracting parameters of an optically levitated nanoparticle from a wavelength scan was developed by James Bateman and can be found in full in reference [3], I then verified this theory experimentally. Only the key information about the theory required to understand how to perform this technique, along with my experimental results of applying this technique, is reported here

$$z_0 = \frac{4J_2(\beta)/J_1(\beta)}{k - 1/z_R}.. \tag{4.22}$$

The amplitudes of the first order and second order peaks can be obtained experimentally. Using the dependence of these amplitudes on the wavenumber k, we can change the wavelength to make the amplitude of one harmonic more prominent than the other. As we know z_0 in terms of volts through the detected signal, γ, the conversion factor from equation 4.15 can be obtained. This means it is therefore possible to obtain mass m and radius r of the particle, without any knowledge of the pressure P_{gas} and damping factor Γ_0. Therefore, this method transcends any assumption about the theoretical kinetic model being used.

The parabolic mirror used has a focal distance of $f = 3.1$ mm. By varying the trapping laser wavelength by 0.25 nm in steps of 5 pm, we are able to vary the phase θ by 1.5π, in steps of 0.03π. The resulting change in amplitude vs wavelength can be seen in figure 4.7, while in figure 4.8 we show an example of the particle PSD's at two different wavelengths.

Comparing the change in amplitude of the first and second order z motion peaks in figure 4.7 and using 4.22, it is possible to extract the maximum position of particle motion in the z direction, $z_0 = 119 \pm 10$ nm. From equipartition theorem: $m = k_b T_{cm}/\omega_0^2 z_0^2$, with $T_{cm} = 300$ K, we can obtain a pressure independent measure of the particles mass m$= 3 \pm 0.5 \times 10^{-19}$ kg. Assuming a spherical particle with density $\rho = 2650$ Kgm^{-3}, the particle has a radius r$= 30 \pm 2$ nm. Finally using $\gamma = V/z_0$ where V is the voltage detected on our photodiode, and equation 4.17 the position resolution can be calculated to be $S_{x,exp} = 200 \pm 20$ fm$/\sqrt{\text{Hz}}$.

The wavelength scan method to evaluate the position resolution presented here is more accurate than the method used in section 4.2. The lower accuracy in fitting to the power spectral density is due to the larger error on the pressure measurement, in the experimental system. By circumventing pressure readings and exclusivity using the measurements of the optical intensity measured by our detector, it is possible to make a more accurate measurement. In principle, this method can be used to measure any particles oscillation amplitude or mass, without knowing its density.

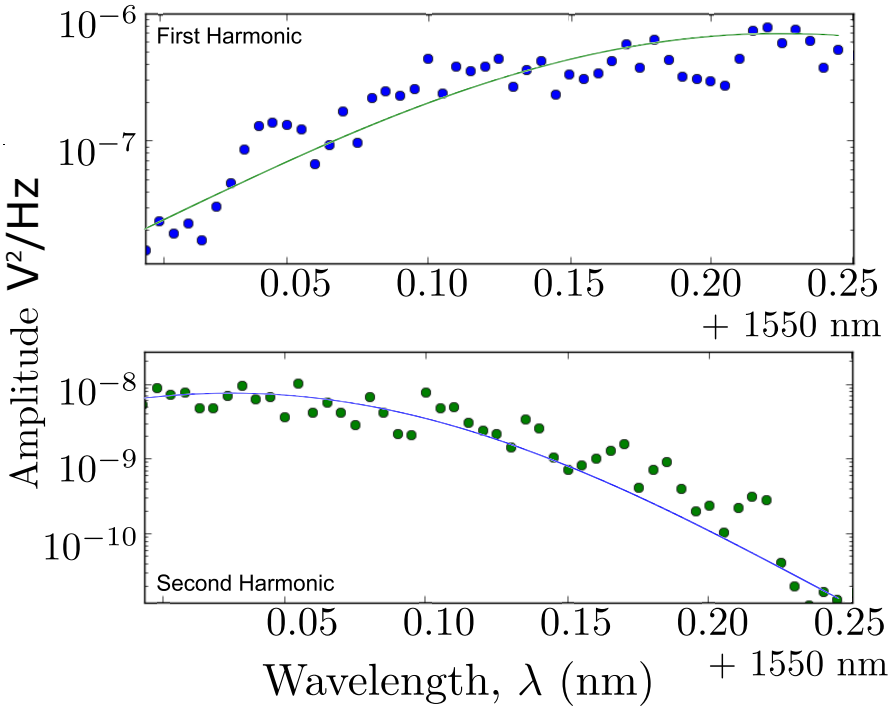

FIGURE 4.7: **Wavelength scan to measure relative amplitude change in the first and second harmonic of the trap frequency for the z-peak.** For a 60 nm diameter silica particle, trapped with 385 mW laser power at 1×10^{-2} mbar, we can observe how the amplitude of the first order peak (top panel, fitted with $2E_{div}E_{scat}\sin(\alpha)2J_1(\beta)\sin(\omega_0 t)$) and second order peak (lower panel, fitted with $2E_{div}E_{scat}\cos(\alpha)2J_2(\beta)\sin(2\omega_0 t)$), changes as the wavelength of the laser if varied to extract a parameter independent position resolution. By varying the trapping laser wavelength by 0.25 nm in steps of 5 pm, we are able to vary the phase θ by 1.5π in steps of 0.03π.

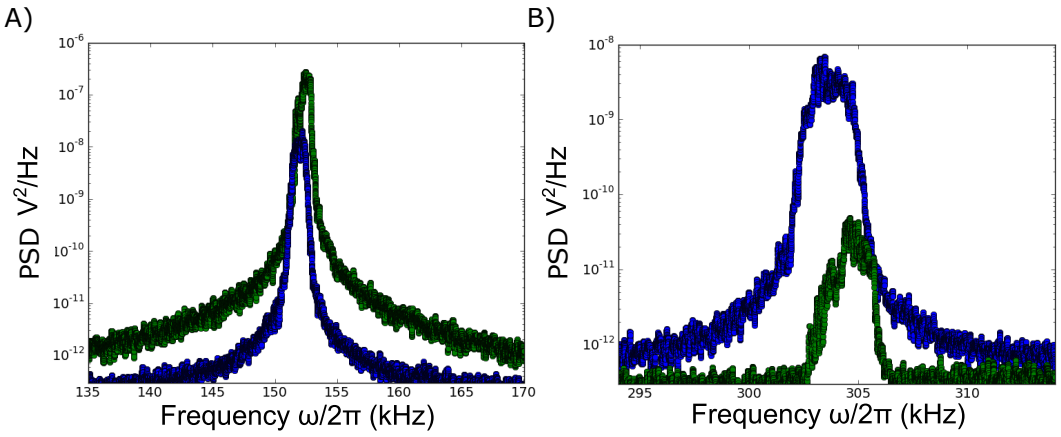

FIGURE 4.8: **PSD's of the particle motion at different wavelengths.** The green data shows the PSD of the particles motion at 1550.225 nm and the blue at 1550 nm. A) The first harmonic. B) The second harmonic.

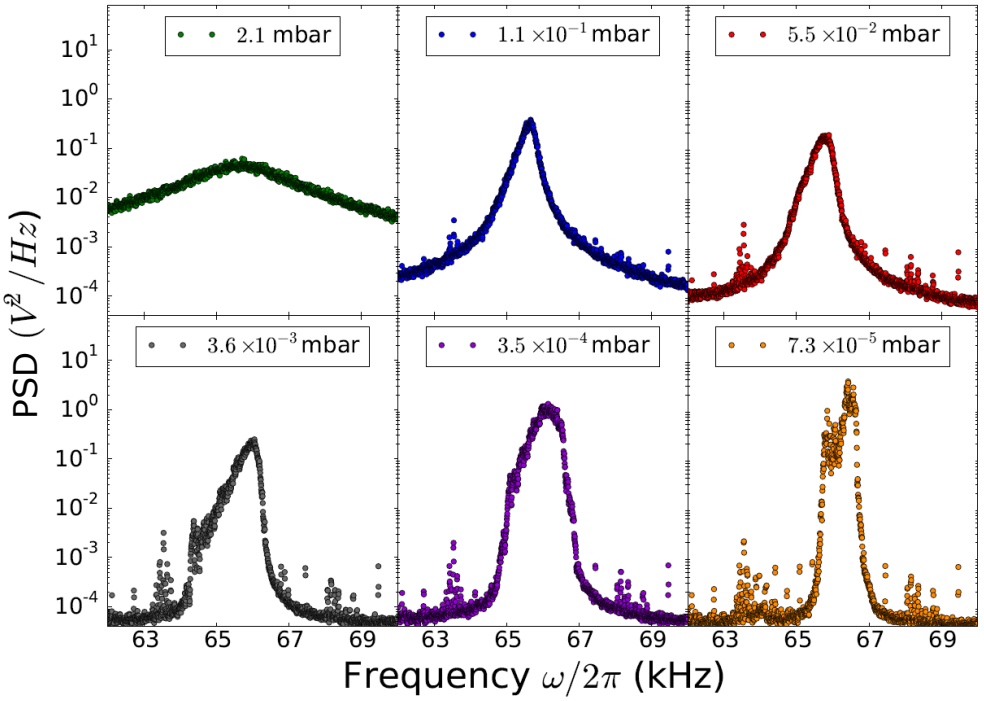

FIGURE 4.9: **PSD of a 100 nm diameter particle at different pressure without feedback.** Particles could be trapped for some hours without significant changes to the PSD. For pressure below roughly 5×10^{-6} mbar the particle was lost from the trap.

4.6 Nonlinear behaviour at low pressures

As shown in figure 4.3, as the pressure is reduced and damping from air collisions become less frequent, the particle motion becomes more pronounced in the PSD of particle motion. The resulting change in the shape of the PSD of particle motion, as pressures are reduced bellow 1×10^{-1} mbar, can be seen in figure 4.9. As the pressure approaches $\approx 1 \times 10^{-1}$ mbar, the error in fitting equation 4.15 starts to increase, because equation 5.13 no longer represents a good description of the underling physics. For the purposes of this thesis, nonlinear effects are not discussed in depth, as parametric feedback cooling (outlined in chapter 6) is used to suppress any nonlinear effects [13]. To prevent our measurements from being subject to nonlinear effects, the mass of a particle is calculated using the particles motion at ≈ 1 mbar. There exist several studies discussing nonlinear effects in optically levitated traps [24, 62] that the author would like to point an interested reader towards.

4.7 Conclusion

Several properties of the levitated particles are measured, including the mass, radius, oscillation amplitude (via the use of a volts-to-meter conversion factor) and the damping experienced at a given pressure. This is done via two methods. The first method required fitting a single Lorentzian to a PSD of the motion of the particle, derived using the kinetic theory of gases, to determine the radius of the particle along with other previously mentioned parameters. The second method demonstrated, utilized a scan of the trapping laser wavelength, to change the amplitudes of the first and second harmonics of nanoparticle motion and determine a nanoparticle size from the ratio of the scan amplitudes. This method is able to determine the mass of the particle, without assumptions of the kinetic model and material density. This method holds great promise for measuring the mass of particles, without knowledge of the underling kinetic model or particle shape [112, 131, 132]. Using the methods outlined in this chapter for measuring nanoparticle size, particles of diameters ranging from 18 nm to 312 nm have been measured within the optical trap, falling within the size range specified for each particle solution by the manufacture.

The ability to control the trap frequencies of all three motional degrees of freedom via the power of the trapping laser is demonstrated. Separation of the transverse frequencies and independent control of the transverse trapping frequencies from the z axis is also demonstrated via the use of elliptically polarized light. The effect of changing the pressure within the chamber on a levitated nanopartile is also explored.

To the contrary of many reports, trapping of nanoparticles down to 10^{-5} mbar, without any active feedback, was achieved. The theoretical model was tested as the pressure was decreased and found that below pressures of roughly 1 mbar, fitting equation 4.15 resulted in increasing amounts of error with further decrease of pressure. This is attributed to the emergence of nonlinearities in the particles motion which result as the pressure in the chamber is reduced. The different frequency components found in the PSD of the signal are shown and their origins explained.

The control of the of the trap frequencies and characterization methods described in this chapter will be used throughout the rest of this thesis to determine properties of the levitated particles, used in each of the experiments.

Chapter 5

Nanoscale temperature measurements using blackbody-like radiation from a levitated nanoparticle

Nanoscale temperature measurements involve the determination of temperature at the sub-micron scale. Previously established temperature measurement techniques such as the use of thermocouples [133], liquid-in-glass thermometry [134], Raman spectroscopy [135–137], fluorescence [138] and optical interferometry [139] have also proved useful in measuring temperature at nanoscale. Using such methods has applications in many fields: temperature mapping in microcircuits [140, 141], measuring emission properties of silica particles [142], measurement of intracellular temperature fluctuations [143, 144], and thermometry in microfluidic devices [145, 146]. Being able to make similar nanoscale temperature measurements on optically levitated nanoparticles promises to be an interesting tool for exploring the melting point size dependence of nanoparticles within optical traps [147]. It will also allow for interesting insights into the possible phase transitions of nanoparticles. The characterisation of heating rates of optically trapped nanoparticles, as well as their equilibrium temperatures calculated from their blackbody emission, will be crucial in influencing the design of nanoparticle matter-wave interferometers [44, 148–150]. Methods of measuring temperature can be classified into categories according to various factors. These factors include the level of physical contact between the measurement device and the medium of interest, as well as whether they are calibration dependent or independent. When characterising thermometric devices in terms of the degree of physical contact between the measurement device and the medium of

interest, the categories of classification are invasive, semi-invasive and non-invasive. Invasive sensors require physical thermal contact with the medium of interest in order to make a measurement. Semi-invasive sensors are technically invasive sensors, whose measurements can be interpreted at a distance non-invasively. Non-invasive temperature measurement sensors make no physical thermal contact with the medium of interest during a measurement. Examples of each include thermocouples [133], thermochromic liquid crystals applied to a surface and observed remotely [151], and infrared pyrometry [134] respectively. In the case of levitated nanospheres, non-invasive methods must be used. When classifying thermometric systems according to the physical process underlying the measurement there are two categories: primary and secondary. Cases where the measurement is characterised by well-established equations of state, which directly relate the measured parameter to temperature, are known as primary, whereas cases in which the system requires calibration are referred to as secondary. Some calibration methods take advantage of identifiable transitions at a specific temperature, an example being phase change. These transitions can be useful for determining a particular temperature accurately, or in identifying whether a temperature has been exceeded.

To date, the only demonstrated method of measuring the internal temperature of a levitated particle is that presented by Millen et al. [2] who, by analyzing the gas surrounding a nanosphere, alongside the sphere's Brownian motion, were able to determine the surface temperature in two spatial dimensions of a levitated sphere. A potential way of improving on this method is presented in this chapter, inspired by infrared thermometers. Infrared thermometers have been used to measure a number of nanoscale objects thus far, including the average temperature of many nanoparticles on substrates [152] and the temperature of molecular ions in ion traps [153]. Infrared thermometers measure the thermal radiation emitted by a body due to its temperature. A body emits energy in the form of thermal radiation, with the quantity of radiation rising with increasing temperature [154]. The energy emitted throughout the electromagnetic spectrum due to the temperature of a blackbody can be modelled by Planck's law [154]. Infrared thermometers are classified depending on whether the device is sensitive to all or a specific band of wavelengths. Those that are sensitive to all wavelengths are classed as total radiation, or broadband thermometers. Devices sensitive to radiation in a specific band of wavelengths are classed as spectral band thermometers. The spectrometer used in the measurements presented in this chapter has a finite wavelength range, and thus only a certain range of temperatures will be measurable. This is due to the reduced photon emission at certain wavelengths, which is dependent on the temperature of the blackbody. For this reason, this method can be considered to be a form of spectral band thermometry.

An infrared temperature measurement system generally consists of three elements: the emitting source of interest, the propagation medium, and the measuring device [139]. In our case an optically levitated nanoparticle will be the source of interest, the propagation medium will be air, and the measurement device will be a spectrometer. Using this setup, a non-invasive secondary temperature measurement of the levitated particle was performed. The temperature was measured by fitting the Planck equation to the thermal spectrum emitted from the levitated particle. The following section will explore the effect both the intensity of the laser light, and the pressure in the vacuum chamber, have on the temperature of the levitated particle.

5.1 Blackbody radiation

Blackbody radiation is the thermal electromagnetic radiation emitted by a blackbody. It has a specific spectrum and intensity that depends only on the body's temperature. For the purposes of the analysis presented in this chapter, it will be assumed that there are no additional effects, beyond that of emissivity, effecting the spectra of the blackbody radiation emitted by trapped particles. A more complete derivation of the expected blackbody-like spectra from an optically trapped nanoparticle is beyond the scope of this thesis, however the theory presented here is sufficient to allow for preliminary investigations to take place. Blackbody spectra display a characteristic peak at a certain frequency. This shifts to higher frequencies with increasing temperature, and at room temperature most of the emission is in the infrared region of the electromagnetic spectrum. The thermal radiation spontaneously emitted by physical objects can be approximated as blackbody radiation. The spectrum of blackbody emission is described by Planck's law, which is normally expressed as a spectral energy density given by [154],

$$U_E(\nu) = \frac{8\pi h\nu^3}{c^3}\frac{1}{e^{hc/\lambda k_b T_{BB}} - 1} \tag{5.1}$$

where ν is frequency, h is Plank's constant, c is the speed of light in vacuum, k_b is the Boltzmann constant and T_{BB} is the temperature of the object emitting blackbody radiation. Therefore U_E has units of J/(m^3 Hz), or energy, per unit volume, per unit frequency interval. We can rewrite the spectral energy density as a function of wavelength. The energy contained in a unit frequency $d\nu$ interval must be equal to the energy in the corresponding wavelength interval $d\lambda$.

$$U_E(\nu)|d\nu| = U_E(\lambda)|d\lambda| \tag{5.2}$$

noting $\nu = c/\lambda$ gives $d\nu/d\lambda = -(c/\lambda^2)$, allowing equation 5.1 to be given as,

$$U_E(\lambda) = U_E(\nu)\left|\frac{d\nu}{d\lambda}\right| = \frac{8\pi hc}{\lambda^5}\frac{1}{e^{hc/\lambda k_b T_{BB}} - 1} \tag{5.3}$$

with units of J/(m^3 m), or energy, per unit volume, per unit wavelength. The scalar irradiance E_0 is the number of photons emitted per unit time or, in other words, the number of photons emitted multiplied by how fast the photons are moving $E_0(\lambda) = U_E(\lambda)c$. As radiation in thermodynamic equilibrium is isotropic and unpolarized $E_0(\lambda) = 4E_d(\lambda)$, where $E_d(\lambda)$ is the plane irradiance. Therefore,

$$E_d(\lambda) = \frac{E_0(\lambda)}{4} = \frac{c}{4}U_E(\lambda) = \frac{2\pi hc^2}{\lambda^5}\frac{1}{e^{hc/\lambda k_b T_{BB}} - 1} \tag{5.4}$$

The photon density can be obtained by dividing equation 5.4 by the energy per photon hc/λ,

$$Q_d(\lambda) = \frac{2\pi c}{\lambda^4}\frac{1}{e^{hc/\lambda k_b T_{BB}} - 1} \tag{5.5}$$

where Q_d has units of photons/(s m^3), or total number of photons emitted, per second, per unit area, per unit wavelength. Figure 5.1 illustrates equation 5.5 for an object at differing temperatures.

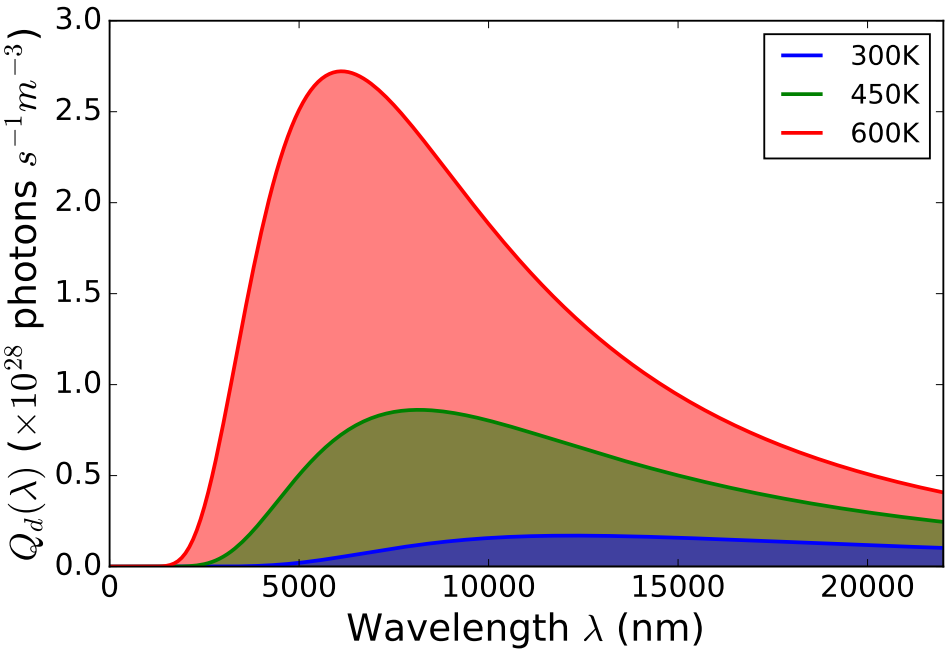

FIGURE 5.1: **Blackbody spectra for an object at different temperatures.**

5.1.1 Total photon density of a blackbody spectrum at different temperatures

As a nanoparticle is much smaller than the surrounding objects, such as the vacuum chamber, the number of blackbody photons emitted will be much smaller (assuming roughly equal temperatures). However, as shown in figure 5.1, the number of photons emitted depends on the temperature of the blackbody in question. It is possible by integrating equation 5.5 over all wavelengths to find the total number of photons emitted by a blackbody, per second, per unit area,

$$Q_d = \sigma_d T_{BB}^3 \tag{5.6}$$

where $\sigma_d = (4.808\pi k^3)/(h^3c^2) = 2.520 \times 10^{15}$ photons s^{-1} m^{-2} K^{-3} and is the photon equivalent of the Stefan-Boltzman constant. The number of photons emitted at different temperatures can be seen in figure 5.2. It can be seen that as the temperature of the particle increases, the number of photons emitted will increase. This will therefore result in an increased number of photons emitted from an optically trapped nanoparticle, in comparison to the background thermal spectrum, resulting in an increased signal to noise ratio.

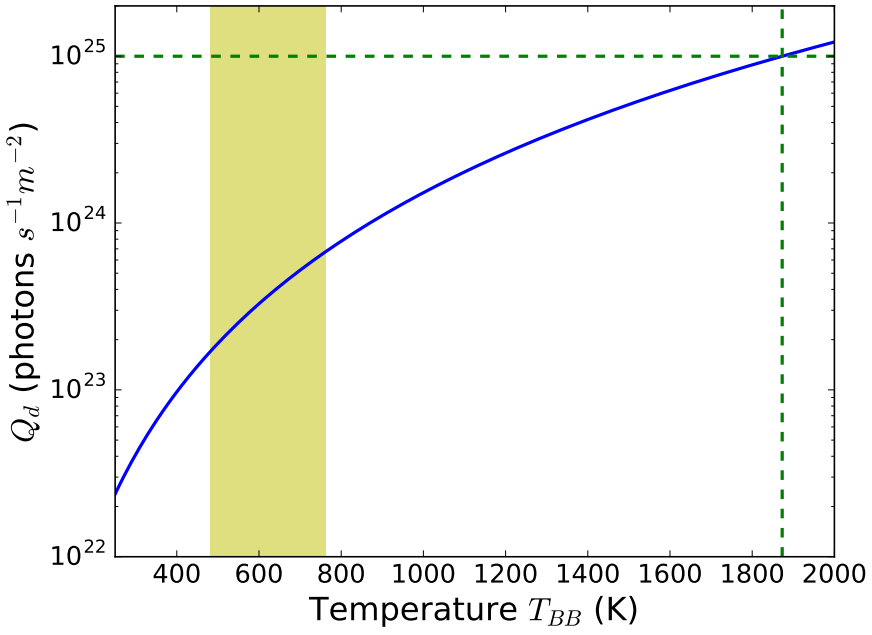

FIGURE 5.2: **Total photon density of a blackbody spectra at different temperatures** (Blue line). The dashed green line shows Q_d at the melting point of silica $T_{melt} = 1873$ K. [2] The shaded yellow area shows the temperature range 486-763 K in which the spectral peak would be visible in spectra measured in these experiments (see figure 5.7).

5.1.2 Blackbody spectrum peak dependence on temperature

As will be discussed in section 5.4, to determine an optically levitated nanoparticles temperature, equation 5.19 will be fitted to the experimentally measured blackbody spectrum. When fitting equations to experimental data, error is greatly reduced when the distinctive features such as a turning point are included in the fit. To work out what temperature range the experimental setup is most sensitive to, it is possible to deduce the wavelength at which most photons will be emitted at a given temperature. This can be calculated by differentiating equation 5.5 with respect to λ and setting it equal to zero, giving

$$\frac{\partial Q_d(\lambda)}{\partial \lambda} = 2\pi c\left(\frac{hc}{k_b T_{BB}\lambda^6}\frac{e^{hc/\lambda k_b T_{BB}}}{(e^{hc/\lambda k_b T_{BB}}-1)^2} - \frac{1}{\lambda^5}\frac{4}{e^{hc/\lambda k_b T_{BB}}-1}\right) = 0. \tag{5.7}$$

Which, when simplified, gives

$$\frac{hc}{k_b T_{BB}\lambda}\frac{e^{hc/\lambda k_b T_{BB}}}{(e^{hc/\lambda k_b T_{BB}}-1)} - 4 = 0 \tag{5.8}$$

defining $x \equiv hc/\lambda k_b T_{BB}$ we can write the equation as

$$\frac{xe^x}{(e^x-1)} - 4 = 0, \tag{5.9}$$

which has a numerical solution $x = 3.92069$. Thus, solving for wavelength in units of nanometers, we find

$$\lambda_{max} = \frac{hc}{xk_b T_{BB}} = \frac{2.28822 \times 10^6 nm.K}{T_{BB}}. \tag{5.10}$$

The wavelength at which the blackbody spectrum peaks, at different temperatures, can be seen in figure 5.3. The shaded yellow area shows the temperature range 486-763 K, in which the blackbody spectral peak would be visible in spectra measured in these experiments.

5.1.3 Experimentally measurable blackbody spectrum

The simple theory presented so far has failed to take several experimental factors into account. For a given wavelength, it is possible to write an expression for the number of photons which can be detected ($N(\lambda)$) from a real world object emitting blackbody

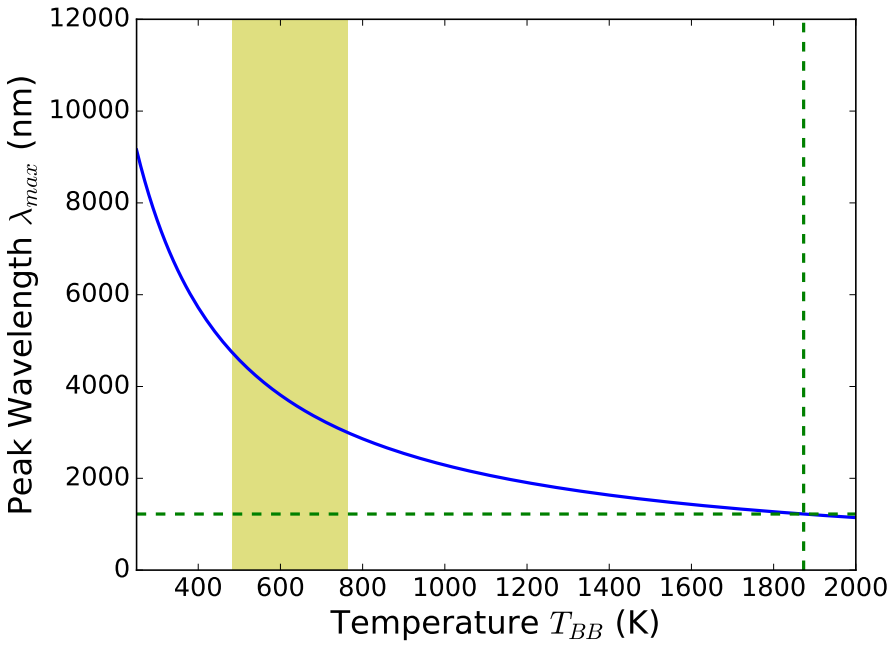

FIGURE 5.3: **The wavelength at which the blackbody spectrum peaks as a function of temperature** (Blue line). The dashed green line shows the wavelength $\lambda_{melt} = 1222$ nm at which the spectral peak occurs for a blackbody at the melting point of silica $T_{melt} = 1873$ K. The shaded yellow area shows the temperature range 486-763 K in which the spectral peak would be visible in spectra measured in these experiments.

radiation. Real objects only emit a fraction of the radiation which would be emitted by an ideal blackbody emitter. The emissivity of real objects accounts for this and is defined as the ratio of the radiant power from the real object, over the radiant power of a perfect blackbody, at the same temperature and wavelength, observed under the same experimental conditions.

$$\epsilon(\lambda) = \frac{Q_{dObject}(\lambda)}{Q_{dBlackbody}(\lambda)} \tag{5.11}$$

Multiplying equation 5.5, by the detectable area of the blackbody in question A_{det}, a factor taking into account the absorption of emitted light by the optics in the experimental setup $\mu(\lambda)$, and finally the emissivity $\epsilon(\lambda)$ of the material it can be shown that,

$$N(\lambda) = A_{det}\mu(\lambda)\epsilon(\lambda)\frac{2\pi c}{\lambda^4}\frac{1}{e^{hc/\lambda k_b T} - 1} \tag{5.12}$$

For the purposes of the analysis in this chapter it is assumed $\mu(\lambda)$ and $\epsilon(\lambda)$ are constant with wavelength. This assumption is justified by noting that $\epsilon(\lambda)$, in the wavelength range measured, varies by less than 0.03 for silica [155] and by less than 0.02 for

aluminium [156]. We also assume $\mu(\lambda)$ of the optical elements is constant across the wavelength range considered, a justification of this assumption will be given in section 5.3.

5.2 Temperature of a levitated particle

In a steady state, T_{BB} is determined by the balance between heating due to laser absorption and cooling due to collisions with the gas, as well as the emission of blackbody radiation. The experiments presented in this chapter occur in the underdamped (Knudsen) regime, where an optically trapped, and therefore heated nanoparticle[1] will have a nonequilibrium gas surrounding it. To understand how a particle will behave under these experimental conditions, the theory derived in reference [2] is used and presented here. We will use the term T_{int}, to define the temperature of the levitated particle as a way to distinguish temperatures calculated by the method presented in reference [2]. However it should be noted that T_{int} should be equal to T_{BB}, providing the assumptions made in the derivation of this theory hold true.

In the case where the temperature of a spherical nanoparticle is higher than its surrounding gas, heat is transferred to the colliding gas particles. The impinging gas particles with a temperature T^{imp} do not equilibriate to the same temperature as the nanoparticle at temperature T_{int} [2]. Instead, they emerge with a different energy, but can be assumed to be thermally distributed for highly inelastic collisions [157] with a different temperature. In this situation, the nanoparticles centre of mass motion adopts a non-equilibrium, steady state, that mediates heat transfer between the two non-interacting thermal baths (the impinging gas and the emerging gas). Under theses conditions the equation for the power spectrum of the nanoparticle's fluctuating position is [2]

$$P(\omega) = \frac{2k_B T_0}{\pi m} \frac{\Gamma_0}{(\omega_0^2 - \omega^2)^2 + \omega^2 \Gamma_0}, \tag{5.13}$$

where the effective damping rate $\Gamma_0 := \Gamma^{imp} + \Gamma^{em}$ and T_0 is an effective centre of mass temperature,

$$T_0 := \frac{T^{imp}\Gamma^{imp} + T^{em}\Gamma^{em}}{\Gamma_0}, \tag{5.14}$$

where the T^{em} is the temperature of the emerging gas particles and T^{im} is the temperature of impinging gas particles. In the experiments considered here the gas particles

[1] Where heating of the nanoparticle is the result of the absorption of light, from the trapping laser.

impinge at room temperature, $T^{im} = 294$ K. Γ^{em} is the damping rate of the sphere due to the emerging gas. It is given by

$$\Gamma^{em} = \frac{\pi}{8}\sqrt{\frac{T^{em}}{T^{imp}}}\Gamma^{imp}, \tag{5.15}$$

where Γ^{im} is the damping rate of the nanoparticle due to the impinging gas, and is given by

$$\Gamma^{imp} = \frac{4\pi}{3}\frac{m_{mol}Nr^2\bar{v}_{T^{imp}}}{m}, \tag{5.16}$$

where m_{mol} is the molecular mass and N is the number density of gas molecules $N = N_0 P_{gas}/P_{atmos}$ [123], where N_0 is the number of gas molecules per cubic meter at atmospheric conditions and P_{atmos} is atmospheric pressure. $\bar{v}_{T^{imp}}$ is the mean thermal velocity of the gas given by

$$\bar{v}_{T^{imp}} = \sqrt{\frac{8k_b T^{imp}}{\pi m_{gas}}}, \tag{5.17}$$

Using the equations outlined in this section, it is possible to calculate temperature of the nanoparticles' using [2],

$$T_{int} = T^{imp} + \frac{T^{em} - T^{imp}}{\alpha_{Silica}}, \tag{5.18}$$

where α_{Silica} is the accommodation coefficient for silica. The accommodation coefficient for silica is 0.777 for moderate surface temperatures is around 300 K [158].

5.3 Experimental Setup

The experimental setup is based upon the setup introduced in section 3, and shown in figure 3.1, however several additional components have been added to allow for the blackbody spectra from levitated particles to be measured. To allow for the blackbody photons to be separated from the E_{div} and E_{scat} fields, a half wave plate and a polarizing beam splitter is used which allows advantage to be taken of the randomly polarized nature of blackbody emission [159]. Once the blackbody spectrum is separated from the E_{div} and E_{scat} fields, a spectrometer (*ARCspectro FT-MIR*) is then used to collect the blackbody photons. The experimental setup can be seen in figure 5.4.

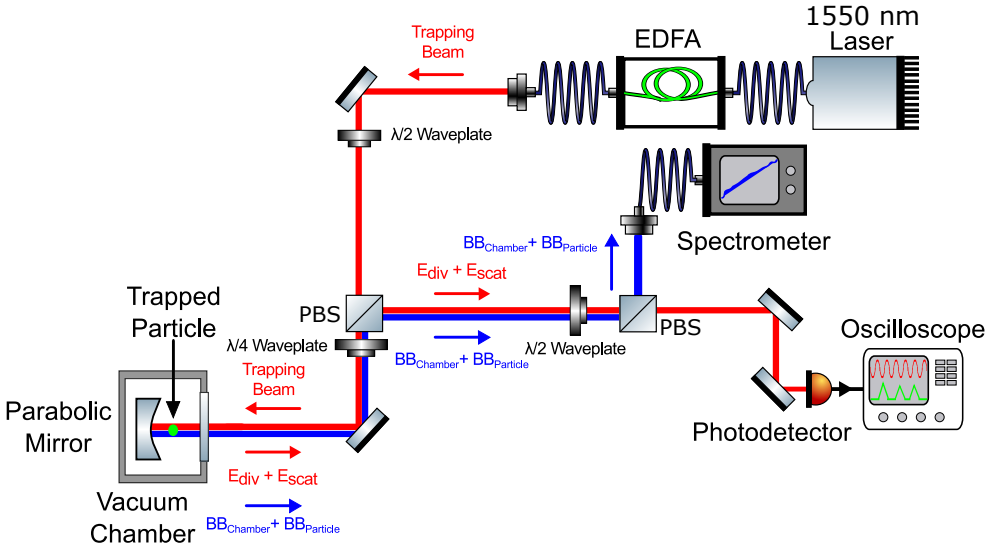

FIGURE 5.4: **Experimental set up used to measure blackbody-like radiation from levitated particles.** The blackbody emission emitted by the chamber $BB_{chamber}$ and the blackbody emission for the levitated particle $BB_{particle}$ are shown in blue. Due to its unpolarized nature, the emitted blackbody radiation is scattered, reflected and transmitted at each beam splitter. For the purposes of this diagram, only the blackbody radiation which will reach the spectrometer will be highlighted.

In the optical trap, a silica particle was optically levitated under different trapping laser powers and pressures, and the photon emission measured over the course of 6 hours under each condition. The PSD for the z motional peak can be seen in figure 5.5, from which it can be evaluated that the particle used in these experiments was 148 ± 2 nm in diameter.

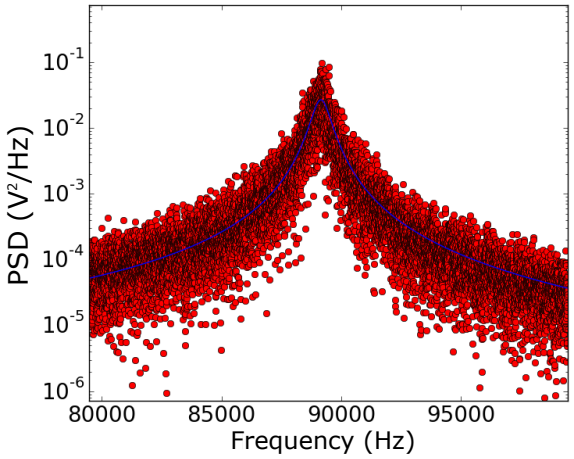

FIGURE 5.5: **PSD of the trapped particle motion in the z degree of freedom.** The blue line shows equation 4.15 fitted to the data. This is used to determine the particle's properties according to the method outlined in section 4.2. The diameter of the particle was 148 ± 2 nm. The data is shown for a pressure of 1.77 mbar.

The levitated particle is trapped at the focus of the parabolic mirror and therefore collects $\approx 50\%$ of the diverging blackbody-like emission from the particle. The collected

blackbody radiation is reflected as a collimated beam. In contrast, the blackbody-like emission from the parabolic mirror diverges, resulting in an increasingly weaker signal the greater the distance between the parabolic mirror and the spectrometer. The beam paths are illustrated in figure 5.6.

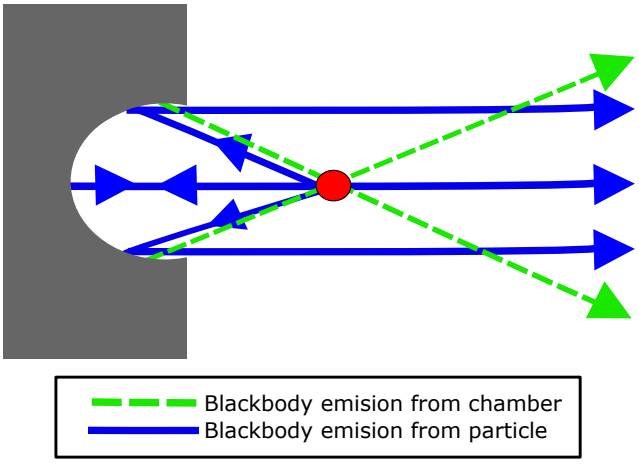

FIGURE 5.6: **The blackbody fields emitted at the trap sight.** The blackbody emission emitted by the mirror BB_{mirror} passes through the focus and diverges. The particle radiates blackbody emission $BB_{particle}$ in all directions. The blackbody emission from the particle is collected by the parabolic mirror, collimated and sent along the same optical path as E_{scatt}.

The collimated blackbody radiation then passes through the optics in the system, before arriving at the spectrometer. Despite the detection range of the spectrometer being between 2-6 μm, the wavelength dependent absorption of the optics reduces the wavelength range of the detected photons which can be reliably used. The transmission spectra can be seen in figure 5.7 and from this it can be seen that the transmission spectra varies significantly at certain wavelengths. For this reason, the flattest part of the transmission spectra, between 3-4.75 μm, is used and allows the assumption of a constant absorption, μ, to be used.

It should be noted that despite the experimental capabilities demonstrated in sections 4 and 6 to trap and hold a particle down to pressures on the order of 10^{-6} mbar, during the week in which the spectrometer was borrowed to perform these experiments, parts of the vacuum system were broken. This limited the lowest pressures that could be achieved in the chamber to the order of 10^{-2} mbar.

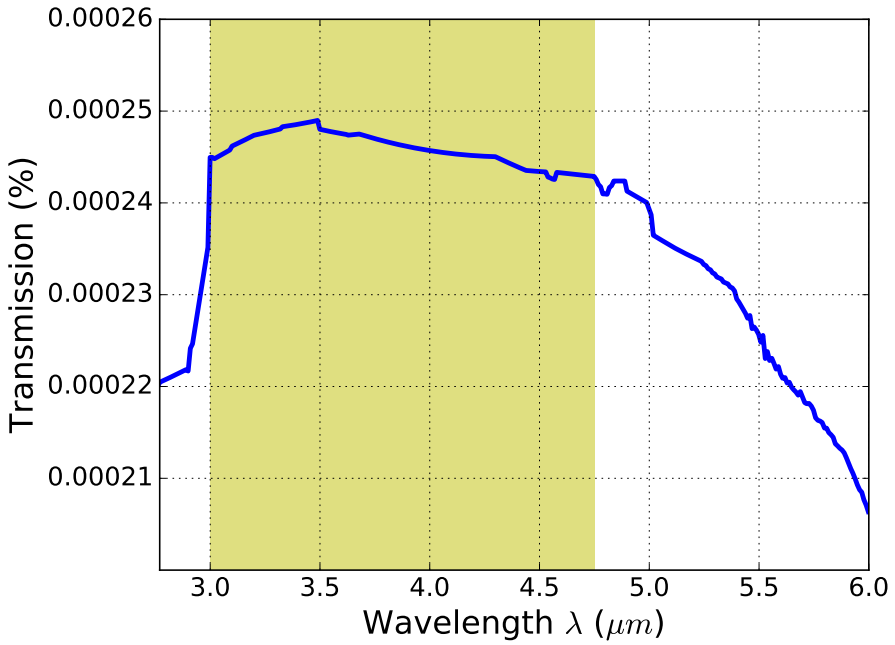

FIGURE 5.7: **The transmission spectra of the blackbody detection optics.** The wavelength range of the data collected, and used in the data analysis, is shown in yellow. The transmission varies by less than 0.00006% in this region, and is therefore assumed to be constant when fitting equation 5.12 to the experimental data.

5.4 Extraction of parameters from fit to measured spectra

Despite attempts to reduce the blackbody radiation from objects other than the nanoparticle reaching the detector, a significant percentage of the photons measured at the detector come from sources external to the levitated nanoparticle. To compensate for this, for each experimental parameter measured, a spectrum was taken both with a particle trapped and without a particle trapped; such spectra can be seen in figure 5.8.

Subtracting the spectrum without a particle, from the spectrum with a particle, gives the spectrum of emitted photons from the levitated nanoparticle, as shown in figure 5.9. To obtain the temperature of the levitated particle, we fit equation 5.12 to the nanoparticle's spectrum, with fit parameters A_{BB} and B_{BB}, giving an equation of the form

$$N(\lambda) = \frac{A_{BB}}{\lambda^4} \frac{1}{e^{B_{BB}\lambda} - 1}, \tag{5.19}$$

where $A_{BB} = A_{det}\mu\epsilon 2\pi c$ and $B_{BB} = hc/k_b T_{BB}$. Therefore, using the fit parameter B_{BB}, we can calculate the temperature of the the levitated particle. The method used to calculate the error in the values of T_{BB} can be found in appendix C.

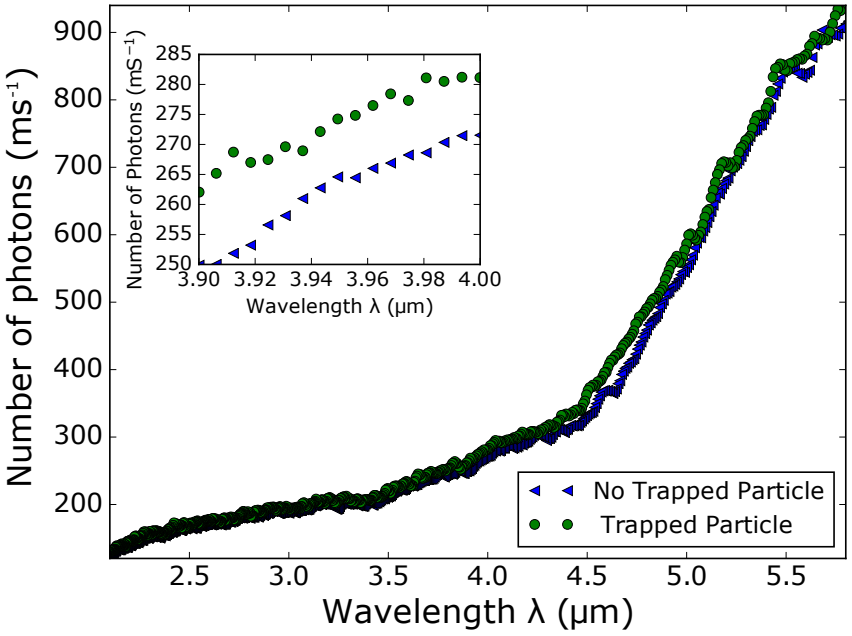

FIGURE 5.8: **Measured spectra with and without a trapped particle.** The spectra displayed were taken with a trapping laser intensity equal to 0.4 TW/m^2 at 10 mbar. The blue data points show the spectrum in the absence of a trapped nanoparticle, and the green where a nanoparticle is trapped. The inserted graph shows a zoomed in section of the data, to demonstrate the higher number of photons collected when there is a trapped particle. It can be seen that at either extreme of the data shown, the difference in the number of photons detected decreases as the transmission of the optics decreases (see figure 5.7).

5.5 Pressure vs particle temperature

At any given trapping laser power, the temperature of levitated nanoparticles depends on the temperature (300 K) of the background gas and the rate of collisions with the background gas. The measured temperature of the particle from figure 5.5, at various pressures, is shown in figure 5.10. It can be seen that, as the pressure is reduced, the temperature of the particle increases. This is owing to the reduction in the rate of cooling from gas collisions.

By varying the pressure between 1000 mbar and 0.04 mbar, it is possible to achieve values of T_{BB} ranging between 388 K and 480 K respectively. It is expected that a similar increase in T_{BB}, as pressure is reduced, would be observed with different particles within the optical trap, as the cooling from background collisions is reduced. An increase in T_{BB} could explain observations of particles being lost at certain pressures, due to the particle burning, graphitization [123] or melting [2].

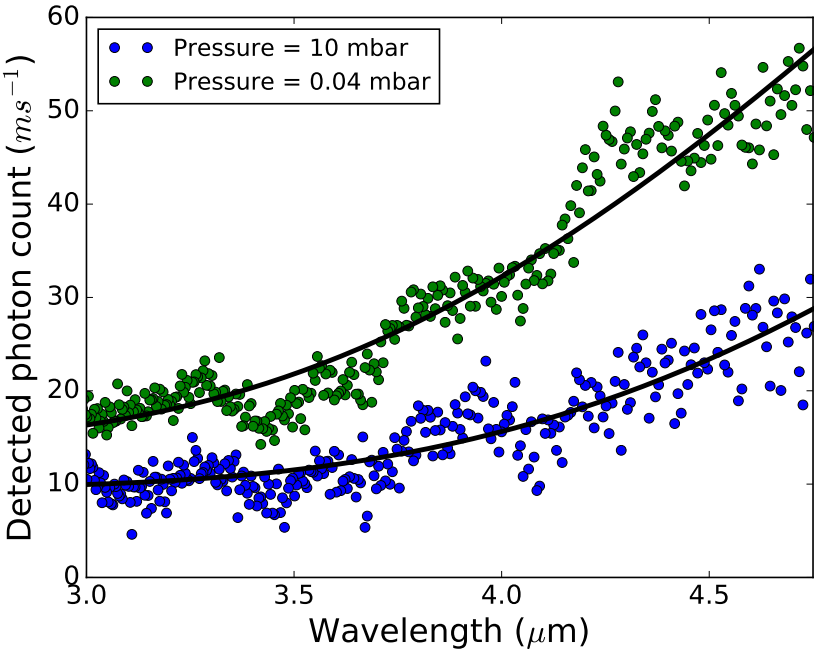

FIGURE 5.9: **Fitting to the particle spectrum.** The spectra displayed were taken with a laser power equal to 0.4 TW/m^2. Each of the particle's spectra is obtained by subtracting the measured spectrum without a particle, from that with a particle. The black lines show equation 5.12, fitted to each spectrum, giving $T_{BB} = 466$ K at a pressure of 10 mbar and $T_{BB} = 480$ K at a pressure of 0.04 mbar.

5.6 Trapping laser intensity vs particle temperature

At any given pressure, the temperature of levitated nanoparticles depends on the intensity of the trapping laser, with an approximately linear dependence $T_{BB} \propto I$, as suggested from reference [123]. To test this relationship, the trapping laser intensity was varied and the temperature of the particle from figure 5.5 was measured. The results are shown in figure 5.11.

It can be seen from figure 5.11, that as the intensity of the trapping laser is increased, T_{BB} increases in a linear relationship, corresponding with similar studies carried out on nanoparticles trapped in liquid solutions [160]. By varying the laser intensity between 0.21 TW/m^2 and 0.4 TW/m^2 it is possible to achieve values of T_{BB}, ranging between 367 K and 463 K respectively. Even though absorption of silica is low at 1550 nm, it can be seen that the temperature of the particle can be raised with increased laser intensity, because of poor heat transfer to surrounding gas at low pressures.

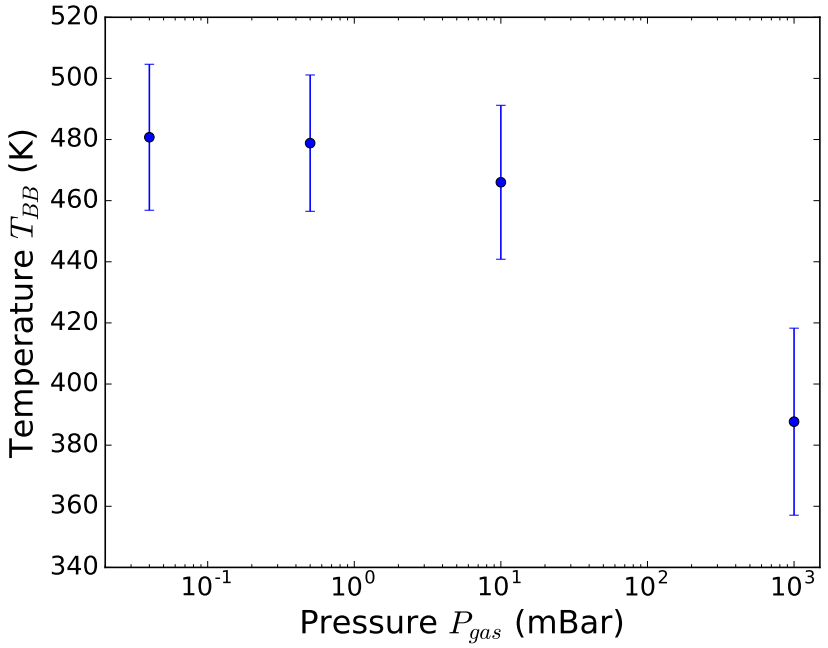

FIGURE 5.10: **Effect of pressure on particle temperature.** The temperatures measured were taken with a trapping laser intensity equal to 0.4 TW/m^2. It can be seen that as the pressure is reduced, the temperature of the particle increases.

5.7 Improving the experimental system

While the work in this chapter has shown that it is possible to determine the temperature of a levitated nanoparticle by measuring its thermal radiation, the system used is far from ideal. The detectable temperature range is limited by the wavelength range which the spectrometer used is capable of measuring. The further away from the peak the spectra is measured, the less photons are emitted, which makes it harder to determine the temperature of the levitated particle. For the purposes of designing a better system, the aim will be to have the peak of the blackbody spectra detectable at any of the possible temperatures the levitated particle can take. The lowest possible temperature a particle within an optical trap could have depends on the temperature of the background gas. Therefore, for a system operating at room temperature, the lowest temperature an optically levitated particle could have would be ∼300 K. The maximum temperature an optically levitated nanoparticle could have is given by its melting temperature; in the case of a silica nanoparticle its melting point is 1873 K. In an ideal system, the spectrometer used would be capable of measuring the peak wavelength within this temperature range (300-1873 K). To achieve this, the spectrometer used would need to have a wavelength range of 1222-7627 nm (see figure 5.3). In addition to having a spectrometer with a greater wavelength range, the optics which the blackbody signal passes through needs to have a flat transmission profile over the same wavelength range as the spectrometer.

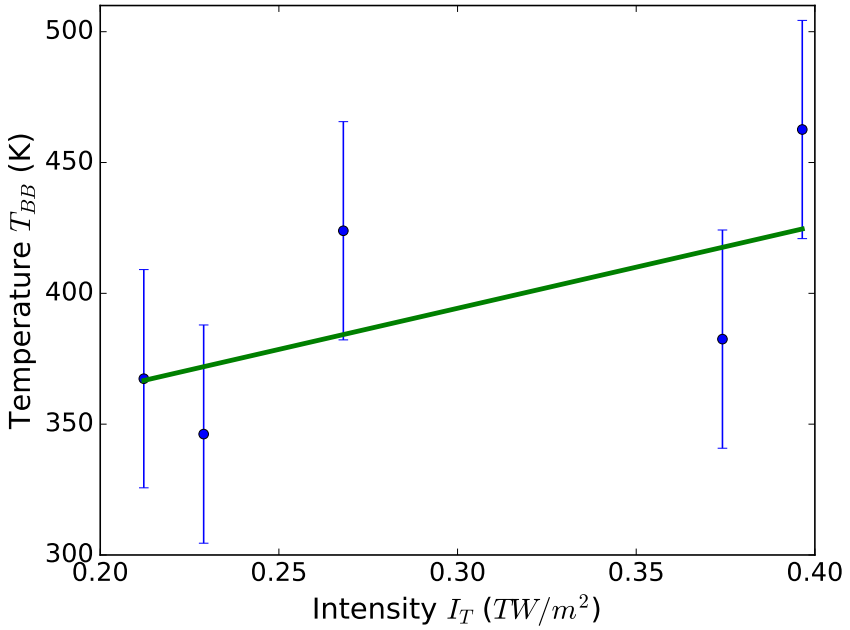

FIGURE 5.11: **Effect of laser power on particle temperature.** The temperatures measured where taken with a pressure equal to 0.04 mbar. It can be seen as the laser power is increased the temperature of the particle increases.

The biggest limiting factor of the current experimental setup is the varying absorption at different wavelengths of the optics in the system. The optics were simply what was available at the time the spectrometer was borrowed and sadly not ideal for the task at hand. The errors in the measurement of the particles' temperature are as large as ± 40 K in the results presented here. This is larger than the errors reported from fitting 5.13 to the PSD of particle motion in reference [2] in order to determine the particles' temperature. However, with optimised components, this problem could be overcome. An improved design for the optical setup is shown in figure 5.12.

In this experimental redesign, the number of optical components has been minimized to reduce absorption loss within the system, and the optics in the detection system have been replaced with optics capable of high transmission over a wider range of wavelengths. A summary of the components follows:

The trapping objective: As discussed in chapter 3, the parabolic mirror used as a trapping objective is machined out of aluminium. This material has a relatively flat transmission over the wavelengths detectable by the spectrometer used, with a reflectivity of $> 95\%$ from 2-20 μm. This can be improved upon by coating the mirror with a layer of gold, which has a flatter reflectance, and a greater average reflectance $> 97\%$ over a larger wavelength range (0.8-20 μm).

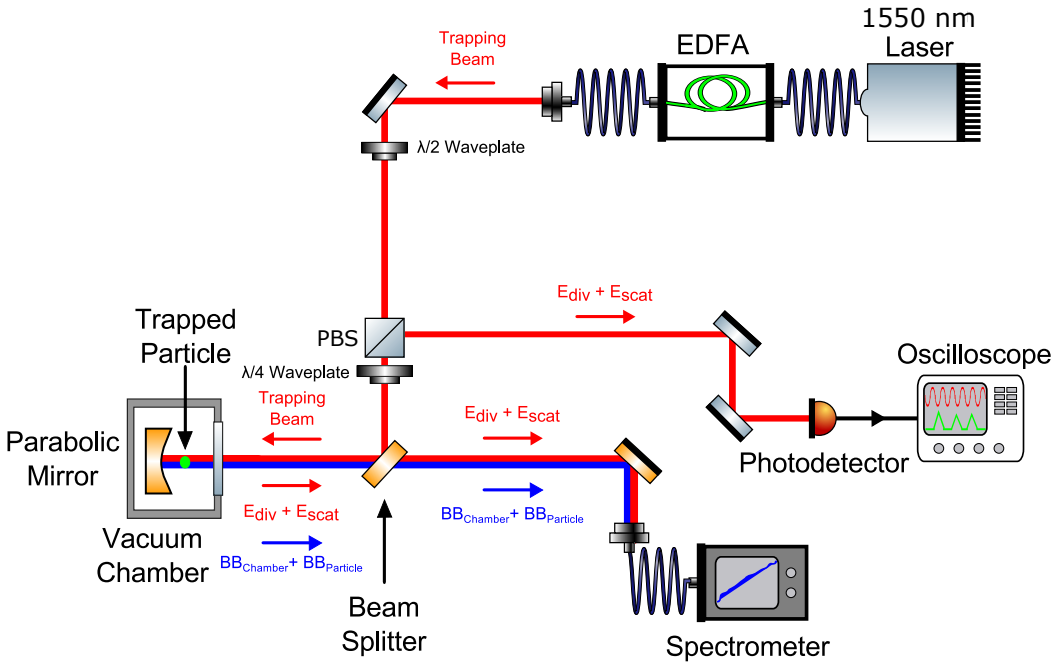

FIGURE 5.12: **Proposed experimental set up for using blackbody-like radiation from a levitated nanoparticle to measure its temperature.** For the purposes of this diagram, only the blackbody radiation which will reach the spectrometer is highlighted.

Vacuum window: The use of a calcium fluoride (CaF_2) window (such as *Eksma optics 530-6710*), which has a useful transmission over the spectral range from 0.2-8 μm, would be beneficial as this would be sufficient to measure the full temperature range which the particle could explore.

Beam spliter: The use of a beam splitter (50:50) such as *Thorlabs BSW11* made of Zinc Selenide would have a useful wavelength range of 1-12 μm, which would allow for the full range of interesting wavelengths to be detected. The drawbacks of using such an optical component however, are that 50% of the blackbody radiation would be lost, due to reflection, and the ability to filter out the trapping laser wavelength (1550 nm) optically would no longer be present. However, due to the narrow line width of the trapping laser, its effect can easily be removed from the spectra when analyzing the data.

Mirrors: While the aluminium mirrors (*Thorlabs PF10-03-G01*) used have a relatively flat transmission over the wavelengths detectable by the spectrometer used, with a reflectivity of $> 95\%$ from $2-20$ μm, improvement is still possible. For example, unprotected Gold Mirrors (such as Thorlabs *PF10-03-M03*) could be used. These would offer both a flatter reflectance and also a greater average reflectance $> 97\%$, over a larger wavelength range (0.8-20 μm).

5.8 Conclusion

The temperature of a levitated particle was measured by fitting the Planck equation to the emitted thermal spectrum of a levitated silica nanoparticle. Varying the pressure between 1000 mbar and 0.04 mbar resulted in an increase of T_{BB}, from 388 K to 480 K, illustrating that the temperature of the nanoparticle increased with decreasing pressure. The trapping laser intensity was varied from 0.21 TW/m^2 to 0.4 TW/m^2, resulting in an increase of T_{BB}, from 367 K to 463 K. This shows that even though the absorption of silica is low at 1550 nm, the temperature of the levitated nanoparticle can be increased, with increasing laser intensity, due to the poor heat transfer to the surrounding gas at low pressures.

While methods do exist to measure the particle temperature in an optical trap by fitting 5.13 to the PSD of the trapped particles motion [2], they are dependent on knowledge or assumptions about the properties of the trapped nanoparticle (accommodation coefficient, shape, material etc), as well as knowledge of the background gas the particle is trapped in (temperature, material etc). Measuring the blackbody spectrum of an optically trapped nanoparticle, in contrast, does not require any such knowledge of the particle's properties beyond the material of the particle, providing an advantage.

If the improvements discussed previously were implemented then this system, and method, could be used to perform a variety of studies. Such studies include measuring the melting point of individual nanoparticles, observing the deviation from Plank's law which occurs at small nanoparticle sizes [161], and investigating why different particles are lost from optical traps, under different experimental parameters, such as pressure, laser wavelength, laser power etc. Limiting the rate of blackbody emission is also important for the design of nanoparticle matter wave interferometers, as it limits the path length of the particles trajectory during interferometry. This technique is therefore a promising tool for designing and building such a device [44].

Chapter 6

Parametric feedback cooling of levitated particles centre of mass motion

Reducing the centre of mass motion of macroscopic oscillators has been shown to be a route to increased force sensitivity [70] and a path towards preparing macroscopic quantum states [162, 163]. Such a macroscopic system in a quantum state opens up a new mass range in which to study quantum effects [39, 40]. A number of proposals already exist to take advantage of such systems at different centre of mass motion temperatures to create macroscopic quantum superpositions. Proposals at non-ground state temperatures include nanoparticle matter wave interferometers, such as the one proposed by Bateman et al. [44] which requires cooling of a 20 nm diamter particle to a temperature of 20 mK. Other proposals requiring ground state cooling include creating quantum superpositions of living organisms [164]. In addition, to the ability to test quantum physics, many applications have been proposed for such systems ranging from detection of exotic forces [70, 165] to detecting gravitational forces such as high frequency gravitational waves [69].

The idea of laser cooling came about shortly after the work of Ashkin in 1970 [80] who demonstrated that radiation pressure could have a noticeable influence on a particle's motion. In 1975 Hänsch and Schawlow used the novel technique of Doppler cooling to cool atoms to a temperature of 0.24 K (reducing the temperature by a factor of 50) [166]. Also in 1975 Dehmelt [167], Hänsch and Schawlow [166] proposed using non-conservative traps for cooling the atomic motion of particles, before being demonstrated by Wineland et al [168] in 1978. The 80s and 90s saw fast development in different cooling techniques, such as sideband cooling [167] and Sisyphus cooling [169], to name

but a few. The introduction of these novel techniques allowed for the temperature of trapped atoms to be reduced to lower and lower temperatures. For more information on the laser cooling and trapping of atoms and their applications, the following references are recommended [170, 171].

Parallel to the aforementioned research into atom cooling, research into cooling macroscopic objects such as cantilevers and mirrors was also explored. The first demonstration of the cooling of a macroscopic mechanical oscillator was achieved by Cohadon et al. [172] in 1999. Cohadon et al. managed to reduce the motional temperature of a mirror by a factor of 40, by monitoring the Brownian motion of the mirror with a feedback loop and applying radiation pressure at the right times. These techniques were further developed by Kleckner and Bouwmeester, who in 2006 managed to cool a cantilever resonator to temperatures of 135 mK. Later Poggio et al. [163] in 2007 managed to cool the fundamental mechanical mode of an ultrasoft silicon cantilever from a base temperature of 2.2 K down to 2.9 mK using active optomechanical feedback. The lowest temperature in this system was limited by the measurement noise present in the system.

In addition to the cooling methods mentioned previously in trapping systems, laser cooling methods have been implemented in several types of nanomechanical oscillators. Nanomechanical oscillators which were involved in the race to reach the ground state include membranes [173], nanobeams [174] and photonics crystals [175]. To date, three groups have independently demonstrated cooling to the ground state of a mechanical oscillator. In 2010 O'Connell et al. [162], reached a phonon occupancy of 0.07. The next year in 2011 Teufel et al. [176] and Chan et al. [177] reached phonon occupancy numbers of 0.34 and 0.85, respectively. For more information on mechanical resonators, the following references are recommended [4, 178].

The mechanical systems mentioned previously (with the exception of trapped atoms) are directly coupled to their thermal and mechanical environment, which imposes limits to thermalization and decoherence. As a consequence, coupled systems often require cryogenic precooling. In contrast, an optically levitated particle in ultrahigh vacuum has no physical contact to the environment and therefore can be considered decoupled from its environment [11, 179].

The first experimental realisation of cooling in a levitated system was reported by Li et al. in 2011 [65], in which they demonstrated trapping and cooling of a microsphere in a scattering force trap. They achieved milliKelvin temperatures by using three orthogonal counter propagating laser beams. Shortly following this Gieseler et al. in 2012 [13] demonstrated cooling of a levitated nanosphere, via a parametric feedback cooling scheme implemented in an gradient force optical trap created with a single laser. This scheme achieved temperatures of 50 mK and was limited by detection noise. Since then

there have been several demonstrations of cooling in levitated systems including: optical cavities [101], hybrid electro-optical traps formed using a Paul trap within a single mode optical cavity [100] and similar optical dipole traps [27]. Each of these experimental realisations have different experimental benefits and challenges. For example in reference [101], cooling is only achieved along the longitudinal motion of the particle and to extend the ability to cool in all spatial degrees of freedom is challenging experimentally. In the case of the hybrid electro-optical trap, they have low trap frequencies and a low finesse cavity which results in low cooling rates.

At the time of writing, there are three setups which have demonstrated milli-kelvin temperature cooling of a levitated nanosphere. Fonseca et al. [99] have demonstrated temperatures of 1-3 mK with use of a hybrid trap consisting of a optical cavity and Paul ion trap, limited by their detection noise and achievable vacuum 10^{-6} mbar. The lowest reported temperature was reported by Jain et al. [27], achieving a temperature of 450 μK (n = 63) in an optical gradient force trap. Their current limitation is due to feedback noise. In addition to this limitation, they observe photon recoil and argue that photon recoil places a limit on reaching the ground state in optically trapped systems. The third setup was designed and built by the author consisting of a gradient force optical trap produced by a parabolic mirror, achieving temperatures on the order of 5-14 mK. A discussion of this setup will form the basis of this chapter and was published in reference [3].

In this chapter, discussion of parametric feedback cooling and application in the author's setup will be discussed. First, the theory of feedback cooling will be presented. Then, the modifications made to allow for parametric feedback cooling to the setup shown in figure 3.1 and described in section 3.1 will be discussed. Experimental studies into the effects of the feedback cooling parameters will be presented. Finally a discussion into the limitations of the system will be presented along with a discussion of the challenges in reducing a levitated particle to the ground state.

6.1 Principle of parametric feedback cooling

The harmonic motion of an optically levitated nanoparticle undergoing small oscillations can be accurately modeled as a parametric oscillator. A parametric oscillator is an oscillator which is driven by varying some parameter of the oscillator, in our case the trap stiffness is varied. It is possible to amplify or reduce the amplitude of the particle motion by varying the trap stiffness at a certain frequency and relative phase to the particle motion. To reduce the amplitude of motion of the particle, the trap stiffness and hence trap depth is increased as the particle climbs the potential well and its kinetic

energy is reduced. As the particle moves back towards the centre of the trap, the trap stiffness is reduced and hence the trap depth. This process is shown in figure 6.1. This results in the particle gaining less kinetic energy as it moves back towards the centre of the trap than it lost climbing the potential well. Modulation of this type results in a reduction in the particle's average kinetic energy, reducing the average positional variance and hence the particle's centre of mass temperature T_{cm}. The modulation described here to cool the particle's motion corresponds to a modulation at twice the trap frequency applied at the correct relative phase to the particle motion, we call the feedback phase ϕ.

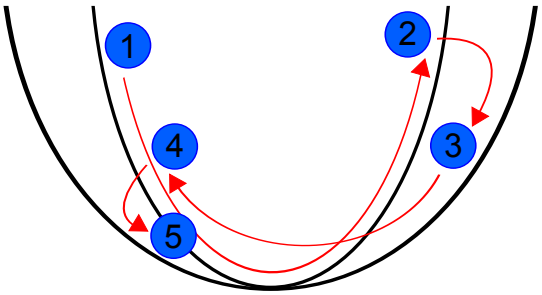

FIGURE 6.1: **The particle motion during feedback cooling. 1)** Before the parametric feedback is activated. **2 and 4**) As the particle moves away from the centre of the trap, the parametric feedback loop is activated and the particle's motion during feedback cooling is hindered by an increase in trap stiffness. **3 and 5**) As the particle moves towards the centre of the trap, the trap stiffness is reduced. The overall effect of steps 2-5 is to cause a reduction in the particle's energy.

By adjusting the size of the modulation depth we can control the amount of damping we induce via feedback cooling and thus raise or lower the temperature of our trapped nanoparticle as desired. From equations 2.26 and 2.27, it can be seen that the trap stiffness is proportional to the laser intensity used to create the trap, therefore by modulating the laser power the trap stiffness can be modulated. The modulation of the trap stiffness applied to achieve feedback cooling to the system can be described as,

$$k_{fb}(t) = k_0 \eta \sin(2\omega_0 t + \phi). \tag{6.1}$$

where we define η to be the modulation depth of the optical feedback signal with $\eta = I_{fb}/I_0$ where I_0 is the laser intensity without feedback and I_{fb} is the amplitude of the feedback modulation. Giving a time varying trap stiffness of the optical trap equal to

$$\begin{aligned} k(t) &= k_0 + k_{fb}(t) \\ &= k_0 + k_0\eta\sin(2\omega_0 t + \phi). \end{aligned} \tag{6.2}$$

This trap stiffness modulation provides a damping force to our particle as it moves within our trapping potential. This force is created by varying the intensity of the trapping laser and is a time-varying, nonconservative optical force. The force that arises due to the parametric feedback cooling feedback force can be written as

$$F_{fb}(t) = k_{fb}(t)x(t). \tag{6.3}$$

we can write the equation of motion for our trapped particle in the x direction (polarization direction) undergoing a feedback cooling force as,

$$\ddot{x}(t) + \Gamma_0\dot{x}(t) + \omega_0^2 x(t) = \frac{1}{m}(F_{th}(t) + F_{fb}(t)), \tag{6.4}$$

As shown in references [3, 13], activating the parametric feedback loop gives rise to additional damping $\delta\Gamma$ and a frequency shift $\delta\omega$. The resulting spectral line shapes are defined by the power spectral density $S_x(\omega)$, which follows from equation 6.4 as

$$S_x(\omega) = \frac{k_b T_0}{\pi m}\frac{\Gamma_0}{([\omega_0 + \delta\omega]^2 + \omega^2)^2 + \omega^2(\Gamma_0 + \delta\Gamma)^2} \tag{6.5}$$

Intergrating both sides over ω gives the mean square displacement

$$\begin{aligned} \langle x^2\rangle &= \int_0^\infty S_x(\omega)d\omega \\ &= \frac{\Gamma_0 k_b T_0}{m}\frac{1}{\omega_0^2(\Gamma_0 + \delta\Gamma)} \end{aligned} \tag{6.6}$$

Using the equipartition theorem we note,

$$\begin{aligned} \frac{1}{2}k_b T_{c.m} &= \frac{1}{2}m\omega_0^2\langle x^2\rangle \\ &= m\omega_0^2 \frac{\Gamma_0 k_b T_0}{m} \frac{1}{\omega_0^2(\Gamma_0 + \delta\Gamma)} \\ \implies T_{c.m} &= T_0 \frac{\Gamma_0}{\Gamma_0 + \delta\Gamma} \end{aligned} \tag{6.7}$$

where T_0 is the equilibrium temperature in the absence of parametric feedback cooling. It is therefore apparent that to implement parametric feedback cooling in the experimental setup shown in figure 3.1, the ability to firstly measure the position of the particle is required, and secondly the ability to produce a modulation of the trapping laser intensity at twice the particle's frequency, with the correct time delay is required.

6.2 Experimental setup

The experimental setup is built upon the setup shown in figure 3.1 and described in section 3 with some additional components. The detected signal at the photodiode can be considered to be a carrier wave containing three signals of differing frequencies, corresponding to the trap frequencies of each spatial degree of freedom plus noise. This signal measured at the photodiode is then sent to three different lock-in amplifiers (*ZI HF2LI Lock-in Amplifier*)[1], where the signals are extracted for each spatial degree of freedom. In each of the lock-in amplifiers the frequency ω_i and phase θ_i of the particle motion in one spatial degree of freedom ($i = z, x, y$) is extracted. This information is then used to create a sine wave with amplitude A_i, at twice the frequency of the trap frequency and a phase shift ϕ_i relative to its measured phase. These frequency-doubled and phase-shifted signals for each spatial degree of freedom are added together, before being sent to a acusto optical modulator (AOM) (*PhotonLines, 80MHz*). The signal sent to the AOM modulates the intensity of the laser light before the laser light reaches the trapping objective. This completes the feedback loop used to perform feedback cooling on levitated particles. The feedback capable setup can be seen in figure 6.2.

The modulation due to the feedback is visible in light detected on the photodiode and can be seen alongside the motional peaks resulting from particle motion as shown in figure 6.3

[1]Originally the process of generating a feedback signal from the detected signal was carried out using a pair of FPGA's (*National Instruments NI-PXIE-7961*). However, due to the ease of use, the lock-in amplifiers became the main device used for cooling.

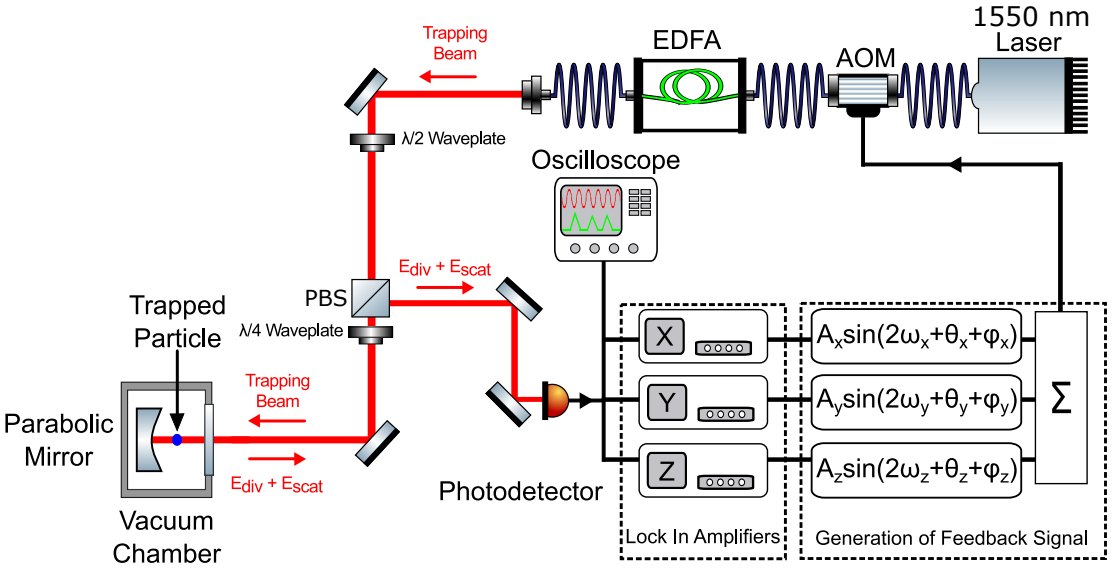

FIGURE 6.2: **Experimental setup for parametric feedback cooling of optically levitated particles.** The output of the laser is intensity modulated by an AOM (*PhotonLines, 80MHz*) according to the feedback signal. The laser light is focused by a paraboloidal mirror, at the focus of which a silica nanoparticle is trapped. The scattered light from the particle is collected and collimated by the parabolic mirror. The scattered light contains encoded in it, the modulation of the light due to the feedback signal and the modulation due to the particle motion. This light is then detected by a photodiode. Once detected, the modulation of the light caused by the particle motion is separated via the use of three lock-in amplifiers. The feedback signal is then generated and fed into the AOM.

6.3 Extracting Experimental Parameters

We assume that the particle without feedback is at thermal equilibrium with the surrounding gas and is approximately at 300 K. Therefore, in a steady state solution we assume the particle is also initially at $T_0 = 300$ K. However upon activating feedback cooling, this is no longer true. To calculate the temperature of a cooled particle we require two lots of information about the particle's motion, one in which the particle is in thermal equilibrium with the surrounding gas and one of the cooled particle respectively. We refer to the data taken for a particle in thermal equilibrium as the reference save. The reference data is taken at roughly 1 mbar without feedback cooling where a fitting with minimal error can be obtained (see section 4.6)[2]. When referring to parameters extracted from the reference save, the subscript 0 is used, while for the cooled data the subscript fb is used. We fit the following equation to the PSD of the cooled particle motion.

[2]It was found that the error in fitting a PSD to the motion of an optically levitated particle did not have a dependence on the laser intensity. For this reason the reference save, was taken at the same power the experiment being conducted.

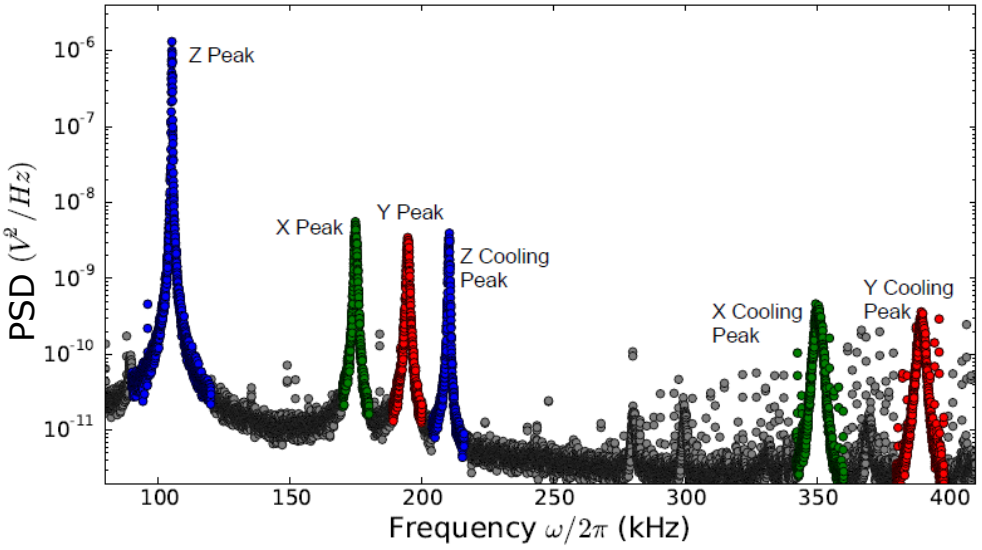

FIGURE 6.3: **Observation of the parametric feedback signal.** For a 66 ± 3 nm silica particle trapped at a pressure of 1×10^{-2} mbar. A feedback signal is applied to each of the three spatial degrees of freedom with the following parameters; $\eta_z = 1\%$, $\phi_z = 45°$, $\eta_x = 1\%$, $\phi_x = 45°$, $\eta_y = 1\%$, $\phi_y = 45°$. The motional peaks and corresponding feedback signal are shown in the same colour. The z motional and feedback peak is shown in blue, x motional and feedback peak are in green and finally the y motional and feedback peak are shown in red.

$$S_x(\omega) = \frac{A_{fb}}{(B_{fb}^2 + \omega^2)^2 + \omega^2 C_{fb}^2}. \tag{6.8}$$

Where the fitting parameters equal,

$$\begin{aligned} A_{fb} &= \gamma^2 \frac{k_b T_0 \Gamma_0}{\pi m} \\ B_{fb} &= \omega_0 + \delta\omega \\ C_{fb} &= \Gamma_0 + \delta\Gamma \end{aligned} \tag{6.9}$$

An example of equations 4.15 and 6.8 fitted to a uncooled and cooled PSD can be seen seen in figure 6.4.

The temperature of a cooled particle can be worked out using equation 6.7 with the extracted fitting parameters from equations 4.15 to the PSD of an uncooled particle and 6.8 to a PSD of the particle's cooled motion. The resulting equation can be written

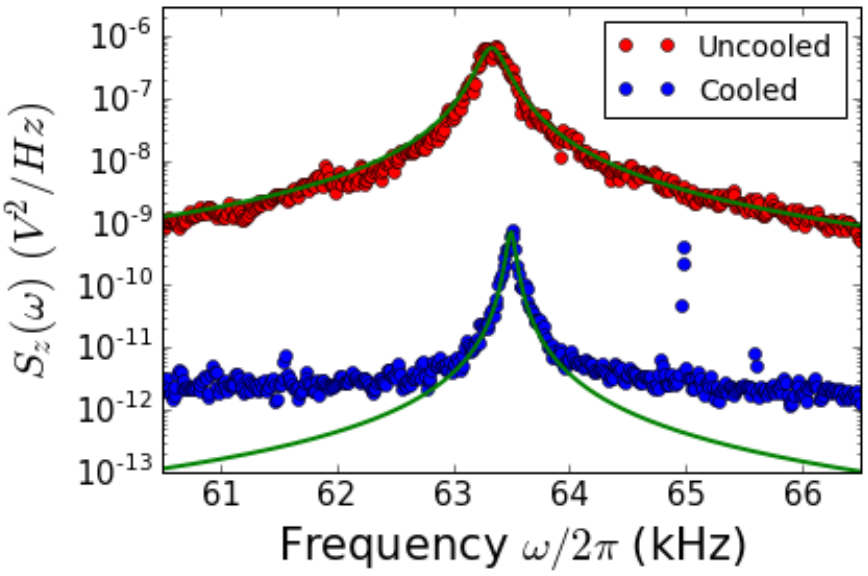

FIGURE 6.4: **Extracting temperature by fitting PSD. Uncooled:** The data is taken at P = 5 mbar, with $T_{cm} = 300$ K and $\Gamma_0 = 243 \pm 3$ Hz evaluated from the fit. **Cooled:** The data is taken at P $= 2 \times 10^{-5}$ mbar, with $T_{cm} = 167 \pm 3$ K and $\Gamma_0 + \delta\Gamma_0 = 74 \pm 2$ Hz evaluated from the fit. The subscript z has been used to indicate that the PSD has been taken for the z spatial degree of freedom.

$$T_{cm} = T_0 \frac{\Gamma_0}{\Gamma_0 + \delta\Gamma} = T_0 . \frac{A_{fb}}{C_{fb}} \frac{C_0}{A_0}. \tag{6.10}$$

In addition to calculating the temperature from the fitting parameters the following parameters can be calculated from the fit parameters.

$$\begin{aligned} \Gamma_0 &= \frac{A_{fb} C_0}{A_0} \\ \delta\Gamma &= C_{fb} - \frac{A_{fb} C_0}{A_0} \\ \delta\omega &= B_{fb} - B_0 \end{aligned} \tag{6.11}$$

The methods used to calculate the errors in these values and T_{cm} can be found in appendix C.

6.4 Optimisation of parametric feedback cooling

There are two tunable variables of concern when implementing parametric feedback cooling, namely the modulation depth and phase of the parametric feedback signal. In this section we study the effect of these parameters on the feedback's cooling rate.

6.4.1 Phase dependence

The first parameter optimised when performing parametric feedback cooling is the phase of the feedback signal. To study the effect of the phase we systematically change ϕ to switch between parametric cooling and parametric heating (while keeping η constant). The relationship between the phase ϕ and motional temperature T_{cm} can be written as [180]:

$$T_{cm} = \frac{T_0}{1 + \frac{\eta\omega_0 sin(2\phi)}{2\Gamma_0}}, \tag{6.12}$$

The effect of changing the feedback phase ϕ on the PSD of particles motion can be seen in figure 6.5, in which we observe a shift in the trap frequency of the particle and a change in the amplitude of PSD peak.

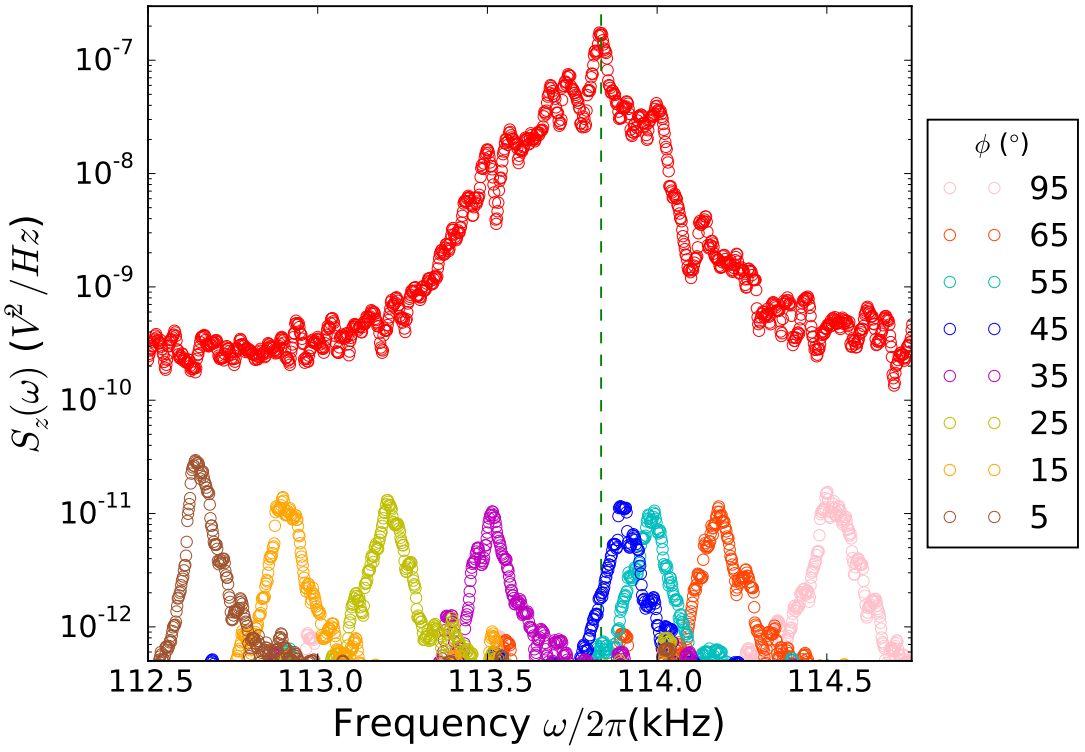

FIGURE 6.5: **Effect of varying the parametric feedback phase on the particle's motional PSD.** The red PSD shows the uncooled particle at 10^{-1} mbar, with the green dashed line showing the central frequency. The other PSD peaks are taken for a cooled particle ($\eta_z = 2\%$) at 10^{-5} mbar. The particle used in these measurements is a 100 ± 2 nm diameter silica particle.

The observed shift in trap frequency can be explained by considering that parametric feedback cooling modulates the trap stiffness and therefore changes the shape of the

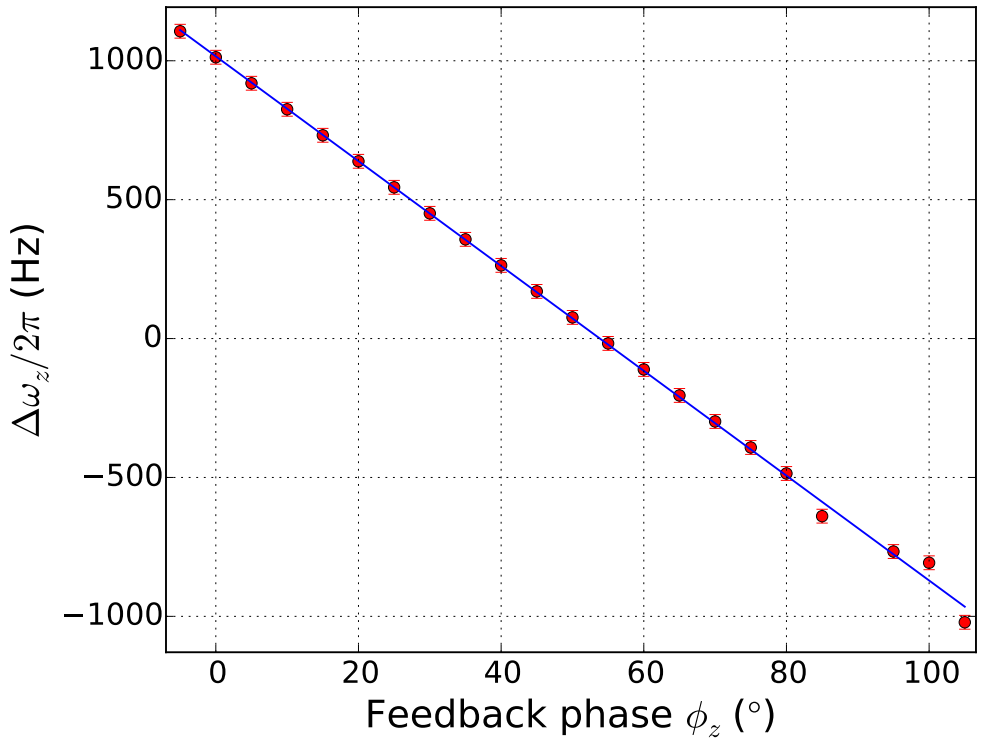

FIGURE 6.6: **The effect of feedback phase on the trap frequency.** It can be seen that as the feedback phase ϕ_z is varied away from the optimal feedback phase the particle's frequency is altered. The data is for a cooled ($\eta_z = 2\%$)100 ± 2 nm diameter silica particle at 10^{-5} mbar.

optical potential. The change in trap frequency with the feedback phase is shown in figure 6.7. A similar effect of this kind has been observed in other systems and is often called the optical spring effect [56, 181, 182]. The observed shift in frequency poses no experimental difficulty, as the bandwidth of the lock-in amplifier is more that sufficient to track any changes.

From equation 6.12 it is easy to see that the optimal cooling occurs when $\phi_z = 45°$. In reality, the phase we implement experimentally is found to be different from this value and depends on the time delay in the feedback loop between the measurement of the particle motion and implementing the trap stiffness modulation of the trap. A typical value for the delay in our setup is on the order of 6 μ s. This delay has been accounted for in figure 6.7, which shows how varying the feedback phase affects the particle's temperature. As the feedback phase moves further from $\phi = 45°$, a heating of the particle motion can be observed. Ultimately, as can be seen from equation 6.12, optimising the feedback phase can only cause a limited amount of cooling and other parameters need to be optimised to achieve a greater cooling of the particle motion.

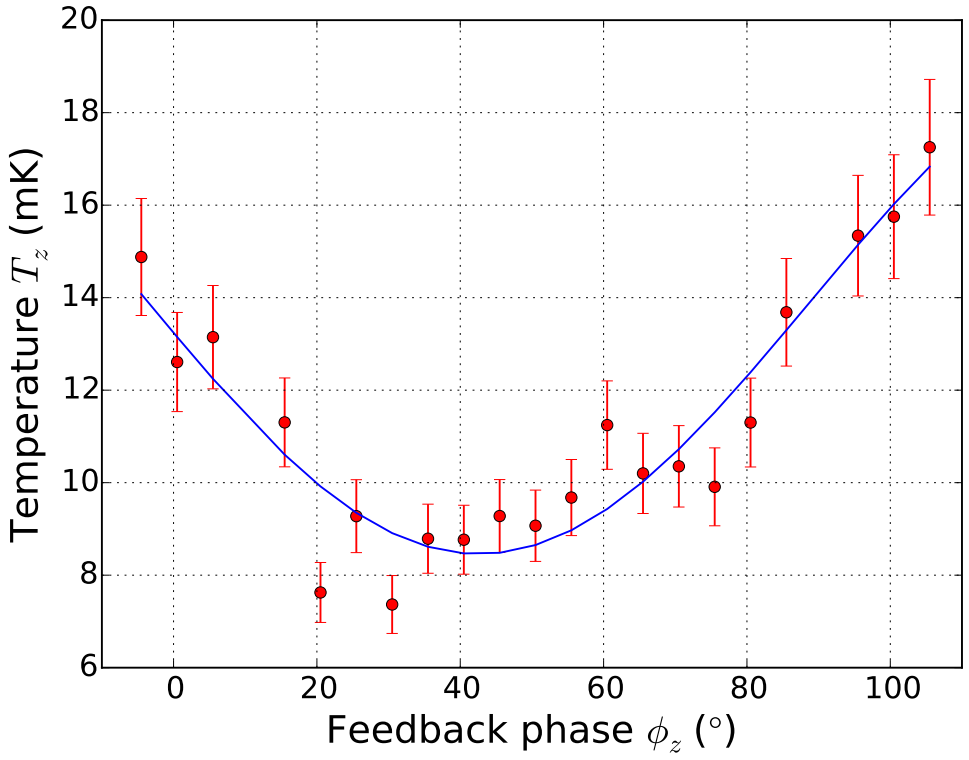

FIGURE 6.7: **Effect in varying the phase on the temperature of a cooled particle.** The maximal cooling occurs at $\phi_z = 45°$. The temperature increases according to equation 6.12 as shown by the blue line. The data is for a cooled ($\eta_z = 2\%$) 100 ± 2 nm diameter silica particle at 10^{-5} mbar.

6.4.2 Modulation depth dependence

The next parameter to be optimised is the modulation depth of the parametric feeback signal. Equation 6.12 shows an inverse relation to the modulation depth η of the feedback introduced to the system. This suggests that as we increase the modulation depth we increase the cooling rate as shown in figure 6.8.

One would therefore naively expect if we increase η to its maximum value we could achieve the lowest temperature at a given feedback phase and pressure. However, as η increases there is initially a decrease in temperature as predicted by equation 6.12, however as the modulation depth approaches $\eta = 0.4\%$ the temperature begins to plateau. As the modulation depth is increased and exceeds 1%, the particle temperature increases. This increase in temperature is suggestive of measurement noise in the system and thus places a limit on the amount of cooling that can be achieved in the system. Further increasing the modulation depth results in further increase in the temperature and the particle becoming lost from the trap. This we infer to be due to the particle

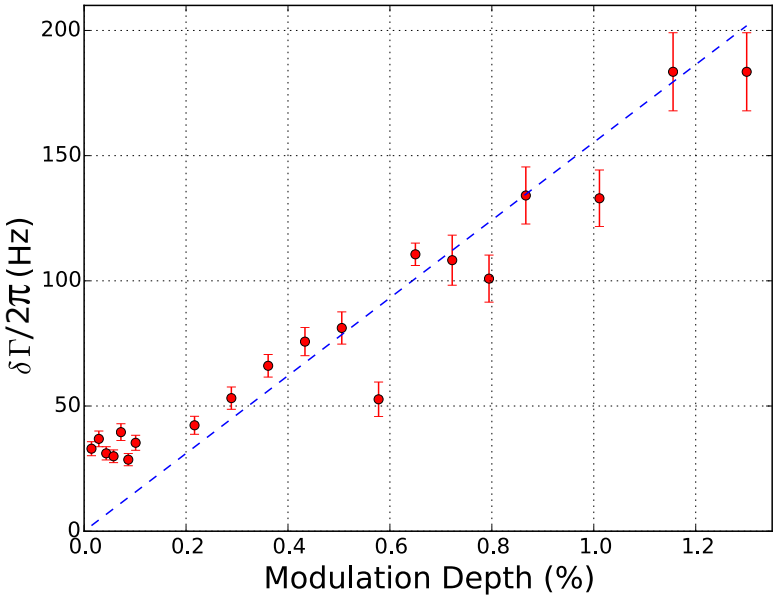

FIGURE 6.8: $\delta\Gamma$ **for different feedback modulation depths** η for a feedback cooled ($\phi = 45°$) 100 ± 2 nm diameter particle at $1{\times}10^{-5}$ mbar. The blue dashed line shows th relation $\delta\Gamma = 2\eta\omega_0\bar{x}^2/x_0^2$ [3]. As the feedback gain is increased $\delta\Gamma$ is also increased.

experiencing a greater impulse at higher modulation depths. The effects described here on the particles temperature can be seen in figure 6.9.

6.5 Pressure dependence

The temperature of the levitated particle is a balance between the cooling rate from feedback cooling and the thermalisation rate from background gas collisions. From equation 4.12 it can be seen that reducing the pressure in the chamber reduces the rate of gas collisions. The effect of pressure on Γ_0 can be seen in figure 6.10. As damping due to the environment decreases in magnitude, the feedback modulation depth is kept constant. This means that the effect of the feedback becomes more dominant as the pressure in the vacuum chamber is reduced. The effect on the particle's motional PSD can be seen in figure 6.11.

As the pressure is reduced the area under the particle's PSD decreases and an increase in $\delta\omega$ is observed. The change in $\delta\omega$ can be seen in figure 6.12. It can be seen that $\omega + \delta\omega$ increases as pressure decreases, before tending towards a constant value. Experimentally this challenge is overcome by setting the bandwidth of the lock-in amplifier so it can track the change in frequency as the pressure is reduced.

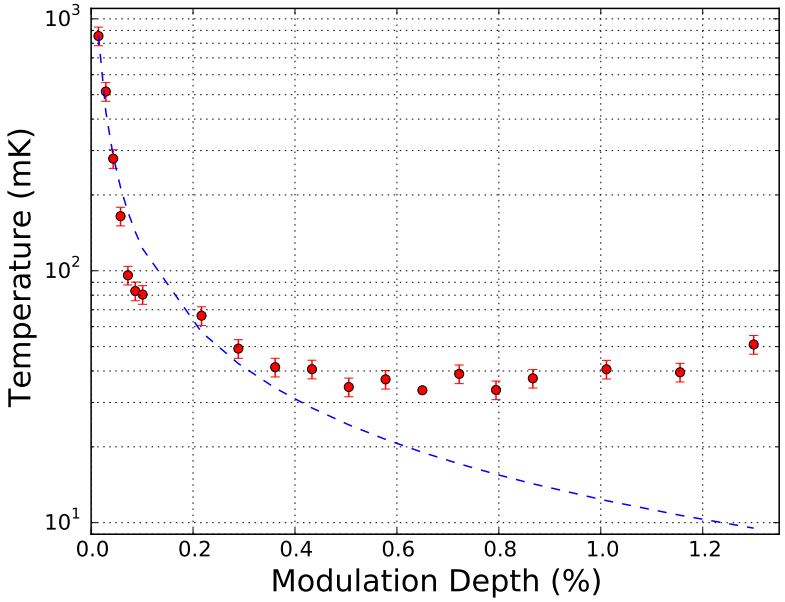

FIGURE 6.9: **Temperature for different feedback modulation depths** η for a feedback cooled ($\phi = 45°$) 100 ± 2 nm diameter particle at $1{\times}10^{-5}$ mbar. As the feedback gain is increased, the expected result is a decrease in temperature as shown by the model fit. However, experimental results show a heating of the particle as the modulation depth is increased above 1%.

The other important observation from figure 6.11 is that the area under the power spectral density of particle motion decreases as the pressure in the vacuum chamber is reduced. The area under the power spectral density of particle motion is proportional to the trapped particle centre of mass motion and hence temperature, suggesting a decrease in temperature. In contrast, it can be seen in figure 4.9 that for the uncooled case the area under the PSD does not change. The temperature of the particle as the pressure decreases can be seen in figure 6.13. The pressure is decreased to 1×10^{-6} mbar, the lowest attainable in the vacuum system described in section 3.1.

6.6 The Quality factor

Another property of the particle motion that is affected by reducing the pressure is the quality factor (Q factor). The quality factor of a mechanical resonator is an important figure of merit for various sensing applications and for observing quantum behaviour. The performance of a mechanical resonator depends critically on its quality factor, which characterises both the maximum response of an oscillator to a disturbance at its resonance frequency and the coupling rate to its surrounding dissipative environment. [183].

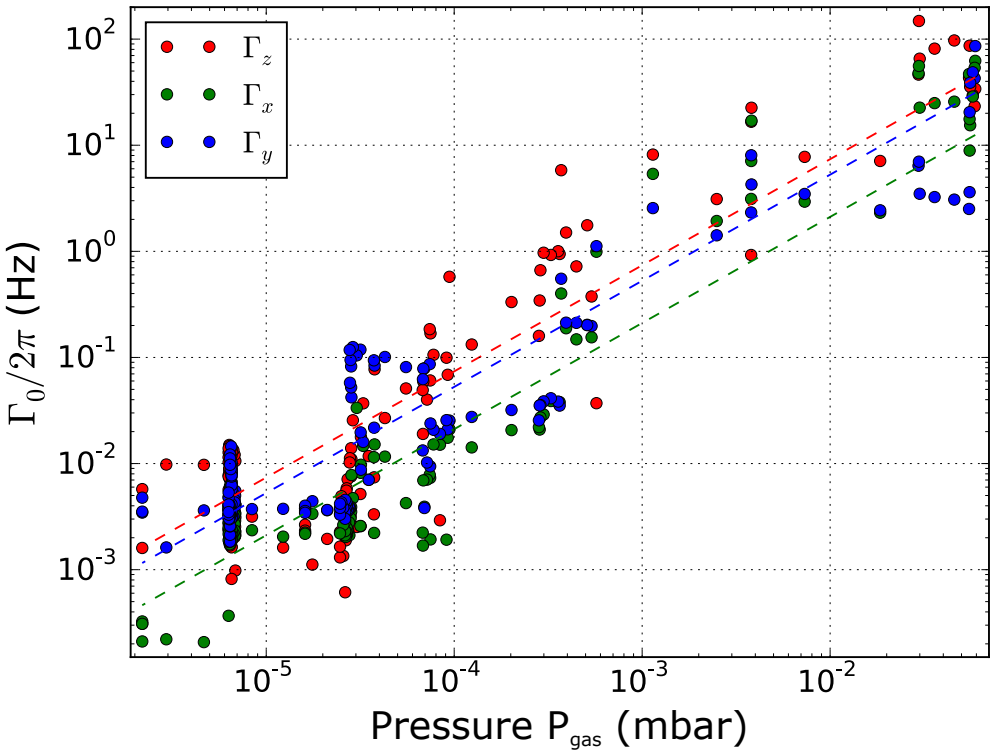

FIGURE 6.10: **The viscous damping experienced by an trapped particle at different pressures.** The damping rate Γ_0 decreases linearly with pressure. The dashed lines show fits according to 4.12. For a perfectly symmetric particle $\Gamma_z = \Gamma_x = \Gamma_y$ should be true. However as observed, this is not the case suggesting that the levitated particle is not perfectly spherical.

The Q factor is defined as the energy stored in the oscillator over the energy dissipated, over one radian of oscillation. For our system, the Q factor is given by

$$Q = \frac{\omega_0}{\Gamma_0}, \tag{6.13}$$

From this equation it is easy to see that reducing the pressure (and hence damping affecting the particle motion) should result in an increasing Q. Experimental verification of this can be seen in figure (6.14). It can be seen that at pressures on the order of 10^{-6} mbar the maximum Q factors are measured for the particle motion. The highest recored Q factors are $Q_z = 4.8 \pm 0.5 \times 10^7$, $Q_x = 1.2 \pm 0.1 \times 10^8$ and $Q_y = 1.7 \pm 0.2 \times 10^7$. Assuming that the scaling from the lines of best fit in figure (6.14) can be extrapolated to ultra-high vacuum, we would expect $Q_m \sim 10^{12}$ at $\sim 10^{-9}$ mbar, in agreement with previous studies [62].

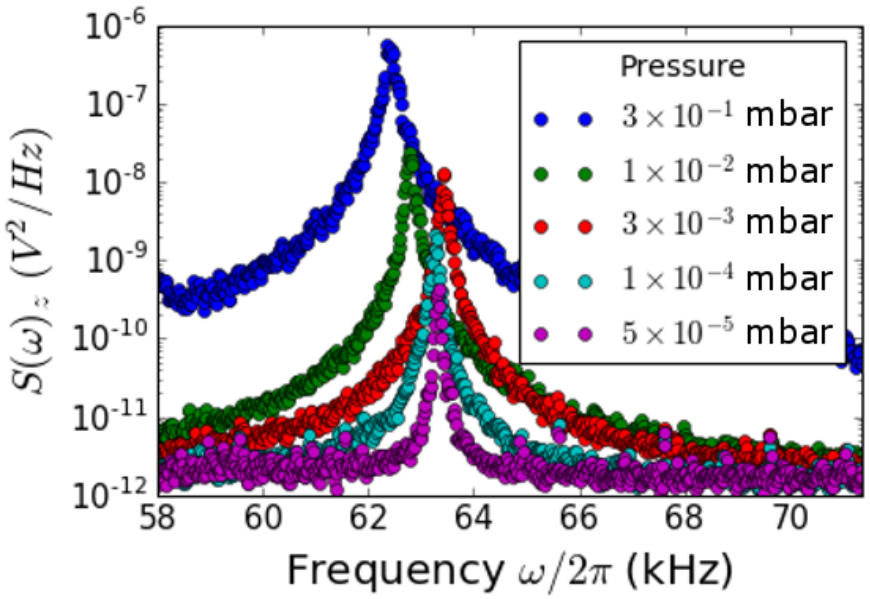

FIGURE 6.11: **Change in PSD of particle motion with pressure.** As the pressure in the vacuum chamber is reduced the area of the power spectral density decreases. The area under the PSD is directly related to the change in temperature of the particle. The change in trap frequency seen in this data is a combination of effects, firstly due to power variation in the trapping laser power and the optical spring effect discussed in section 6.4.1.

From the measured Q factors it is possible to calculate the force sensitivity limit [63, 71]. In the case of a mechanical oscillator, the force sensitivity limit arises from the classical thermal noise, and can be expressed as

$$S_{FF}^{th} = \sqrt{\frac{4k_b T_0 m\omega_0}{Q}}. \tag{6.14}$$

The maximum force sensitivity measured in the system for each degree of freedom (z, x and y) using the Q factors from figure 6.14 are $S_{FF,z}^{th} = 1.5 \pm 0.9 \times 10^{-20}\ N/\sqrt{Hz}$, $S_{FF,x}^{th} = 1.2 \pm 0.7 \times 10^{-20}\ N/\sqrt{Hz}$ and $S_{FF,y}^{th} = 3 \pm 1 \times 10^{-20}\ N/\sqrt{Hz}$. These values show that this system is on a similar level of sensitivity to other levitated systems [71]. With further reduction in pressure and temperature it is expected that the force sensitivity would increase.

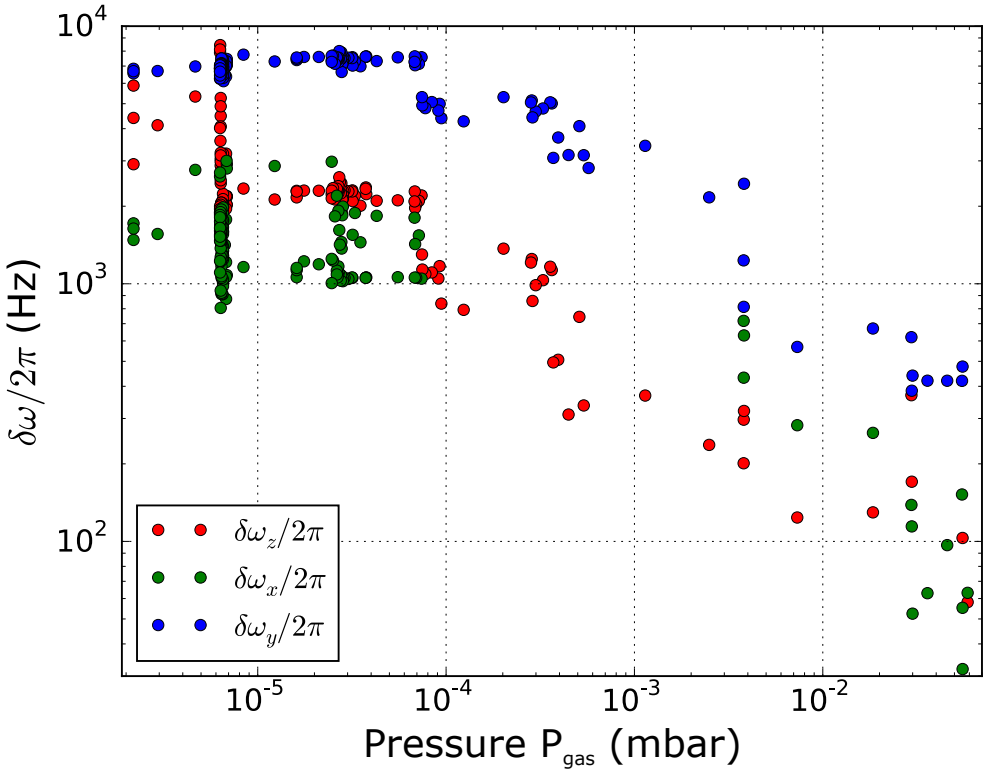

FIGURE 6.12: **Change in $\delta\omega$ with pressure.** It can be seen that as the pressure decreases $\delta\omega$ increases by less than 10 kHz between 6×10^{-2} mbar and 2×10^{-6} mbar. This change of frequency lies within the bandwidth of the lock-in amplifier and poses no issue for the parametric feedback cooling loop.

6.7 Lowest achievable temperature

Optimising the feedback parameters to $\eta = 0.6\%$ and $\phi = 45°$ for each spatial degree of freedom and reducing the pressure in the vacuum chamber to its lowest pressure 1×10^{-6} mbar, we achieve temperatures of $T_z = 14 \pm 1$ mK, $T_x = 5 \pm 1$ mK and $T_y = 7 \pm 1$ mK (as shown in figure 6.15). Temperatures on this order are the lowest achievable in the experimental system described in section 6.2. However, this is not the lowest temperature which could be theoretically achieved for an optically levitated particle.

The ground state of a quantum mechanical system (such as a particle in an optical trap) is its lowest energy state. For atoms in optical traps, their ground state has been realised experimentally [184, 185]. However, this has yet to have been achieved for nanoparticles in optical traps. A mechanical oscillator in the quantum ground state exhibits discrete states which are separated in energy by $\hbar(\omega_0 + \delta\omega) \sim \hbar\omega_0$ [186, 187]. The mean thermal occupancy $\langle n \rangle$ is given by,

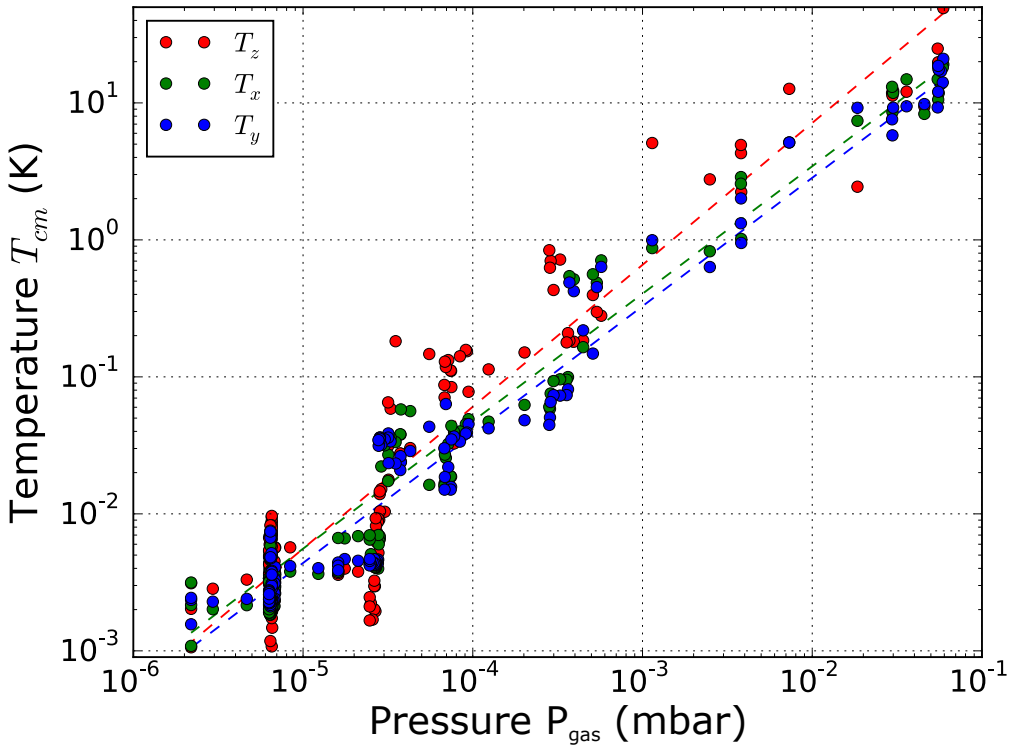

FIGURE 6.13: **Dependence of the center of mass temperature on pressure.** It can be seen that the particles temperature varies linearly with pressure. Assuming that this trend continues, it is predicted that ground state temperatures could be achieved at pressures on the order of 10^{-9} mbar.

$$\langle n \rangle = \frac{k_b T_{cm}}{\hbar \omega_0}. \tag{6.15}$$

The quantum ground state can be achieved when $\langle n \rangle < 1$. Therefore the ground state temperature T_{ground} for a harmonic oscillator can be written as,

$$T_{ground} = \frac{\hbar \omega_0}{k_b}. \tag{6.16}$$

For the particle in figure 6.15 we find the ground state temperatures for each degree of freedom to be $T^z_{ground} = 4$ μK, $T^x_{ground} = 7$ μK and $T^y_{ground} = 8$ μK. Therefore it can be seen that, to cool the particle to the ground state an improvement of the systems ability to cool by factor of roughly 10^2 needs to be achieved. For the particle in figure 6.15 we find the phonon occupancy to be $n_z = 3250$, $n_x = 670$ and $n_y = 830$ phonons.

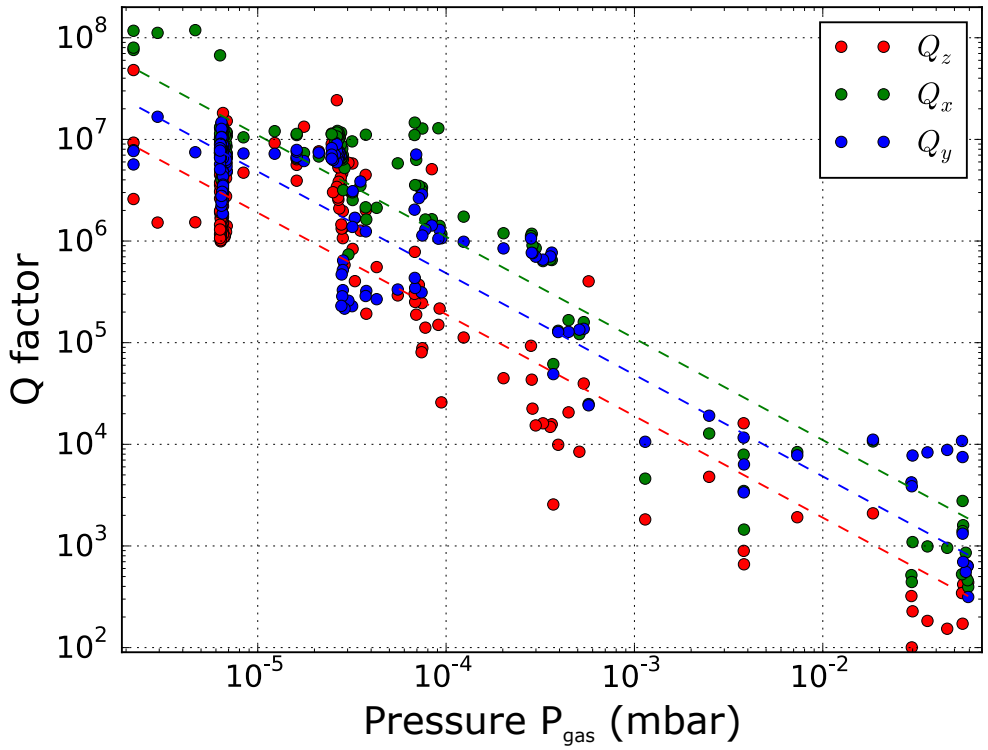

FIGURE 6.14: **The Q factor of particle motion at different pressures.** It can be seen that as the pressure is reduced the reduced damping results in an increased Q factor with the highest values measured in the system to be $Q_z = 4.8 \times 10^7$, $Q_x = 1.2 \times 10^8$ and $Q_y = 1.7 \times 10^7$.

6.8 Feedback Limitations and reaching the ground state

The obvious question is, can the system be modified to allow for improved if not ground state cooling? In this section we discuss what limits the experimental systems ability to cool an optically trapped particle. The ability to cool a particle depends upon the resolution of which its position can be measured and how accurately the feedback modulation can be applied. There are several sources of noise in the system which need to be minimized, to produce the highest possible position resolution, including measurement uncertainty due to the random arrival of photons at the particles location and measurement back action due to momentum transfer from photons to the particle.

6.8.1 Electrical noise floor

From figure 6.15 it may appear that there is still a significant amount of cooling which could be achieved before reaching the noise floor, however in this figure the noise floor of the oscilloscope is shown. The actual limiting factor in the system is the noise present in

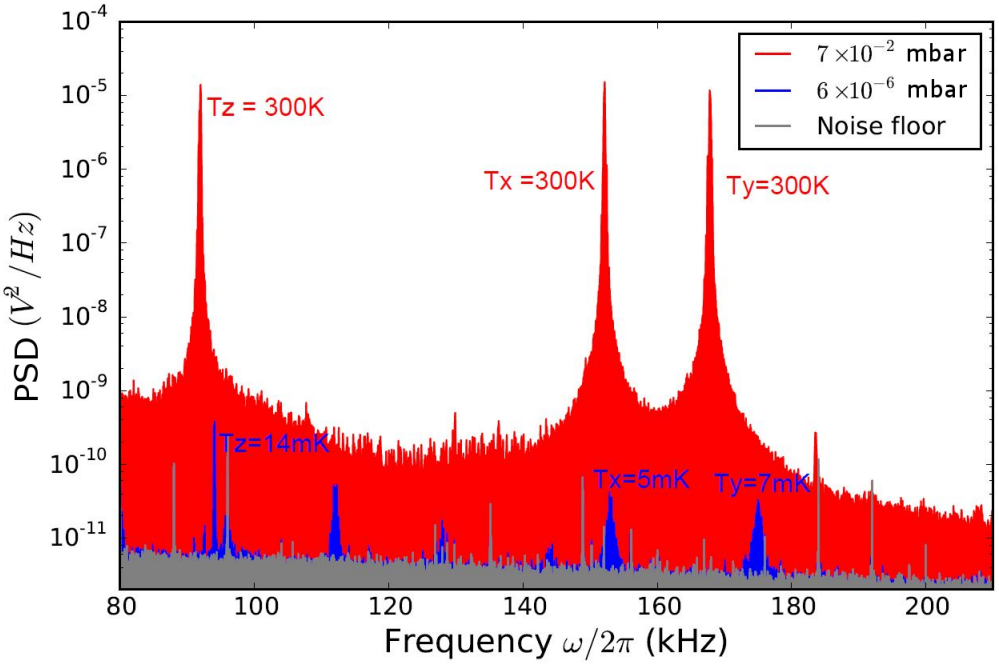

FIGURE 6.15: **PSD's showing the cooling of the center of mass motion of a levitated nanoparticle from 300 K to a few mK.** The red coloured PSD is of the particle motion at room temperature without any cooling trapped at 7×10^{-2} mbar. The blue coloured PSD shows the particle motion with cooling at 6×10^{-6} mbar, where $T_z = 14 \pm 1$ mK, $T_x = 5 \pm 1$ mK and $T_y = 7 \pm 1$ mK.

the feedback loop, specifically due to the lock-in amplifiers used to create the feedback signal. The noise floor of the lock-in amplifier can be seen along with the PSD peaks for a particle at various temperatures in figure 6.16. It can be seen that to reduce the temperature lower than ∼1 mK, the noise floor needs to be reduced. To reach the ground state, the noise floor would need to be reduced by a factor of roughly 10^{-2}, or the signal to noise ratio (SNR) increased by a factor of 10^2. The noise floor level can be lowered by replacing the *ZI HF2LI Lock-in Amplifier* with lower noise feedback electronics. The SNR can be increased by placing a low noise voltage amplifier after the photodetector (Such as a *FEMTO DHPVA-100* amplifier)[3], therefore allowing for the ZI HF2LI Lock-in Amplifier to cool the particle motion to lower temperatures.

6.8.2 Pressure reduction

As discussed in section 6.5, collisions from background gas limits the temperature which can be achieved in the experimental setup. Looking at figure 6.13 and making the assumption that the pressure and temperature will continue to decrease together in

[3]Alternatively the SNR could be increased optically, by using a higher NA parabolic objective or a material which is more reflective to 1550 nm laser light.

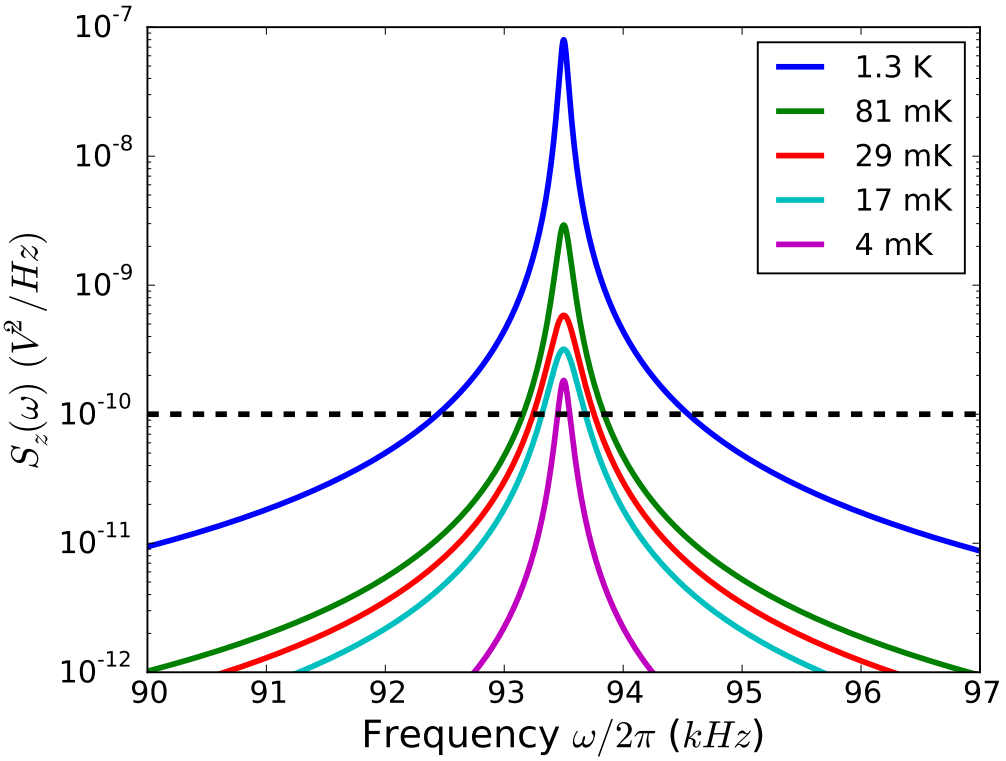

FIGURE 6.16: **Fitted PSD's to the motional amplitude of a nanoparticle at various Temperatures.** Solid lines show equation 6.8 fitted to experimental data at different temperatures. Dotted line is the back ground noise level of the lock-in amplifiers used to generate the feedback signal.

a linear relation, it is possible by extrapolating from the data shown to estimate the pressure required for which the particle may reach its motional ground state is 10^{-9} bar. To overcome this problem, one of the last changes the author was able to implement in the experimental system was to upgrade the vacuum system with the addition of cryopump (*TVLK160, VAB*) and a more powerful turbo pump (*Pfeiffer PMP03901*) to the vacuum system. The system is now capable of pumping down to pressures on the order of 10^{-11} mbar, which should fulfill the pressure requirement of the system to reach ground state.

6.8.3 Detection resolution limits

To examine whether the particle motion is resolvable in the ground state we consider the motion of the particle in the ground state given by

$$\sqrt{\langle x^2_{ground}\rangle} = \sqrt{\frac{\hbar}{2m\omega_0}}. \tag{6.17}$$

The ground state for a 60 nm silica particle with $\omega_0 = 2\pi \times 100$ kHz is $\langle x_{ground} \rangle = 17$ pm. The detection resolution of our system has been measured in section 4.5 to be $S_{x,exp} = 200 \pm 20\ fm/\sqrt{Hz}$. The detector used in these experiments has a bandwidth of 100 kHz, meaning that the minimum change in position that could be resolved is 8 pm. This resolution is sufficient to resolve ~ 2 points per oscillation satisfying Nyquist theorem. While theoretical the detection resolution should not limit the progress towards ground state cooling, Increasing the bandwidth of detector would still be beneficial.

6.8.4 Detection efficiency limits

To examine the detection efficiency in our system we consider the difference in interferometric signal across the wavefunction width. Maximum detection efficiency occurs when 100% of information carrying photons are collected by the detector in the system. To examine the detection efficiency in our system we must consider the fraction of laser light passing through the focus the particle interacts with. The area of the laser focus is given by $\sigma_{waist} = \pi \mathrm{W}_0^2/2$. The amount of light scattered by the particle is given by the Rayleigh scattering cross-section,

$$\sigma_s = \frac{2\pi^5}{3} \frac{(2r)^6}{\lambda} \left(\frac{n^2 - 1}{n^2 + 2} \right)^2 . \tag{6.18}$$

For a given laser power P_0, the power scattered by a nanoparticle within the trap is given by,

$$P_{scat} = \frac{\sigma_s}{\sigma_{waist}} P_0 . \tag{6.19}$$

Therefore we can find the number of photons scattered in a second, by dividing P_{scatt} by the energy of an individual photon,

$$N_{scat} = P_{scatt}/h f_{laser} \qquad , \tag{6.20}$$

where f_{laser} is the frequency of the trapping laser. The percentage of photons collected, η_{trans}, can be calculated by accounting for the number of photons lost by absorption in the optical components and the amount of photons collected by the parabolic mirror optical trapping majority, which collects 50% of the scattered photons (a significant improvement on lens based traps). Combining this with the quantum efficiency of the detector η_Q, we can write an expression for the power detected as

$$P_{det} = \eta_Q \eta_{trans} P_{scat}. \tag{6.21}$$

Where the signal amplitude measured on the detector in volts is given by $V_{det} = P_{det} \times 1.0$ A/W $\times$ G, the transimpedence gain is given by $G \sim 10^5$ V/A. The phase of scattered light is modulated by the position, and we can expect a phase difference $\theta \sim k\langle x_{ground}\rangle/\lambda \sim 70$ μrad (see equation 4.21) across the ground state, along the optical axis. Thus we expect about 100 nV of difference in electrical signal from the detector, according to the estimated fraction of the Rayleigh scattered photons incident on it. The sensitivity of the balanced photo detector is 70 $nV/\sqrt{Hz}$ and a bandwidth of 100 kHz, which gives a NEP of 0.2 nV for the detector, meaning ground state motion should be resolvable. Therefore, it can be seen that the detection efficiency does not provide a constraint on the approach to the ground state. It should be pointed out that parametric cooling should work on timescales shorter than $1/\Gamma_0$, even without continuously tracking position, providing that the frequency and phase of the centre of mass motion is known.

6.8.5 The standard quantum limit

Information about the particle position in our optical trap is obtained from photons scattering off the trapped particle. Greater amounts of information can be obtained by increasing the number of photons which interact with a trapped particle N_P. However, the stochastic arrival of photons adds an uncertainty to these measurements (even for an ideal detector). For a laser beam with N_P photons we find an uncertainty in photon number $\triangle n = \sqrt{N_P}$ due to shot noise [188]. Consequently, there is a momentum uncertainty $\triangle p$ of

$$\triangle p = \sqrt{N_P}\hbar k_q, \tag{6.22}$$

where k_q is the wave vector of a scattered photon traversing direction q. Thus from the uncertainty principle we can write

$$\triangle q = 1/2k_q(\sqrt{N_P}). \tag{6.23}$$

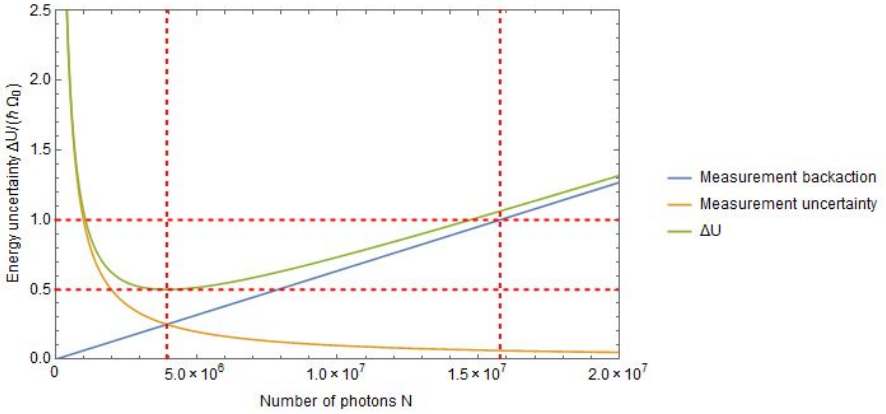

FIGURE 6.17: **Measurement back action** The standard quantum limit is reached when the measured position uncertainty is equal to the momentum imparted by the photons that carry the positional information.

It can be seen now that momentum uncertainty increases with an increasing number of photons ($\triangle p \sim \sqrt{N_P}$). In contrast, position uncertainty increases with decreasing number of photons ($\triangle q \sim 1/\sqrt{N_P}$). This must be taken into account when trying to reduce the uncertainty in measured energy $\triangle U$. $\triangle U$ is given by,

$$\triangle U = \frac{1}{2} m \Omega_0^2 \triangle q^2 + \triangle \frac{p^2}{m}. \tag{6.24}$$

Uncertainty is minimised when both terms are equal and is referred to as the quantum limit (see figure 6.17).

6.8.6 Photon Recoil Limit

The measurement uncertainty can be reduced by increasing the number of photons reaching our detector as is evident from equation (6.23). This can be achieved by increasing the intensity of the trapping laser. However, each photon from the laser which traps the particle, when it scatters off the nanoparticle, imparts a momentum kick to the trapped particle. The imparted momentum transfer can be of up to $p = h/\lambda$ depending on the scattering angle. The imparted scattering angle can be considered to be quasi random with a small preference to the forward direction allowing the resulting force to be modelled as a stochastic driving force. The power of the scattered photons can be calculated from $P_{scatt} = \sigma_R I_0$, where I_0 is the intensity at the focus, σ_R is the Rayleigh scattering cross-section from the particle equal to,

$$\sigma_R = \frac{8\pi^3}{3\epsilon_0^3}\frac{\alpha^2}{\lambda^4} \tag{6.25}$$

considering this equation and the equation for the particle polarisability 2.17 we can write,

$$P_{scatt} = \sigma_R I_0 = \frac{128\pi^5}{3}\frac{r^6}{\lambda^4}\left(\frac{n^2-1}{n^2+2}\right)^2 I_0 \tag{6.26}$$

Where I_0 given by,

$$I_0 = \frac{2P_0}{\pi_0^2} = \frac{8P_0\mathrm{NA}^2}{\pi\lambda^2} \tag{6.27}$$

where P_0 is the laser power. Using equation 6.26 and 6.27 for particle with a radius of 33 nm in a 0.7 W laser where the laser focus is is formed by a NA= 0.995 focusing objective, we find $P_{scatt} = 0.14$ μW. From reference [27] the photon recoil rate is given by,

$$\Gamma_{recoil} = \frac{1}{5}\frac{P_{scatt}}{mc}\frac{2\pi}{\lambda\omega_0}. \tag{6.28}$$

In our system the collisional damping from background gases is much larger than this effect. However, as the particle is cooled and the temperature reduced, a point will be reached where photon recoil will become an observable effect. Using the values quoted in this section we find for our system $\Gamma_{recoil} = 2\pi \times 239$ Hz.

6.8.7 Detector bandwidth

Finally we discuss the possibility of improving the position uncertanty by using a detector with a narrower bandwidth. We can relate our uncertainty in measuring position q and the bandwidth of our detector B by taking $\triangle t = 1/B$ and using equations (6.23) and the number of scattered photons $N_{scatt} = P_{scatt}\Delta t/\hbar\omega$. We can write our position uncertainty as

$$\triangle q \geq \sqrt{\frac{B\hbar\omega}{P_{scat}4k^2}}. \tag{6.29}$$

From this one could argue that by reducing the bandwidth of the detector it is possible to reduce the error in position uncertainty. However, for a full understanding we must take into account the classical particle trajectory, which can be expressed as $q(t) = q_0(t)sin(\Omega_0 t + \phi(t))$, where $q_0(t)$ and $\phi(t)$ vary over time scales of the order $\sim 1/\Gamma_{recoil}$. This means that the maximum time for measurements of position $t_{measure}$, is the time for which $q(t + \triangle t_{measure})$ is correlated with $q(t)$.

In ultrahigh vacuum, the dominant decoherence process is recoil heating and therefore $\Gamma_{decoher} = \Gamma_{recoil} \propto P_{scat}$. Setting $B \approx \Gamma_{recoil}$, the position uncertainty (6.29) can be written as

$$\triangle q \geq \sqrt{\frac{\hbar\omega}{4k_q^2}}. \tag{6.30}$$

Therefore, we can see that the position uncertainty becomes independent of power. Thus the minimum uncertainty in position measurement is given by zero point motion. This means that it is possible to work in the region where photon shot noise is the only limiting factor.

6.9 Conclusion

We have demonstrated a parametric feedback scheme to cool the motion of an optically trapped nanoparticle in high vacuum in all three spatial degrees of freedom. Theoretical considerations show that with some improvements to the experimental system, centre of mass temperatures and thus low phonon numbers close to the quantum ground state could be achieved. Potentially, to reach the ground state of a laser trapped nanoparticle, parametric feedback cooling could be combined with other optical cooling methods such as passive dynamical back-action cooling [5]. Passive dynamical cooling could be implemented with the addition of an optical cavity to the system [101, 120]. The observed Q factors on the order of 10^7, with predicted Q factors on the order of 10^{12}, hold great promise for ultrasensitive detection and sensing. With the system presented here, having a force sensitivity on the order of 10^{-20} N/Hz. Potential applications include detecting gravitational forces such as high frequency gravitational waves [69], sensing van der Waals and Casimir forces [70], sensing non-Newtonian gravity [71], nuclear spins [72] and detecting dark matter [73].

Chapter 7

Classical squeezing of the motion of levitated nanoparticles

Squeezing a quantum state of light has been implemented in a huge variety of experiments and systems [189], however in contrast the squeezing of a massive mechanical harmonic oscillators has not had many experimental realisations to date. The first demonstration of squeezing in a classical mechanical oscillator was by Rugar and Grütter [190] in 1991, who used parametric amplification to squeeze the motion of a microcantilever. Since then, squeezing of classical motional states in electromechanical devices by parametric amplification and weak measurements has been proposed [191] and has been demonstrated experimentally in an optomechanical micro-oscillator [192]. Schemes have also been proposed and discussed by numerous authors which rely on sinusoidal modulation of the spring constant [193–196]. In regards to squeezing below the ground state fluctuations in optomechanical cavities, Genoni et al. [197] proposed that this may be possible via continuous measurements and feedback. Experimental demonstration of quantum squeezing in optomechanical systems include high frequency microwave optomechanical device [198, 199] and in a hybrid photonic-phononic waveguide [200].

An alternative method to those mentioned previously is via non-adiabatic shifts of the mechanical frequency [201]. This method has previously been discussed in relation to light fields [202, 203] and similar ideas, utilising impulse kicks on a mechanical oscillator [204, 205]. This method of mechanical squeezing via non-adiabatic frequency shifts of a levitated particle motion will be demonstrated in this chapter. The non-adiabatic frequency shifts will be applied in a pulse scheme to levitated nanoparticles. Each pulse will consist of the trap frequency being rapidly reduced for a time, before being brought back to the original trap frequency.

In this chapter a discussion of the theory behind squeezing a levitated particle will be presented, followed by a description of the experimental setup. Several experimental studies will then be presented. The first of which will be the optimisation of a single pulse, both in terms of pulse duration and depth. Next, this method will be extended to applying multiple pulses to the levitated nanoparticle. The effect from varying the time between two pulses will be investigated, allowing for an optimal pulsing scheme to be devised. Then, the effect of applying greater number of pulses on the phase space and amount of squeezing to the particle motion will be explored. This will be followed by the application of squeezing pulses to parametric feedback cooled particles. Finally, a discussion about combining the techniques of parametric feedback cooling and squeezing pulses to achieve a quantum state will be presented.

7.1 Principle of squeezing by repeated frequency jumps

Under normal unperturbed motion of the particle in an optical trap, the motion is harmonic and the particle can be considered to be in a thermal state. The effect of squeezing on a harmonic oscillator is quite prenounced in the root mean square (rms) of the particle motion, but also visible in the phase space of the harmonic oscillator. The phase space of a dynamic system is the space in which all possible states of that system are represented, with each possible state corresponding to a single unique point in that phase space. For a levitated nanoparticle the phase space consists of all possible values of position and momentum variables. A harmonic oscillator in a thermal state has a symmetric and circular phase space distribution. If a harmonic oscillator undergoes a non-adiabatic frequency change, or in other words a sudden frequency jump, then the harmonic oscillator's motion becomes squeezed [201]. In the experiments carried out in this chapter, repeated frequency jumps will be used to enhance this squeezing effect.

The squeezing pulse scheme implemented here can be seen in figure 7.1. Point 1, the particle's motion is harmonic and unsqueezed - the corresponding phase space is shown as a blue circle. The sudden change in frequency between point 1 and 2 from ω_1 to ω_2 (note: $\omega_1 > \omega_2$) leads to squeezing in one quadrature and the phase space of the particle motion becomes an oval. If the oscillation frequency of the particle was to immediately jump back, it would cancel quadrature squeezing and restore the particle to its original state. If the particle motion is allowed to evolve for a quarter of a period of the new frequency, the phase space rotates such that its largest spatial extent is in the other quadrature (shown at point 3). At this point, a sudden jump back to the original frequency ω_1 enhances the amount of squeezing (as shown by the further elongated oval at point 4). The process of undergoing steps 1-4 is referred to as a frequency pulse in this work. It

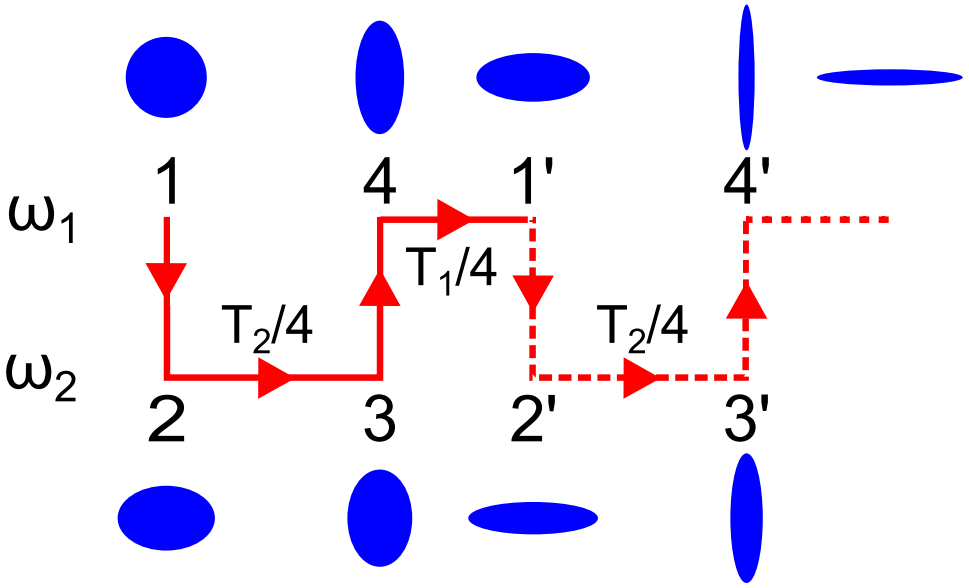

FIGURE 7.1: **Squeezing by repeated frequency pulses.** The particle begins with an oscillation frequency of ω_1 at point one with a circular phase space distribution (shown in blue). Undergoing an abrupt frequency change from ω_1 to ω_2 at point 2 causes a transformation in the phase space resulting in an oval-shaped phase space. Allowing for an evolution in time equal to $T_2/4$, where $T_2 = 2\pi/\omega_2$, the oval shaped phase space will have rotated by 90 degrees shown at point 3. A sudden frequency jump from 3 to 4, back to the original frequency, enhances the squeezing. Allowing the system to develop for a time equal to $T_1/4$, where $T_1 = 2\pi/\omega_1$, and then applying a pulse (steps 1-4) again will enhance the squeezing effect, causing the phase space to become a more and more elongated oval.

is possible (as will be shown in this chapter) to enhance the squeezing experienced by the particle, by allowing the particle to evolve for a quarter of its oscillation time, before applying another squeezing pulse (show by the red dashed line). This process can be repeated many times.

7.2 Theory of Squeezing

The model presented here was developed by Tommaso Tufarelli and Muynshik Kim. The model can be found in reference [206]. We present the derivation here to provide a theoretical basis for the work carried out in this chapter.

A quantum mechanical treatment of the squeezing protocol implemented in this chapter will be presented, in anticipation that future experiments may achieve quantum squeezing. However, it should be pointed out that since a levitated nanoparticle within an optical trap behaves as an harmonic oscillator, the classical and quantum equations of motion for position and momentum are formally identical. Therefore, the classical

analysis of these squeezing experiments only requires $\hat{X}$ and $\hat{P}$ to be interpreted as classical variables rather than quantum operators and the expectation values interpreted as ensemble averages in the classical sense,

$$\langle f(\hat{X}, \hat{P}) \rangle = \int \mathbb{P}(x, p) f(x, p) dx dp. \tag{7.1}$$

for any function f of the canonical variables, $P(x, p)$ being the joint probability density for classical position and momentum. Differences between the classical and quantum treatments would only become apparent when close to the quantum ground state. The experiments carried out in this section, even those implemented with parametric feedback cooling, are carried out in the regime of high thermal excitation.

To achieve squeezing, our system comprising of a nanosphere trapped in a harmonic potential is manipulated along the z axis, by switching between two Hamiltonians $\hat{H}_1$ and $\hat{H}_2$, where

$$\hat{H}_j = \frac{\hat{p}^2}{2m} + \frac{1}{2} m \omega_j^2 \hat{z}^2, \tag{7.2}$$

where $\hat{z}$ is the z component of the position operator, $\hat{p}$ the z component of momentum operator and the trapping frequency ω_j able to assume either a value of ω_1 or ω_2. As shown in figure 7.1 $\omega_1 > \omega_2$. As mentioned previously, the squeezing protocol presented here relies on the rapid switching between these two Hamiltonians [202, 203]. The annihilation operators corresponding to these two trap frequencies $\hat{a}$ and $\hat{b}$ can be written as

$$\hat{a} = \sqrt{\frac{m\omega_1}{2\hbar}} \Big(\hat{x} + \frac{i}{m\omega_1} \hat{p} \Big), \tag{7.3}$$

$$\hat{b} = \sqrt{\frac{m\omega_2}{2\hbar}} \Big(\hat{x} + \frac{i}{m\omega_2} \hat{p} \Big). \tag{7.4}$$

Note we have set $\hbar = 1$. The annihilation operators are related by a squeezing transformation of the form,

$$\hat{b} = \cosh(r) \hat{a} - \sinh(r) \hat{a}^\dagger. \tag{7.5}$$

with the squeezing parameter given by,

$$r \equiv \frac{1}{2}\log\left(\frac{\omega_2}{\omega_1}\right). \tag{7.6}$$

Before squeezing takes place, the particle is initially prepared in an arbitrary thermal state of $\hat{H}_1$. At time $t = 0$ the trap frequency is rapidly changed from ω_1 to ω_2 and the Hamiltonian becomes $\hat{H}_2$. The system is then allowed to evolve for a time t, equal to τ (the pulse duration), before rapidly switching back to the Hamiltonian $\hat{H}_1$. In the Heisenberg picture, this is a simple harmonic evolution of the operator $\hat{b}$ given by,

$$\hat{b} \to \hat{b}e^{-i\omega_2\tau} \tag{7.7}$$

In terms of the quadratures,

$$\hat{X} = \frac{\hat{a} + \hat{a}^\dagger}{\sqrt{2}} \tag{7.8}$$

and

$$\hat{P} = \frac{-i(\hat{a} - \hat{a}^\dagger)}{\sqrt{2}} \tag{7.9}$$

The matrix transformation can be written as $(\hat{X}, \hat{P}) \to M(\hat{X}, \hat{P})^\top$ where,

$$M = \begin{pmatrix} cos(\omega_2\tau) & e^{2r}sin(\omega_2\tau) \\ -e^{2r}sin(\omega_2\tau) & cos(\omega_2\tau) \end{pmatrix}. \tag{7.10}$$

The matrix M contains a combination of rotation and squeezing in the phase space of mode $\hat{a}$. The squeezing parameter $\lambda(\tau)$ is encoded in the singular values of MM and can be found as follows: Using $det(MM^\top) = 1$ it is possible to parametrise the eigenvalues of $MM^\top$ as $(\mu, 1/\mu)$ for some parameter, where $\mu > 0$. Note $\sqrt{\mu}$ quantifies the deformation of the standard deviations of the rotated quadratures. The mechanical squeezing parameter can be written as,

$$\lambda(\tau) = 10\ |log_{10}(\sqrt{\mu})| \tag{7.11}$$

where $\lambda(\tau)$ is given in units of decibels. The analytical expression for $\lambda(\tau)$ is unwieldy if τ is left generic. However, under the condition $\omega_2\tau = \pi/2$ maximum squeezing λ_{max} is obtained and it can be written,

$$\lambda_{max} = 10\ log_{10}\left(\frac{\omega_1}{\omega_2}\right). \tag{7.12}$$

7.3 Experimental Methods

To experimentally realise squeezing of an optically levitated particle non-adiabatic trap frequency jumps need to be introduced. The trap frequency is proportional to the square root of the trap stiffness and hence the square root of the trapping laser power (see equations 2.29, 2.29 and 2.31). Therefore to switch the trap frequency between one at a higher frequency ω_1 and one at a lower frequency ω_2, the trapping laser power needed to be manipulated. To achieve this rapid switching between potentials, a pulse modulation is imparted to the trapping laser. The experimental set up to achieve this is built upon the setup shown in figure 3.1, described in section 3 with additional components. The laser light is directed through an AOM, where it is modulated by an FPGA (Field programmable gate array)[1], which is used to generate a negative pulse profile. The light from the AOM is amplified by an EDFA, before being split by a beam splitter into two beams. One of the beams is low in power and used to trigger the oscilloscope. The second more powerful beam is then directed into the paraboloidal mirror, at the focus of which is a trapped silica nanosphere. The Rayleigh scatter from the trapped particle is collected and directed onto the single photodiode, where it is recorded by the scope. The optical set up used is shown in figure 7.2.

7.3.1 Pulse Generation, data sampling and recording

The optical pulses applied to the system are controlled by a program which runs on the FPGA[2] and generates a voltage signal to send to the AOM. The AOM is capable of modulating the laser light by 100%, however this full modulation is not used as the particle would be lost from the trap. A pulse is generated every 4 seconds and takes roughly 6 μs delay before it travels through the trap and is recorded by photodetector 2 (as labeled in figure 7.2) and recorded by the oscilloscope.

The photodetector 1 (as labeled in figure 7.2) is used to trigger the oscilloscope at the fall of the negative pulse. Both signals pertaining to the trapped nanosphere and pulse applied to the AOM are recorded. The recorded signal or time traces are 2 seconds long, with the centre being at the trigger of a negative pulse. To analyse the data, roughly

[1]The FPGA system used consisted of the following national instruments products: *NI PXIE-1062Q, NI PXIE-8133, NI 5781* and a *NI PXIE-7961.*

[2]The Labview/VHDL program was written by Ash Setter.

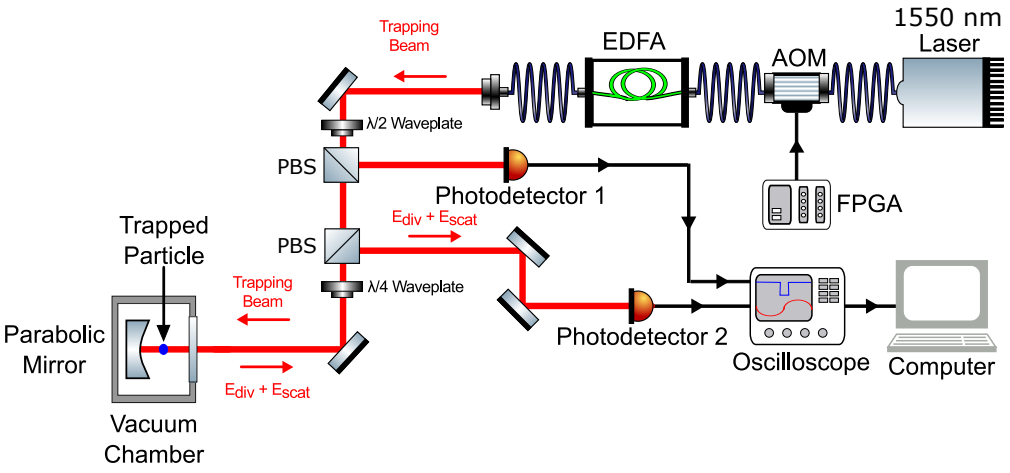

FIGURE 7.2: **Optical setup for squeezing of an optically trapped nanoparticle.** A 1550 nm laser light is directed through an AOM, before being amplified by an EDFA. The AOM modulates the laser light according to a signal from an FPGA, to generate a squeezing pulse at regular intervals. The light from the AOM is then split into two beams, one used to trigger the oscilloscope and the other directed into the paraboloidal mirror, at the focus of which is a trapped silica nanosphere. The Rayleigh scatter from the trapped particle is collected and directed on to a single photodiode and the particle's motion within the trap recorded.

1500-2000 samples are taken for each experimental parameter varied, the methods used will be described in section 7.4.2 and 7.4.3.

7.3.2 Generated Pulses

The pulses are generated in an FPGA, before being sent to the AOM to modulate the light. The FPGA which generates the squeezing pulses runs on a clock rate of 40 MHz and therefore can give a spatial resolution of 25 ns. The analog-to-digital converter allows a voltage output resolution of 0.3 μV; this allows for a squeezing pulse to be created to high precision (see figure 7.3 A). Providing the AOM is operating within the linear regime, it is capable of recreating the pulses, however, the pulse becomes deformed as it passes through EDFA [3]. The pulse deformation occurs due to a non-uniform pumping of the gain medium in time. As the power entering the EDFA drops, the EDFA attempts to compensate for this. The result of the EDFA compensation is that the pulse overshoots the original laser power and then quickly decays to its original value (see figure 7.3 B).

[3] Considering the work done in reference [206], a sensible question would be, why was the same experimental set up not used? In short, the laser (*IPG fiber laser* ($\lambda = 1550$ nm, 10 W)) used in those experiments broke and no new grants were won to allow for a new laser more suited to the task at hand to be purchased.

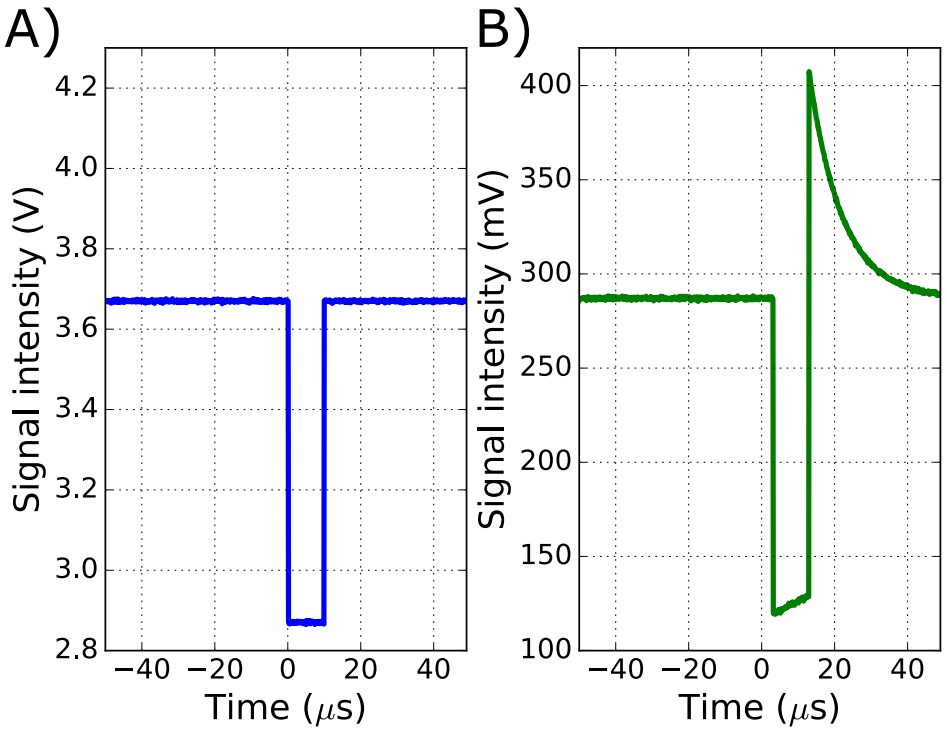

FIGURE 7.3: **Generated Squeezing pulse.** A) Squeezing pulse generated by the FPGA. B) Squeezing pulse in the laser light measured on photodiode 1. It can be seen that after the pulse is implemented, the laser power over-shoots its original value and then quickly decays back to its original value. Rapidly switching laser frequency, without allowing time for the phase space to decay is expected to produce no net squeezing.

7.4 Methods of data analysis

As will be discussed in this chapter, the effect of squeezing pulses on particle motion becomes more prominent when analysing multiple instances of the particle undergoing a squeezing pulse. 1500 samples of each pulse parameter are taken. As discussed, a squeezing pulse is created by rapidly dropping the trapping laser power. This has the effect of drastically reducing the signal measured on the photodetecor 2. The consequence of this is that for the duration of a squeezing pulse it is not possible to accurately determine the particle motion. In addition to this, the work presented here is interested in the behaviour of the particle before and immediately after the pulse, therefore the motion of the particle for the duration of the pulse time will be ignored. This section will detail the experimental methods used to extract information about the motional behaviour of the particle, before and after the squeezing pulse.

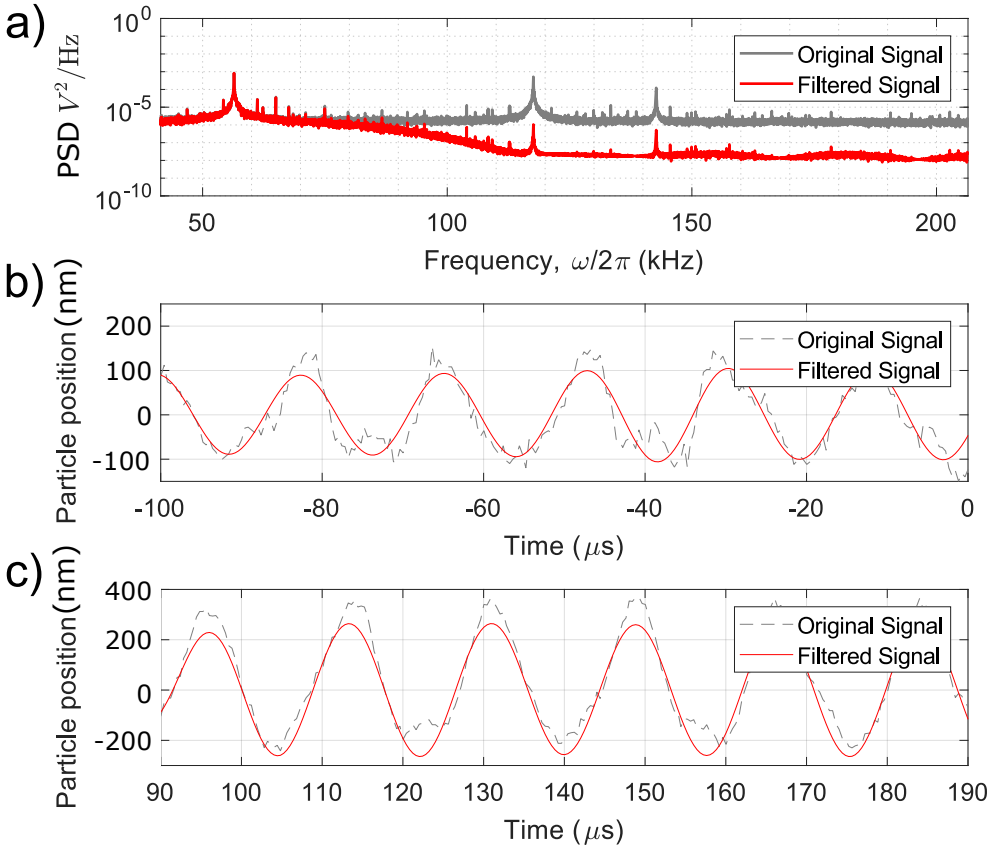

FIGURE 7.4: **Filtering of a single time trace.** As squeezing is applied to the z motional axis the motion of the other motional degrees of freedom are filtered out. a) The filtered and unfiltered PSD of particle motion b) Original and filtered time trace before the optical pulse. c) Original and filtered time trace after the optical pulse.

7.4.1 Filtering of experimental data

As discussed in section 3.5.2, the detected signal contains information about all three spatial degrees of freedom. As the squeezing pulse is only optimized to the z spatial degree of freedom, the motion from the other spatial degrees of freedom are filtered out via the use of a band-pass finite impulse response filter. Due to the presence of the pulse in the time trace, the signal is divided up into two sections; the region before the pulse and the region after the pulse. Each of these sections is then filtered independently. An unwanted consequence of this is that close to the pulse, the filtering results in edge effects. The edge effects of filtering generally mean that the phase space cannot reliably be calculated until roughly 46 μs after the pulses have ended. The time at which these edge effects are present in the data is excluded from the analysis of particle motion. The result of this filtering can be seen in figure 7.4.

7.4.2 Root mean square of the particle motion x_{rms}

The effect of the applied pulses on the motion of a particle can be seen more clearly by taking the root mean square of the particle motion. The root mean square of the particle motion can be calculated from multiple time traces of the particle motion. The root mean square (rms) of the time traces of the signal is given by

$$z_{rms}(t) = \sqrt{\frac{1}{Num}\Big((z_1(t))^2 + (z_2(t))^2 + (z_3(t))^2 + (z_4(t))^2 + ... + (z_{Num}(t))^2\Big)}, \quad (7.13)$$

where Num is the number of time traces used in the calculation, while the subscript indicates the number of the time trace used and t indicates the time at which each value of z is taken from the time traces. The z_{rms} for a pulse applied to a levitated particle is shown in figure 7.6. As expected, for a harmonic oscillator the z_{rms} is constant before the pulse. In contrast, the region after after the pulse oscillates - this is a signature of quadrature squeezing and is caused by the oscillation between suppression and expansion of the position quadrature of the particle.

7.4.3 Phase space analysis

Phase space distributions consist of a multidimensional space, in which each axis of the coordinates is required to specify the state of a physical system. In the case of a harmonic oscillator, the state can be described at an instant in time by position and momentum. The position of the particle is known in time and thus the momentum can be calculated using

$$p_z(t) = mv_z(t) = m\frac{dz(t)}{dt}. \quad (7.14)$$

where $v_z(t)$ is the velocity of the levitated particle. A phase space plot can be generated for a given time, using the positional information in each of the 1500 data sets. The experiments in this thesis are performed in the classical regime, in that we observe quadrature variances that are several orders of magnitude larger than those in the quantum ground state. Therefore, we may estimate the particles momentum by taking the time differential of the position measurement. In passing we note that, in the quantum regime, our continuous measurement process would require a more rigorous treatment [207]. To generate the phase space plots, such as that seen in figure 7.5, a squeezing pulse is applied to the system 1500 times and the motion of the particle recorded before

and after each pulse, creating 1500 time traces. For each time trace the corresponding momentum of the particle is calculated before and after the pulse using equation 7.15. The phase space is then generated by plotting the momentum and position of a particle at a time t defined relative to the start of the optical pulse, for each time trace. An example of the resulting phase space can be seen in figure 7.5.

7.4.4 Calculating the squeezing parameter λ

To characterise the amount of squeezing caused by a squeezing pulse we use the definition of squeezing given in equation 7.12, rewritten in terms of the quadrature variances [206],

$$\lambda = 10log_{10}\left(\frac{\Delta z_1}{\Delta z_2}\right). \tag{7.15}$$

where Δz_1 and Δz_2 are the positional variance before and after the pulse respectively. The positional variance is extracted by working out the variance in the position projection of the phase space. It should be noted that the same results would be obtained using the momentum variance.

7.5 Single Pulse Squeezing

Initial investigations were carried out using a single pulse to optimise the squeezing protocol. Before application of the squeezing pulse the circular phase space distribution (as expected for a thermal state) is observed (see figure 7.5 A). Upon application of the pulse the telltale signs of squeezing were seen, namely a reduction in one of the phase space axes and elongation in the other (see figure 7.5 B). The squeezed state is observed to rotate in phase space (see figure 7.5 B-C) and decay back into a thermal state.

7.5.1 Decay time of the squeezed state

To examine the decay of the squeezed state we look at the change of the z_{rms} with time, as shown in figure 7.6 A. Initially, before the application of the squeezed state of the particle, the z_{rms} is roughly constant, as the phase of the oscillation is random between the 1500 individual pulse applications. The pulse region has been highlighted in gray in figure 7.6 A. The region after the squeezing pulse illustrates damped phase coherent oscillations of the z_{rms} position of the particle. The oscillations are at twice the frequency of particle motion, see figure 7.6B. This is a signature sign of quadrature

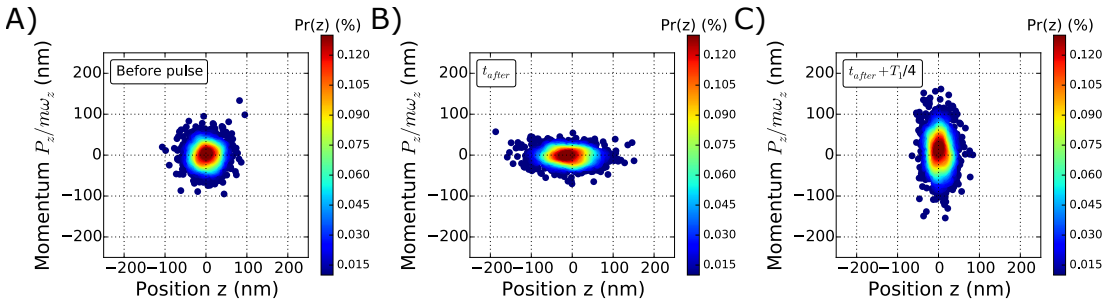

FIGURE 7.5: **Experimentally measured phase space distributions of the particles mechanical state, before and after the squeezing pulse.** Density plots of the phase space distributions for z motion, at three different times, for a pulse duration, $= T_2/4$. The average displacement of the state has been subtracted in each graph. **A) State of the particle motion before the pulse is applied.** The state is well approximated by a Gaussian distribution, as is expected for a thermal state. **B) Phase space distribution shortly after the pulse has been applied (time t_{after}).** Note how it presents clear signatures of squeezing. **C) The phase space distribution at a time $t_{after}+T_1/4$.** The squeezed state rotates in phase space while squeezing degrades with time, due to background gas collisions that restore the initial thermal distribution.

squeezing. The oscillation in the z_{rms} amplitude of the particle position is due to the oscillation between suppression and expansion of the position and velocity quadratures of the particle. The z_{rms} oscillation decays within about 1550 μs to 1600 μs, which gives a rate of thermalisation to the temperature of the background gas molecules between 605 Hz and 625 Hz. This is in good agreement with the value for Γ_0 estimated via Lorentzian fit of equation 4.15 and the expected theoretical value for a particle at P_{gas}=4.3×10^{-2} mbar (from equation 4.12). The offset of the z_{rms} motion observed in figure 7.6 A is interpreted as noise, due to the rapid switching of voltage to implement the pulse and will be accounted for in section 7.5.2.

7.5.2 Introduction of the noise model

The model presented here was developed by Tommaso Tufarelli and Muynshik Kim. The model can be found in reference [206]. We present the derivation here, to provide a theoretical basis for the work carried out in this chapter.

To account for the noise observed in the system, phase noise is introduced into the theoretical model used to describe the effect of the squeezing model. The most significant phase noise generated is during the abrupt voltage change. This is modelled in the system by assuming that the squeezing operation induces some loss of coherence to mode $\hat{b}$, which is independent of the pulse duration τ_2. We note that, all the adopted pulse lengths demonstrated in this work are short enough to prevent other τ_2 dependent

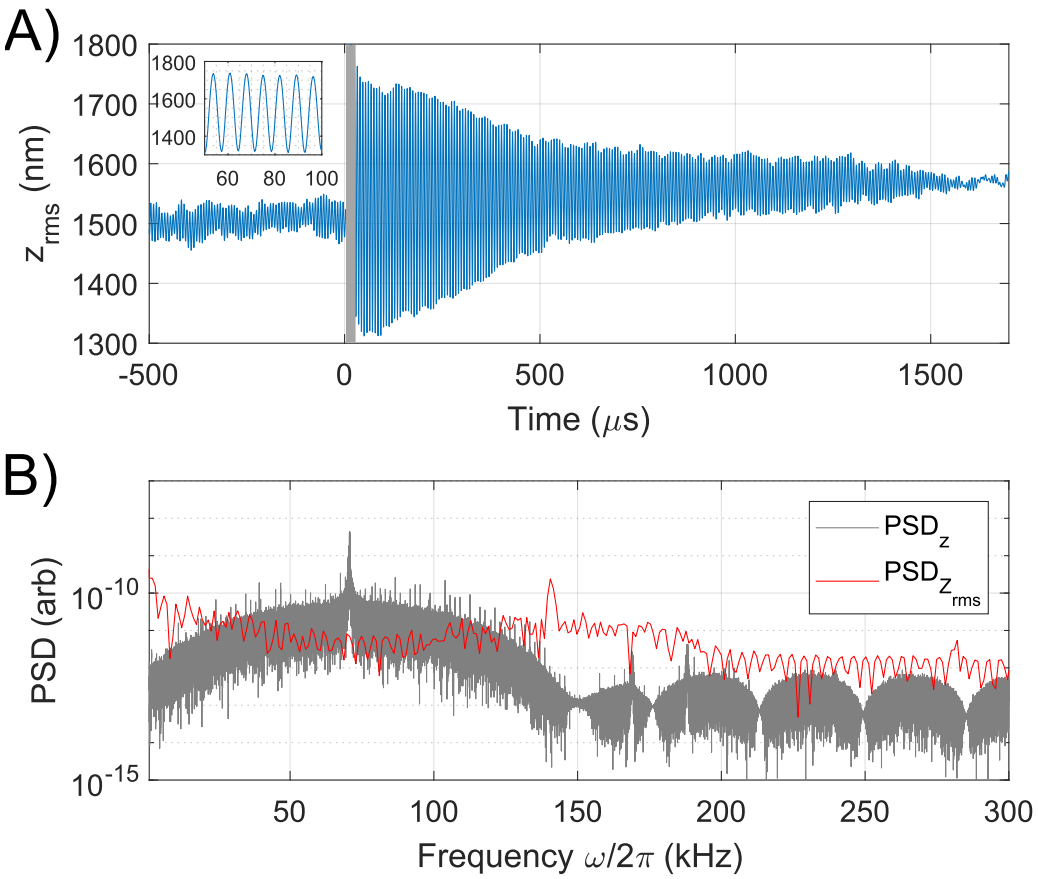

FIGURE 7.6: **A) Root mean square position z_{rms} as a function of time** obtained from 1500 pulse sequences applied to the same particle The region of pulse duration has been highlighted in grey. The sub graph shows a zoom in on the z_{rms} oscillations. **B) z_{rms} oscillation frequency** The grey PSD shows the the power spectral density of the filtered data PSD_z. The red PSD shows the power spectral density of the z_{rms}. It can be seen that the z_{rms} oscillates at $\omega_{z_{rms}} = 140 \times 2\pi$ kHz, twice the trap frequency of the levitated particle $\omega_z = 70 \times 2\pi$ kHz. It can be seen that the amplitudes of the z_{rms} before the pulse at times t=-500 μs and t= 1550 μs are not equal. The z_{rms} amplitude is observed to vary in the between each pulse application, making it difficult to determine an accurate decay time of the squeezed state.

forms of noise affecting the motion of the particle in a significant way. The noise in the system is formulated in terms of covariance matrices [208].

The state of the system is initially thermal, therefore the assumption can be made without loss of generality that $\langle \hat{a} \rangle = \langle \hat{b} \rangle = 0$ throughout the dynamics. The covariance matrix of mode $\hat{a}$ therefore can be defined as

$$\sigma_a = \begin{pmatrix} 2\langle \hat{X}^2 \rangle & \langle \hat{X}\hat{P} + \hat{P}\hat{X} \rangle \\ \langle \hat{X}\hat{P} + \hat{P}\hat{X} \rangle & 2\langle \hat{P}^2 \rangle \end{pmatrix}. \tag{7.16}$$

where $\langle\hat{A}\rangle \equiv \top\mathrm{r}[\rho\hat{A}]$ for any operator $\hat{A}$, and ρ is the density matrix for the z motion of the levitated particle. In the convention used here, the covariance matrix of the vacuum state is unit determinant. We assume that in an initial thermal state of mode a, characterised by the covariance matrix

$$\sigma_a(0) = \begin{pmatrix} 2N_1+1 & 0 \\ 0 & 2N_1+1 \end{pmatrix}. \tag{7.17}$$

where,

$$N_1 \equiv \frac{1}{e^{\frac{\hbar\omega_1}{k_b T}} - 1}. \tag{7.18}$$

The subsequent dynamics of the covariance matrix, as induced by the Hamiltonian $\hat{H}_2$, can be determined by noting that $\langle\hat{b}^\dagger\hat{b}\rangle$ is independent of time, while

$$\langle\hat{b}(\tau)^2\rangle = \langle\hat{b}(0)^2\rangle e^{-i\omega_2\tau}. \tag{7.19}$$

The loss of coherence is modelled by rescaling $\langle\hat{b}^2\rangle \to \Upsilon\langle\hat{b}^2\rangle$, with $0 \leq \Upsilon \leq 1$ with $\langle\hat{b}^\dagger\hat{b}\rangle$ unchanged. Using the relationship between $\hat{a}$ and $\hat{b}$, we can obtain the matrix elements for $\sigma_a(\tau)$

$$[\sigma_a(\tau)]_{11} = (2N_1+1)\left[\frac{1+c(\tau)}{2} + \frac{\omega_1^2}{\omega_2^2}\frac{1-c(\tau)}{2}\right] \tag{7.20}$$

$$[\sigma_a(\tau)]_{22} = (2N_1+1)\left[\frac{1+c(\tau)}{2} + \frac{\omega_2^2}{\omega_1^2}\frac{1-c(\tau)}{2}\right] \tag{7.21}$$

$$[\sigma_a(\tau)]_{12} = (2N_1+1)s(\tau)\frac{\omega_1^2-\omega_2^2}{2\omega_1\omega_2} \tag{7.22}$$

$$[\sigma_a(\tau)]_{21} = [\sigma_a(\tau)]_{12} \tag{7.23}$$

where we have defined,

$$s(\tau) \equiv \Upsilon sin(2\omega_2\tau) \text{ and } c(\tau) \equiv \Upsilon cos(2\omega_2\tau) \tag{7.24}$$

To calculate the amount of squeezing that has been applied to the levitated particle we define,

$$\mu_{min} \equiv \text{smallest eigenvalue of } \sigma_a(\tau). \tag{7.25}$$

which quantifies the variance in the squeezed quadrature. We can define a squeezing parameter (in units of decibels) by comparing μ_{min} with the initial variance of the particle oscillation quadratures in thermal equilibrium $\mu_{min}(0) = 2N_1 + 1$. Therefore we can write,

$$\lambda = -\frac{1}{2} 10\ log_{10}\left(\frac{\mu_{min}(t)}{2N_1 + 1}\right). \tag{7.26}$$

The factor of 1/2 occurs because squeezing is defined in terms of standard deviation rather than variances.

7.5.3 Pulse duration

It can be seen from figure 7.1 that to achieve maximum squeezing, the duration of a pulse should be $T_2/4$, that is to say, the time in which it takes for the phase space of the particle motion to be rotated 90°. To quantify the effect of pulse duration τ on the strength of the squeezing on the particle, a pulse of different pulse length was applied to a levitated particle. The applied pulse jumped between $\omega_1 = 2\pi \times 70$ kHz and $\omega_2 = 2\pi \times 22$ kHz. The values of λ at different values of τ can be seen in figure 7.7. It can be seen that maximum squeezing occurred at $T_2/4$ as expected. A reasonable fit can be obtained to the data in figure 7.7 by assuming that the squeezing pulse is affected by phase noise, whose strength is τ independent, as described in section 7.5.2. It should be noted that the largest squeezing factor achieved experimentally from a single squeezing pulse is 3.2 dB, which is lower than the expected $\lambda_{max} = 5$ dB from equation 7.12 and is attributed to phase noise.

7.5.4 Increasing λ

The first and most obvious route to increasing λ would be to increase the difference between ω_1 and ω_2, as can be seen from equation 7.12. This however is more experimentally difficult than it would first seem, within the experimental set up. To increase the ratio ω_1/ω_2 the laser power used to create the trap needs to be increased (as $\omega_0 \propto$

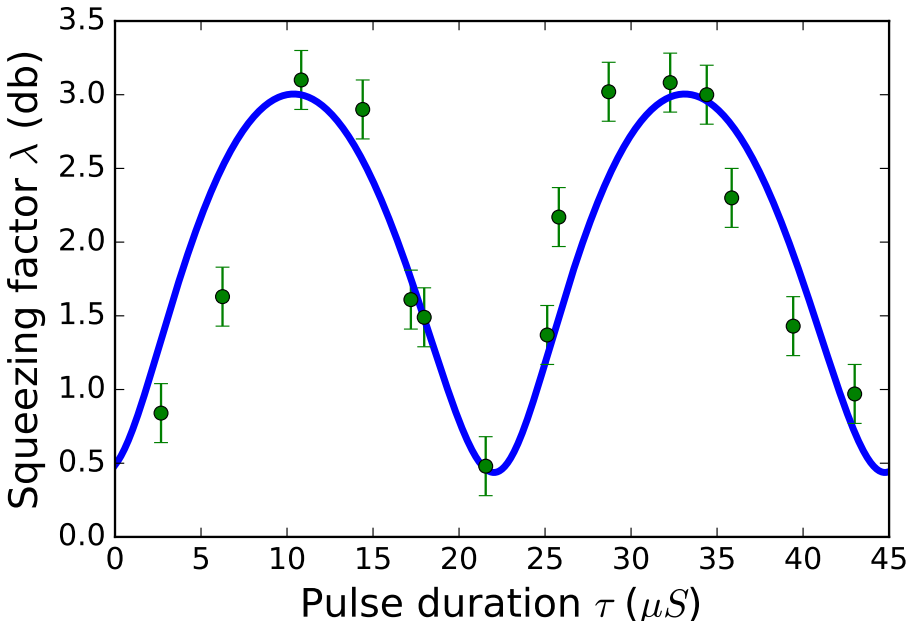

FIGURE 7.7: **Squeezing factor λ as a function of pulse duration τ.** The theoretical fit to the data (blue line) has been done according to equation 7.26. It can be seen that maximum squeezing occurs when τ equals $T_2/4 = 11$ μs and $3T_2/4 = 34$ μs. While minimum squeezing occurs when τ equals $T_2/2 = 23$ μs and $T_2 = 45$ μs . The data shown here is for a squeezing pulse applied to a levitated 26 ± 2 nm diameter silica nanosphere of mass $2.6 \pm 0.2 \times 10^{-20}$ kg.

$\sqrt{\text{laser power}}$) and the light modulated by a greater amount. While the AOM is capable of modulating the laser light by larger amounts and quick enough, the EDFA used was already operating at maximum power and thus the trap frequency could not be increased. The solution therefore explored, is by use of multiple pulses as described in figure 7.1.

7.6 Multiple Pulses

To increase the effect of squeezing, multiple pulses are implemented in the fashion shown in figure 7.1. It is expected that if the pulses are applied optimally, each successive pulse will increase the amount, by which the particle motion is squeezed by the same amount allowing us to write,

$$\lambda_{max} = 5N \ log_{10}\left(\frac{\omega_1}{\omega_2}\right). \tag{7.27}$$

Where N is the number of squeezing pulses applied to the levitated particle.

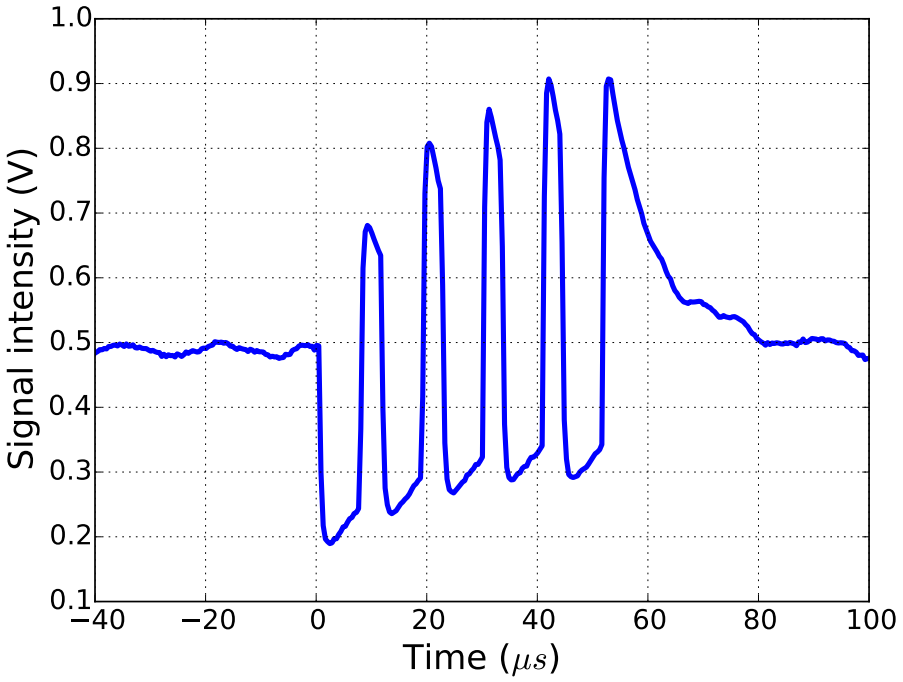

FIGURE 7.8: **The measured optical signal for a 5 consecutive squeezing pulses.** The EDFA causes the laser to overshooting its original intensity. The effect becomes more prominent with each successive pulse till the 4th pulse, after which a maximum of optical intensity is reached.

7.6.1 Generating multiple pulses

To generate multiple pulses the experimental set up in figure 7.2 is used. The only difference is that the FPGA now generates a signal containing multiple pulses, which is used to modulate the laser light. The optical response to a 5 pulse electrical signal can be seen in figure 7.8. The overshoot of the laser intensity caused by the EDFA becomes more prominent with each successive pulse, until the 4th pulse where a maximum in optical intensity is reached.

7.6.2 Time Between Pulses τ_1

It can be seen from figure 7.1 that the correct time to apply a second pulse to achieve maximum squeezing is after the phase space of particle motion has rotated 90° after the first pulse has ended. To investigate this, two successive pulse were applied to a levitated 20 ± 2 nm diameter silica nanosphere of mass $1.1 \pm 0.2 \times 10^{-20}$ kg, trapped at $\omega_1 = 2\pi \times 56$ kHz. The effect of applying two squeezing pulses with a different time between the pulses λ_1 can be seen in figure 7.9. It can be seen that maximum squeezing occurs at around $\tau_1 = 4.5$ μs and $\tau_1 = 12.5$ μs, which corresponds to roughly $T_1/4$ and

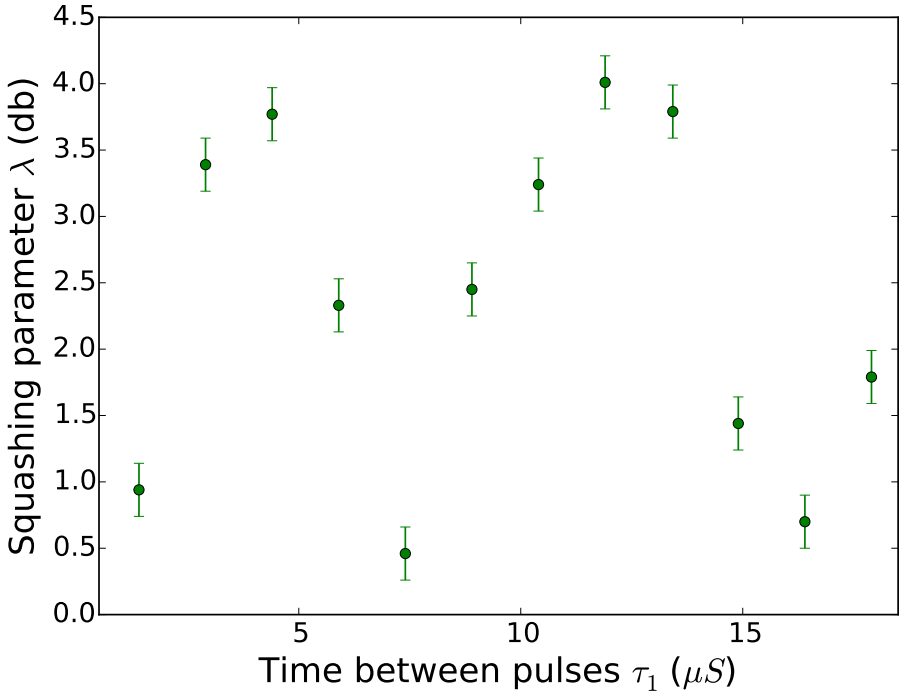

FIGURE 7.9: **Squeezing factor λ for the effect of two pulses as a function of time beteen pulses τ_1.** The maximum squeezing occurs at roughly $T_1/4$ and $3T_1/4$, while the minimum occurs at at around $T_1/2$ and T_1.The data shown here is for a squeezing pulse applied to a levitated 20 ± 2 nm diameter silica nanosphere of mass $1.1 \pm 0.2 \times 10^{-20}$ kg.

$3T_1/4$ respectively. While the minima occurs at around $\tau_1 = 7$ μs and $\tau_1 = 16$ μs, which corresponds to roughly $T_1/2$ and T_1 respectively. This suggests as would be expected, a similar relationship as to that shown in figure 7.7, for the width of a squeezing pulse and λ.

7.6.3 Effect of multiple squeezing pulses on the phase space

The natural question once knowing the optimal time to leave between pulses, is to ask what the relation between the number of pulses applied and the squeezing factor would be. Therefore to investigate this, an increasing number of pulses was applied to a 62 ± 2 nm diameter levitated particle. The pulses applied to the system had the following ratio: $\omega_1/\omega_2 = 1.7 \pm 0.2$.The results of which can be seen in figure 7.10.

It can be seen that upon the application of a second pulse (See figure 7.10 C), the phase space becomes more oval, as expected from the combined effect of two squeezing pulses. However, upon application of the 3rd pulse, the phase space distribution starts to extend into the nonlinear region of the trap (see section 2.3.6) and the phase space of particle motion starts to curl at the edges (see figure 7.10 D). This effect becomes more

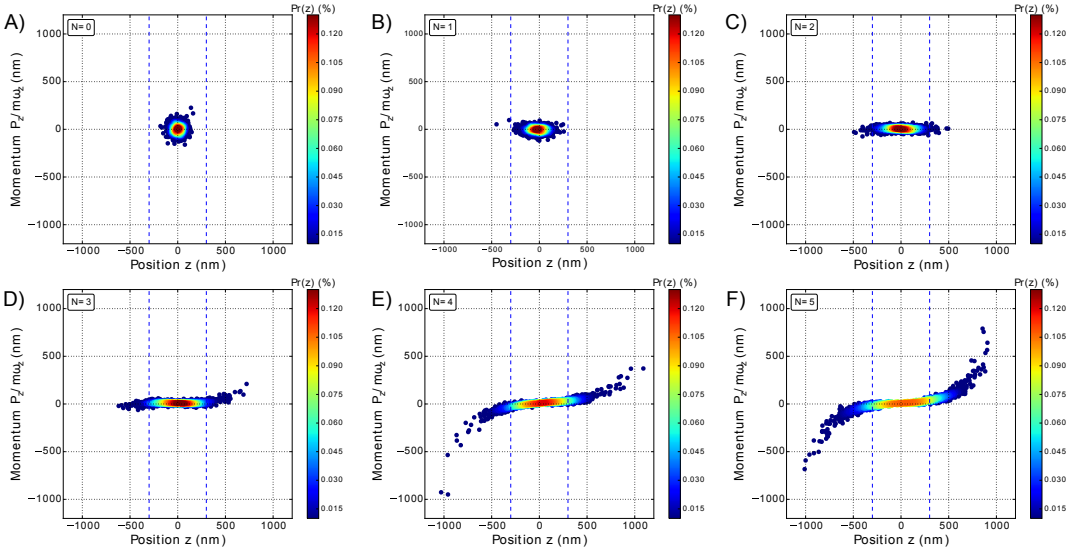

FIGURE 7.10: **Effect of multiple squeezing pulses on the phase space of particle motion.** The blue dashed lines shows the distance from the centre of the trap where linear spring approximation starts to break down. The data shown is for a 62 ± 2 nm diameter particle trapped at 2×10^{-2} mbar. The phase spaces are shown for a time $t_{after} = 70$ μs after the applied pulses have finished. **A) N=0** The particle's phase space in a thermal state is circular in shape. **B) N=1** Squeezing of the particle motion is observed. **C) N=2** The second pulse further squeezes the phase space distribution. **D) N=3** Nonlinear effects start to appear as the particle's motion is squeezed into the nonlinear region of the optical trap. **E) N=4** The effect of squeezing is increased and the nonlinear effects become more apparent. **F) N=5** Both the effects of squeezing and nonlinear affects are increased further.

pronounced as the number of applied pulses increases, meaning the particle is squeezed into the greater extremes of the optical trap (see figure 7.10 D-F). The application of the 6th pulse to the levitated particle resulted in it being lost from the trap. The current working theory for the 6th pulse, resulting in a particle becoming lost from the trap is that, during the duration of the 6 pulses being applied to the system, the laser power is not sufficient for the particle to remain trapped. This theory however, needs further testing.

7.6.4 Nonlinearities in particle motion

As discussed in section 2.3.6, at large displacements the optical potential becomes anharmonic as the linear spring approximation breaks down. Therefore, at large oscillations the particle can be considered to be a Duffing oscillator and the optical potential can now be considered to feature a Duffing nonlinearity. For the Gaussian field distribution used in these experiments, the nonlinear coefficients in the z spatial degree of freedom is given by [62]

$$\xi = -2/W_z^2, \tag{7.28}$$

where W_z is the beam waist in the z spatial degree of freedom. It should be noted that similar equations apply to the x and y spatial degree of freedom. For small displacements $|z| << |\xi_z^{-1/2}|$, the nonlinearity is negligible and the three motional degrees of freedom decouple. In the situation where $|z| >> |\xi_z^{-1/2}|$ the linear spring approximation (described in section 2.3.6) is no longer valid the gradient force (equation 2.19), no longer accurately describes the experimental system. In this situation the gradient force is more accurately described by the modified equation

$$\mathbf{F}_{grad}^{Duff} = -k_z\left(1 + \sum \xi_z z^2\right) z \tag{7.29}$$

The equation of motion can thus be written as

$$\ddot{z} + \omega_z Q_z^{-1}\dot{z} + \omega_z\left(1 + \sum \xi_z z^2\right) z = \mathbf{F}_{th}/m \tag{7.30}$$

To fully understand the spiral-like phase spaces that occur after multiple squeezing pulses, the additional terms that arise in the equation of motion due to nonlinear nature of the trap at its extremities will need to be modelled. This currently remains work for the future.

7.6.5 Evolution of the phase space after the squeezing pulses

After the squeezing pulse, the phase space rotates and slowly decays back into its original thermal state. The decay that occurs after 5 consecutive squeezing pulses is shown in figure 7.11. It can be seen that the outermost edges of the phase space start to resemble a spiral galaxy. This is because the outer most part of the phase space rotates slower than the centre of the phase space and the outermost edges start to wrap around the centre. This wrapping effect appears to be similar to whorls which are not associated with classical stochasticity and occur in time independent anharmonic oscillators [209].

7.6.6 Squeezing parameter vs number of squeezing pulses

The ultimate characterization of the effectiveness of the squeezing pulses applied to the system is given by the squeezing parameter. For each of the phase spaces in figure 7.10,

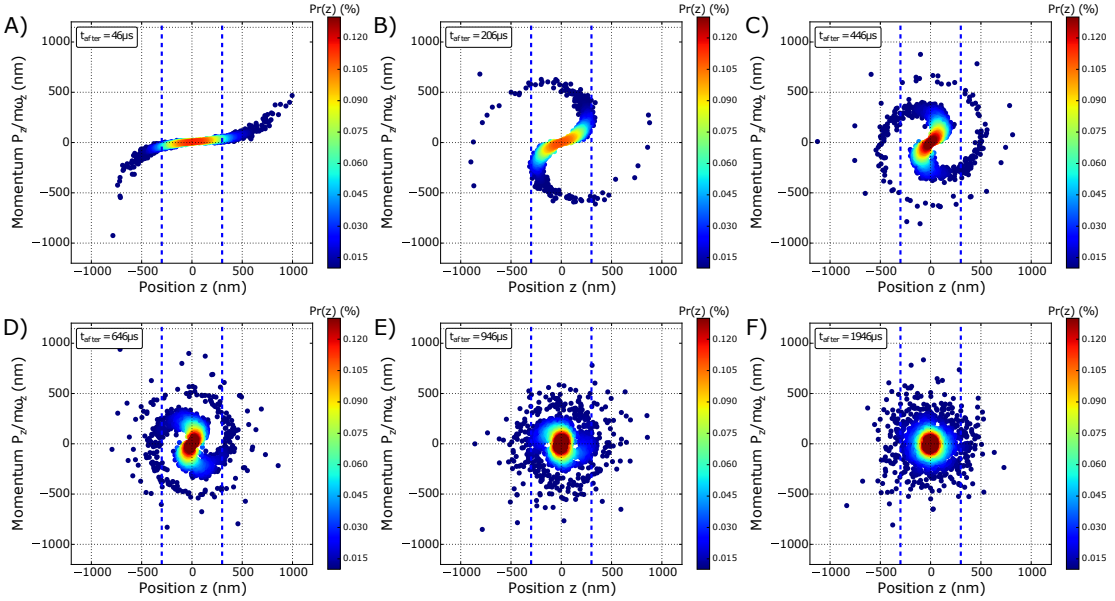

FIGURE 7.11: **Decay of the squeezed state created by the application of 5 squeezing pulses.** The blue dashed lines shows the distance from the centre of the trap where the linear spring approximation starts to break down. The data shown is for a 62 ± 2 nm diameter particle trapped at 2×10^{-2} mbar. **A)** $\mathbf{t_{after} = 46}$ **μs** Due to the limitations in the data analysis methods used to analyze the system the state in terms of the phase space can not be measured before this point. **B)** $\mathbf{t_{after} = 206}$ **μs** As the squeezed state decays the phase space starts to wrap around itself. **C)** $\mathbf{t_{after} = 446}$ **μs** The phase space spirals around itself. **D)** $\mathbf{t_{after} = 646}$ **μs** The phase space starts to broaden as the squeezing decays, **E)** $\mathbf{t_{after} = 946}$ **μs** The squeezed state becomes more circular while still retaining some signature of squeezing. **F)** $\mathbf{t_{after} = 1946}$ **μs** The effect of squeezing in the system is gone and the system decays into a thermal state heated by the phase noise in the system. This heated state decays back into a thermal state at 300K before the next pulse is applied.

the squeezing factor is evaluated and plotted as a function of a number of pulses in figure 7.12. It is expected that with each successive pulse applied to the system, it will squeeze the particle by,

$$\lambda_N = N\lambda_1 \tag{7.31}$$

Where λ_N is the squeezing parameter after N pulses and λ_1 is the squeezing parameter for a single pulse. In figure 7.12 it can be seen that this relationship is not observed exactly as expected. While the squeezing factor does increase with each successive pulse, the increment is reduced slightly each time. It is believed that the this may be explained by considering the decay in time of the squeezed state. Between the time in which the final pulse is applied and the first snapshot of the phase space that can be taken (see section 7.4.1), the phase space will have decayed from its original squeezed state by some amount. This means that, if the phase space changes significantly during this time, the true value of the squeezing can no longer be measured. The further from the centre

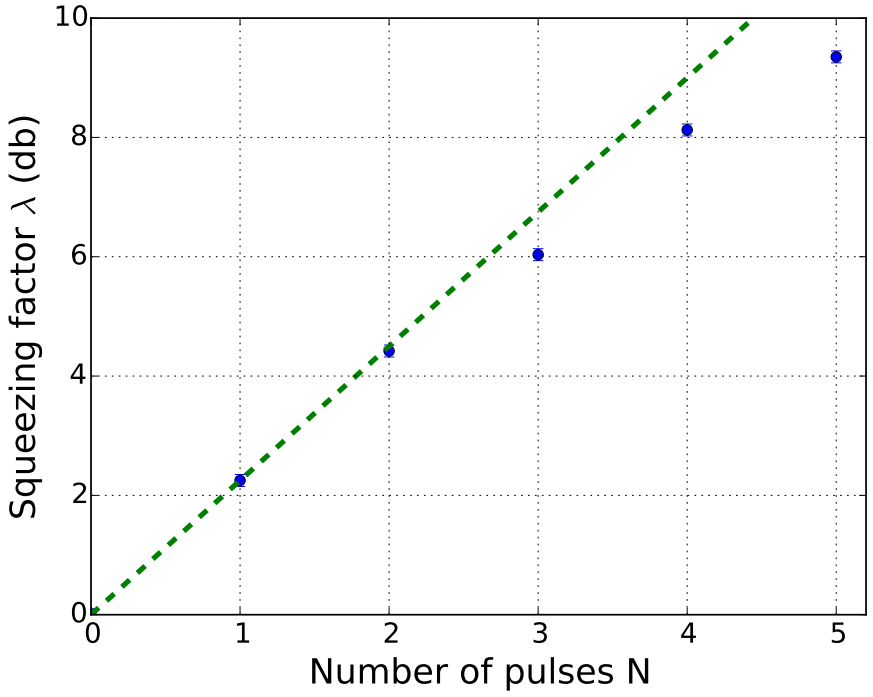

FIGURE 7.12: **The squeezing parameter as a function of pulse number.** The dashed line is the expected λ calculated using equation 7.31. The data shown is for a 62 ± 2 nm diameter particle trapped at 2×10^{-2} mbar.

of the trap, the nonlinear effects are expected to have a greater effect on the particles motion, explaining why this effect would be more pronounced in a shorter period of time for the application of a greater number of pulses. Other effects which may play a role includes increasing amount of phase space noise and the non-ideal pulse shapes, which may reduce the effectiveness of the squeezing pulses implemented. The maximum amount of squeezing measured after the application of 5 pulses, is characterised by the squeezing factor as $\lambda = 9.4 \pm 0.1$ dB.

7.7 Squeezing of a cooled levitated nanoparticle

Parametric feedback cooling of the particle's centre of mass temperature (demonstrated in chapter 6), results in a suppression of both phase space quadrants, therefore, decreasing the particle's average position and momentum. The amount in which the position and momentum quadratures can be reduced is limited by noise in the system. In contrast, squeezing suppresses the distribution of states in one quadrature at the expense of the other. Therefore, squeezing provides a potential method in which to increase the amplitude suppression, achieved by parametric feedback cooling.

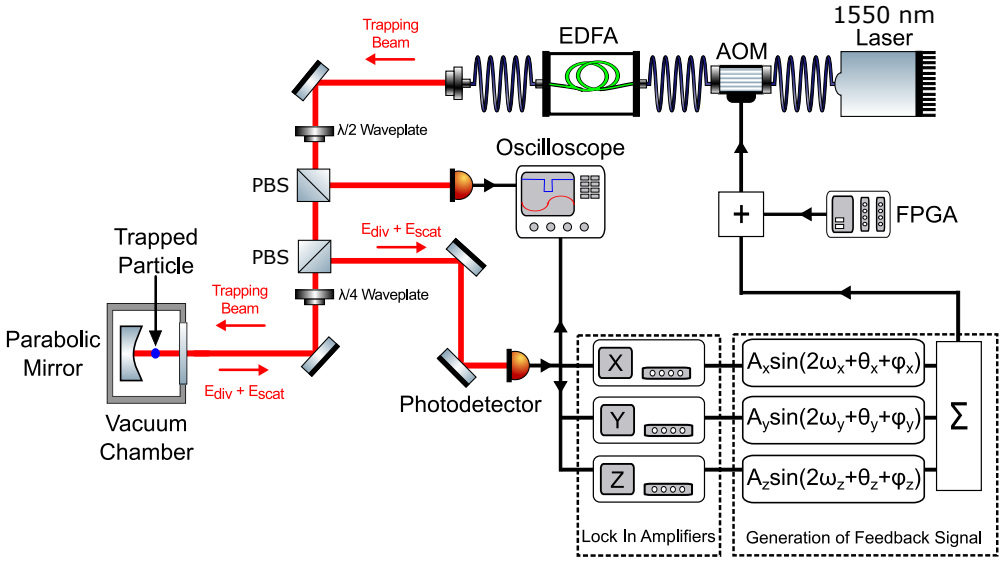

FIGURE 7.13: **Optical setup for squeezing a cooled optically levitated nanoparticle.** A 1550 nm laser light is directed through an AOM, before being amplified by an EDFA. The AOM modulates the laser light according to the parametric feedback signal and a signal from an FPGA, which generates squeezing pulses at regular intervals. The light from the AOM is then split into two beams, one used to trigger the oscilloscope and the other directed into the paraboloidal mirror, at the focus of which is a trapped silica nanosphere. The Rayleigh scatter from the trapped particle is collected and directed onto a single photodiode and the particle's motion within the trap recorded. Once detected, the modulation of the light caused by the particle motion is separated via the use of three lock-in amplifiers. The feedback signal is then generated and added to the squeezing pulse, before being fed into the AOM.

7.7.1 Experimental setup

To implement squeezing pulses to a cooled nanoparticle, the parametric feedback loop described in section 6.2 and the squeezing apparatus from section 7.3 were implemented in a single setup (shown in figure 7.13). Both systems operate independently, generating an electrical signal each; these signals are added together using a built in feature of the *ZI HF2LI Lock-in Amplifier*. The same AOM is used to modulate the light, for both the feedback cooling and squeezing pulses.

7.7.2 Effect of parametric feedback cooling on the phase space of particle motion

Parametric feedback cooling, when activated in the optical trap, has the effect of cooling the particle motion; that is to say, reducing the amplitude of particle motion and hence its energy. As the centre of mass energy is reduced, both the maximum amplitude and velocity of the particle are reduced proportionately and the particle motion remains in a thermal state. The effect on the phase space of particle motion for a 60 ± 3 nm

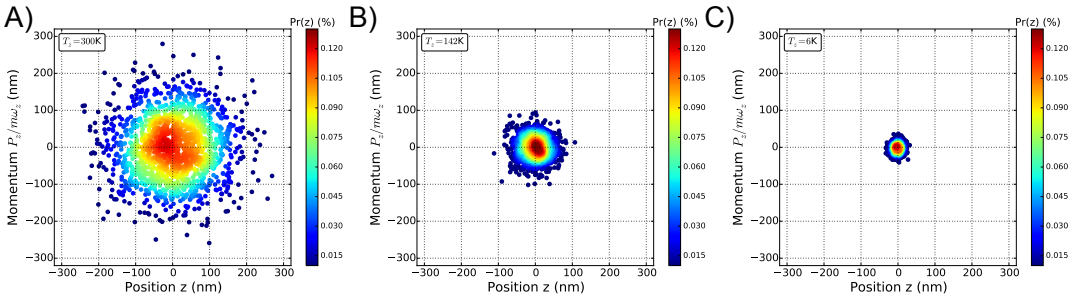

FIGURE 7.14: **Effect of parametric feedback cooling on the phase space of particle motion.** The data shown is for a 60 ± 3 nm silica nanoparticle at 5×10^{-2} mbar. **A) $\mathbf{T_z = 300}$ K** The phase space of an uncooled particle. **B) $\mathbf{T_z = 142}$ K** It can be seen that as the particle is cooled the phase space reduces in size. **C) $\mathbf{T_z = 6}$ K** The phase space continues to decrease in equal proportion in the momentum and positional dimensions, as the amount of cooling is increased.

diameter silica nanoparticle can be seen in figure 7.14. For more details on the effect parametric feedback cooling has on the motion of the particle more detail has been provided previously in chapter 6.

7.7.3 Effect of parametric feedback cooling on the decay rate of λ

To see how parametric feedback effects the the squeezed states rate of decay, the modulation depth and hence the strength of parametric feedback cooling was varied, while keeping the squeezing pulse constant, and the squeezing parameter measured. Figure 7.15 A shows the values of squeezing obtained at time 46 μs after the pulse for a variety of modulation depths. Figure 7.15 B, shows the corresponding centre of mass temperature for each squeezing factor measured[4]. It can be seen that as the strength of the parametric feedback cooling is increased, the measured value of the squeezing factor at time 46 μs after the pulse is reduced. The feedback force acts in such a way as to reduce the energy of the levitated particle and hence bring the particle back into a thermal state. Increasing the strength of parametric feedback cooling reduces the decay time of the squeezed state, resulting in the measured squeezing for a particular pulse appearing reduced in effectiveness. To measure the true squeezing factor achieved from a squeezing pulse the particle motion would have to be measured immediately as the pulse finishes. The ability to do this is not currently built into the experimental system due to data analysis limitations (see section 7.4.1).

[4]It is worth noting that parametric feedback is on both during and after the pulse.

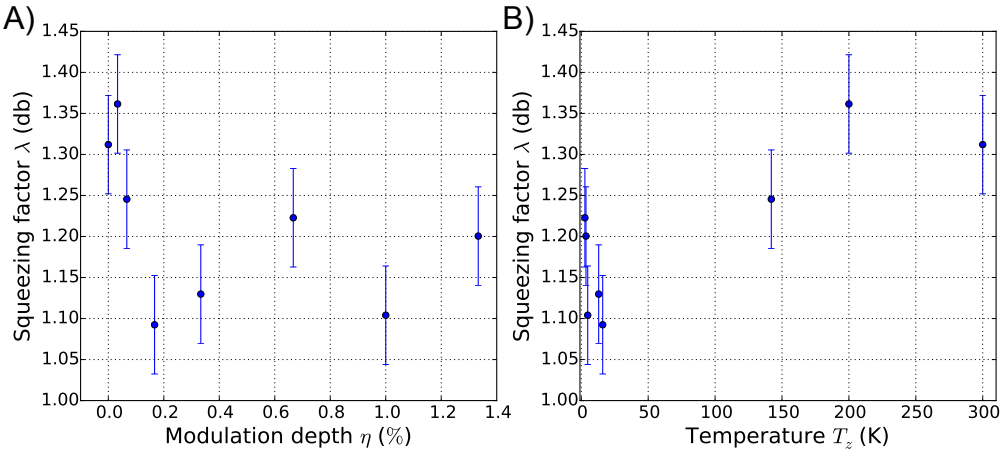

FIGURE 7.15: **The effect of parametric feedback cooling on the measured λ.** The data shown is taken at a time $t_{after} = 46$ μs after the application of a single squeezing pulse to an optically levitated 60 ± 3 nm silica nanoparticle at 5×10^{-2} mbar. **A) The effect of modulation depth on the measured λ.** It can be seen that as the modulation depth is increased, the measured value of λ decreases, before flattening out. Similar to figure 6.9 **B) The measured λ for a squeezed particle at different temperatures.** The measured squeezing factor decreases with decreasing temperature.

7.7.4 Application of multiple pulses to a parametrically cooled levitated particle

The effect of increasing the number of squeezing pulses on a nanoparticle was investigated on a 64 ± 2 nm diameter particle. The pulses applied to the particle each had $\omega_1/\omega_2 = 1.9 \pm 0.2$. The results can be seen in figure 7.16. It can be seen that upon the application of a second pulse (See figure 7.16 C), the phase space becomes more oval as expected, from the combined effect of two squeezing pulses. However, upon application of the 3rd pulse, the phase space distribution starts to extend into the nonlinear region of the trap (see section 2.3.6). The phase space of particle motion starts to curl at the edges (see figure 7.16 D). As the number of pulses applied to the system increases, the curling effect becomes more pronounced, until the phase space has fully curled back on itself (See 7.16 D-F). The application of the 6th pulse to the levitated particle resulted in it being lost from the trap. The current working theory for the 6th pulse resulting in a particle becoming lost from the trap is, that during the duration of the 6 pulses being applied to the system, the laser power is not sufficient for the particle to remain trapped. This theory however, needs further testing, similarly to the uncooled case.

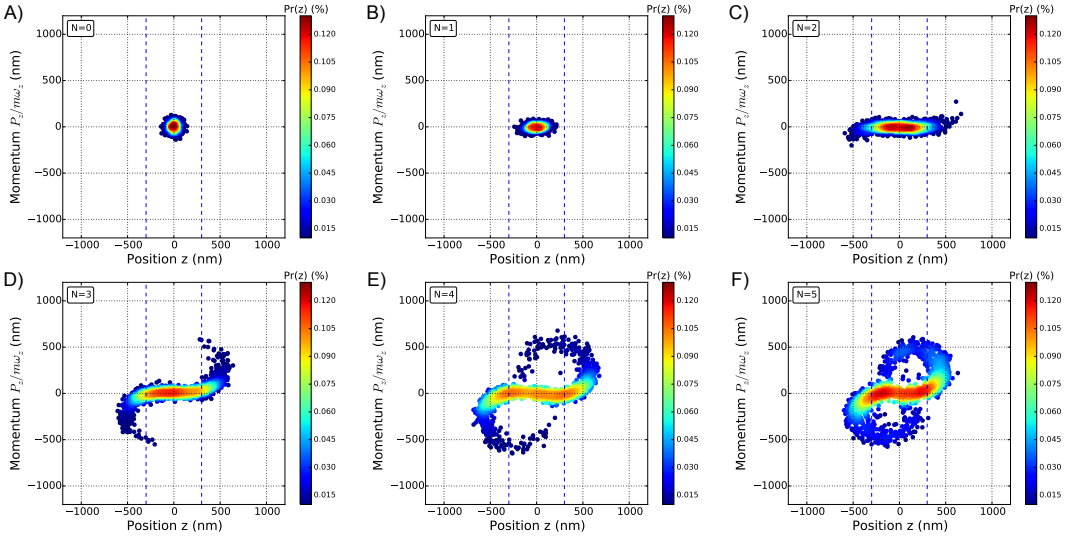

FIGURE 7.16: **The effect on the phase space of a parametrically feedback cooled levitated particle, after applying different numbers of squeezing pulses.** The blue dashed lines show the distance from the centre of the trap, where the linear spring approximation starts to break down. The data shown is for a 64 ± 2 nm diameter particle trapped at 3×10^{-2} mbar, parametrically cooled in all 3 axes with $T_z = 114$ K in the dimension of interest. The phase spaces are shown for a time $t_{after} = 70$ μs after the applied pulses have finished. **A) N=0** The phase space of the parametrically cooled particle in a thermal state. **B) N=1 C) N=2 D) N=3** The particles phase space starts to curl back on itself. **E) N=4** The phase space starts to resemble a figure of eight. **F) N=5** The phase space wraps back onto itself resembling a figure of eight.

7.7.5 Evolution of the phase space after the application of squeezing pulses to a parametrically cooled levitated particle

The phase space of a particle after 5 squeezing pulses, at various times after the pulse, is shown in figure 7.17. It can be seen that the phase space decays differently to the equivalent number of pulses for an uncooled system 7.11 due to the difference in the initial phase space after squeezing. No curls develop as the phase space rotates, but instead, the outer region of the phase space becomes circular, while the central part still resembles that of a squeezed state.

7.7.6 Squeezing parameter vs number of squeezing pulses applied to a parametrically cooled particle

In figure 7.18, it can be seen that the relationship in equation 7.31 is not observed exactly as expected. While the squeezing factor does increase with each successive pulse, the increment is reduced slightly each time and at a greater rate than that observed in figure 7.12, for the uncooled case. There are number of possible reasons why this may be the

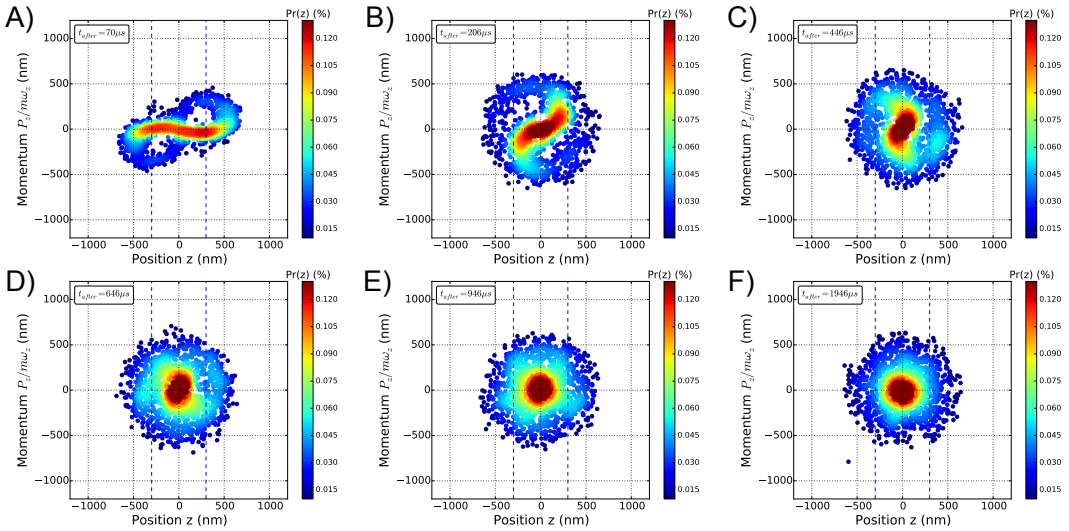

FIGURE 7.17: **Decay of the squeezed state after the application of 5 squeezing pulses to a parametrically cooled levitated nanoparticle.** The blue dashed lines shows the distance from the centre of the trap where the linear spring approximation starts to break down. The data shown is for a 64 ± 2 nm diameter particle trapped at 3×10^{-2} mbar, parametrically cooled in all 3 axes with $T_z = 114$ K in the dimension of interest. **A)** $\mathbf{t_{after} = 46}$ μ**s** The initial phase space measured resembles that of a figure of 8. **B)** $\mathbf{t_{after} = 206}$ μ**s** As the system rotates the phase space becomes more spherical and the size of the holes in the phase space decreases. **C)** $\mathbf{t_{after} = 446}$ μ**s** The holes in the phase space disappear and the distribution at the centre of the phase space still shows some signs of squeezing. **D)** $\mathbf{t_{after} = 646}$ μ**s** The phase space begins to resemble that of a thermal state. **E)** $\mathbf{t_{after} = 946}$ μ**s** The system resembles that of a heated thermal state. **F)** $\mathbf{t_{after} = 1946}$ μ**s** The phase space starts to decrease in extent, towards that of its original state.

case. Firstly, due to the methods of data analysis close to the time of the pulse, edge effects come into play due to the filtering of the data and the phase space cannot be calculated until roughly 46 μs after the pulses have ended. In this time the phase space will have had time to evolve and in the cases of high pulse numbers nonlinear effects have developed, distorting the phase space from its expected phase space immediately after the pulse. The effect of parametric cooling seems to amplify this effect. In addition to this, the phase noise and non-ideal pulse shapes will reduce the effectiveness of the squeezing pulses implemented. The maximum amount of squeezing measured after the application of 5 pulses is characterized by the squeezing factor as $\lambda = 8.4 \pm 0.1$ dB.

7.7.7 Possibility of generating quantum states

To generate a quantum state, the particle motion needs to be squeezed into or below its ground state. We can write an expression to calculate the strength of the squeezing required, to squeeze the motion of the particle equal to that of its ground state.

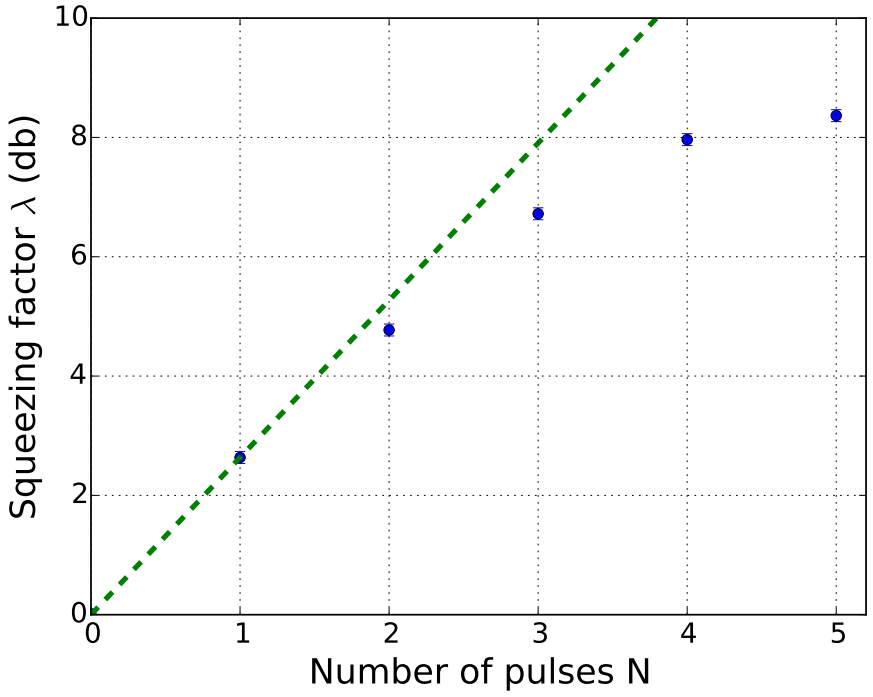

FIGURE 7.18: **The squeezing parameter as a function of pulse number for a cooled nanoparticle.** The dashed line is the expected λ calculated using equation 7.31. The data shown is for a 64 ± 2 nm diameter particle trapped at 2×10^{-2} mbar.

$$\lambda_{ground} = 10log_{10}\left(\frac{\Delta z}{\Delta z_{ground}}\right) \tag{7.32}$$

where $\Delta z = \sqrt{k_b T_z / m\omega_z^2}$ and $\Delta z_{ground} = \sqrt{\hbar / 2m\omega_z}$, allowing us to write,

$$\lambda_{ground} = 10log_{10}\left(\sqrt{\frac{k_b T_z}{\hbar\omega_z}}\right) \tag{7.33}$$

This equation is plotted in figure 7.19 for a range of temperatures. It can be seen that for a nanoparticle with a temperature $T_z = 5$ mK, a squeezing factor of $\lambda_{ground} = 15.1$ dB would be needed to squeeze one quadrature of the particles phase space into a quantum state.

The measurement scheme implemented here relies on a continuous monitoring of the particles position. At first this might appear to be undesirable, when considering the prospect of approaching the quantum regime, due to the well known disturbance induced by the quantum measurement process. However, it has been recently shown that, if correctly accounted for, continuous monitoring may in fact improve the achievable mechanical squeezing [24].

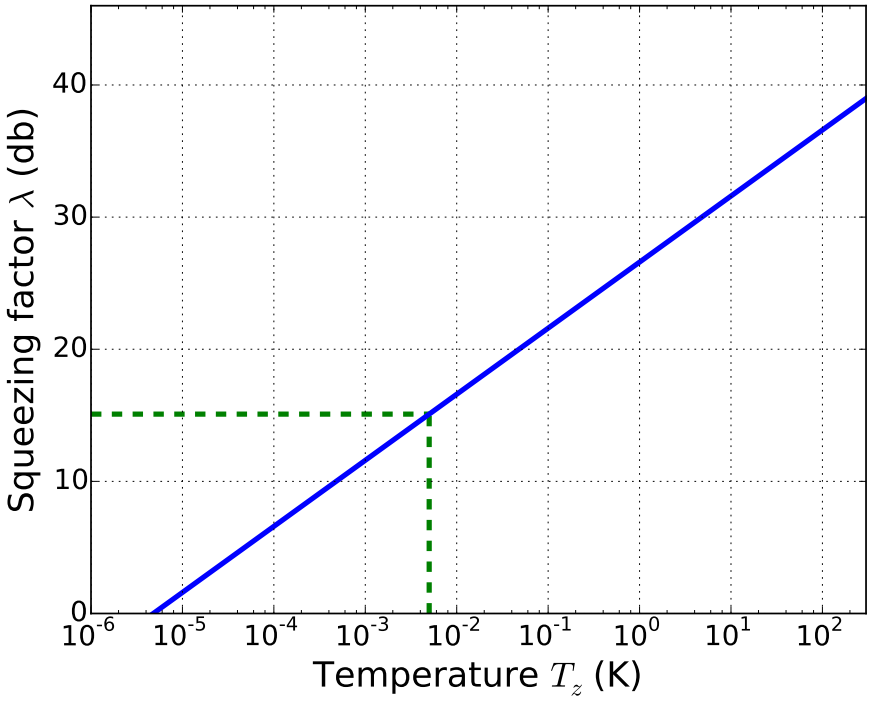

FIGURE 7.19: **The squeezing parameter required to squeeze one of the particles phase space quadratures into a quantum state as a function of temperature.** The solid line is equation 7.33 plotted for a particle oscillating at $\omega_z = 2\pi \times 100$ kHz. The dashed line shows the squeezing factor needed ($\lambda_{ground} = 15.1$ dB) to squeeze the motion of a nanoparticle, with a centre of mass temperature $T_z = 5$ mK, such that one of its quadratures is in the ground state.

7.8 Conclusion

In conclusion, a quadrature squeezing method has been demonstrated on optically levitated nanoparticles. The pulsed squeezing scheme implemented operates via non-adiabatic shifts in the trap frequency. The squeezing pulses implemented consist of a rapid drop in the trap frequency, followed by brief period in time where the system is allowed to evolve, before the trapping frequency is rapidly brought up to its original value.

Initial investigations were carried out using a single pulse. It was found that the greatest amount of squeezing was achieved when the duration of pulse was at multiples of a quarter of the trap period ($2\pi/\omega_2$). The smallest amount of squeezing occurred at multiples of half the trap period during the pulse ($2\pi/\omega_2$). The amount of squeezing was characterized and the maximum value was found to be $\lambda = 3.2 \pm 0.2$ dB.

To further increase the amount of squeezing applied to the levitated nanoparticle, a multiple pulse scheme was implemented. The effect of varying the time between pulses was investigated and the optimal time was found to be at multiples of a quarter of the

trap period ($2\pi/\omega_1$). The minimum amount of squeezing occured at multiples of half the trap period during the pulse ($2\pi/\omega_1$). The amount of squeezing applied to the system was also characterized after application of multiple pulses and it was found that after 5 pulses a squeezing factor of $\lambda = 9.4 \pm 0.1$ dB was achieved.

The multiple pulse scheme was then applied to parametrically feedback cooled nanoparticles. The effect of the phase space and decay of the phase space after the application of squeezing pulses was characterized. The amount of squeezing applied to the system was also characterized after application of multiple pulses and it was found that after 5 pulses a squeezing factor of $\lambda = 8.4 \pm 0.1$ dB was achieved.

The squeezing demonstrated here is classical in nature, however it may be possible to prepare an optically levitated nanoparticle in a quantum state. To create a quantum state in the experimental system described in this chapter, an optically levitated nanoparticle would need to be cooled to the lowest achievable temperature, and multiple squeezing pulses applied until one of the quadratures has been sufficiently suppressed. To achieve this for a nanopartilce at 5 mK, a squeezing factor of $\lambda_{ground} = 15.1$ dB would be needed.

The techniques demonstrated in this chapter could be used for many applications, including enhanced sensing and metrology based on levitated optomechanics, such as for force sensing applications [210] and non-equilibrium dynamics studies [100]. It has even been suggested that by using a squeezed particle motion in a nano heat engine, it may be possible to beat the Carnot limit [211]. Finally, as discussed in this chapter it may be possible to achieve quantum squeezing by pre-cooling the motional state [13, 100, 119]. Either by using parametric feedback cooling as demonstrated in this thesis (see chapter 6) and by others [27, 99], or by using alternative methods such as quantum measurement techniques [207, 212], which have been successfully applied to membrane and cantilever optomechanical devices [213, 214].

Chapter 8

Conclusion

In brief, the work undertaken during my doctoral research project involved the design and creation of a novel setup, in which the optical levitation of single nanoparticles could be achieved. The properties of each particle levitated within the trap were calculated from experimental data, and the setup's sensitivity to nanoparticle motion was determined. The effects of varying the trapping laser intensity, as well as the pressure in the vacuum chamber, on the internal temperature of a levitated particle was measured. Parametric feedback cooling and squeezing pulses were used, both in isolation and in conjunction, in order to manipulate the centre of mass motion of the optically levitated nanoparticles. This chapter will provide a summary of the key experimental results and will also discuss the potential applications of the techniques developed. In addition, possible improvements to the experimental systems developed will be suggested.

8.1 Experimental methods and setup for optical trapping of nanoparticles

The experimental set up described in this thesis was formed using a paraboloidal mirror (NA$\sim$ 0.995) to create a diffraction limited gradient force trap for nanoparticles, the movement of which was detected using a single photodiode. The advantages of using a paraboloidal mirror over a lens based system include achromatic focusing, alongside high numerical apertures. The particular paraboloidal mirrors used in this set up had an uncoated aluminium body, a further benefit which resulted in ultra high vacuum compatibility. The detection system was aligned using a Poisson spot and the inherent homodyne detection system was produced by the interference of Rayleigh scatter from the particle and the diverging focused beam. The best signal to noise ratio was found to occur when the two fields were of equal magnitude.

8.1.1 Future outlook

Increasing the versatility of what particles can be loaded into the trap, both in terms of their material and shape, as well as the loading pressure at which they can be transferred into the trap, will allow for future experiments currently not possible. Additionally, as the optical trap is the basis of all the experiments outlined in this thesis, improving it will improve the overall measurement sensitivity as well as the quality of the trap.

Improved nanoparticle source: One of the underlying experimental issues concerns how particles should be fed into the trap. Despite the nebuliser providing a workable solution, there is still much room for improvement. Several possible options exist to improve upon the nebuliser method, including:

- **Nitrogen immersed nebulizer:** One of the downsides of the nebuliser used in the current system is that particles sprayed into the vacuum chamber come into contact with oxygen and, dependent on material, can become oxidised. For the silica particles which were used in this experiment, this was not an issue. However, for particles such as nanodiamonds and carbon nanotubes, it could be. To counter this, a technique was developed, whereby the nebuliser is placed inside a separate chamber, which is connected to the main chamber, but which can be sealed off using a gate valve. This chamber, along with the main vacuum chamber, is back-filled with nitrogen gas in order to prevent the nanoparticle from coming into contact with oxygen. This system, however, is limited to near atmospheric loading pressures.
- **Hollow core optical fibre feed through:** A novel method has recently been demonstrated, where a standing wave optical trap is used to transport a single nanoparticle through a hollow core fibre between two chambers, one at low pressure and the other at high pressure [122]. Such a transport system could be adapted for our paraboloidal mirror geometry, to efficiently feed nanoparticles into the trap at a variety of pressures.
- **Particle juggling:** Finally, for applications in which having a single particle would be beneficial, such as nanoparticle matter-wave interferometry [44], it may be possible to recycle the same particle over and over again. This would reduce the need to transfer multiple particles into a high vacuum environment. To recycle the particle, it would need to be ejected from the optical trap, allowed to undergo a parabolic trajectory, before finally being caught in the same optical trap. This could potentially be achieved by turning off the laser light used to create the optical trap when the particle has the correct velocity, engineered by a combination of parametric feedback and squeezing pulses.

Improving the optical trap: The quality of the optical trap was of paramount importance in ensuring the accuracy of the aforementioned experiments. The quality of an optical trap can be improved by generating a tighter, more uniform laser focus. As discussed in section 3.5, the experimental setup described here used a Poisson spot in order to align the detection arm of the experimental system. However, when conducting the experiment itself, an iris was used in order to remove the Poisson spot, improving the signal to noise ratio. It was noticed however, that the system had a slight asymmetric geometry, which is now believed to have been due to the iris, which introduces artifacts in the beam, due to misalignment that arises over time. It would be possible to resolve these issues by removing the Poisson spot via another means, hence removing the need for the iris. For example, the Poisson spot could be removed by scratching the aluminium surface around the mirror, to create a rough surface. It should be noted however that whilst useful, the detection arm of the experiment can still be aligned without the Possion spot.

8.2 Optomechanics of levitated particles

Within this experimental setup, nanoparticles ranging from 18 nm to 312 nm in diameter were trapped and several of their properties measured. These included the mass, radius, oscillation amplitude (via the use of a volts-to-meter conversion factor) and the damping experienced at a given pressure. This was done using two methods. The first, widely established, method required fitting a power spectral density, derived using the kinetic theory of gases, to the motion of the particle. The second, novel method, developed by the author and James Bateman, involved scanning the wavelength of the trapping laser. Using this method, it was possible to determine the mass of a levitated particle without assuming the kinetic model and material density. From the wavelength scan, the sensitivity of the experimental system was measured to be 200 $fm/\sqrt{Hz}$.

The ability to control the trap frequencies of all three motional degrees of freedom, through varying the power of the trapping laser, was demonstrated. The ability to independently control and separate the transverse trapping frequencies from one another, as well as from the z axis, was also shown to be possible, using elliptically polarized light. The effect of changing the pressure inside the chamber in which a levitated nanoparticle is trapped is also explored. Trapping of nanoparticles at pressures as low as 10^{-5} mbar, without any active feedback, was achieved. The different frequency components found in the PSD of the signal were shown and their origins explained.

8.2.1 Future outlook

Increasing system sensitivity: A simple suggestion to improve the signal-to-noise ratio of the system would be to increase the percentage of photons, scattered by the particle, that reach the detector. The paraboloidal mirror has an NA of ~ 0.995 and therefore collects roughly 50% of the scattered photons. The percentage of photons collected could be increased by simply increasing the NA of the paraboloidal mirror. Another way of doing this would be to use a more reflective material, at $\lambda = 1550$ nm, for the reflective optics in the experimental system. Using gold, for example, rather than aluminium, would mean that a larger percentage of the photons would be reflected, rather than absorbed.

Mass measurement of nonspherical particles: The kinetic model used to describe the motion of nonspherical particles in an optical trap is significantly more complicated than that used for spherical particles, and assumptions about the shape of the nanoparticle are needed [112, 131, 132]. By using the method outlined in section 4.5, knowledge of the nanoparticle shape is not required, allowing for a measurement of the nanoparticle mass, independent of the kinetic model, to be performed.

8.3 Nanoscale temperature measurements using black body like radiation from a levitated nanoparticle

To determine the internal temperature of a levitated particle, the spectra of blackbody radiation emitted from the particle was measured and the Planck equation used to determine its temperature. The effect of pressure within the vacuum chamber was investigated by varying the pressure from 1000 mbar to 0.04 mbar. This resulted in an increase of T_{BB}, from 388 K to 480 K, demonstrating that the temperature of the nanoparticle increases with decreasing pressure. Additionally, the effect of the trapping laser intensity on particle temperature was investigated by varying the intensity from 0.21 TW/m^2 to 0.4 TW/m^2, which resulted in an increase of T_{BB}, from 367 K to 463 K. This shows that, even though the absorption of silica is low at 1550 nm, the temperature of the levitated nanoparticle can be raised by increasing the laser intensity. This is owing to the poor heat transfer to the surrounding gas at low pressures.

8.3.1 Future outlook

Studies of the emitted blackbody radiation from levitated nanoparticles open up many new avenues for experimental investigations within optical traps. However, before these

studies can be realised, the levitated nanoparticle system discussed in chapter 3 needs to be improved.

Improvements to the experimental system: In section 5.7, several improvements are suggested to increase the range of temperatures at which an optically levitated nanoparticle could be accurately measured at. This would be achieved by increasing the range over which the peak of the blackbody spectra can be observed. These improvements would allow for measurements between room temperature ($\sim$ 300 K) and the melting point of silica $T_{melt} = 1873$ K, while also increasing the collection efficiency of emitted photons. Further improvements to the system could include the addition of a second laser, with a wavelength more heavily absorbed by the trapped particle, allowing for a greater amount of laser heating to be achieved. Alternatively, the same effect could be achieved by using a more highly powered trapping laser, or one which emits a wavelength at which the trapped particle has a higher absorption.

Studies of melting-point depression: It has been observed that as a material is reduced in size, its melting point is also reduced. This phenomenon is referred to as melting-point depression and is prominent in nanoscale materials, which melt at temperatures significantly lower than bulk materials [215–219]. Combining the ability to optically trap single nanoparticles and measure their radius, using the techniques from chapter 4 holds great promise for studying this phenomenon in greater detail than previously possible.

Studies into particle loss mechanisms: It became apparent that as the pressure in the vacuum chamber was reduced, nanoparticles were often lost from the trap. Measuring the nanoparticle's blackbody spectrum provides the tools with which to test by which mechanism particles are lost by.

8.4 Parametric feedback cooling of a levitated particle's centre of mass motion

To control the centre of mass motion of levitated particles within the optical trap, parametric feedback cooling was implemented by modulating the trap depth. Using this technique, the effect different feedback parameters have on particle motion was explored. The combination of optimizing the feedback parameters, alongside reducing the pressure, resulted in temperatures of $T_z = 14 \pm 1$ mK, $T_x = 5 \pm 1$ mK and $T_y = 7 \pm 1$ mK. At 10^{-6} mbar, the Q factors of the system were measured to be on the order of 10^7. From these measurements it can be predicted that at a pressure of 10^{-9} mbar, the observed Q factors would be on the order of 10^{12}. These high Q factors hold great

promise for ultrasensitive force detection, with the system presented here having a force sensitivity on the order of 10^{-20} N/Hz. Theoretical considerations show that, with some improvements to the experimental system, centre of mass temperatures and thus low phonon numbers close to the quantum ground state could be achieved.

8.4.1 Future outlook

Cooling nanoparticle centre of mass motion to the ground state: As discussed in section 6.8, the electrical noise floor currently present in the system needs to be reduced, in order to achieve lower temperatures. It seems that the fundamental reason for the high electrical noise floor is the ZI lock-in amplifier, which is used to generate the feedback signal. By producing the feedback signal on an FPGA, which has a lower noise floor, this limit can be overcome. Parallel to this, the use of thermoelectrically cooled detectors would provide a far lower NEP, further helping to lower the noise floor level. It is also anticipated that if the electrical noise floor limits can be overcome, at low phonon numbers photon recoil will limit the temperature the system can reach. In order to potentially reach the ground state and overcome the photon recoil limit, parametric feedback cooling could be combined with other optical cooling methods, such as passive dynamical back-action cooling [5], by adding an optical cavity into the system [101, 120].

8.5 Classical squeezing of nanoparticle motion of a levitated nanoparticle

Another method to control the center of mass motion of a levitated nanoparticle used squeezing pulses, to classically squeeze its mechanical motion. This quadrature squeezing was achieved via non-adiabatic shifts of the nanoparticle's trap frequency and was carried out on a number of particles. The squeezing pulses implemented consisted of a rapid reduction in the trap frequency, followed by brief period in time where the system was allowed to evolve, before the trapping frequency was rapidly returned to its original value.

Initial investigations were carried out using a single pulse. The maximum amount of squeezing produced in the system occurred when the pulse duration was equal to multiples of a quarter of the trap period ($2\pi/\omega_2$). The minimal amount of squeezing resulted from pulses with a duration equal to multiples of half the trap period during the pulse ($2\pi/\omega_2$). The maximum amount of squeezing from a single pulse was measured to be $\lambda = 3.2 \pm 0.2$ dB. To further increase the amount of squeezing applied to the levitated nanoparticle, a multiple pulse scheme was implemented. The effect of varying the time

between pulses was investigated and the optimal time was found to be at multiples of a quarter of the trap period ($2\pi/\omega_1$). The time between pulses that produced a minimum amount of squeezing was at multiples of half the trap period ($2\pi/\omega_1$). The amount of squeezing applied to the system was also measured following the application of multiple pulses and it was found that after 5 pulses a squeezing factor of $\lambda = 9.4 \pm 0.1$ dB was achieved. The multiple pulse scheme was then applied to parametrically feedback cooled nanoparticles, and the affect that this had on the phase space, along with its rate of decay, was observed. The amount of squeezing applied to the system was measured after 5 pulses, and a squeezing factor of $\lambda = 8.4 \pm 0.1$ dB was achieved.

8.5.1 Future outlook

Squeezing theory/modeling of multiple pulse scheme: The work currently carried out in sections 7.6 and 7.7 currently has no comprehensive theory to explain it. An extension to the theory presented in sections 7.2 and 7.5.2, to include additional pulses and the effect of parametric feedback cooling on the particle motion, is currently being developed by Tommaso Tufarelli.

Improve quality of optical pulses: As discussed in section 7.3.2, the pulses generated are not perfectly rectangular in shape as desired. This issue arises due to the fibre AOM being upstream of the EDFA in the optical system, as the EDFA distorts the optical pulse. An attempt to circumvent this was made, using a free space AOM after the EDFA. However, when using the first order output of the AOM, the loss in laser intensity across the AOM made trapping nanoparticles impractical. Attempts instead to use the zeroth order output of the AOM meant the amount by which the laser could be modulated was too small to produce significant squeezing. However, this issue can easily be over come by using a more powerful EDFA (greater than 1W), thus making a free space AOM a practical alternative.

Improve detection scheme: Currently, due to the rapid drop in intensity of the laser beam during a squeezing pulse, the ability to detect the motion of the particle during, and shortly after, the pulse is not possible. This problem is linked to the fact that the trapping laser is also used to detect the particle motion. To overcome this issue, a second, weaker laser beam could be used to separately monitor the motion of the particle during and after the pulse. This would allow for λ to be determined immediately after the optical pulse, ensuring a greater degree of accuracy.

Increase the amount of squeezing achieved: The first and most obvious route to increasing λ, would be to increase the difference between ω_1 and ω_2, as can be seen from equation 7.12. To increase the ratio ω_1/ω_2, the laser power used to create the

trap needs to be increased (as $\omega_0 \propto \sqrt{\text{laser power}}$) and the light intensity modulated by a greater amount. The other solution, as demonstrated in chapter 7, is by the use of multiple pulses. It is believed the reason that the particle currently falls out of the optical trap after 6 pulses, is because the gradient force is too small, for an extended period during the squeezing pulses, to keep the particle confined in the trap. Potentially, this limitation can be overcome by performing a larger number of shallower pulses.

Squeezing particle motion in 3D: Currently squeezing has only been demonstrated in a single spatial degree of freedom. To achieve three dimensional squeezing, there are several methods which could be explored. Since the transverse frequencies can be controlled via the polarisation of the trapping laser light, modulating the polarization of the laser light using an EOM could be used to squeeze the transverse frequencies, independent of the z degree of freedom. Alternatively, modulation of the laser's power could be used in order to squeeze all three spatial degrees of freedom simultaneously. This could be achieved by optimizing the pulse duration τ for all three axis, although a draw back of this method would be that maximum squeezing would not be achieved for any individual degree of freedom.

Squeezing nanoparticle motion into a quantum state:

To generate a quantum state using the squeezing method demonstrated here, both the temperature of the nanoparticle needs to be reduced, and the amount of squeezing applied to it increased. It is predicted that for a particle with a temperature of 5 mK, a squeezing factor of $\lambda_{ground} = 15.1$ dB would be required in order to squeeze the system into a quantum state.

Appendix A

Derivation of scattering force dominance condition in optical traps.

As discussed in section 2.3.2, the scattering force will dominate the gradient force in cases where particles are larger than a certain size. In this appendix, the condition for this case will be derived.

A.1 Derivation of the condition for scattering force dominance.

To derive the condition at which the radius of a nanoparticle will become large enough for the scattering force to dominate the gradient force, we divide equation 2.24, by 2.19, to get

$$\frac{\mathbf{F}_{scat}}{\nabla \mathbf{F}_{grad}} = \frac{16\pi^4 r^3}{3\lambda^4} \frac{I}{\nabla I} \left(\frac{m^2 - 1}{m^2 + 2} \right) \tag{A.1}$$

When the ratio of $\mathbf{F}_{scat}/\nabla \mathbf{F}_{grad}$ is greater than 1, the scattering force will dominate the gradient force and a particle will no longer be optically trapped. Instead, it will be pushed out of the trapping region by the scattering force. This occurs when the following condition is met

$$1 < \frac{16\pi^4 r^3}{3\lambda^4} \frac{I}{\nabla I} \left(\frac{m^2 - 1}{m^2 + 2} \right). \tag{A.2}$$

Rearranging for r, we find the condition for which a particle will be too large to be optically trapped is as follows

$$r > \sqrt[3]{\frac{3\lambda^4}{16\pi^4} \frac{\nabla I}{I} \left(\frac{m^2 + 2}{m^2 - 1} \right)}. \tag{A.3}$$

Appendix B

Nanoparticle Preparation and Storage

The importance of ensuring the correct preparation and storage of nanoparticles to be used within optical trapping experiments was one of the earliest experimental realisations to arise from the aforementioned studies. In this case, correct preparation and storage can be taken to mean in such a way that the desired properties of the nanoparticle, present in the commercial solutions used, are still in place when a particle enters the optical trap. The experiments described in this thesis used a number of commercial nanoparticle solutions from many different suppliers and manufacturers including *micro-particles GmbH, iolilec nano-materials* and *Corpuscular*.

B.1 Storage of the nanoparticle solution

The shelf life of the commercial nanoparticle solutions was found to be roughly 3-4 months, from experience, after which the nanoparticles where found to aggregate. At this point, obtaining the desired particles from the solution became harder. Once nanoparticles aggregate, additional effects such as rotation and torsion can be observed. Effects such as these were not studied as part of this work, owing to time constraints, as it was not thought that doing so would further the original aims of the project. The shelf life of the nanoparticle solution can be increased by wrapping Parafim "M" laboratory film (made by *Bemis Flexible packaging*) around the seal of the vial in order to prevent air from entering, and then storing it in a fridge in order to reduce the particles' energy and slow down their rate of interaction, and hence aggregation.

After loading the nanoparticle suspension into the nebuliser however, the particles were observed to slowly aggregate at different rates, dependent on the type of nanoparticle and concentration. Typically, the solution remained useful on the order of a week. It was found that the aggregation of the particles in the nebuliser could be mostly reversed by sonicating the particles (37 kHz, for 15 minutes, 300 K). However, better results where obtained by simply replacing the solution with a fresh batch.

B.2 Preparation of the nanoparticle solution

The method for preparing the nanoparticles and loading them into the particle trap has been described in section 3.3.2 and so will not be discussed further here. Instead, this section will focus on some of the finer aspects and outline the protocol concerning preventing contamination of the prepared nanoparticle solution. Preventing contamination is a key requirement when working with nanoparticles in an optical trap. Contamination can either result in irreversible aggregation, leading to particles too large to trap, or the addition of impurities that may cause absorption of the trapping light and lead to internal heating of the particle. This internal heating could potentially cause the particle to melt whilst in the optical trap, rendering it useless.

In order to prevent contamination from occurring, *Microflex XCEED* nitrate gloves (powder free) were worn whilst preparing or handling any of the equipment used to create the nanoparticle solutions. When diluting the shop brought solutions, volumes were measured using *Eppendorf research plus* micro-pipettes. The tips were only used to transfer a single measure of solution before being replaced. The nanoparticle solutions were prepared inside micro centrifuge tubes 1.5 ml with cap, and during the sonication a custom foam flotation device was used to keep the rim of the cap from coming into contact with water in the sonicator. In the sonicator, deionised water was used and changed regularly.

B.3 Cleaning the Nebuliser

Between the uses of nanoparticle solutions the nebuliser head seen in figure 3.2 was cleaned in an attempt to remove any contaminant which may have built up. To clean the nebuliser, the head was sonicated in a solution of isoproponal at 37kHz, for 15 minutes at a temperature of 300 K. This was found to be sufficient to clean the nebuliser head, and thus prevent aggregation of the nanoparticle solutions stored inside.

Appendix C

Error analysis

In this appendix, the methods used to calculate the error of the values extracted from experimental data will be given. The majority of values calculated as part of this work are found by fitting equations to experimental data; Variance in the errors observed in the main text of this thesis will therefore depend on several factors including: the sample frequency, the number of points sampled and the quality of the fit.

C.1 Error in particle radius α_r

Equation 4.12 is used to calculate the radius of the particle and depends both on the error in the fitting parameter $C_0 = \Gamma_0$, as shown in equation 4.15, and the accuracy of the pressure sensor used. The equation for the error in r can be written as

$$\alpha_r = 0.619 \frac{9\pi}{\sqrt{2}} \frac{\eta_{air} d^2}{\rho k_B T_0} r \sqrt{\left(\frac{\alpha_{P_{gas}}}{P_{gas}}\right)^2 + \left(\frac{\alpha_{\Gamma_0}}{\Gamma_0}\right)^2}. \tag{C.1}$$

In the case of these experiments, a *Oerlikon Leybold Vacuum, D-50968 Koln, Type: ITR 90 No: 12094, F-No:1669/2012* pressure sensor was used, yielding an accuracy of $\alpha_{P_{gas}}/P_{gas} = 0.15$ in the pressure readings. This device introduced by far the largest error when calculating the radius and mass of a particle. It therefore seems clear that replacing this device with a more precise sensor would, in future, yield more accurate results.

C.2 Error in particle mass α_m

The mass of a trapped particle was calculated from the particle's radius, as measured within the trap. The error can be written as,

$$\alpha_m = 4\pi\rho r^2 \alpha_r m. \tag{C.2}$$

C.3 Error in internal temperature $\alpha_{T_{BB}}$

The internal temperature was calculated by fitting equation 5.19 to experimental data, as described in section 5.4, and using $T_{BB} = hc/k_b B_{BB}$. The error for T_{BB} can be calculated from,

$$\alpha_{T_{BB}} = \frac{hc}{k_b}\frac{\alpha_{B_{BB}}}{B_{BB}^2} T_{BB}. \tag{C.3}$$

C.4 Error in Damping α_{Γ_0}

The method used to calculate the error in the damping depends on whether or not the particle has been cooled by parametric feedback. In the case where the particle has not been cooled by parametric feedback, the error in the damping is equal to the error in the fit parameter C_0, from equation 4.15. However, in the case where parametric feedback is applied, both extracting the damping rate, and calculating the error in this value, is more complex. This is shown by equation 6.11. The error in the case where the particle has been cooled is given by

$$\alpha_{\Gamma_0} = \Gamma_0 \sqrt{\left(\frac{\alpha_{A_{fb}}}{A_{fb}}\right)^2 + \left(\frac{\alpha_{C_0}}{C_0}\right)^2 + \left(\frac{\alpha_{A_0}}{A_0}\right)^2}. \tag{C.4}$$

C.5 Error in centre of mass temperature α_T

The centre of mass temperature of a levitated particle is calculated by fitting equation 4.15 to an uncooled particle and equation 6.8 to a cooled particle. The fit parameters can then be used to calculate the temperature, using equation 6.10. As $\alpha_{C_{fb}} = \alpha_{\Gamma_0+\delta\Gamma}$, the error in temperature measurements can be calculated using

$$\alpha_T = T_0 T \sqrt{\left(\frac{\alpha_{C_{fb}}}{C_{fb}}\right)^2 + \left(\frac{\alpha_{\Gamma_0}}{\Gamma_0}\right)^2}. \tag{C.5}$$

C.6 Error in feedback rate $\alpha_{\delta\Gamma}$

The feedback rate is calculated using equation 6.11, and the error can be calculated as follows

$$\alpha_{\delta\Gamma} = \sqrt{\alpha_{C_{fb}}^2 + \alpha_{\Gamma_0}^2}. \tag{C.6}$$

C.7 Error in frequency shift introduced by parametric feedback $\alpha_{\delta\omega}$

$\delta\omega$ is calculated using equation 6.11 and the error in the value is given by

$$\alpha_{\delta\omega} = \sqrt{\alpha_{B_{fb}}^2 + \alpha_{B_0}^2}. \tag{C.7}$$

C.8 Error in Q factor α_Q

The Q factor is calculated from equation 6.13 and the error can be calculated as follows

$$\alpha_Q = Q \sqrt{\left(\frac{\alpha_{\omega_0}}{\omega_0}\right)^2 + \left(\frac{\alpha_{\Gamma_0}}{\Gamma_0}\right)^2}, \tag{C.8}$$

C.9 Error in force sensitivity limit $\alpha_{S_{FF}^{th}}$

The force sensitivity limit S_{FF}^{th} is calculated from equation 6.14 and the error can be calculated as follows

$$\alpha_{S_{FF}^{th}} = S_{FF}^{th} \sqrt{4k_b T_0} \sqrt{\left(\frac{\alpha_{\omega_0}}{\omega_0}\right)^2 + \left(\frac{\alpha_m}{m}\right)^2 + \left(\frac{\alpha_Q}{Q}\right)^2}, \tag{C.9}$$

C.10 Error in squeezing factor α_λ

As discussed in section 7, equation 7.15 is used to calculate the squeezing factor. The error in the squeezing factor is calculated using the error of the phase spaces positional variance, both before squeezing $\alpha_{\Delta z_1}$ and after $\alpha_{\Delta z_2}$. The equation for the error can be written as

$$\alpha_\lambda = \frac{10}{ln(10)} \frac{\Delta z_2}{\Delta z_1} \sqrt{\left(\frac{\alpha_{\Delta z_1}}{\Delta z_1}\right)^2 + \left(\frac{\alpha_{\Delta z_2}}{\Delta z_2}\right)^2}. \tag{C.10}$$

Bibliography

[1] Summers MD, Burnham DR, McGloin D. Trapping solid aerosols with optical tweezers: A comparison between gas and liquid phase optical traps. Optics Express. 2008 May 26;16(11):7739–47.

[2] Millen J, Deesuwan T, Barker P, Anders J. Nanoscale temperature measurements using non-equilibrium Brownian dynamics of a levitated nanosphere. Nature Nanotechnology. 2014 Jun 1;9(6):425–9.

[3] Vovrosh J, Rashid M, Hempston D, Bateman J, Paternostro M, Ulbricht H. Parametric feedback cooling of levitated optomechanics in a parabolic mirror trap. Journal of the Optical Society of America B. 2017 Jul 7;34(7):1421–28.

[4] Aspelmeyer M, Kippenberg TJ, Marquardt F. Cavity optomechanics. Reviews of Modern Physics. 2014 Dec 30;86(4):1391–452.

[5] Kippenberg TJ, Vahala KJ. Cavity opto-mechanics. Optics Express. 2007 Dec 10;15(25):17172–205.

[6] Favero I, Karrai K. Optomechanics of deformable optical cavities. Nature Photonics. 2009 Apr 1;3(4):201–5.

[7] Corbitt T,Chen Y, Innerhofer E, Müller-Ebhardt H, Ottaway D, Rehbein H, Sigg D, Whitcomb S, Wipf C, Mavalvala N. An all-optical trap for a gram-scale mirror. Physical Review Letters. 2007 Apr 13;98(15):150802.

[8] Corbitt T, Mavalvala N. Review: Quantum noise in gravitational-wave interferometers. Journal of Optics B: Quantum and Semiclassical Optics. 2004 Jul 27;6(8):S675.

[9] Abbott BP, Abbott R, Abbott TD, Abernathy MR, Acernese F, Ackley K, Adams C, Adams T, Addesso P, Adhikari RX, Adya VB, Affeldt C, Agathos M, Agatsuma K, Aggarwal N, Aguiar OD, Aiello L, Ain A, Ajith P, Allen B, Allocca A, Altin PA, Anderson SB, Anderson WG, Arai K, Arain MA, Araya MC, Arceneaux CC, Areeda JS, Arnaud N, Arun KG, Ascenzi S, Ashton G, Ast M, Aston SM, Astone P,

Aufmuth P, Aulbert C, Babak S, Bacon P, Bader MKM, Baker PT, Baldaccini F, Ballardin G, Ballmer SW, Barayoga JC, Barclay SE, Barish BC, Barker D, Barone F, Barr B, Barsotti L, Barsuglia M, Barta D, Bartlett J, Barton MA, Bartos I, Bassiri R, Basti A, Batch JC, Baune C, Bavigadda V, Bazzan M, Behnke B, Bejger M, Belczynski C, Bell AS, Bell CJ, Berger BK, Bergman J, Bergmann G, Berry CPL, Bersanetti D, Bertolini A, Betzwieser J, Bhagwat S, Bhandare R, Bilenko IA, Billingsley G, Birch J, Birney R, Birnholtz O, Biscans S, Bisht A, Bitossi M, Biwer C, Bizouard MA, Blackburn JK, Blair CD, Blair DG, Blair RM, Bloemen S, Bock O, Bodiya TP, Boer M, Bogaert G, Bogan C, Bohe A, Bojtos P, Bond C, Bondu F, Bonnand R, Boom BA, Bork R, Boschi V, Bose S, Bouffanais Y, Bozzi A, Bradaschia C, Brady PR, Braginsky VB, Branchesi M, Brau JE, Briant T, Brillet A, Brinkmann M, Brisson V, Brockill P, Brooks AF, Brown DA, Brown DD, Brown NM, Buchanan CC, Buikema A, Bulik T, Bulten HJ, Buonanno A, Buskulic D, Buy C, Byer RL, Cabero M, Cadonati L, Cagnoli G, Cahillane C, Bustillo Calder J, Callister T, Calloni E, Camp JB, Cannon KC, Cao J, Capano CD, Capocasa E, Carbognani F, Caride S, Casanueva Diaz J, Casentini C, Caudill S, Cavaglià M, Cavalier F, Cavalieri R, Cella G, Cepeda CB, Cerboni Baiardi L, Cerretani G, Cesarini E, Chakraborty R, Chalermsongsak T, Chamberlin SJ, Chan M, Chao S, Charlton P, Chassande-Mottin E, Chen HY, Chen Y, Cheng C, Chincarini A, Chiummo A, Cho HS, Cho M, Chow JH, Christensen N, Chu Q, Chua S, Chung S, Ciani G, Clara F, Clark JA, Cleva F, Coccia E, Cohadon P.-F, Colla A, Collette CG, Cominsky L, Constancio M, Conte A, Conti L, Cook D, Corbitt TR, Cornish N, Corsi A, Cortese S, Costa CA, Coughlin MW, Coughlin SB, Coulon J.-P, Countryman ST, Couvares P, Cowan EE, Coward DM, Cowart MJ, Coyne DC, Coyne R, Craig K, Creighton JDE, Creighton TD, Cripe J, Crowder SG, Cruise AM, Cumming A, Cunningham L, Cuoco E, Dal Canton T, Danilishin SL, D'Antonio S, Danzmann K, Darman NS, Da Silva Costa CF, Dattilo V, Dave I, Daveloza HP, Davier M, Davies GS, Daw EJ, Day R, De S, DeBra D, Debreczeni G, Degallaix J, De Laurentis M, Deléglise S, Del Pozzo W, Denker T, Dent T, Dereli H, Dergachev V, DeRosa RT, De Rosa R, DeSalvo R, Dhurandhar S, Díaz MC, Di Fiore L, Di Giovanni M, Di Lieto A, Di Pace S, Di Palma I, Di Virgilio A, Dojcinoski G, Dolique V, Donovan F, Dooley KL, Doravari S, Douglas R, Downes TP, Drago M, Drever RWP, Driggers JC, Du Z, Ducrot M, Dwyer SE, Edo TB, Edwards MC, Effler A, Eggenstein H.-B, Ehrens P, Eichholz J, Eikenberry SS, Engels W, Essick RC, Etzel T, Evans M, Evans TM, Everett R, Factourovich M, Fafone V, Fair H, Fairhurst S, Fan X, Fang Q, Farinon S, Farr B, Farr WM, Favata M, Fays M, Fehrmann H, Fejer MM, Feldbaum D, Ferrante I, Ferreira EC, Ferrini F, Fidecaro F, Finn LS, Fiori I, Fiorucci D, Fisher RP, Flaminio R, Fletcher M, Fong H, Fournier J.-D, Franco S, Frasca S, Frasconi F, Frede M, Frei Z, Freise,

A, Frey R, Frey V, Fricke TT, Fritschel P, Frolov VV, Fulda P, Fyffe M, Gabbard HAG, Gair JR, Gammaitoni L, Gaonkar SG, Garufi F, Gatto A, Gaur G, Gehrels N, Gemme G, Gendre B, Genin E, Gennai A, George J, Gergely L, Germain V, Ghosh Abhirup, Ghosh Archisman, Ghosh S, Giaime JA, Giardina KD, Giazotto A, Gill K, Glaefke A, Gleason JR, Goetz E, Goetz R, Gondan L, González G, Gonzalez Castro JM and Gopakumar A, Gordon NA, Gorodetsky ML, Gossan SE, Gosselin M, Gouaty R, Graef C, Graff PB, Granata M, Grant A, Gras S, Gray C, Greco G, Green AC, Greenhalgh RJS, Groot P, Grote H, Grunewald S, Guidi GM, Guo X, Gupta A, Gupta MK, Gushwa KE, Gustafson EK, Gustafson R, Hacker JJ, Hall BR, Hall ED, Hammond G, Haney M, Hanke MM, Hanks J, Hanna C, Hannam MD, Hanson J, Hardwick T, Harms J, Harry GM, Harry IW, Hart MJ, Hartman MT, Haster C.-J, Haughian K, Healy J, Heefner J, Heidmann A, Heintze MC, Heinzel G, Heitmann H, Hello P, Hemming G, Hendry M, Heng IS, Hennig J, Heptonstall AW, Heurs M, Hild S, Hoak D, Hodge KA, Hofman D, Hollitt SE, Holt K, Holz DE, Hopkins P, Hosken DJ, Hough J, Houston EA, Howell EJ, Hu YM, Huang S, Huerta EA, Huet D, Hughey B, Husa S, Huttner SH, Huynh-Dinh T, Idrisy A, Indik N, Ingram DR, Inta R, Isa HN, Isac J.-M, Isi M, Islas G, Isogai T, Iyer BR, Izumi K, Jacobson MB, Jacqmin T, Jang H, Jani K, Jaranowski P, Jawahar S, Jiménez-Forteza F, Johnson WW, Johnson-McDaniel NK, Jones DI, Jones R, Jonker RJG, Ju L, Haris K, Kalaghatgi CV, Kalogera V, Kandhasamy S, Kang G, Kanner JB, Karki S, Kasprzack M, Katsavounidis E, Katzman W, Kaufer S, Kaur T, Kawabe K, Kawazoe F, Kéfélian F, Kehl MS, Keitel D, Kelley DB, Kells W, Kennedy R, Keppel DG, Key JS, Khalaidovski A, Khalili FY, Khan I, Khan S, Khan Z, Khazanov EA, Kijbunchoo N, Kim C, Kim J, Kim K, Kim Nam-Gyu, Kim N, Kim YM, King EJ, King PJ, Kinzel DL, Kissel JS, Kleybolte L, Klimenko S, Koehlenbeck SM, Kokeyama K, Koley S, Kondrashov V, Kontos A, Koranda S, Korobko M, Korth WZ, Kowalska I, Kozak DB, Kringel V, Krishnan B, Królak A, Krueger C, Kuehn G, Kumar P, Kumar R, Kuo L, Kutynia A, Kwee P, Lackey BD, Landry M, Lange J, Lantz B, Lasky PD, Lazzarini A, Lazzaro C, Leaci P, Leavey S, Lebigot EO, Lee CH, Lee HK, Lee HM, Lee K, Lenon A, Leonardi M, Leong JR, Leroy,N, Letendre N, Levin Y, Levine BM, Li TGF, Libson A, Littenberg TB, Lockerbie NA, Logue J, Lombardi AL, London LT, Lord JE, Lorenzini M, Loriette V, Lormand M, Losurdo G, Lough JD, Lousto CO, Lovelace G, Lück H, Lundgren AP, Luo J, Lynch R, Ma Y, MacDonald T, Machenschalk B, MacInnis M, Macleod DM, Magaña-Sandoval F, Magee RM, Mageswaran M, Majorana E, Maksimovic I, Malvezzi V, Man N, Mandel I, Mandic V, Mangano V, Mansell GL, Manske M, Mantovani M, Marchesoni F, Marion F, Márka S, Márka Z, Markosyan AS, Maros E, Martelli F, Martellini L, Martin IW, Martin RM, Martynov DV, Marx JN, Mason K, Masserot A, Massinger TJ, Masso-Reid

M, Matichard F, Matone L, Mavalvala N, Mazumder N, Mazzolo G, McCarthy R, McClelland DE, McCormick S, McGuire SC, McIntyre G, McIver J, McManus DJ, McWilliams ST, Meacher D, Meadors GD, Meidam J, Melatos A, Mendell G, Mendoza-Gandara D, Mercer RA, Merilh E, Merzougui M, Meshkov S, Messenger C, Messick C, Meyers PM, Mezzani F, Miao H, Michel C, Middleton H, Mikhailov EE, Milano L, Miller J, Millhouse M, Minenkov Y, Ming J, Mirshekari S, Mishra C, Mitra S, Mitrofanov VP, Mitselmakher G, Mittleman R, Moggi A, Mohan M, Mohapatra SRP, Montani M, Moore BC, Moore CJ, Moraru D, Moreno G, Morriss SR, Mossavi K, Mours B, Mow-Lowry CM, Mueller CL, Mueller G, Muir AW, Mukherjee A, Mukherjee D, Mukherjee S, Mukund N, Mullavey A, Munch J, Murphy DJ, Murray PG, Mytidis A, Nardecchia I, Naticchioni L, Nayak RK, Necula V, Nedkova K, Nelemans G, Neri M, Neunzert A, Newton G, Nguyen TT, Nielsen AB, Nissanke S, Nitz A, Nocera F, Nolting D, Normandin MEN, Nuttall LK, Oberling J, Ochsner E, O'Dell J, Oelker E, Ogin GH, Oh JJ, Oh SH, Ohme F, Oliver M, Oppermann P, Oram, Richard J, O'Reilly B, O'Shaughnessy R, Ott CD, Ottaway DJ, Ottens RS, Overmier H, Owen BJ, Pai A, Pai SA, Palamos JR, Palashov O, Palomba C, Pal-Singh A, Pan H, Pan Y, Pankow C, Pannarale F, Pant BC, Paoletti F, Paoli A, Papa MA, Paris HR, Parker W, Pascucci D, Pasqualetti A, Passaquieti R, Passuello D, Patricelli B, Patrick Z, Pearlstone BL, Pedraza M, Pedurand R, Pekowsky L, Pele A, Penn S, Perreca A, Pfeiffer HP, Phelps M, Piccinni O, Pichot M, Pickenpack M, Piergiovanni F, Pierro V, Pillant G, Pinard L, Pinto IM, Pitkin M, Poeld JH, Poggiani R, Popolizio P, Post A, Powell J, Prasad J, Predoi V, Premachandra SS, Prestegard T, Price LR, Prijatelj M, Principe M, Privitera S, Prix R, Prodi GA, Prokhorov L, Puncken O, Punturo M, Puppo P, Pürrer M, Qi H, Qin J, Quetschke V, Quintero EA, Quitzow-James R, Raab FJ, Rabeling DS, Radkins H, Raffai P, Raja S, Rakhmanov M, Ramet CR, Rapagnani P, Raymond V, Razzano M, Re V, Read J, Reed CM, Regimbau T, Rei L, Reid S, Reitze DH, Rew H, Reyes SD, Ricci F, Riles K, Robertson NA, Robie R, Robinet F, Rocchi A, Rolland L, Rollins JG, Roma VJ, Romano JD, Romano R, Romanov G, Romie JH, Rosińska D, Rowan S, Rüdiger A, Ruggi P, Ryan K, Sachdev S, Sadecki T, Sadeghian L, Salconi L, Saleem M, Salemi F, Samajdar A, Sammut L, Sampson LM, Sanchez EJ, Sandberg V, Sandeen B, Sanders GH, Sanders JR, Sassolas B, Sathyaprakash BS, Saulson PR, Sauter O, Savage RL, Sawadsky A, Schale P, Schilling R, Schmidt J, Schmidt P, Schnabel R, Schofield RMS, Schönbeck A, Schreiber E, Schuette D, Schutz BF, Scott J, Scott SM, Sellers D, Sengupta AS, Sentenac D, Sequino V, Sergeev A, Serna G, Setyawati Y, Sevigny A, Shaddock DA, Shaffer T, Shah S, Shahriar MS, Shaltev M, Shao Z, Shapiro B, Shawhan P, Sheperd A, Shoemaker DH, Shoemaker DM, Siellez K, Siemens X, Sigg D, Silva AD, Simakov D, Singer A, Singer LP, Singh A, Singh R, Singhal A,

Sintes AM, Slagmolen BJJ, Smith JR, Smith MR, Smith ND, Smith RJE, Son EJ, Sorazu B, Sorrentino F, Souradeep T, Srivastava AK, Staley A, Steinke M, Steinlechner J, Steinlechner S, Steinmeyer D, Stephens BC, Stevenson SP, Stone R, Strain KA, Straniero N, Stratta G, Strauss NA, Strigin S, Sturani R, Stuver AL, Summerscales TZ, Sun L, Sutton PJ, Swinkels BL, Szczepańczyk MJ, Tacca M, Talukder D, Tanner DB, Tápai M, Tarabrin SP, Taracchini A, Taylor R, Theeg T, Thirugnanasambandam MP, Thomas EG, Thomas M, Thomas P, Thorne KA, Thorne KS, Thrane E, Tiwari S, Tiwari V, Tokmakov KV, Tomlinson C, Tonelli M, Torres CV, Torrie CI, Töyrä D, Travasso F, Traylor G, Trifirò D, Tringali MC, Trozzo L, Tse M, Turconi M, Tuyenbayev D, Ugolini D, Unnikrishnan CS, Urban AL, Usman SA, Vahlbruch H, Vajente G, Valdes G, Vallisneri M, van Bakel N, van Beuzekom M, van den Brand JFJ, Van Den Broeck C, Vander-Hyde DC, van der Schaaf L, van Heijningen JV, van Veggel AA, Vardaro M, Vass S, Vasúth M, Vaulin R, Vecchio A, Vedovato G, Veitch J, Veitch PJ, Venkateswara K, Verkindt D, Vetrano F, Viceré A, Vinciguerra S, Vine DJ, Vinet JY, Vitale S, Vo T, Vocca H, Vorvick C, Voss D, Vousden WD, Vyatchanin SP, Wade AR, Wade LE, Wade M, Waldman SJ, Walker M, Wallace L, Walsh S, Wang G, Wang H, Wang M, Wang X, Wang Y, Ward H, Ward RL, Warner J, Was M, Weaver B, Wei LW, Weinert M, Weinstein AJ, Weiss R, Welborn T, Wen L, Weßels P, Westphal T, Wette K, Whelan JT, Whitcomb SE, White DJ, Whiting BF, Wiesner K, Wilkinson C, Willems PA, Williams L, Williams RD, Williamson AR, Willis JL, Willke B, Wimmer MH, Winkelmann L, Winkler W, Wipf CC, Wiseman AG, Wittel, H, Woan G, Worden J, Wright JL, Wu G, Yablon J, Yakushin I, Yam W, Yamamoto H, Yancey CC, Yap MJ, Yu H, Yvert M, Zadrożny A, Zangrando L, Zanolin M, Zendri JP, Zevin M, Zhang F, Zhang L, Zhang M, Zhang Y, Zhao C, Zhou M, Zhou Z, Zhu XJ, Zucker ME, Zuraw SE, Zweizig J. Observation of gravitational waves from a binary black hole merger. Physical Review Letters. 2016 Feb 11;116(6):061102.

[10] Gigan S, Böhm HR, Paternostro M, Blaser F,Langer G, Hertzberg JB, Schwab KC, Bäuerle D, Aspelmeyer M, Zeilinger A. Self-cooling of a micromirror by radiation pressure. Nature. 2006 Nov 2;444(7115):67–70.

[11] Ashkin A, Dziedzic J. Optical levitation in high vacuum. Applied Physics Letters. 1976 Mar 15;28(6):333–5.

[12] Li T, Kheifets S, Medellin D, Raizen MG. Measurement of the Instantaneous Velocity of a Brownian Particle. Science. 2010 Jun 25;328(5986):1673–5.

[13] Gieseler J, Deutsch B, Quidant R, Novotny L. Subkelvin Parametric Feedback Cooling of a Laser-Trapped Nanoparticle. Physical Review Letters. 2012 Sep 7;109(10):103603.

[14] Poggio M, Degen CL. Force-detected nuclear magnetic resonance: recent advances and future challenges. Nanotechnology. 2010 Jul 30;21(34):342001.

[15] Mohideen U, Roy A. Precision measurement of the Casimir force from 0.1 to 0.9 μm. Physical Review Letters. 1998 Nov 23;81(21):4549.

[16] Chan HB, Aksyuk VA, Kleiman RN, Bishop DJ, Capasso F. Quantum mechanical actuation of microelectromechanical systems by the Casimir force. Science. 2001 Mar 9;291(5510):1941–4.

[17] Decca RS, López D, Fischbach E, Klimchitskaya G, Krause D, Mostepanenko V. Tests of new physics from precise measurements of the Casimir pressure between two gold-coated plates. Physical Review D. 2007 Apr 23;75(7):077101.

[18] Ashkin A, Dziedzic JM, Yamane T. Optical trapping and manipulation of single cells using infrared laser beams. Nature. 1987 Dec 31;330(6150):769–71.

[19] Ashkin A, Dziedzic JM. Optical trapping and manipulation of viruses and bacteria. Science. 1987 Mar 20;235:1517–21.

[20] Ashkin A. History of optical trapping and manipulation of small-neutral particle, atoms, and molecules. IEEE Journal of Selected Topics in Quantum Electronics. 2000 Nov;6(6):841–56.

[21] Prikulis J, Svedberg F, Käll M, Enger J, Ramser K, Goksör M, et al. Optical spectroscopy of single trapped metal nanoparticles in solution. Nano Letters. 2004 Jan 14;4(1):115–8.

[22] Martínez IA, Roldán É, Dinis L, Petrov D, Parrondo JM, Rica RA. Brownian carnot engine. Nature physics. 2015 Oct 26;12(1):67–70.

[23] Martínez IA, Roldán É, Dinis L, Petrov D, Rica RA. Adiabatic processes realized with a trapped Brownian particle. Physical Review Letters. 2015 Mar 27;114(12):120601.

[24] Gieseler J, Quidant R, Dellago C, Novotny L. Dynamic relaxation of a levitated nanoparticle from a non-equilibrium steady state. Nature Nanotechnology. 2014 May 1;9(5):358–64.

[25] Marquardt F, Girvin SM. Optomechanics (a brief review). arXiv preprint arXiv:09050566. 2009 May 5;.

[26] Neukirch LP, Vamivakas AN. Nano-optomechanics with optically levitated nanoparticles. Contemporary Physics. 2015 Jan 2;56(1):48–62.

[27] Jain V, Gieseler J, Moritz C, Dellago C, Quidant R, Novotny L. Direct measurement of photon recoil from a levitated nanoparticle. Physical Review Letters. 2016 Jun 13;116(24):243601.

[28] Leggett AJ. Testing the limits of quantum mechanics: motivation, state of play, prospects. Journal of Physics: Condensed Matter. 2002 Apr 4;14(15):R415.

[29] Arndt M, Nairz O, Vos-Andreae J, Keller C, Van der Zouw G, Zeilinger A. Wave–particle duality of C60 molecules. Nature. 1999 Oct 14;401(6754):680–2.

[30] Kasevich M, Chu S. Atomic interferometry using stimulated Raman transitions. Physical Review Letters. 1991 Jul 8;67(2):181.

[31] Davisson C, Germer LH. Diffraction of electrons by a crystal of nickel. Physical Review. 1927 Dec 1;30(6):705.

[32] Laloë F. Do we really understand quantum mechanics? Cambridge University Press; 2012 Aug 30.

[33] Joos E, Zeh HD. The emergence of classical properties through interaction with the environment. Zeitschrift für Physik B Condensed Matter. 1985 Jun 1;59(2):223–43.

[34] Schlosshauer M. Decoherence, the measurement problem, and interpretations of quantum mechanics. Reviews of Modern physics. 2005 Feb 23;76(4):1267.

[35] Zurek WH. Decoherence and the transition from quantum to classical-revisited. Los Alamos Science. 2002 Nov 27;27:86–109.

[36] Adler SL. Quantum theory as an emergent phenomenon: The statistical mechanics of matrix models as the precursor of quantum field theory. Cambridge University Press; 2004 Aug 26.

[37] Joos E, Zeh HD, Kiefer C, Giulini DJ, Kupsch J, Stamatescu IO. Decoherence and the appearance of a classical world in quantum theory. Springer Science & Business Media; 2013 Mar 9.

[38] Zurek WH. Decoherence, einselection, and the quantum origins of the classical. Reviews of modern physics. 2003 May 22;75(3):715.

[39] Bassi A, Lochan K, Satin S, Singh TP, Ulbricht H. Models of wave-function collapse, underlying theories, and experimental tests. Reviews of Modern Physics. 2013 Apr 2;85(2):471.

[40] Romero-Isart O, Pflanzer AC, Juan ML, Quidant R, Kiesel N, Aspelmeyer M, Cirac JI. Optically levitating dielectrics in the quantum regime: Theory and protocols. Physical Review A. 2011 Jan 7;83(1):013803.

[41] Eibenberger S, Gerlich S, Arndt M, Mayor M, Tüxen J. Matter–wave interference of particles selected from a molecular library with masses exceeding 10000 amu. Physical Chemistry Chemical Physics. 2013 Jul 5;15(35):14696–700.

[42] Arndt M, Hornberger K. Testing the limits of quantum mechanical superpositions. Nature Physics. 2014 Apr 1;10(4):271–7.

[43] Bahrami M, Paternostro M, Bassi A, Ulbricht H. Proposal for a noninterferometric test of collapse models in optomechanical systems. Physical Review Letters. 2014 May 29;112(21):210404.

[44] Bateman J, Nimmrichter S, Hornberger K, Ulbricht H. Near-field interferometry of a free-falling nanoparticle from a point-like source. Nature Communications. 2014 Sep 2;5:4788.

[45] Gimzewski JK, Joachim C. Nanoscale science of single molecules using local probes. Science. 1999 Mar 12;283(5408):1683–8.

[46] Ritort F. The nonequilibrium thermodynamics of small systems. Comptes Rendus Physique. 2007 Jun 1;8(5-6):528–39.

[47] Seifert U. Stochastic thermodynamics: principles and perspectives. The European Physical Journal B-Condensed Matter and Complex Systems. 2008 Aug 1;64(3):423–31.

[48] Wang GM, Sevick EM, Mittag E, Searles DJ, Evans DJ. Experimental demonstration of violations of the second law of thermodynamics for small systems and short time scales. Physical Review Letters. 2002 Jul 15;89(5):050601.

[49] Campisi M, Hänggi P, Talkner P. Colloquium: Quantum fluctuation relations: Foundations and applications. Reviews of Modern Physics. 2011 Dec 19;83(3):771.

[50] Jarzynski C. Equalities and inequalities: irreversibility and the second law of thermodynamics at the nanoscale. Annual Review of Condensed Matter Physics. 2011 Mar 10;2(1):329–51.

[51] Sekimoto K. Langevin equation and thermodynamics. Progress of Theoretical Physics Supplement. 1998 Jan 1;130:17–27.

[52] Sekimoto K. Stochastic energetics. vol. 799. Springer; 2010 Mar 10.

[53] Seifert U. Stochastic thermodynamics, fluctuation theorems and molecular machines. Reports on Progress in Physics. 2012 Nov 20;75(12):126001.

[54] Ciliberto S, Gomez-Solano R, Petrosyan A. Fluctuations, linear response, and currents in out-of-equilibrium systems. Annual Review of Condensed Matter Physics. 2013 Apr 1;4(1):235–61.

[55] Bui AA, Stilgoe AB, Khatibzadeh N, Nieminen TA, Berns MW, Rubinsztein-Dunlop H. Escape forces and trajectories in optical tweezers and their effect on calibration. Optics Express. 2015 Sep 21;23(19):24317–30.

[56] Dechant A, Kiesel N, Lutz E. All-optical nanomechanical heat engine. Physical Review Letters. 2015 May 6;114(18):183602.

[57] Roßnagel J, Dawkins ST, Tolazzi KN, Abah O, Lutz E, Schmidt-Kaler F, et al. A single-atom heat engine. Science. 2016 Apr 15;352(6283):325–9.

[58] Zhang K, Bariani F, Meystre P. Theory of an optomechanical quantum heat engine. Physical Review A. 2014 Aug 12;90(2):023819.

[59] Blickle V, Bechinger C. Realization of a micrometre-sized stochastic heat engine. Nature Physics. 2012 Feb 1;8(2):143–6.

[60] Roßnagel J, Abah O, Schmidt-Kaler F, Singer K, Lutz E. Nanoscale Heat Engine Beyond the Carnot Limit. Physical Review Letters. 2014 Jan 22;112:030602.

[61] Moser J, Güttinger J, Eichler A, Esplandiu MJ, Liu DE, Dykman MI, Bachtold A. Ultrasensitive force detection with a nanotube mechanical resonator. Nature Nanotechnology. 2013 Jul 1;8(7):493–6.

[62] Gieseler J, Novotny L, Quidant R. Thermal nonlinearities in a nanomechanical oscillator. Nature Physics. 2013 Dec 1;9:806.

[63] Hempston D, Vovrosh J, Toro M, Winstone G, Rashid M, Ulbricht H. Force sensing with an optically levitated charged nanoparticle. Applied Physics Letters. 2017 Sep;111(13):133111.

[64] Hoang TM, Ma Y, Ahn J, Bang J, Robicheaux F, Yin ZQ, Li T. Torsional optomechanics of a levitated nonspherical nanoparticle. Physical Review Letters. 2016;117(12):123604.

[65] Li T. Millikelvin cooling of an optically trapped microsphere in vacuum. In: Fundamental Tests of Physics with Optically Trapped Microspheres. Springer; 2013. p. 81–110.

[66] Hsu JF, Ji P, Lewandowski CW, DUrso B. Cooling the motion of diamond nanocrystals in a magneto-gravitational trap in high vacuum. Scientific Reports. 2016 Jul 22;6.

[67] Geiselmann M, Juan ML, Renger J, Say JM, Brown LJ, De Abajo FJG, Koppens F, Quidant R. Three-dimensional optical manipulation of a single electron spin. Nature Nanotechnology. 2013 Mar 1;8(3):175–9.

[68] Neukirch LP, Gieseler J, Quidant R, Novotny L, Vamivakas AN. Observation of nitrogen vacancy photoluminescence from an optically levitated nanodiamond. Optics Letters. 2013 Aug 15;38(16):2976–9.

[69] Arvanitaki A, Geraci AA. Detecting high-frequency gravitational waves with optically levitated sensors. Physical Review Letters. 2013 Feb 14;110(7):071105.

[70] Geraci AA, Papp SB, Kitching J. Short-Range Force Detection Using Optically Cooled Levitated Microspheres. Physical Review Letters. 2010 Aug 30;105(10):101101.

[71] Ranjit G, Atherton DP, Stutz JH, Cunningham M, Geraci AA. Attonewton force detection using microspheres in a dual-beam optical trap in high vacuum. Physical Review A. 2015 May 26;91(5):051805.

[72] Rugar D, Budakian R, Mamin HJ, Chui BW. Single spin detection by magnetic resonance force microscopy. Nature. 2004 July 15;430(6997):329–32.

[73] Bateman J, McHardy I, Merle A, Morris TR, Ulbricht H. On the Existence of Low-Mass Dark Matter and its Direct Detection. Scientific Reports. 2015 Jan 27;5:8058.

[74] Ashkin A, Dziedzic JM. Optical Levitation by Radiation Pressure. Applied Physics Letters. 1971;19(8):283–5.

[75] Ashkin A. Acceleration and Trapping of Particles by Radiation Pressure. Physical Review Letters. 1970 Jan 26 Jan 26;24:156–9.

[76] Zemánek P, Jonáš A, Šrámek L, Liška M. Optical trapping of Rayleigh particles using a Gaussian standing wave. Optics Communications. 1998 Jun 1;151(4):273–85.

[77] Zemánek P, Jonáš A, Šrámek L, Liška M. Optical trapping of nanoparticles and microparticles by a Gaussian standing wave. Optics Letters. 1999 Nov;24(21):1448–1450.

[78] Ashkin A, Dziedzic JM, Bjorkholm JE, Chu S. Observation of a single-beam gradient force optical trap for dielectric particles. Optics Letters. 1986 May 1;11(5):288–90.

[79] Kepler J. De cometis libelli tres. 1963;.

[80] Ashkin A. Acceleration and trapping of particles by radiation pressure. Physical Review Letters. 1970;24(4):156.

[81] Ashkin A, Dziedzic J. Stability of optical levitation by radiation pressure. Applied Physics Letters. 1974 Oct 15;24(12):586–8.

[82] Ashkin A, Dziedzic J. Optical levitation by radiation pressure. Applied Physics Letters. 1971 Oct 15;19(8):283–5.

[83] Omori R, Kobayashi T, Suzuki A. Observation of a single-beam gradient-force optical trap for dielectric particles in air. Optics Letters. 1997 Jun 1;22(11):816–8.

[84] Ashok PC, Dholakia K. Optical trapping for analytical biotechnology. Current Opinion in Biotechnology. 2012 Feb 29;23(1):16–21.

[85] Perkins TT. Optical traps for single molecule biophysics: a primer. Laser & Photonics Reviews. 2009 Feb 24;3(1-2):203–20.

[86] Neuman KC, Nagy A. Single-molecule force spectroscopy: optical tweezers, magnetic tweezers and atomic force microscopy. Nature Methods. 2008 Jun;5(6):491.

[87] Svoboda K, Block SM. Biological applications of optical forces. Annual Review of Biophysics and Biomolecular Structure. 1994 Jun;23(1):247–85.

[88] Abbott B, Abbott R, Adhikari R, Ajith P, Allen , B, Allen G, Amin R, Anderson SB, Anderson WG, Arain MA, Araya M, Armandula H, Armor P, Aso Y, Aston S, Aufmuth P, Aulbert C, Babak S, Ballmer S, Bantilan H, Barish BC, Barker C, Barker D, Barr B, Barriga P, Barton MA, Bastarrika M, Bayer K, Betzwieser J, Beyersdorf PT, Bilenko IA, Billingsley G, Biswas R, Black E, Blackburn K, Blackburn L, Blair D, Bland B, Bodiya TP, Bogue L, Bork R, Boschi V, Bose S, Brady PR, Braginsky VB, Brau JE, Brinkmann M, Brooks A, Brown DA, Brunet G, Bullington A, Buonanno A, Burmeister O, Byer RL, Cadonati L, Cagnoli G, Camp JB, Cannizzo J, Cannon K, Cao J, Cardenas L, Casebolt T, Castaldi G, Cepeda C, Chalkley E, Charlton P, Chatterji S, Chelkowski S, Chen , Y, Christensen N, Clark D, Clark J, Cokelaer T, Conte R, Cook D, Corbitt , T, Coyne D, Creighton JDE, Cumming A, Cunningham L, Cutler RM, Dalrymple J, Danilishin S, Danzmann , K, Davies G, DeBra D, Degallaix J, Degree M, Dergachev V, Desai S, DeSalvo R, Dhurandhar S, Daz M, Dickson J, Dietz A, Donovan F, Dooley KL,

Doomes EE, Drever RWP, Duke I, Dumas J-C, Dupuis RJ, Dwyer JG, Echols C, Effler A, Ehrens P, Espinoza E, Etzel T, Evans T, Fairhurst S, Fan Y, Fazi D, Fehrmann H, Fejer MM, Finn LS, Flasch K, Fotopoulos N, Freise A, Frey R, Fricke ,T, Fritschel P, Frolov VV, Fyffe M, Garofoli J, Gholami I, Giaime , JA, Giampanis S, Giardina KD, Goda K, Goetz E, Goggin L, Gonzlez G, Gossler S, Gouaty R, Grant A, Gras S, Gray C, Gray M, Greenhalgh RJS, Gretarsson AM, Grimaldi F, Grosso R, Grote H, Grunewald S, Guenther M, Gustafson EK, Gustafson R, Hage B, Hallam JM, Hammer D, Hanna C, Hanson J, Harms J, Harry G, Harstad E, Hayama K, Hayler T, Heefner J, Heng IS, Hennessy M, Heptonstall A, Hewitson M, Hild S, Hirose E, Hoak D, Hosken D, Hough J, Huttner SH, Ingram D, Ito M, Ivanov A, Johnson B, Johnson WW, Jones DI, Jones G, Jones R, Ju L, Kalmus P, Kalogera V, Kamat S, Kanner J, Kasprzyk D, Katsavounidis E, Kawabe K, Kawamura S, Kawazoe F, Kells W, Keppel DG, Ya Khalili F, Khan R, Khazanov E, Kim C, King P, Kissel JS, Klimenko S, Kokeyama K, Kondrashov V, Kopparapu RK, Kozak D, Kozhevatov I, Krishnan B, Kwee P, Lam PK, Landry M, Lang MM, Lantz B, Lazzarini A, Lei M, Leindecker N, Leonhardt V, Leonor I, Libbrecht K, Lin H, Lindquist P, Lockerbie NA, Lodhia D, Lormand M, Lu P, Lubinski M, Lucianetti A, Lck , H, Machenschalk B, MacInnis M, Mageswaran M , Mailand K, Mandic V, Mrka S, Mrka Z, Markosyan A, Markowitz J, Maros E, Martin I, Martin RM, Marx JN, Mason K, Matichard F, Matone L, Matzner R, Mavalvala N, McCarthy R, McClelland DE, McGuire SC, McHugh M, McIntyre G, McIvor G, McKechan D, McKenzie K, Meier T, Melissinos A, Mendell G, Mercer RA, Meshkov S, Messenger CJ, Meyers D, Miao H, Miller , J, Minelli J, Mitra S, Mitrofanov VP, Mitselmakher G, Mittleman R, Miyakawa O, Moe B, Mohanty S, Moreno G, Mossavi K, Mow-Lowry C, Mueller G, Mukherjee S, Mukhopadhyay H, Mller-Ebhardt H, Munch J, Murray P, Myers E, Myers J, Nash T, Nelson J, Newton G, Nishizawa A, Numata K, O'Dell J, Ogin G, O'Reilly B, O'Shaughnessy R, Ottaway DJ, Ottens RS, Overmier H, Owen BJ, Pan Y, Pankow C, Papa , MA, Parameshwaraiah V, Patel P, Pedraza M, Penn S, Perreca A, Petrie T, Pinto IM, Pitkin M, Pletsch HJ, Plissi MV, Postiglione F, Principe M, Prix R, Quetschke V, Raab F, Rabeling DS, Radkins H, Rainer N, Rakhmanov M, Ramsunder M, Rehbein H, Reid S , Reitze DH, Riesen R, Riles K, Rivera B, Robertson , NA, Robinson C, Robinson EL, Roddy S, Rodriguez A, Rogan AM, Rollins J, Romano JD, Romie J, Route R, Rowan S, Rdiger A, Ruet L, Russell P, Ryan K, Sakata S, Samidi M, Sancho de la Jordana L, Sandberg V, Sannibale V, Saraf S, Sarin P, Sathyaprakash BS, Sato S, Saulson PR, Savage R, Savov P, Schediwy SW, Schilling R, Schnabel R, Schofield R, Schutz , BF, Schwinberg P, Scott SM, Searle AC, Sears B, Seifert F, Sellers D, Sengupta AS, Shawhan P, Shoemaker DH, Sibley A, Siemens X, Sigg D, Sinha S, Sintes , AM, Slagmolen BJJ, Slutsky

J, Smith JR, Smith MR, Smith ND, Somiya , K, Sorazu B, Stein LC, Stochino A, Stone R, Strain KA, Strom DM, Stuver A, Summerscales TZ, Sun K-X, Sung M, Sutton PJ, Takahashi H, Tanner DB, Taylor R, Taylor R, Thacker J, Thorne KA, Thorne KS, Thring A, Tokmakov KV, Torres C, Torrie C, Traylor G, Trias M, Tyler W, Ugolini D, Ulmen J, Urbanek K, Vahlbruch H, Van Den Broeck C, van der Sluys M, Vass S, Vaulin R, Vecchio A, Veitch J, Veitch P, Villar A, Vorvick C, Vyatchanin SP, Waldman SJ, Wallace L, Ward H, Ward R, Weinert M, Weinstein A, Weiss R, Wen S, Wette K, Whelan JT, Whitcomb SE, Whiting BF, Wilkinson C, Willems PA,Williams HR,Williams L, Willke , B, Wilmut I, Winkler W, Wipf CC, Wiseman AG, Woan G, Wooley R, Worden J, Wu W, Yakushin I, Yamamoto H, Yan Z, Yoshida S, Zanolin M, Zhang J, Zhang L, Zhao C, Zotov N, Zucker M, Zweizig J. Observation of a kilogram-scale oscillator near its quantum ground state. New Journal of Physics. 2009 Jul 16;11(7):073032.

[89] Romero-Isart O. Quantum superposition of massive objects and collapse models. Physical Review A. 2011 Nov 26;84(5):052121.

[90] La Porta A, Wang MD. Optical torque wrench: angular trapping, rotation, and torque detection of quartz microparticles. Physical Review Letters. 2004 May 14;92(19):190801.

[91] Bishop AI, Nieminen TA, Heckenberg NR, Rubinsztein-Dunlop H. Optical microrheology using rotating laser-trapped particles. Physical Review Letters. 2004 May 14;92(19):198104.

[92] Bhattacharya M, Meystre P. Using a Laguerre-Gaussian beam to trap and cool the rotational motion of a mirror. Physical Review Letters. 2007 Oct 10;99(15):153603.

[93] Arita Y, Mazilu M, Dholakia K. Laser-induced rotation and cooling of a trapped microgyroscope in vacuum. Nature Communications. 2013;4:2374.

[94] Gittes F, Schmidt CF. Interference model for back-focal-plane displacement detection in optical tweezers. Optics Letters. 1998 Jan 1 Jan;23(1):7–9.

[95] Neuman KC, Block SM. Optical trapping. Review of Scientific Instruments. 2004 Sep 7;75(9):2787–809.

[96] Molloy JE, Padgett MJ. Lights, action: optical tweezers. Contemporary Physics. 2002 Jul 1;43(4):241–58.

[97] Chang DE, Regal CA, Papp SB, Wilson DJ, Ye J, Painter O, Kimble HJ, Zoller P. Cavity opto-mechanics using an optically levitated nanosphere. Proceedings of the National Academy of Sciences. 2010 Jan 19;107(3):1005–10.

[98] Chang DE, Regal CA, Papp SB, Wilson DJ, Ye J, Painter O, et al.;.

[99] Fonseca PZG, Aranas EB, Millen J, Monteiro TS, Barker PF. Nonlinear Dynamics and Strong Cavity Cooling of Levitated Nanoparticles. Physical Review Letters. 2016 Oct 21;117(17):173602.

[100] Millen J, Fonseca PZG, Mavrogordatos T, Monteiro TS, Barker PF. Cavity Cooling a Single Charged Levitated Nanosphere. Physical Review Letters. 2015 Mar 27;114(12):123602.

[101] Kiesel N, Blaser F, Deli U, Grass D, Kaltenbaek R, Aspelmeyer M. Cavity cooling of an optically levitated submicron particle. Proceedings of the National Academy of Sciences. 2013 Aug 27 Aug 27;110(35):14180–5.

[102] Asenbaum P, Kuhn S, Nimmrichter S, Sezer U, Arndt M. Cavity cooling of free silicon nanoparticles in high vacuum. Nature Communications. 2013;4:3743.

[103] Hecht E. Optics 4th edition; 1998.

[104] Feng S, Winful HG. Physical origin of the Gouy phase shift. Optics Letters. 2001 Apr 15;26(8):485–7.

[105] Chaumet PC. Fully vectorial highly nonparaxial beam close to the waist. Journal of the Optical Society of America A. 2006 Dec 1;23(12):3197–202.

[106] Harada Y, Asakura T. Radiation forces on a dielectric sphere in the Rayleigh scattering regime. Optics Communications. 1996 Mar 15;124(5-6):529–41.

[107] Bradshaw DS, Andrews DL. Manipulating particles with light: radiation and gradient forces. European Journal of Physics. 2017 March 8;38(3):034008.

[108] Török P, Varga P, Laczik Z, Booker GR. Electromagnetic diffraction of light focused through a planar interface between materials of mismatched refractive indices: an integral representation. Journal of the Optical Society of America A. 1995 Feb 12;12(2):325–332.

[109] Godazgar T, Shokri R, Reihani SNS. Potential mapping of optical tweezers. Optics Letters. 2011 Aug;36(16):3284–3286.

[110] Montes-Usategui M, Pleguezuelos E, Andilla J, Martín-Badosa E. Fast generation of holographic optical tweezers by random mask encoding of Fourier components. Optics Express. 2006 Aug 1;14(6):2101–7.

[111] Brau RR, Tarsa PB, Ferrer JM, Lee P, Lang MJ. Interlaced optical force-fluorescence measurements for single molecule biophysics. Biophysical Journal. 2006;91(3):1069–77.

[112] Kuhn S, Asenbaum P, Kosloff A, Sclafani M, Stickler BA, Nimmrichter S, Hornberger K, Cheshnovsky O, Patolsky F, Arndt M. Cavity-assisted manipulation of freely rotating silicon nanorods in high vacuum. Nano Letters. 2015 Jul 15;15(8):5604–8.

[113] Li T. Fundamental tests of physics with optically trapped microspheres. Springer Science & Business Media; 2012 Nov 2.

[114] Rashid M, Tufarelli T, Bateman J, Vovrosh J, Hempston D, Kim MS, Ulbricht H. Experimental Realization of a Thermal Squeezed State of Levitated Optomechanics. Physical Review Letters. 2016 Dec;117:273601.

[115] Li T, Kheifets S, Raizen MG. Millikelvin cooling of an optically trapped microsphere in vacuum. Nature Physics. 2011 Jul 1;7(7):527–30.

[116] Neukirch LP, Gieseler J, Quidant R, Novotny L, Vamivakas AN. Observation of nitrogen vacancy photoluminescence from an optically levitated nanodiamond. Optics Letters. 2013 Aug 15 Aug;38(16):2976–9.

[117] Hoang TM, Ma Y, Ahn J, Bang J, Robicheaux F, Yin Z-Q, Li T. Torsional Optomechanics of a Levitated Nonspherical Nanoparticle. Physical Review Letters. 2016 Sep 15 Sep;117:123604.

[118] Neukirch LP, Haartman Ev, M RJ, Vamivakas AN. Multi-dimensional single-spin nano-optomechanics with a levitated nanodiamond. Nature Photonics. 2015 Oct 1;9(10):6537.

[119] Kiesel N, Blaser F, Delić U, Grass D, Kaltenbaek R, Aspelmeyer M. Cavity cooling of an optically levitated submicron particle. Proceedings of the National Academy of Sciences. 2013 Aug 27;110(35):14180–5.

[120] Millen J, Fonseca P, Mavrogordatos T, Monteiro T, Barker P. Cavity Cooling a Single Charged Levitated Nanosphere. Physical Review Letters. 2015 Mar 27;114(12):123602.

[121] Frimmer M, Luszcz K, Ferreiro S, Jain V, Hebestreit E, Novotny L. Controlling the net charge on a nanoparticle optically levitated in vacuum. Physical Review A. 2017 Jun 6;95(6):061801.

[122] Grass D, Fesel J, Hofer SG, Kiesel N, Aspelmeyer M. Optical trapping and control of nanoparticles inside evacuated hollow core photonic crystal fibers. Applied Physics Letters. 2016 May 30;108(22):221103.

[123] Rahman ATMA, Frangeskou AC, Kim MS, Bose S, Morley GW, Barker PF. Burning and graphitization of optically levitated nanodiamonds in vacuum. Scientific Reports. 2016 Feb 22;6.

[124] Mahajan VN. Strehl ratio for primary aberrations in terms of their aberration variance. Journal of the Optical Society of America. 1983 Jun 1;73(6):860–1.

[125] Varga P, Török P. Focusing of electromagnetic waves by paraboloid mirrors. II. Numerical results. Journal of the Optical Society of America A. 2000 Nov 1;17(11):2090–5.

[126] Phillips WD. Nobel Lecture: Laser cooling and trapping of neutral atoms. Reviews of Modern Physics. 1998 Jul 1;70:721–41.

[127] Zhong MC, Zhou JH, Ren YX, Li YM, Wang ZQ. Rotation of birefringent particles in optical tweezers with spherical aberration. Applied Optics. 2009 Aug 1;48(22):4397–402.

[128] Beresnev S, Chernyak V, Fomyagin G. Motion of a spherical particle in a rarefied gas. Part 2. Drag and thermal polarization. Journal of Fluid Mechanics. 1990 Oct 1;219:405–21.

[129] Bearden JA. A Precision Determination of the Viscosity of Air. Physical Review. 1939 Nov 15;56:1023–40.

[130] Sone Y. Molecular Gas Dynamics: Theory, Techniques, and Applications. Modeling and Simulation in Science, Engineering and Technology. Birkhäuser Boston; 2007.

[131] Kuhn S, Kosloff A, Stickler BA, Patolsky F, Hornberger K, Arndt M, Millen J. Full rotational control of levitated silicon nanorods. Optica. 2017 Mar 20;4(3):356–60.

[132] Bareil PB, Sheng Y. Angular and position stability of a nanorod trapped in an optical tweezers. Optics Express. 2010 Dec 6;18(25):26388–98.

[133] Chu D, Wong WK, Goodson KE, Pease RFW. Transient temperature measurements of resist heating using nanothermocouples. Journal of Vacuum Science & Technology B: Microelectronics and Nanometer Structures Processing, Measurement, and Phenomena. 2003 Nov;21(6):2985–9.

[134] Childs PR. Practical temperature measurement. Butterworth-Heinemann; 2001.

[135] Piscanec S, Cantoro M, Ferrari AC, Zapien JA, Lifshitz Y,Lee ST, Hofmann S, Robertson J. Raman spectroscopy of silicon nanowires. Physical Review B. 2003 Dec 24;68(24):241312.

[136] Calizo I, Balandin AA, Bao W, Miao F, Lau C. Temperature dependence of the Raman spectra of graphene and graphene multilayers. Nano Letters. 2007 Sep 12;7(9):2645–9.

[137] Beechem T, Graham S, Kearney SP, Phinney LM, Serrano JR. Invited Article: Simultaneous mapping of temperature and stress in microdevices using micro-Raman spectroscopy. Review of Scientific Instruments. 2007 Jun;78(6):061301.

[138] Okabe K, Inada N, Gota C, Harada Y, Funatsu T, Uchiyama S. Intracellular temperature mapping with a fluorescent polymeric thermometer and fluorescence lifetime imaging microscopy. Nature Communications. 2012 Feb 28;3:705.

[139] Cahill DG, Goodson K, Majumdar A. Thermometry and thermal transport in micro/nanoscale solid-state devices and structures. Journal of Heat Transfer. 2002 Apr 1;124(2):223–41.

[140] Aigouy L, Tessier G, Mortier M, Charlot B. Scanning thermal imaging of microelectronic circuits with a fluorescent nanoprobe. Applied Physics Letters. 2005;87(18):184105.

[141] Jung W, Kim YW, Yim D, Yoo JY. Microscale surface thermometry using SU8/Rhodamine-B thin layer. Sensors and Actuators A: Physical. 2011 Nov 30;171(2):228–32.

[142] Lee J. Estimation of emission properties for silica particles using thermal radiation spectroscopy. Applied Optics. 2011 Aug 1;50(22):4262–7.

[143] Suzuki M, Tseeb V, Oyama K, Ishiwata S. Microscopic detection of thermogenesis in a single HeLa cell. Biophysical Journal. 2007 Mar 15;92(6):L46–8.

[144] Zohar O, Ikeda M, Shinagawa H, Inoue H, Nakamura H, Elbaum D, Alkon DL, Yoshioka T. Thermal imaging of receptor-activated heat production in single cells. Biophysical Journal. 1998 Jan 31;74(1):82–9.

[145] Gosse C, Bergaud C, Löw P. Molecular probes for thermometry in microfluidic devices. In: Thermal Nanosystems and Nanomaterials. Springer; 2009. p. 301–41.

[146] Mao H, Yang T, Cremer PS. A microfluidic device with a linear temperature gradient for parallel and combinatorial measurements. Journal of the American Chemical Society. 2002 Apr 24;124(16):4432–4435.

[147] Richardson HH, Hickman ZN, Govorov AO, Thomas AC, Zhang W, Kordesch ME. Thermooptical properties of gold nanoparticles embedded in ice: characterization of heat generation and melting. Nano Letters. 2006 Apr 12;6(4):783–8.

[148] Brezger B, Arndt M, Zeilinger A. Concepts for near-field interferometers with large molecules. Journal of Optics B: Quantum and Semiclassical Optics. 2003 Apr 2;5(2):S82.

[149] Hornberger K, Gerlich S, Haslinger P, Nimmrichter S, Arndt M. *Colloquium* : Quantum interference of clusters and molecules. Reviews of Modern Physics. 2012 Feb 8;84(1):157–73.

[150] Scala M, Kim M, Morley G, Barker P, Bose S. Matter-wave interferometry of a levitated thermal nano-oscillator induced and probed by a spin. Physical Review Letters. 2013 Oct 29;111(18):180403.

[151] Childs PRN, Greenwood JR, Long CA. Review of temperature measurement. Review of Scientific Instruments. 2000 Aug;71(8):2959–78.

[152] Landström L, Heszler P. Analysis of blackbody-like radiation from laser-heated gas-phase tungsten nanoparticles. The Journal of Physical Chemistry B. 2004 May 20;108(20):6216–21.

[153] Koelemeij JCJ, Roth B, Schiller S. Blackbody thermometry with cold molecular ions and application to ion-based frequency standards. Physical Review A. 2007 Aug 17;76(2):023413.

[154] Leighton RB. Principles of modern physics. International series in pure and applied physics. McGraw-Hill; 1959.

[155] Muley SV, Ravindra NM. Emissivity of Electronic Materials, Coatings, and Structures. The Journal of The Minerals, Metals Materials Society. 2014 Apr 1;66(4):616–36.

[156] Bartl J, Baranek M. Emissivity of aluminium and its importance for radiometric measurement. Measurement Science Review. 2004;4(3):31–6.

[157] Epstein PS. On the Resistance Experienced by Spheres in their Motion through Gases. Phys Rev. 1924 Jun;23:710–733.

[158] Ganta D, Dale EB, Rezac JP, Rosenberger AT. Optical method for measuring thermal accommodation coefficients using a whispering-gallery microresonator. The Journal of Chemical Physics. 2011;135(8):084313.

[159] Huang K. Statistical mechanics. 1963;.

[160] Peterman EJG, Gittes F, Schmidt CF. Laser-induced heating in optical traps. Biophysical Journal. 2003 Feb 28;84(2):1308–16.

[161] Dedkov GV, Kyasov AA. On thermal vacuum radiation of nanoparticles and their ensembles. Physica B: Condensed Matter. 2014 Jan 15;433:67–71.

[162] OConnell AD, Hofheinz M, Ansmann M, Bialczak RC, Lenander M, Lucero E, et al. Quantum ground state and single-phonon control of a mechanical resonator. Nature. 2010 Apr 1;464(7289):697–703.

[163] Poggio M, Degen CL, Mamin HJ, Rugar D. Feedback cooling of a cantilevers fundamental mode below 5 mK. Physical Review Letters. 2007 Jul 2;99(1):017201.

[164] Romero-Isart O, Juan ML, Quidant R, Cirac JI. Toward quantum superposition of living organisms. New Journal of Physics. 2010 Mar 1,;12(3):033015.

[165] Manjavacas A, García de Abajo FJ. Vacuum Friction in Rotating Particles. Physical Review Letters. 2010 Sep 8 Sep;105:113601.

[166] Hänsch TW, Schawlow AL. Cooling of gases by laser radiation. Optics Communications. 1975 Jan 1;13(1):68–9.

[167] Wineland D, Dehmelt H. Proposed 1014 delta upsilon less than upsilon laser fluorescence spectroscopy on t1+ mono-ion oscillator iii. In: Bulletin of the American Physical Society. vol. 20; 1975. p. 637.

[168] Wineland DJ, Drullinger RE, Walls FL. Radiation-pressure cooling of bound resonant absorbers. Physical Review Letters. 1978 Jun 19;40(25):1639.

[169] Wineland DJ, Dalibard J, Cohen-Tannoudji C. Sisyphus cooling of a bound atom. Journal of the Optical Society of America B. 1992 Jan 1;9(1):32–42.

[170] Metcalf HJ, van der Straten P. Laser Cooling and Trapping. Graduate Texts in Contemporary Physics. Springer New York; 2001.

[171] Stenholm S. The semiclassical theory of laser cooling. Reviews of Modern Physics. 1986 Jul 1;58:699–739.

[172] Cohadon PF, Heidmann A, Pinard M. Cooling of a Mirror by Radiation Pressure. Physical Review Letters. 1999 Oct;83:3174–7.

[173] Thompson JD, Zwickl BM, Jayich AM, Marquardt F, Girvin SM, Harris JGE. Strong dispersive coupling of a high-finesse cavity to a micromechanical membrane. Nature. 2008 Mar 6;452(7183):72–5.

[174] Anetsberger G, Arcizet O, Unterreithmeier QP, Rivière, R, Schliesser A, Weig EM, Kotthaus JP, Kippenberg TJ. Near-field cavity optomechanics with nanomechanical oscillators. Nature Physics. 2009 Dec 1;5(12):909–14.

[175] Eichenfield M, Camacho R, Chan J, Vahala KJ, Painter O. A picogram- and nanometre-scale photonic-crystal optomechanical cavity. Nature. 2009 May 28;459(7246):550–5.

[176] Teufel JD, Donner T, Li D, Harlow JW, Allman MS, Cicak Katarina, Sirois AJ, Whittaker JD, Lehnert KW, Simmonds RW. Sideband cooling of micromechanical motion to the quantum ground state. Nature. 2011 Jul 21;475(7356):359–63.

[177] Chan J, Alegre TPM, Safavi-Naeini AH, Hill JT, Krause A, Gröblacher S, Aspelmeyer M, Painter O. Laser cooling of a nanomechanical oscillator into its quantum ground state. Nature. 2011 Oct 6;478(7367):89–92.

[178] Craighead HG. Nanoelectromechanical systems. Science. 2000 Nov 24;290(5496):1532–5.

[179] Ashkin A, Dziedzic JM. Feedback stabilization of optically levitated particles. Applied Physics Letters. 1977 Feb 24;30(4):202–4.

[180] Rugar D, Grütter P. Mechanical parametric amplification and thermomechanical noise squeezing. Physical Review Letters. 1991 Aug 5;67(6):699–702.

[181] Villanueva LG, Karabalin RB, Matheny MH, Kenig E, Cross MC, Roukes ML. A nanoscale parametric feedback oscillator. arXiv preprint arXiv:12110298. 2012;.

[182] Poot M, Fong KY, Tang HX. Classical non-Gaussian state preparation through squeezing in an optoelectromechanical resonator. Physical Review A. 2014 Dec 4;90(6):063809.

[183] Harlow JH. Electric Power Transformer Engineering, Second Edition. The Electric Power Engineering Hbk, Second Edition. CRC Press; 2007.

[184] Reiserer A, Nölleke C, Ritter S, Rempe G. Ground-State Cooling of a Single Atom at the Center of an Optical Cavity. Physical Review Letters. 2013 May 30;110(22):223003.

[185] Kaufman AM, Lester BJ, Regal CA. Cooling a Single Atom in an Optical Tweezer to Its Quantum Ground State. Physical Review X. 2012 Nov 29;2(4):041014.

[186] Griffiths DJ. Introduction to Quantum Mechanics. Pearson international edition. Pearson Prentice Hall; 2005.

[187] Liboff RL. Introductory Quantum Mechanics. Addison-Wesley; 2003.

[188] Fox M. Quantum Optics : An Introduction. Oxford Master Series in Physics. OUP Oxford; 2006.

[189] Andrews DL. Photonics, Fundamentals of Photonics and Physics. 2015;1.

[190] Rugar D, Grütter P. Mechanical parametric amplification and thermomechanical noise squeezing. Physical Review Letters. 1991 Aug 5;67(6):699.

[191] Szorkovszky A, Doherty AC, Harris GI, Bowen WP. Mechanical squeezing via parametric amplification and weak measurement. Physical Review Letters. 2011 Nov 15;107(21):213603.

[192] Pontin A, Bonaldi M, Borrielli A, Cataliotti FS, Marino F, Prodi GA, Serra E, Marin F. Squeezing a thermal mechanical oscillator by stabilized parametric effect on the optical spring. Physical Review Letters. 2014 Jan 15;112(2):023601.

[193] Farace A, Giovannetti V. Enhancing quantum effects via periodic modulations in optomechanical systems. Physical Review A. 2012 Jul 16;86(1):013820.

[194] Mari A, Eisert J. Gently modulating optomechanical systems. Physical Review Letters. 2009 Nov 18;103(21):213603.

[195] Serafini A, Retzker A, Plenio MB. Generation of continuous variable squeezing and entanglement of trapped ions in time-varying potentials. Quantum Information Processing. 2009 Dec 1;8(6):619–30.

[196] Woolley MJ, Doherty AC, Milburn GJ, Schwab KC. Nanomechanical squeezing with detection via a microwave cavity. Physical Review A. 2008 Dec 3;78(6):062303.

[197] Genoni MG, Bina M, Olivares S, De Chiara G, Paternostro M. Squeezing of mechanical motion via qubit-assisted control. New Journal of Physics. 2015 Jan 20;17(1):013034.

[198] Wollman EE, Lei CU, Weinstein AJ, Suh J, Kronwald A, Marquardt F, Clerk AA, Schwab KC. Quantum squeezing of motion in a mechanical resonator. Science. 2015 Aug 28;349(6251):952–5.

[199] Pirkkalainen JM, Damskägg E, Brandt M, Massel F, Sillanpää MA. Squeezing of quantum noise of motion in a micromechanical resonator. Physical Review Letters. 2015 Dec 7;115(24):243601.

[200] Riedinger R, Hong S, Norte RA, Slater JA, Shang J, Krause AG, et al. Non-classical correlations between single photons and phonons from a mechanical oscillator. Nature. 2016 Feb 18;530(7590):313–6.

[201] Agarwal GS, Kumar SA. Exact quantum-statistical dynamics of an oscillator with time-dependent frequency and generation of nonclassical states. Physical Review Letters. 1991 Dec 23;67(26):3665.

[202] Janszky J, Yushin YY. Squeezing via frequency jump. Optics Communications. 1986 Aug 15;59(2):151–4.

[203] Lo C. Squeezing by tuning the oscillator frequency. Journal of Physics A: Mathematical and General. 1990 Apr 7;23(7):1155.

[204] Asjad M, Agarwal G, Kim M, Tombesi P, Di Giuseppe G, Vitali D. Robust stationary mechanical squeezing in a kicked quadratic optomechanical system. Physical Review A. 2014 Feb 28;89(2):023849.

[205] Alonso J, Leupold FM, Solèr ZU, Fadel M, Marinelli M, Keitch BC, Negnevitsky V, Home JP. Generation of large coherent states by bang-bang control of a trapped-ion oscillator. Nature Communications. 2016 Apr 5;7.

[206] Rashid M, Tufarelli T, Bateman J, Vovrosh J, Hempston D, Kim MS, Ulbricht H. Experimental realization of a thermal squeezed state of levitated optomechanics. Physical Review Letters. 2016 Dec 30;117(2)(27):273601.

[207] Genoni MG, Zhang J, Millen J, Barker PF, Serafini A. Quantum cooling and squeezing of a levitating nanosphere via time-continuous measurements. New Journal of Physics. 2015 Jul 14;17(7):073019.

[208] Serafini A, Paris MGA, Illuminati F, De Siena S. Quantifying decoherence in continuous variable systems. Journal of Optics B: Quantum and Semiclassical Optics. 2005 Feb 18;7(4):R19.

[209] Berry MV. Evolution of semiclassical quantum states in phase space. Journal of Physics A: Mathematical and General. 1979 May 12;12(5):625.

[210] Ranjit G, Cunningham M, Casey K, Geraci AA. Zeptonewton force sensing with nanospheres in an optical lattice. Physical Review A. 2016 May 2;93(5):053801.

[211] Roßnagel J, Abah O, Schmidt-Kaler F, Singer K, Lutz E. Nanoscale heat engine beyond the Carnot limit. Physical Review Letters. 2014 Jan 22;112(3):030602.

[212] Wiseman HM, Milburn GJ. Quantum theory of field-quadrature measurements. Physical Review A. 1993 Jan 1;47(1):642.

[213] Vanner MR, Hofer J, Cole GD, Aspelmeyer M. Cooling-by-measurement and mechanical state tomography via pulsed optomechanics. Nature Communications. 2013 Aug 15;4.

[214] Ringbauer M, Weinhold TJ, White AG, Vanner MR. Generation of Mechanical Interference Fringes by Multi-Photon Quantum Measurement. arXiv preprint arXiv:160205955. 2016 Feb 18;.

[215] Sun J, Simon S. The melting behavior of aluminum nanoparticles. Thermochimica Acta. 2007 Oct 25;463(1):32–40.

[216] Lopeandia AF, Rodriguez-Viejo J. Size-dependent melting and supercooling of Ge nanoparticles embedded in a SiO_2 thin film. Thermochimica Acta. 2007 Sep 15;461(1):82–7.

[217] Lai SL, Guo JY, Petrova V, Ramanath G, Allen LH. Size-dependent melting properties of small tin particles: nanocalorimetric measurements. Physical Review Letters. 1996 Jul 1;77(1):99.

[218] Allen G, Bayles R, Gile W, Jesser W. Small particle melting of pure metals. Thin Solid Films. 1986 Nov 15;144(2):297–308.

[219] Buffat P, Borel JP. Size effect on the melting temperature of gold particles. Physical Review A. 1976 Jun 1;13(6):2287.